Computational models for the pre-operative planning of spinal surgeries

A thesis submitted in partial fulfilment of the requirements for the degree of Doctor of Philosophy

By:

Marco Sensale

Supervisors:

Dr. Enrico Dall'Ara
Dr. Claudia Mazzà
Dr. Michel Rochette

The University of Sheffield
Faculty of Medicine, Dentistry & Health
Department of Oncology and Metabolism

December 2021

Acknowledgments

Several times during the last three years I thought about this section and the time when I would write acknowledgments of my thesis. I have read acknowledgments of many researchers and thought I would have also enjoyed the writing of my own to the fullest.

First and foremost, I am immensely grateful to Enrico Dall'Ara, my first academic supervisor, and to Michel Rochette, my line manager at Ansys. It is difficult to explain how lucky I have been to meet two wonderful people and professionals as you. You've been more than supervisors, transmitting to me every day a true passion for your work.

Enrico, in every single meeting we had I have deeply appreciated the fact that you always and constantly aimed at developing myself and my skills. Every challenge was to make me grow, to develop my independence and critical thinking. Every time I needed an answer, you put me on the appropriate path to find it on my own. We have worked remotely for three years and met just a few times in person, but you've been extremely willing to help, and I am grateful for that. Thank you also for the patience you had to thoroughly review this manuscript.

Michel, it is difficult to express in words my gratitude to you. You and Nadine welcomed me in your home as a member of your family. It has been a privilege to seat at your table more often than I sat at mine. You shared with me your food and wine culture and initiated me into the "art de vivre à la française". Michel, your passion for biomedical engineering and willingness to introduce pervasive simulation into the clinics is a source of inspiration. Thanks for pushing me to work closely with clinicians to bridge these two worlds.

Thank you also to Claudia Mazzà, my second supervisor, for her willingness to help and discuss over the last three years.

I would like to express my gratitude to Tanguy Vandeuvre, Arnaud Germaneau and Kévin Aubert for their warm welcome during my visiting periods in Poitiers and enriching discussions. Thanks to all the people I met at PRISMATICS at the CHU of Poitiers and their help with ethical approval procedures. I would like to acknowledge Abdollah Yassine Moufid for the help with the acquisition of data.

I wish to give a special thank you to all the great people I met at Ansys Lyon and their smiling and positive attitude which makes the Lyon office a legendary work environment. A big thanks to the Healthcare and ROM teams: Christelle, Clementine, François, Hussein, Jeroen, Juliette, Karim,

Kexin, Louise, Sophie, Romain, Valery, Wenfeng; to the guys from the support team Bruno, Oscar, Amanda, Gabriel, and also to Gianluca, Christine, Mounia and Bruno.

It is important to me to say thank you to the friends I made in Lyon and shared funny evenings during unprecedented times: Maxime, Lucas, Nicolas, Hongyi, Leonardo, Giammarco, Carlo, Dona, Filippo, Hugo. I owe a debt of gratitude to Leonardo for technical help with mesh morphing as well as food hunting when I contracted covid.

I would like to acknowledge also my funding from the H2020 Spinner project (Marie Skłodowska-Curie grant agreement Spinner No. 766012) and from the EPSRC MultiSim project (grant nr. EP/K038771X/1), as well as all the partners of the Spinner project that I collaborated with, in particular Aesculap and RBF-Morph. I also owe a great deal to Davide who helped me with the application to Spinner and for his support to find a PhD position, and to Carlos for the precious tricks he shared to write the thesis. I welcome this opportunity to thank the Spinn-ESRs Cameron, Chloé, Denata, Jennifer and Jose for sharing with me all the ups and down of this tricky and challenging journey over the last three years.

My acknowledgments would not be complete without thanking my big family and my friends from Montefalcione and Avellino, and ma petite puce Robi for their unconditional love.

À vaincre sans péril, on triomphe sans gloire!

Publications in scientific journals

Sensale M, Vendeuvre T, Schilling C, Grupp T, Rochette M, Dall'Ara E (2021)

Patient-Specific Finite Element Models of Posterior Pedicle Screw Fixation: Effect of Screw's Size and Geometry. Front Bioeng Biotechnol 9:643154.

doi: 10.3389/fbioe.2021.643154.

Presentations in international and local conferences

Sensale M, Vendeuvre T, Schilling C, Grupp T, Rochette M, Dall'Ara E. Sensitivity analyses for subject-specific Finite Element models of spine fixation, International Conference on the Virtual Physiological Human (VPH), 26-28th August, 2020, Paris (online), France. *Oral presentation.*

Sensale M, Geronzi L, Biancolini ME, Vendeuvre T, Rochette M, Dall'Ara E. Application of Reduced Order Modelling techniques for stress analysis in spine fixation, 26th Congress of the European Society of Biomechanics (ESB), 11-14th July, 2021, Milan (online), Italy. *Oral presentation.*

Sensale M, Vendeuvre T, Germaneau A, Grivot C, Dall'Ara E, Rochette M. Prediction of the shape of human lumbar vertebrae from adjacent ones by Singular Values Decomposition, XXVIII Congress of the International Society of Biomechanics (ISB), 25-29th July, 2021, Stockholm (online), Sweden. *Oral presentation.*

Sensale M, Vendeuvre T, Germaneau A, Grivot C, Dall'Ara E, Rochette M. Prediction of the pre-fracture shape of the L1 vertebral body from adjacent vertebrae, BioMedEng21 conference, 6-7th September, 2021, Sheffield (online), UK. *Poster presentation.*

Abstract

Spinal surgeries are common to treat different types of diseases and injuries as trauma, tumours, deformity and degenerative diseases. Conventional open spine surgery has several reported limitations and there is a trend towards minimally invasive techniques due to lower complication rates and morbidity. Percutaneous pedicle screw fixation and vertebral augmentation are two widespread minimally invasive techniques that are often chosen to treat vertebral fractures. The pre-planning of spinal surgeries is based on anatomical measurements taken on clinical images and on the experience of surgeons. Post-operative complications may arise impacting the quality of life of patients. Computational models can provide important patient-specific information about the biomechanics and the geometry of the spine.

Finite element (FE) models have the potential to predict the biomechanical outcomes of surgeries and are often proposed as possible tools for planning pedicle screw fixation. However, before their application, these models have to be verified and the sensitivity of metrics used to assess metal and bone failure have to be assessed with respect to the screw size and geometry. This was the aim of the first study. Patient-specific Computed Tomography (CT)-based FE models of the human vertebra with two pedicle screws were verified for both realistic and simplified geometry of screws. The diameter of the screw played a major role on the mechanics of the screw-vertebral structure with respect to the length. Simplified screws could accurately estimate the deflection and the strain of the implanted vertebrae, but resulted in a systematic underestimation of the peak stress in the screws. FE models can be used to optimize surgery-related parameters, but take a long time to compute and are thus insufficient to fulfil the demands of most clinical settings. Reduced Order Models (ROMs) are useful tools to improve the efficiency of FE models, and, in this thesis, were applied to FE models of the implanted vertebra to optimise screws' size and orientation showing accurate prediction of the deflection and the stress of the screws. A third study included the development of a CT-scan based procedure to estimate the pre-fracture 3D shape of a L1 vertebra that could be used by surgeons to restore the pre-fracture biomechanics. The methodology was validated on a dataset with 40 patients and showed excellent reconstruction accuracy.

In conclusion, FE models of the implanted vertebra were integrated with ROMs to build a computational pipeline for the optimisation of dimensions and positioning of pedicle screws. Also, the geometric pre-fracture shape of a L1 vertebra was reconstructed. These approaches can be used to provide more quantitative biomechanical and geometric information to surgeons for planning the treatment of vertebral fractures.

Abbreviations

BMD - Bone mineral density

CAD - Computer-Aided Design

CT- Computed Tomography

d_{max} – Maximum deflection

D – Diameter

DOE – Design of Experiments

DOF – Degrees of freedom

FE- Finite Element

GP – Gaussian Process

GPMM – Gaussian Process Morphable Model

HU – Hounsfield unit

KP – Kyphoplasty

L - Length

microCT- micro Computed Tomography

microFE- micro Finite Element

PCA – Principal Component Analysis

PDM – Point Distribution Models

RBF – Radial Basis Functions

ROM – Reduced Order Model

σ_{VM} – von Mises stress

SSM – Statistical Shape Model

SVD – Singular Value Decomposition

VA – Vertebral Augmentation

Contents

Chapter 1: Background

1.1 Summary

This chapter aims at providing the background information required to understand the research projects illustrated in the next chapters of the thesis. First, the fundamental aspects of bone anatomy will be reviewed with a particular focus on the human vertebra. Then, the clinical problem that is addressed in the thesis will be presented (i.e., vertebral fractures). The different approaches taken in the clinics to treat vertebral fractures will be discussed. A section will be dedicated to minimally invasive surgeries and the main post-operative complications related to these surgeries will be described. Afterwards, Finite Element modelling will be briefly described focusing on computational workflows to build vertebral models. In the last sections, a general introduction to Mesh Morphing and Reduced Order Modelling is briefly provided.

1.2 Bone anatomy

The skeletal system is made principally by bones, that are linked to each other by ligaments, tendons and cartilages to support and protect the human body. Bone is a composite material made of mainly two constituent materials: (1) an organic matrix composed of type I collagen fibers (85-90%), water (5-6%) and other organic substances (5%); (2) a mineral phase made of hydroxyapatite micro-crystals ($Ca_{10}(PO_4)_6(OH)_2$) that constitute over the 60-70% of the bone (Currey, 2006). It is possible to distinguish between cortical and trabecular bone according to the microstructure of the bone tissue. The exterior layer of all bones is cortical bone, which is mostly present in the appendicular skeleton, especially in the diaphysis of long bones (Monier-Faugere et al., 1998). Cancellous bone is mostly found in the axial skeleton, where it is present between the cortices of smaller flat and short bones like scapulae, vertebrae, and pelvis (Monier-Faugere et al., 1998). The microstructure of cortical bone is characterized by solid lamellar structures called osteons with a cylindrical shape (diameter of about 200 micron) (Cowin, 2013). The trabecular bone instead is a porous material characterized by a network of plate-and-beam like structures called trabeculae (thickness between 100 and 650 micron) (Cowin, 2013). The trabecular bone can present a high porosity (up to 50%) and the trabeculae are organised along the principal lines of stress which provide resistance to the load (Keaveny et al., 2001). The cavities of trabecular bone are filled with

bone marrow that is enriched with blood vessels and capillaries. Overall, cortical bone presents a higher density than trabecular bone. The proportion of the skeletal mass is about 80% cortical bone and 20% trabecular bone (Ott, 2018). Due to its composition and microstructure, bone is an inhomogeneous, anisotropic, non-linear material (Keaveny et al., 2004).

1.3 Anatomy of the human vertebra

The spine has the function of bearing the weight of the upper body and allowing extended motions thanks to the muscles acting on it. Consequently, evolution processes have shaped vertebrae and spinal structures to optimize their geometry in function of physiological loading (Noailly and Lacroix, 2012). From cranial to caudal, the 29 vertebrae composing the spine are often classified as cervical (C1-C7), thoracic (T1-T12), lumbar (L1-L5) and sacral (S1-S5). Each vertebra is composed of an anterior part, the vertebral body, and a posterior one, composed of different substructures called posterior elements (Figure 1.1). The vertebral body is constituted of a centre of trabecular bone surrounded by a thin cortical shell (thickness $\approx 0.38 \pm 0.06$ mm) (Eswaran et al., 2006) and two biconcave cortical endplates located at cranial and caudal faces of the vertebral body. Between the superior endplate of one vertebra and the inferior endplate of the adjacent vertebra, there are intervertebral discs. The vertebral bodies are linked to the posterior part of the vertebra through pedicles. Pedicles surround a channel, called vertebral foramen, that protects the spinal cord, other spinal nerves and blood vessels. Other posterior elements are the spinous process, the superior and inferior articular processes and the transverse process. Between inferior and superior processes of adjacent vertebrae there are facet joints.

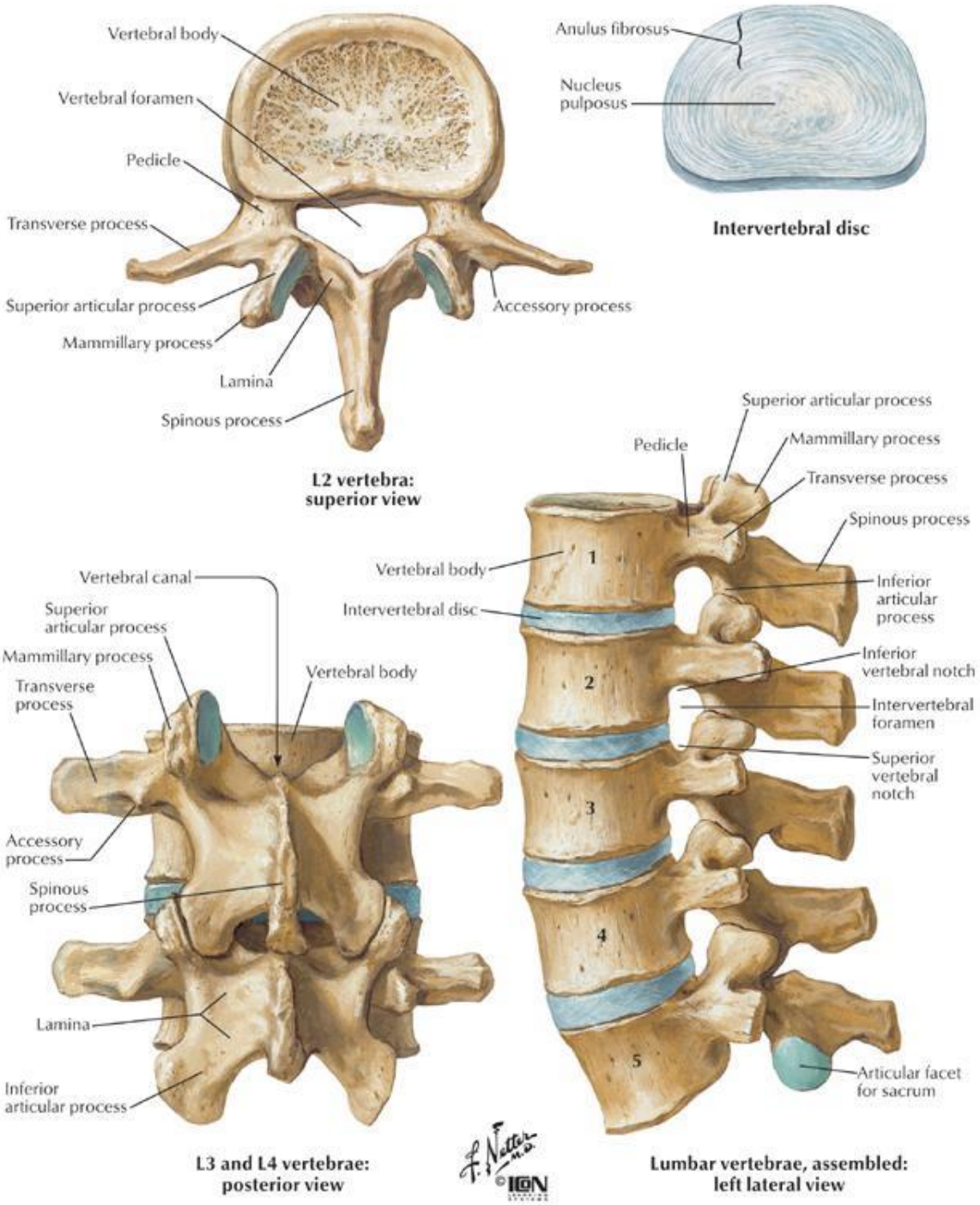

Figure 1.1 – Vertebral body anatomy. Reprinted from Thompson (2015).

1.4 Vertebral fractures

Many risk factors were identified in literature for vertebral fractures. Aging-associated-diseases, especially osteoporosis, bone metastases, and high-energy phenomena as falls, represent conditions with a high risk of fractures. In a recent review, Schousboe (2016) reported data referring to published studies on the epidemiology of vertebral fractures. Studies involving large cohorts of patients of different nationalities with a radiologic vertebral fracture, showed that the probability of a vertebral fracture to happen increased with age. Since the population is becoming older worldwide, proportionally, there will be more and more cases causing a lower quality of life and higher healthcare costs. Besides, it has been estimated that a vertebral fracture causes an increase in healthcare costs for the following 5 years when it occurs.

The epidemiology of fractures in England and Wales was studied retrospectively by van Staa et al., (2001). By analysing a large cohort of patients (about 220.000 cases of fractures both men and women) in a 10-years-period, the incidence of vertebral fractures was estimated as 4.5 persons per 10.000 persons each year. During the years, many systems have been proposed to classify the whole range of different types of vertebral fractures. In fact, there is a high variability between the different shapes of the fractured vertebrae according to differences between each loading scenario generating injuries and the underlying bone conditions. The purpose of these classification systems is not only to provide a general and shared terminology, but primarily to create a methodology upon which to base the treatment strategy and the clinical decision. Indeed, even if an accurate classification does not imply effective cures, which depend on the choices of the surgeon, it gives the possibility to monitor, assess, analyse, and modify the management of injuries in a systematic way. However, Pneumaticos et al., (2013) stated that there is still need of more accurate validation in prospective studies for the existing classification systems.

A well-established method of classification was proposed by Magerl et al. (1994). This classification system is used by our clinical partner at the University Hospital Centre of Poitiers (France) as a diagnostic tool, but it is not associated with a table of decision for the treatment. It is based on 1445 consecutive thoracolumbar fracture cases. It identifies three types of vertebral fractures (A, B and C) according to the three main actions generating the fracture: compression, distraction (tension) and axial torque, based on the assumption that the injury pattern is correlated with the mechanism (Figure 1.2). Each type is furtherly divided in three groups consistent with the morphology of fracture, and then in three subgroups with further specifications. Although the

degree of instability is not used directly as a criterion to build the classification, this system allows to identify a progressing degree of damage and instability of the spine from A to C, and within each group and subgroup.

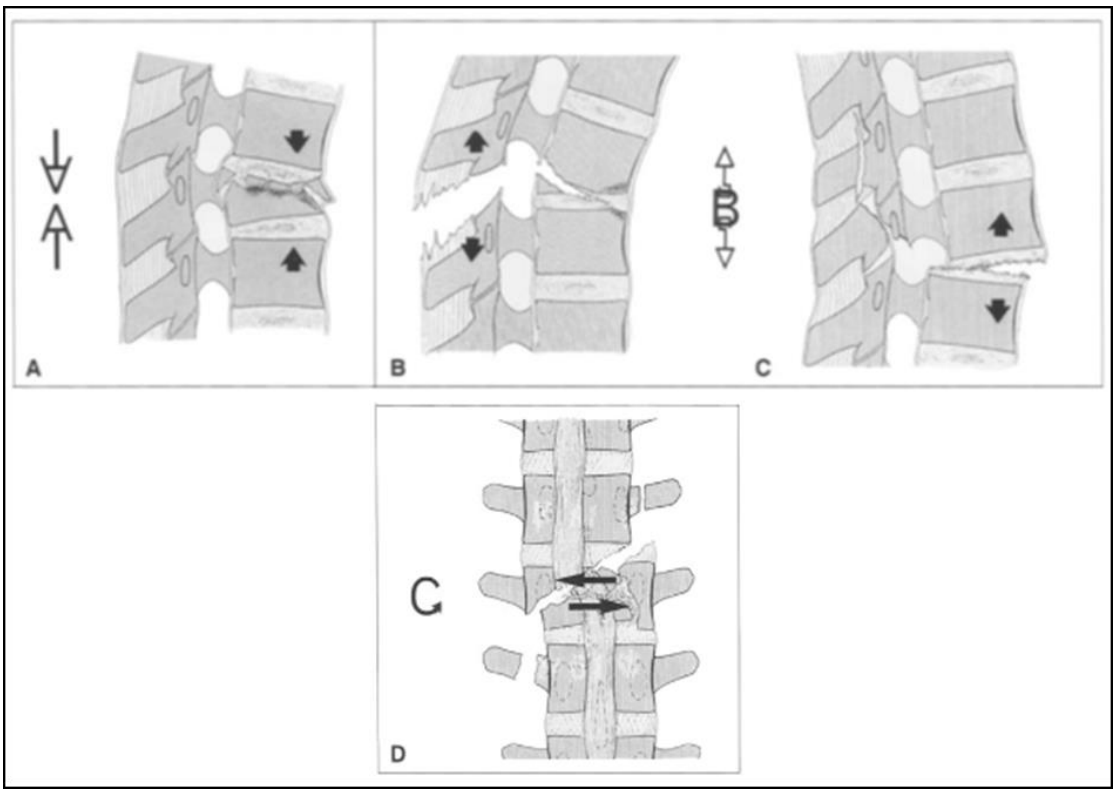

Figure 1.2 – Characteristics of the main types of injuries described in Magerl et al. (1994). (A) compression fracture of the anterior part; either posterior (B) or anterior (C) transverse disruption; (D) injury with rotation. Reprinted from Magerl et al. (1994) with permission.

Type A fractures represented 66% of the total, whereas type B and type C the 15% and 19 %, respectively. In that study, 48% of all spinal fractures occurred at the thoracolumbar junction, and in particular 28% at L1. This is the region between the thoracic and lumbar spine, where the curvature has an inflection point passing from convex, called kyphosis, to concave, called lordosis. While the thoracic region is more rigid, the lumbar spine is flexible, and a structural change happens in this zone which may generate a delicate and sensitive area (Blondel et al., 2011).

An important classification system was proposed by Genant et al., (1993) for the specific class of osteoporotic fractures based on a semi-quantitative approach with visual inspection. This method

uses X-ray images to identify the degree of vertebral height decrease and morphological changes with respect to adjacent vertebrae (Genant et al., 1993).

For young patients, the most common cause of compression fractures is a high-energy trauma with an acceleration-deceleration pattern. Often, it is the case of motor vehicle or motorcycle accidents or falls. On the other hand, fractures seem to be mainly due to osteoporosis in the elderly (Pneumaticos et al., 2013).

1.5 Surgical treatments of vertebral fractures

According to the AO Spine association, the main goals of any treatment of vertebral fractures are, in order of importance: the functional recovery of the injured neural elements; the anatomical reduction; a stable fixation; the preservation of vascularity; an early active mobilisation (Aebi, 2007). According to the severity of the injuries, surgeons must choose the optimal treatment to achieve these objectives in order of priority. Historically, there are two main currents for the treatment of vertebral fractures. A conservative approach foresees the usage of corsets, braces, or plaster casts to immobilize the spine without any surgical procedures. The goal of this approach is to allow the fracture to reduce spontaneously thanks to the natural properties of self-healing of the bone. The immobilisation facilitates this process by preventing movements and overloads. Many surgeons prefer to operate the spine to provide stability and guide the repairing process by means of instrumentations implanted in the spine (Kumar et al., 2015). In comparison with conservative treatment, an immediate mobilization and an earlier rehabilitation may follow an operative strategy, providing a better restoration of the sagittal curvature (Wood et al., 2014).

When a surgeon decides to operate, benefits deriving from surgery must override its associated risks. For example, an open surgery carries an associated morbidity due to infections, blood loss and a prolonged hospital stay to recover. To access the spine posteriorly, it is necessary to incise skin and paraspinal muscles. However, muscles play an important role in the biomechanics of the spine and their impairment influences the recovery.

1.5.1 Minimally invasive surgeries

Minimally invasive (MI) surgeries are associated with reduced healthcare costs for shorter intervening time, reduced risk of complications and faster recovery. For spine fractures, preservation of paraspinal muscles and soft tissues may result in improved stability because their functionality is left intact and may facilitate the recovery. Generally, less blood loss, reduced

scarring and risk of infections, in turn, reduce the morbidity connected with a minimally invasive surgery.

Pedicle screw fixation is the most common method for achieving spinal fusion and stabilisation in the lumbar spine (Verma et al., 2016). In the United States alone, over 415,000 spinal fusion procedures were done in 2018 (Rajaee et al., 2012). According to Fior Markets, the worldwide pedicle screw system market is expected to grow by roughly 32% from 2018 to 2025 (Fior Markets, 2019). Pedicle screw fixation is the primary surgical approach for treating a variety of spine illnesses as trauma, tumours, deformity (e.g., scoliosis surgery) and degenerative disease (herniated disc removal, spinal stenosis decompression and/or fusion aiming to avoid these problems) (Mobbs et al., 2011). In this thesis the focus will be mainly on the treatment of thoracolumbar fractures. In general, the idea of posterior fixation is to create a bridge by means of metal rods and screws to stabilize the fractured segment by shifting part of the load on the implant. In this way, there is a correction of the alignment of the segments, and fragments are in close proximity so that healing can occur. By posterior pedicle screw fixation screws are inserted a level (short-segment Figure 1.3A) or two levels (long-segment Figure 1.3B) above and below the fractured vertebra and are tight together by a rod with a pre-set curvature. Some surgeons added instrumentation also in the fractured vertebra (Mahar et al., 2007) (Figure 1.3C). Others proposed a mono-segment procedure where the above vertebra is fixed to the well-preserved segments of the fractured vertebra thus including only two vertebrae in the construct (Perera et al., 2015) (Figure 1.3D). Posterior fixation can be done as a minimally invasive treatment (percutaneous pedicle screw fixation) for numerous spinal pathologies (Mobbs et al., 2011).

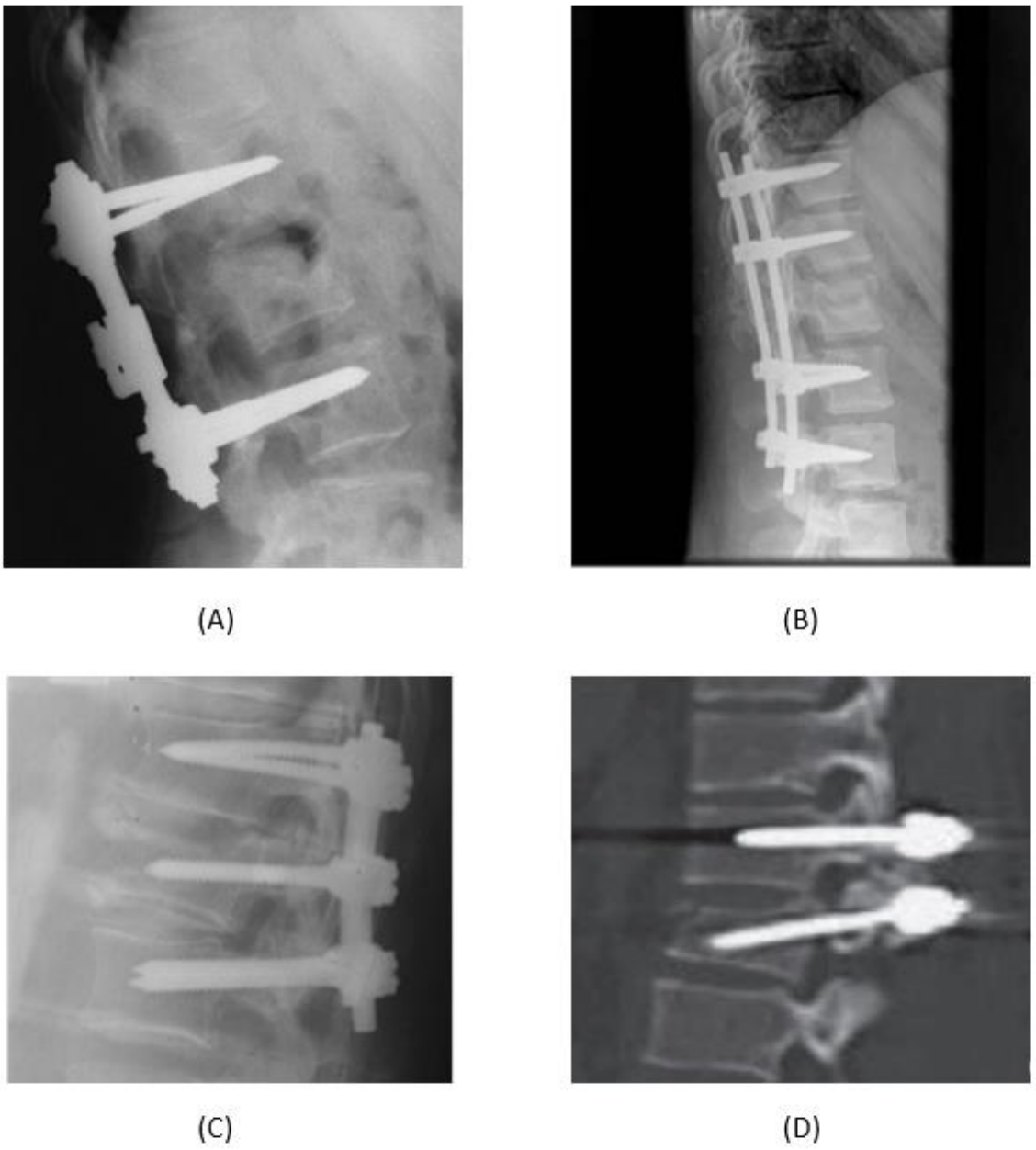

Figure 1.3 – Different techniques of posterior pedicle screw fixation. Short-segment (Sanderson et al., 1999) (A), long-segment (Kumar et al., 2015) (B), short-segment including fractured vertebra (Wang et al., 2013) (C) and mono-segment (Perera et al., 2015) (D) techniques. Images adapted with permission.

Percutaneous pedicle screw fixation (PPSF) has been performed alone or combined with vertebral augmentation (VA). VA consists in the injection of a biomaterial (usually a bone cement) in a vertebra through a percutaneous cannula (Figure 1.4). Bone cement has a short time of solidification and gives stability to the structure. When a dilatator is used in this procedure, it takes the name of

kyphoplasty (KP). A tube is inserted in the vertebra before inserting the cannula. Through this tube a balloon is inserted and inflated to obtain reduction of the fracture deformity and to restore the original height. Then, the balloon is deflated and removed, leaving a cavity. Bone cements typically used are Polymethyl methacrylate (PMMA) and calcium phosphate cement (CPC).

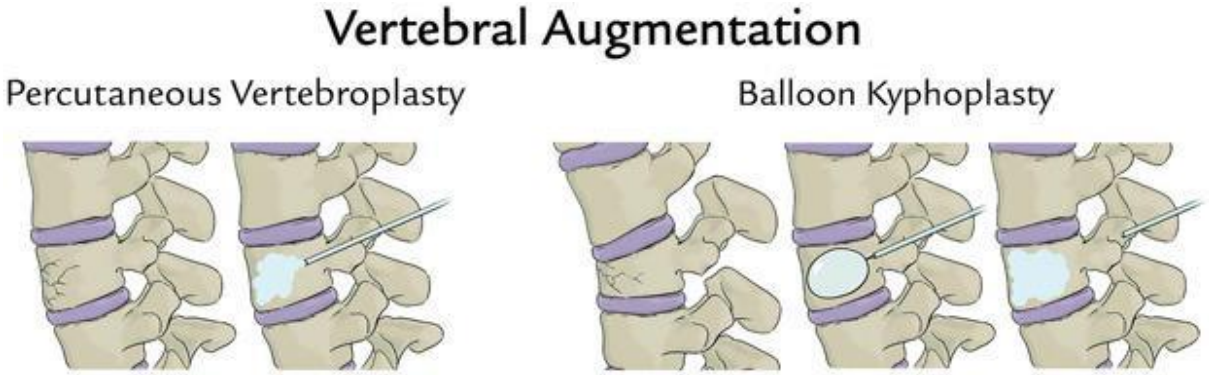

Figure 1.4 – Percutaneous vertebroplasty and balloon kyphoplasty. Reprinted from Ebeling et al. (2019).

1.5.1.1 Post-operative complications

Despite the extensive use of pedicle screws in the current clinical practice, different post-operative complications may arise. Inadequate reduction of the fracture, post-operative loss of reduction as well as wall fracture of the pedicle are common early post-operative problems that have been associated with mispositioned screws and narrow pedicles (Zhao et al., 2018). Screw loosening and screw breakage are recurring late mechanical complications of spinal fixation that can bring to a revision surgery in about 6% of cases (Prud'homme et al., 2015; Bredow et al., 2016). Screw loosening and breakage have been associated to different phenomena (Galbusera et al., 2015). When pedicle screws are implanted, the load applied on the spine is shifted from the bones to the implants. Consequently, the stimulus for bone remodelling diminish and the bone will become less dense and weaker in the region around the implant (stress shielding). In some cases where there is no adequate anterior support, the bone/screws interface is overloaded and subjected to high stresses and strains, that could result in microfracture of the bone and consequent mobility of the screws. The risks of screw loosening and breakage are amplified in case of osteopenic or osteoporotic bone, which has a reduced capability to support stresses without failure (Ponnusamy et al., 2011). Indeed,

in elderly female patients with deteriorated Bone Mineral Density (BMD) postoperative vertebral fracture following posterior spinal instrumentation fusion had higher incidence than patients aged under 70 years (Nakahashi et al., 2019). Screws positioning and angular orientation have been shown to essentially impact the screw–bone load mechanism, hence examined to decrease the rate of post-operative complications both experimentally and numerically (Zindrick et al., 1986; Santoni et al., 2009; Ueno et al., 2015; Newcomb et al., 2017; Molinari et al., 2021). In the current clinical practice, the size of pedicle screws is chosen by taking anatomical measurements on clinical images without considering the biomechanics of the spine from a quantitative and patient-specific point of view.

Among side effects of VA, attention should be paid to cement leakage. If cement leaks to the spinal cord or nerve roots, there can be neurologic deficit. Other vital organs close to the vertebral bodies may be impaired too. Complications may also arise if there is an outflow of cement in blood circulation as it may reach the lungs and cause pulmonary embolism. However, it has been proposed that the compression of trabecular bone due to the inflation of the balloon itself, may create a layer which prevents cement from leaking into the spinal canal (Zhao et al., 2018). Additionally, some authors investigated the effect of VA on the adjacent levels (Uppin et al., 2003). In fact, VA is correlated with the risks of adjacent vertebral fractures. First, cement increases the stiffness of the whole segment altering the biomechanics of load transfer to adjacent vertebrae (Berlemann et al., 2002). Secondly, after the reduction of the fracture by VA there may still be a loss of height of the vertebral body with respect to the pre-fracture shape, i.e., an increase of thoracic kyphosis, the inversion of lumbar lordosis and the forward shift of the centre of gravity. In normal conditions, the muscular efforts needed to maintain the upright position are minimal; when an anterior unbalance of the gravity line happens in consequence of a vertebral fracture, the gravity line is shifted anteriorly resulting in an increased bending moment. In these cases, the efforts to keep the balance are much higher as complex compensatory mechanisms at the musculo-ligamentous system happen, resulting in pain and degradation of the spine. Therefore, from a mechanical point of view, it is essential to restore the anterior heights in order to create backward bending moment, preserving the spine and reducing the risk of fracture of the nearest vertebrae (Pesce et al., 2013). In fact, after a vertebral fracture a reduction of the height of the vertebral body is frequent (Genant et al., 1993). Because of the lack of information at the time before the fracture, it is challenging to estimate which is the entity of the height that must be restored following a vertebral fracture.

1.6 Finite Element (FE) models

One common problem in structural mechanics is to determine the mechanical response of a structure subjected to a certain loading condition. This problem could be solved in closed form for structures with simple geometries and material properties. Instead, for more complex situations an analytical solution is very difficult to obtain. Numerical methods are key to solve those problems that require complex calculations. The Finite Element (FE) method is a numerical technique that gives an approximate solution to problems that are difficult to solve in a closed form due to complex geometries, non-linear material properties and difficult boundary conditions (Zienkiewicz et al., 2000). In FE models, the geometry of complex structures is discretized through small components of a pre-defined shape (e.g., tetrahedrons) which are called elements. Elements are defined by their nodes, which, in turn, are associated to a certain number of degrees of freedom (DOF) (displacements or rotations). According to the element type used in the FE model, the edges of each element can have a linear, a quadratic or higher order shape based on the degree of the associated polynomial shape function. In structural problems, the nodal DOFs and loads of each element are related by an element stiffness matrix that depends on the geometry of the element and its material properties. By assembling the stiffness matrix of each element of the structure, a global stiffness matrix is calculated. After the application of boundary conditions to describe the interaction of the structure with external systems, the equilibrium equations are solved and DOFs are calculated. Once the DOFs are obtained, the strains are calculated by differentiation, and the stresses by using stress-strain relationships. In cases where large deformations occur, or the mechanics of contact forces is non-linear, or material properties are non-linear, the stiffness matrix is not constant during the load application. One of the most common methods to solve non-linear analyses is the Newton-Raphson method (Fung et al., 2017). With this method, the load is divided in small load increments, and, for each increment, a linear approximation of the solution is found in an iterative process. FE modelling was introduced in biomedical engineering in recent years as an effective tool to simulate different conditions of human structures (Fagan et al., 2002).

1.6.1 Patient specific FE models of the vertebra

The FE method is a convenient tool to explore the spine as its physiology and pathology are influenced by complex mechanical factors. FE analyses allow the acquisition of quantitative information that is hard to access in experimental or clinical settings as stress or strain fields within the tissues. However, FE models require thorough verification and validation protocols, or alternatively could be calibrated on a clinical basis.

FE models of the vertebrae are generated based on CT-scan images. The resolution of clinical CT-scan images allows to isolate the external surface of the vertebrae from adjacent soft tissues, while it cannot resolve the internal architecture and microstructure. In this case, the vertebra is modelled as a continuum structure. A particular class of FE models are homogenised FE models (Figure 1.5): the bone is modelled as heterogeneous material and material properties are derived by local BMD estimated by CT-scan images (Kopperdahl et al., 2002; Schileo et al., 2008). In fact, the grey levels (or Hounsfield units - HU) of CT-scan images represent the X-ray attenuation coefficients which are a function of the density of the scanned object. If the CT-scan is equipped with a hydroxyapatite-equivalent calibration phantom, it is possible to convert the HUs to equivalent BMD values. The phantom can be scanned simultaneously with the patient (in-line calibration phantoms) or off-line. The equivalent BMD values are then converted to Young's moduli thanks to experimental equations that depend on anatomic site due to differences in bone architecture (Morgan et al., 2003). The heterogeneous material properties can be mapped directly from the CT-scan images element by element. As information about the geometry of trabeculae and the cortical shell of vertebrae cannot be measured by CT-scan images, the bone is assumed as isotropic material.

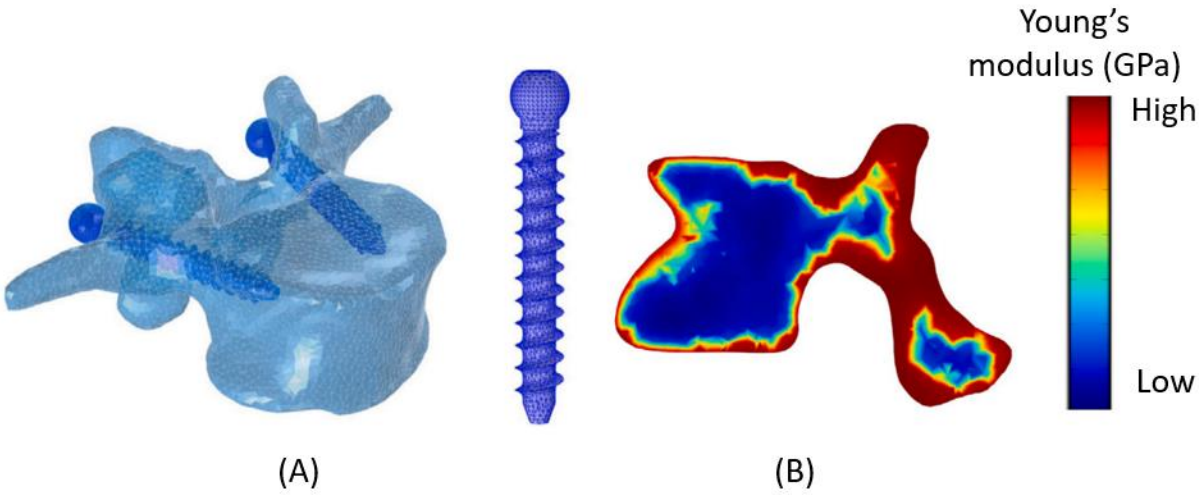

Figure 1.5 – Homogenised FE model of the human vertebra implanted with two pedicle screws. Discretization with unstructured tetrahedral mesh (A) and colour map representing the distribution of elastic modulus (B). Adapted from Molinari et al., (2021).

Vertebrae can be meshed with tetrahedral (Pahr et al., 2014) or hexahedral elements (Dall'Ara et al., 2012). With a voxel-based Cartesian mesh the hexahedral elements are obtained directly by CT-scan voxels, but they are unable to represent the smooth boundaries of the bone surface. On the other hand, a smooth mesh with tetrahedrons allow to better represent the geometry of the vertebra, but requires more complex pre-processing for the generation of the mesh. Both meshing methods are affected by the partial volume effect which corresponds to an averaging of the attenuation coefficients of the structures on the boundaries of the bone resulting in lower grey levels for the cortical bone (Varghese et al., 2011).

The reliability of predictions of FE models of the vertebra depends on the boundary conditions that, to be clinically relevant, need to mimic the *in-vivo* system. The mechanical loads that act on the spine in physiological conditions are mainly due to the upper body weight and any voluntary motions that are transmitted to spinal structures through the action of muscles, posterior elements, and intervertebral discs. By combining the effect of those elements, FE models may be loaded to achieve flexion, extension, lateral bending, axial rotation, compression. When implants are modelled, forces could be applied to the vertebra, to the implant or to both. The definition of boundary conditions to simulate physiological loads is a complex task as the loading acting on the spine and the contribution of each sub-structure have not been fully characterized yet (Molinari and Falcinelli, 2021). In fact, little is known about loading conditions acting on the vertebrae in daily activities due to the limitations of *in vivo* measurements, as for example intervertebral disc pressure or loads on internal spinal fixation devices (Rohlmann et al., 1997, 2008). Computational musculoskeletal models can be used to predict the loads acting on the spine taking into account the effect of muscles, ligaments and other anatomical parts. However, the validation of musculoskeletal models is challenging due to the difficulty to measure the predicted forces (Ignasiak et al., 2016). and it is hard to apply these models in the clinical setting as it is not possible to inform the models with patient-specific data (e.g., gait analysis).

1.7 Mesh morphing

Mesh morphing is a computational method for adapting an existing mesh to a new CAD (Computer-Aided Design) geometry. This method is especially well suited to complicated geometries that cannot be automatically meshed, as well as to optimization problems requiring a high number of design modifications. For example, the solid mesh of a lumbar vertebra of one patient could take a new shape by updating the positions of nodes (Figure 1.6). In this way, the topology of the mesh (number of nodes, number of elements, table of connectivity) remains the same, and only the coordinates of nodes undergoing a shape modification are updated.

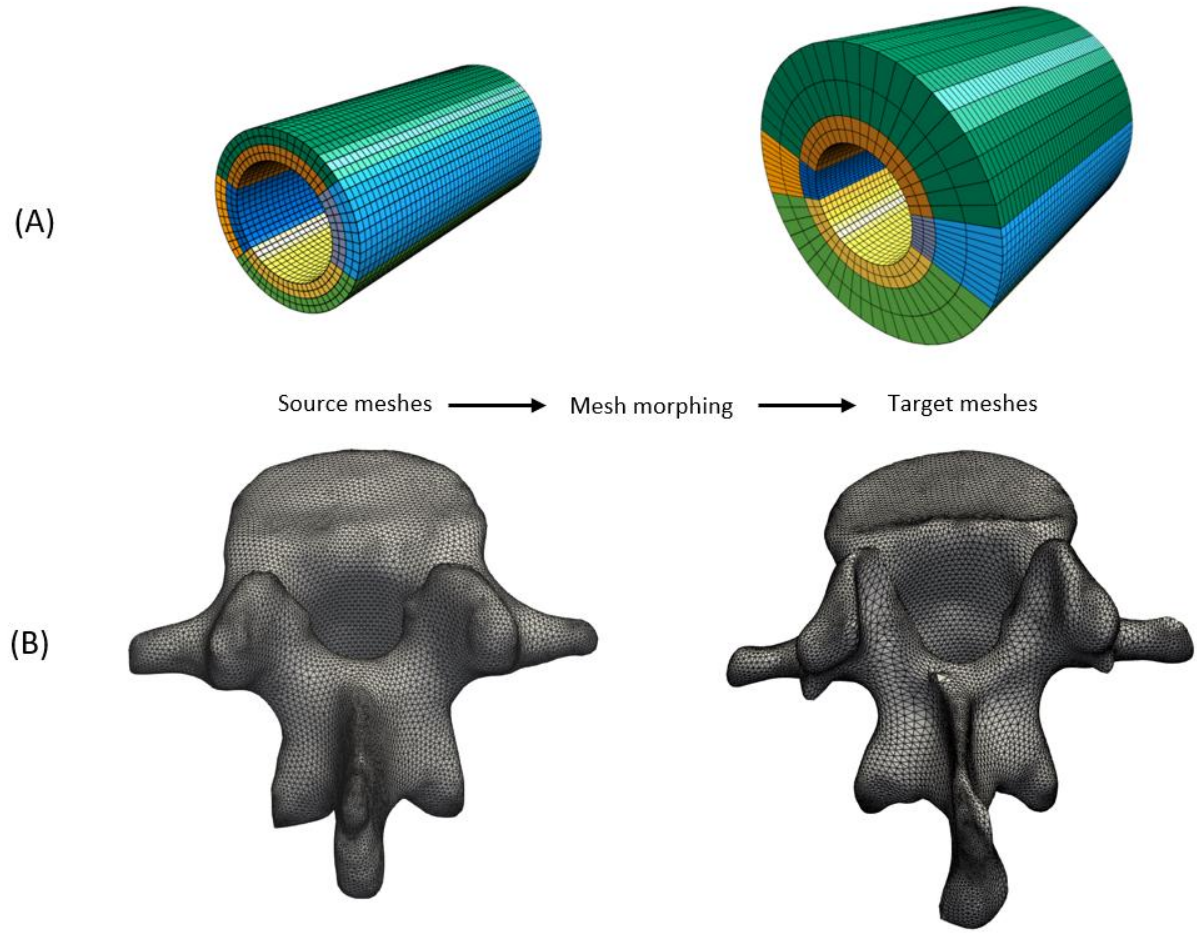

Figure 1.6 – Application of mesh morphing to an hexahedral mesh of a hollow cylinder (Sieger et al., 2013) (A) and to a tetrahedral mesh of a lumbar vertebra (B). Image adapted with permission from Sieger et al., (2013).

Mesh morphing presents different advantages with respect to typical remeshing. First, it avoids the generation of remeshing noise, in fact, as the same mesh is adapted to a new shape, the effect of one parameter under study is not confused with the effect of a new mesh. Secondly, it allows to build a Reduced Order Model (ROM) based on reduced basis approaches (see Section 1.8) that aims at exploring the effect of shape modifications of the model. In fact, for the nature of compression methods used to build the ROM, the topology of the mesh has to be consistent among different models. Some distortion of the elements deformed by mesh morphing (stretching/compression) may occur and it is important to preserve the quality of the morphed mesh. Mesh morphing approaches seek to preserve element quality as much as possible, allowing for as many geometric changes as feasible before remeshing is required due to element inversion.

In the following sections, a brief introduction to two different methods to perform mesh morphing is provided. Gaussian Process Morphable Models were used in this thesis to morph triangular meshes and build statistical shape models of the lumbar vertebrae. Radial Basis Functions mesh morphing is more suited to morph volumetric meshes, and it was used in this thesis to adapt the mesh of a vertebra implanted with pedicle screws.

1.7.1 Mesh morphing through Gaussian Process Morphable Models (GPMM)

Gaussian Process Morphable Models (GPMM) are a generalization of Point Distribution Models (PDMs), which are an important class of statistical shape models (SSMs). In PDMs, the shape Γ_i of an object is represented by a vector $\boldsymbol{s}_i \in \mathbb{R}^{3N}$ containing the position x, y, z of N points (nodes) belonging to its external surface:

$$\boldsymbol{s}_i = (x_1^i + y_1^i + z_1^i, \dots, x_1^N + y_1^N + z_1^N) \qquad \text{(Eq. 1.1)}$$

It is assumed that shape variations can be modelled through a normal distribution:

$$\boldsymbol{s} \sim \mathcal{N}(\bar{\boldsymbol{s}}, \boldsymbol{S}) \qquad \text{(Eq. 1.2)}$$

where the mean shape $\bar{\boldsymbol{s}}$ and the covariance matrix $\boldsymbol{S}$ are estimated from the data:

$$\bar{\boldsymbol{s}} = \frac{1}{n}\sum_{i=1}^{n} \boldsymbol{s}_i \qquad \text{(Eq. 1.3)}$$

$$\boldsymbol{S} = \frac{1}{n-1}\sum_{i=1}^{n}(\boldsymbol{s}_i - \bar{\boldsymbol{s}})\ (\boldsymbol{s}_i - \bar{\boldsymbol{s}})^T \qquad \text{(Eq. 1.4)}$$

Starting from the n data-sets in correspondence, the covariance matrix $\boldsymbol{S}$ can be represented using n mode vectors through Principal Component Analysis (PCA):

$$\boldsymbol{s} = \bar{\boldsymbol{s}} + \sum_{i=1}^{n} \alpha_i \sqrt{d_i}\, \mathbf{u}_i \qquad \text{(Eq. 1.5)}$$

where $(\boldsymbol{u}_i, d_i), i = 1, \dots, n$ are the eigenvectors and eigenvalues of the covariance matrix $\boldsymbol{S}$ and α_i are scalar coefficients. The point distribution model $\boldsymbol{s}$ could be seen as a model of deformations $\boldsymbol{\phi} = \sum_{i=1}^{n} \alpha_i \sqrt{d_i}\, \mathbf{u}_i \sim \mathcal{N}(0, \boldsymbol{S})$ that is added to the mean shape $\bar{\boldsymbol{s}}$. Therefore, the deformations of the mean shape are modelled through a normal distribution. Similarly, GPMMs define a probabilistic model on the deformations. However, this model is independent from the example data and is defined based on analytical functions. In fact, the deformations are modelled as a Gaussian Process (GP) characterised by a covariance function (or kernel) k. The covariance function does not need to be learned from data, but any positive definite covariance function can be used. In this way, it is possible to define models that have any capability of deformation. A common kernel which is able to enforce smooth deformations is the Gaussian kernel, defined as:

$$k_g = e^{-\frac{\|x-y\|^2}{\sigma^2}} \qquad \text{(Eq. 1.6)}$$

where the parameter σ is associated the degree of smoothness of the deformation field (Luthi et al., 2018) (Figure 1.7).

A Gaussian process may be represented using a set of basis functions, similar to how a PDM can be represented using PCA. Once the GPMM is created, this can be deformed in order to fit a target shape. This results in a non-rigid registration approach, also known as mesh morphing. The purpose of the registration problem is to find the deformation field that put in relationships the source and the target shapes. This problem may be expressed as a minimization problem where a measure of the distance between the two shapes is minimised. Any mesh morphing algorithm that is conceived to work with PDMs is suitable to GPMM fitting (Cootes et al., 1995; Vanden Berghe et al., 2017) because the models have a similar structure based on principal modes of deformation.

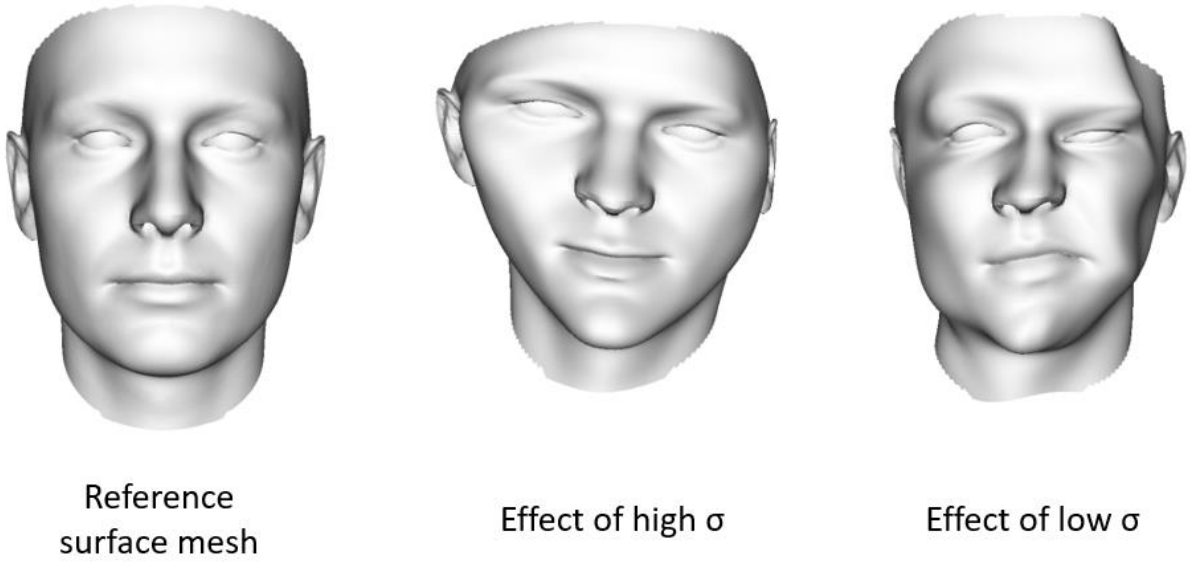

Figure 1.7 – Gaussian Process Morphable Models based on a Gaussian kernel applied to a surface mesh of the human face. Smooth global deformations or local deformations may be applied by using high or low values of the parameter σ. Adapted from Luthi et al., (2018).

1.7.2 Radial Basis Functions (RBF) mesh morphing

Radial Basis Functions (RBF) mesh morphing is a class of mesh morphing algorithms that takes its name from the type of functions used in this method (Biancolini, 2017). Known displacements must be assigned to a limited and sufficient number of control points in the space (these control points must not necessarily be physical nodes of the mesh, i.e., it is a meshless method) and then, through interpolation, the displacement of the whole set of nodes is calculated to obtain the morphing. This interpolation is performed through RBFs (Figure 1.8).

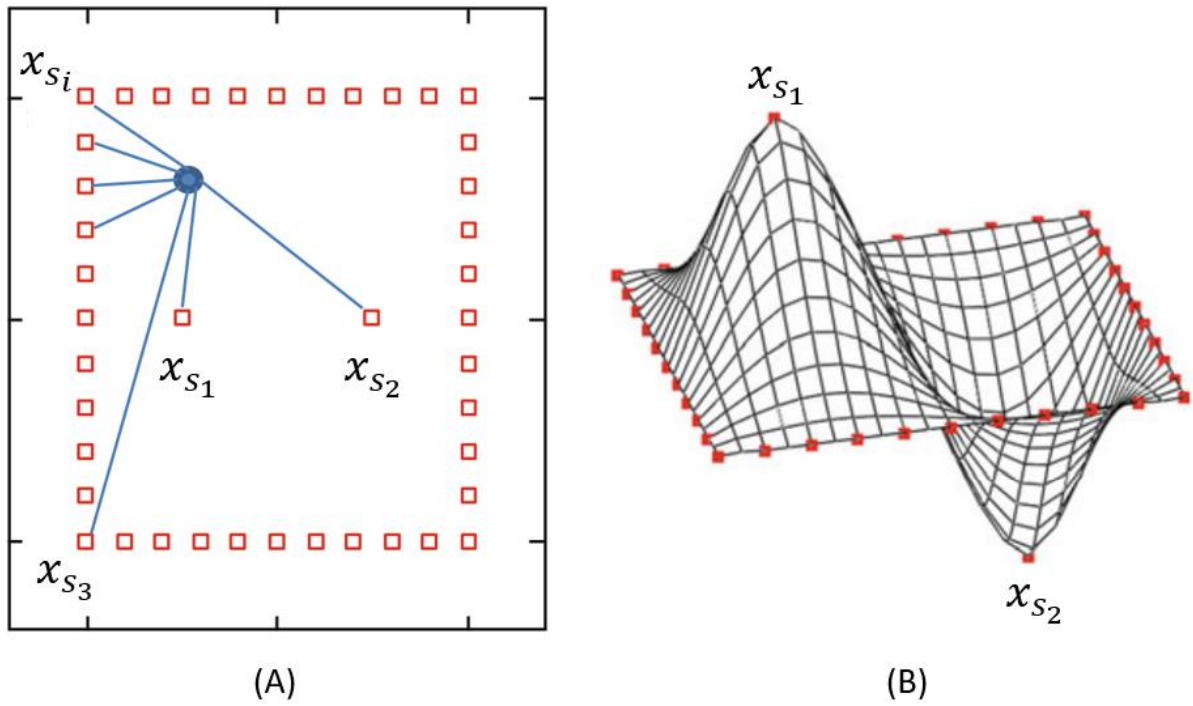

Figure 1.8 – Example of RBF mesh morphing on a two-dimensional quadrilateral grid. Displacements are assigned to control points highlighted in red (A). $\boldsymbol{x}_{s_1}$ and $\boldsymbol{x}_{s_2}$ have non-zero opposite displacements, while other control points have zero displacements. The effect of the displacement field interpolated through RBFs is showed onto the deformed configuration of a uniformly spaced mesh defined inside the square (B). Images adapted from Biancolini, (2017).

The new nodal positions after interpolating the displacements can be calculated per each node as:

$$\boldsymbol{x}_{\boldsymbol{node}_{\boldsymbol{new}}} = \boldsymbol{x}_{\boldsymbol{node}} + s_x\,(\boldsymbol{x}_{\boldsymbol{node}})\,s_y\,(\boldsymbol{x}_{\boldsymbol{node}})\,s_z\,(\boldsymbol{x}_{\boldsymbol{node}}) \qquad \text{(Eq. 1.7)}$$

where $s(\cdot)$ is a scalar interpolation function which represents a transformation $\mathbb{R}^N \rightarrow \mathbb{R}$. The interpolation function is composed by an RBF and by a polynomial term $h(\boldsymbol{x})$ that is added to ensure the uniqueness of the problem and polynomial precision allowing to retrieve exactly rigid body motions:

$$s(\boldsymbol{x}) = \sum_{i=1}^{N} \gamma_i \varphi\left(\|\boldsymbol{x} - \boldsymbol{x}_{\boldsymbol{c}_i}\|\right) + h(\boldsymbol{x}) \qquad \text{(Eq. 1.8)}$$

where N is the number of control points, γ_i are scalar weights, φ is the basis function that has centre at control points and depends on the distance between the nodes of the mesh to morph $\boldsymbol{x}$ and the control points $\boldsymbol{x_{c_i}}$. In fact, once the coefficients are found, the displacement of a given node of the mesh can be calculated as the superimposition of the radial contributions of each source point.

The weights and the coefficients of the polynomial functions can be found by imposing that the interpolated displacements at control points must be exactly those assigned to control points g_s:

$$s(\boldsymbol{x_{c_i}}) = g_{s_i}, \qquad 1 \leq i \leq N \tag{Eq. 1.9}$$

Also, a condition of orthogonality on the polynomial functions is needed to determine the interpolant. If the function φ is a conditionally positive definite function of order m ≤ 2, a linear polynomial can be used. In a 3D space the linear polynomial has the form:

$$h(\boldsymbol{x}) = \beta_1 + \beta_2 x + \beta_3 y + \beta_4 z. \tag{Eq. 1.10}$$

The linear system of equations can be written in matrix form as:

$$\begin{bmatrix} \boldsymbol{M} & \boldsymbol{P} \\ \boldsymbol{P^T} & \boldsymbol{0} \end{bmatrix} \begin{bmatrix} \boldsymbol{\gamma} \\ \boldsymbol{\beta} \end{bmatrix} = \begin{bmatrix} \boldsymbol{g} \\ \boldsymbol{0} \end{bmatrix} \tag{Eq. 1.11}$$

where **M** is the interpolation matrix containing all the radial interactions between control points:

$$M_{ij} = \varphi\left(\|\boldsymbol{x_{c_i}} - \boldsymbol{x_{c_j}}\|\right), \qquad 1 \leq i \leq N, 1 \leq j \leq N \tag{Eq. 1.12}$$

P is the matrix containing the polynomial terms that has for each row *j* the coordinates of control points in the form $P_j = \begin{bmatrix} 1 & x_{c_j} & y_{c_j} & z_{c_j} \end{bmatrix}$, $\boldsymbol{g}$ the known terms of displacement at control points. To determine a deformation field in 3D, each component of the displacement assigned to control points is interpolated as:

$$s_x(\boldsymbol{x}) = \sum_{i=1}^{N} \gamma_i^x \, \varphi\left(\left\|\boldsymbol{x} - \boldsymbol{x_{c_i}}\right\|\right) + h^x(\boldsymbol{x}) \qquad \text{(Eq. 1.13)}$$

$$s_y(\boldsymbol{x}) = \sum_{i=1}^{N} \gamma_i^y \, \varphi\left(\left\|\boldsymbol{x} - \boldsymbol{x_{c_i}}\right\|\right) + h^y(\boldsymbol{x})$$

$$s_z(\boldsymbol{x}) = \sum_{i=1}^{N} \gamma_i^z \, \varphi\left(\left\|\boldsymbol{x} - \boldsymbol{x_{c_i}}\right\|\right) + h^z(\boldsymbol{x})$$

In this study RBF Morph software was used for mesh morphing (Biancolini, 2017; RBF Morph). Coordinates of control points together with respective assigned displacements are passed directly to the RBF Morph solver to determine the displacement of all the nodes subjected to mesh morphing.

1.8 Reduced Order Modelling

Reduced Order Modelling (ROM) techniques allow to reduce the computational cost of complex numerical simulations associated with parametric workflows, as for example optimization, statistical sampling etc, without simplifying the underlying physics of the model. Real-time *online* computations are obtained after a more intensive *offline* phase that must be done beforehand.

Reduced basis approaches are a class of *a posteriori* ROM techniques founded on the processing of a set of training solutions available from previous simulations (called snapshots). The core concept is to approximate the response of the model in the space of parameters based on a limited number of runs. In fact, reduced basis approaches aim at reducing the number of variables (i.e., the dimensionality of solution vectors) of the model by projection on a certain basis. If the underlying model is a FE model, the solution vectors are the results of simulations evaluated on the nodes of the mesh. Therefore, their size is a multiple of the number of nodes considered, depending on if the quantity of interest is a scalar or a field. Principal component analysis (PCA) can be used to build a reduced basis from a set of snapshots. The extrapolation of the reduced basis from the snapshots is mathematically done by Singular Value Decomposition (SVD). Considering $\boldsymbol{M}$ as the matrix in which each column represents the values of each snapshot $\boldsymbol{s_i}$, this matrix can be written as:

$$\boldsymbol{M = U \, \Sigma \, V^T} \qquad \text{(Eq. 1.14)}$$

where $\boldsymbol{\Sigma}$ is a diagonal matrix composed of σ_i the singular values of $\boldsymbol{M}$ matrix, $\boldsymbol{U}$ and $\boldsymbol{V}$ are composed of the left singular vectors and the right singular vectors, respectively. The matrix $\boldsymbol{M}$ can be approximated by a linear combination of the first r left singular vectors $\boldsymbol{u_i}$, typically called modes. Once the basis has been built, the snapshots can be projected on the basis and expressed in terms of the coefficients α_i and the modes of the basis:

$$\boldsymbol{s}_i = \sum_{\boldsymbol{i=1}}^{\boldsymbol{r}} \alpha_i \, \boldsymbol{u_i} \qquad \text{(Eq. 1.15)}$$

This allows to express the snapshots with a reduced dimensionality that depends on the number of modes chosen to build the basis. In fact, for each mode within the basis, the coefficients of modes of the snapshots are interpolated to build a response surface. The ROM is the result of the construction of the response surfaces of the coefficients α_i of each mode as a function of the input parameters (Ben Salem and Tomaso, 2018). The ROM allows to obtain the basis coefficients α_i at points that were not considered for construction of the basis with a certain approximation error, and therefore significantly reduce the dimensionality of the response of a system by expressing it in terms of its basis coefficients.

The construction of a ROM relies on the definition of an appropriate Design of Experiments (DOE). Once defined the space of variability of input parameters, the number of learning snapshots and their location within the parametric space must be defined. Different types of designs have been proposed as Full factorial design, Fractional factorial design, Central-Composite design, Box-Behnken design etc., that can be chosen according to the amount of runs that can be computed and the target error of approximation. ROM is particularly challenging in case of a large number of input variables and output quantities that are high dimensional fields (for instance, the field resulting from the six independent components of the stress or the strain tensors in each node of one structure) as the number of simulations needed to build the ROM varies exponentially with respect to the number of input parameters. The computational cost associated with the construction of the learning snapshots may be high according to the complexity of the model and some methods have been proposed to efficiently choose the number of learning snapshots (Gogu and Passieux, 2013). The accuracy of the ROM must be tested not only on the learning snapshots, but also on a set of results that were not used to build the ROM. This is called validation and is fundamental to assess

the performance of the ROM and the error of approximation within the space of variability of inputs. The validation-set/learning-set size ratio has to be chosen according to the application.

Chapter 2: Motivations and Literature review

2.1 Finite Element models of pedicle screw fixation

The biomechanics of human vertebrae implanted with pedicle screws has been studied with patient-specific FE models including multiple vertebral levels (Li et al., 2014; Xu et al., 2014; Elmasry et al., 2017; Su et al., 2018; Wang et al., 2018, 2019; Liu et al., 2019) or a single level (Chen et al., 2003; Chevalier et al., 2018; Bianco et al., 2019; Matsukawa et al., 2020; Molinari et al., 2021). Different failure modes of the instrumented structure (screw breakage, screw migration, screw loosening etc.) have been investigated by considering metrics both in the bone or in the implants.

Patient-specific FE models of the thoracolumbar spine instrumented with rods and screws aimed at comparing different posterior fixation techniques with respect to the mechanical stability and the risk of rupture of the construct (Li et al., 2014; Xu et al., 2014; Elmasry et al., 2017; Su et al., 2018; Wang et al., 2018, 2019; Liu et al., 2019). In fact, these studies focused on failure modes associated with the implants as instrumentation failure.

The insertion of additional pedicle screws at the intermediate (fractured) level increased the stiffness of the construct and lowered the von Mises stress on implants, and, therefore, the risk of rupture of implants, with respect to the traditional technique with pedicle screws one level above and one level below the fractured vertebra (Li et al., 2014; Wang et al., 2018) (Figure 2.1A). If the fractured level was instrumented, a unilateral procedure was indicated as a better option than a bilateral one because it is equally stable but less invasive (Su et al., 2018) (Figure 2.1B). A broadly similar point has also recently been made by Liu et al., (2019), who highlighted the importance of using polyaxial screws at upper or fractured level to decrease the peak Von Mises stress of the rods and provide larger ranges of motion. A reduction of the number of levels included in the construct to only two levels (included the fractured one) resulted in preserving the adjacent segments as the stress at adjacent levels and intervertebral discs diminished (Wang et al., 2019) (Figure 2.1C). This result conflicts with Xu's et al., (2014) study which found that the biomechanics of the instrumented segment in terms of ranges of motion and stress of bony and metal structures was not improved by adding pedicle screws at the fractured level. While pedicle screws at the fractured level were found to improve the performance of the construct, a long-segment fixation with screws from two levels above to two levels below the fractured level was indicated as a biomechanically superior option (Elmasry et al., 2017) (Figure 2.1D). However, FE models of spine segments and implants are often

based on a non-realistic geometry of the fractured vertebra, often modelled as a resected vertebra (Figure 2.1), and on the assumption of many different parameters (e.g., material properties of soft-tissues; geometry of discs, cartilages and ligaments) which are not easily identifiable from CT-scan images. Therefore, it is difficult to understand the impact of these parameters on the outcomes of the simulations, and to verify and to validate the model against experimental measures.

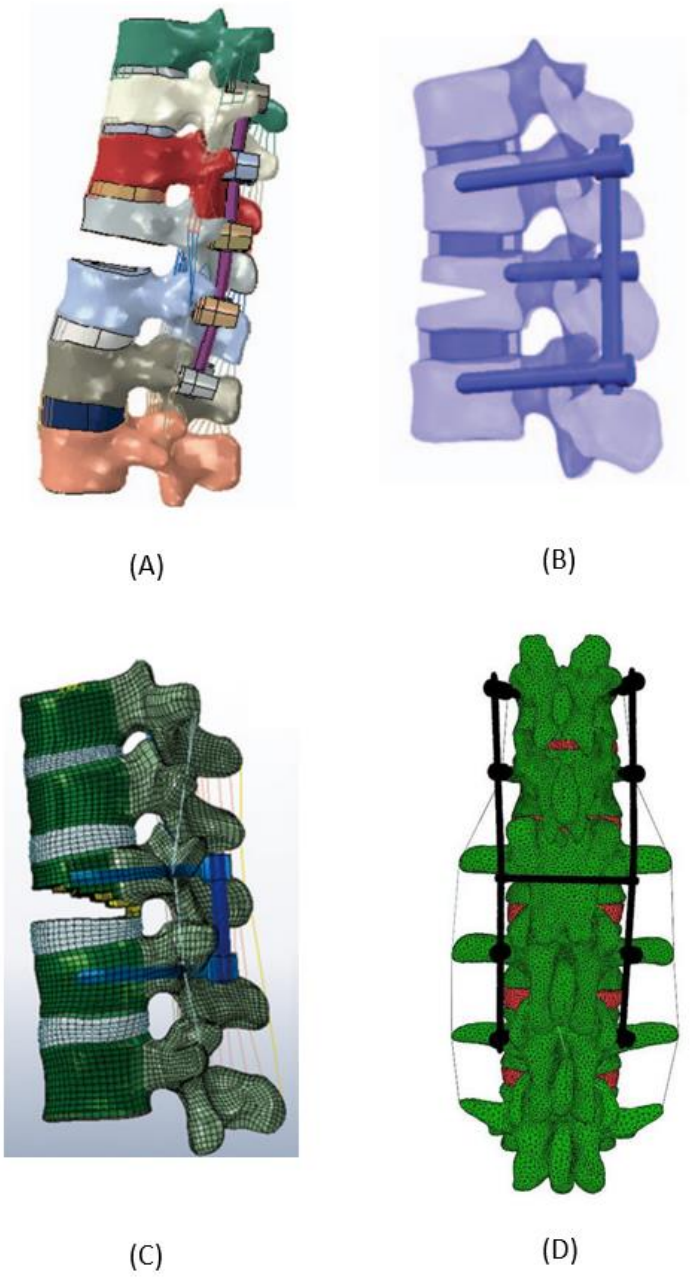

Figure 2.1 – Studies using FE models to determine the best strategy for posterior fixation presented different outcomes: (A) long-segment fixation with additional screws at the fractured level (Wang et al., 2018); (B) short-segment fixation with short screws at the fractured level (Su et al., 2018); (C) Mono-segment procedure at the fracture level (Wang et al., 2019); (D) long-segment fixation (Elmasry et al., 2017). Images adapted with permission.

Other researchers preferred to focus on a single vertebral level to study more in depth the screws-vertebra interaction and to gain more insight into the effect of some geometric features of pedicle screws (Chen et al., 2003; Matsukawa et al., 2015, 2016, 2017, 2020; Bianco et al., 2017, 2019; Newcomb et al., 2017; Abbeele et al., 2018; Chevalier et al., 2018; Biswas et al., 2019; Molinari et al., 2021).

In most recent studies FE models validated with experimental measures have been developed: FE models (Abbeele et al., 2018) and micro-FE models (Chevalier et al., 2018) were found to be good predictors of pull-out strength and stiffness obtained by experimental tests better than apparent density estimated from high-resolution micro-CT images. Micro-CT images allow to study the mechanical behaviour of the vertebra in function of the trabecular bone microstructure. However, clinical CT has a limited resolution, which provide sufficient details for clinical use, but cannot resolve the bone microstructure. Furthermore, due to the large number of elements needed to model the trabecular architecture, a small portion of the bone is modelled and, therefore, simplified boundary conditions are applied which may not be physiologically relevant. As micro-CT and micro-FE models have not been used in this thesis, no further details are provided.

The sensitivity of mechanical properties estimated by FE models to different geometric features and insertion-related parameters of pedicles screws has been assessed by using FE models with homogeneous (Bianco et al., 2017, 2019; Newcomb et al., 2017) and heterogenous (Chen et al., 2003; Matsukawa et al., 2015, 2016, 2017, 2020; Biswas et al., 2019; Molinari et al., 2021) bone's material properties. Chen et al., (2003) showed by using a patient-specific CT-scan based FE model of a lumbar vertebra that the screw length had no significant impact on both the displacement and maximum principal stress of the screws, for models with bonded or frictional screws-vertebra interface. Conversely, Matsukawa et al., (2016) reported that the effect of length and diameter of screws on the pull-out strength and vertebral strength was similar by analysing FE models of 20 vertebrae instrumented with pedicle screws with a cortical bone trajectory (Figure 2.2). The role of the amount of screw length within the vertebral body with respect to the actual screw length has been stressed (Matsukawa et al., 2016, 2020)

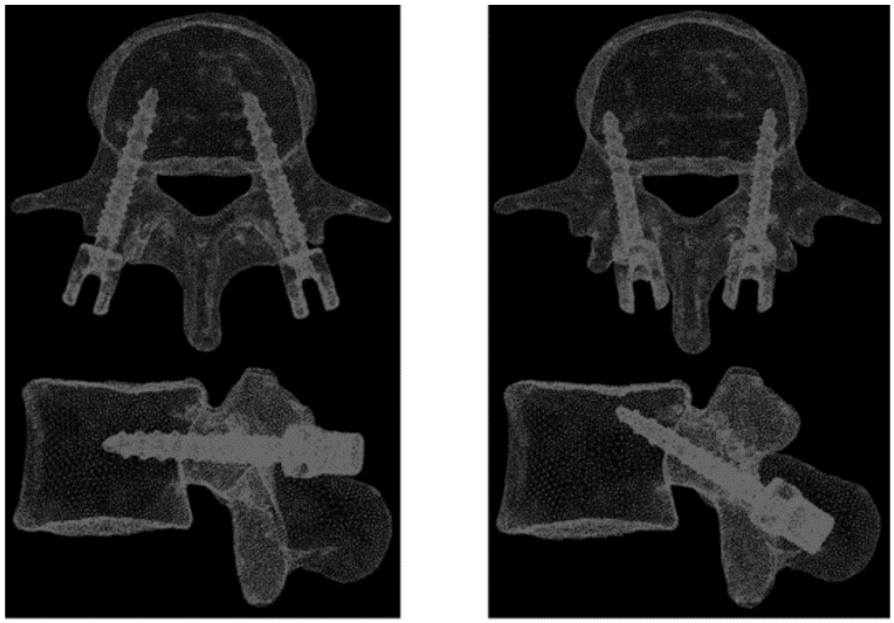

Figure 2.2 – Finite element models of the implanted vertebra with traditional trajectory with screws parallel to the superior endplate and convergent to the centre of the vertebral body, and cortical bone trajectory. with screws along cranio-lateral direction. Note the reduced length of the screw in cortical bone trajectory to avoid perforation of the cortical bone. Image reproduced from Matsukawa et al., (2015) with permission of AANS.

Several studies have reported the predominant effect of the diameter of screws with respect to their length in homogeneous FE models of healthy thoracic (Bianco et al., 2019) and lumbar (Bianco et al., 2017; Biswas et al., 2019) vertebrae and of heterogeneous osteoporotic lumbar vertebrae (Matsukawa et al., 2020). Various numerical studies have established that varying the pedicle screw orientations in the axial and sagittal planes had a significant effect on the biomechanics of the implanted vertebra, but there has been disagreement on the best trajectory to minimise the risks of fracture of the instrumented vertebra or failure of the screws (Matsukawa et al., 2015, 2017; Newcomb et al., 2017; Molinari et al., 2021). The effect of cortical bone removal has also been addressed by testing different entry point preparation to simulate the action of a bone rongeur (Bianco et al., 2019) (Figure 2.3).

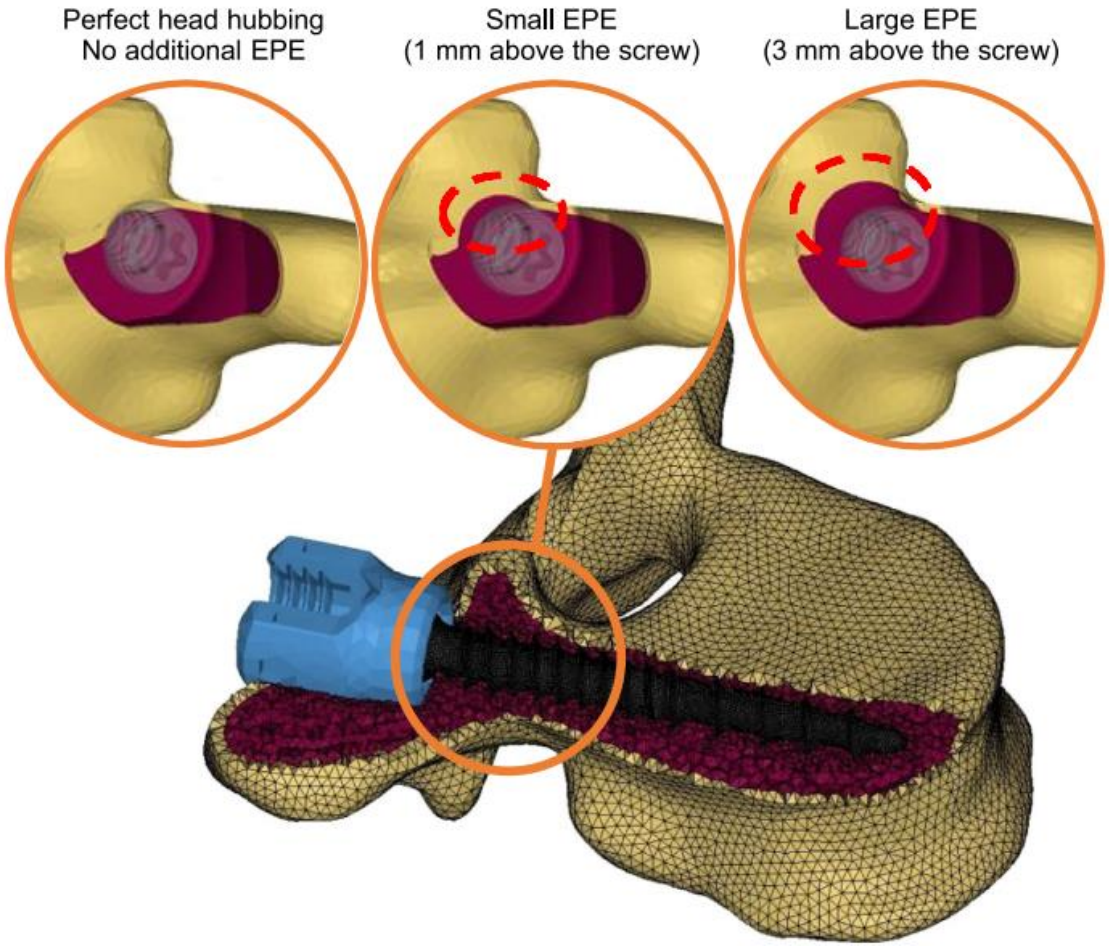

Figure 2.3 – Example of Finite Element model of an instrumented thoracic vertebra by Bianco et al., (2019). Three entry point enlargements (EPE) were simulated with a different degree of bone removal to simulate the screw head hubbing. Image reproduced from Bianco et al., (2019) with permission.

CT-based FE models of the screws-vertebra construct have often been proposed as potential tools for the pre-operative planning of posterior fixation. Before clinical applications, FE models must undergo the process of verification and validation (Assessing Credibility of Computational Modeling through Verification & Validation: Application to Medical Devices - ASME). Verification is a fundamental step to demonstrate the reliability of FE models. The verification step aims at providing evidence that the model is solved correctly, and has to be performed on the level of software platform, the numerical code and the calculations (Musuamba et al., 2021). As it concerns the calculations, it is important to estimate the effect of discretisation errors, as well as solver and human errors on the outcomes of the models. However, most of the studies reviewed report poor information about the verification of FE models. When information about the effect of

the mesh size is reported, it often refers to global metrics such as strain energy density or mean stress that are not directly used for the biomechanical analysis of the structure under investigation. Moreover, several studies compared the effect of the length and the diameter of the screws on mechanical outputs of FE models but reported contrasting results. Therefore, for each application a detailed sensitivity analysis is needed to assess the effect of size and geometry of pedicle screws. An approach to comprehensively assess the effect of the mesh size and the sensitivity of the models to the screws' size and geometry on biomechanical metrics in the bone and in the screws is missing. These approaches may help in establishing the potential of the FE models in evaluating the biomechanics of the implanted vertebrae in the pre-operative clinical setting.

2.2 Reduced Order Models

In the biomedical field, the application of reduced order modelling techniques has attracted the attention of researchers in cardiovascular biomechanics (Manzoni et al., 2012), soft tissue biomechanics (Niroomandi et al., 2012; Calka et al., 2021) and biomechanics of the musculoskeletal system (Zou et al., 2018; Niroomandi et al., 2020). In fact, the computational time necessary for simulations of biomechanical models including high number of DOFs, material non-linearities or non-linear contact mechanics might not fit with the healthcare system, and reduced order modelling techniques have the potential to provide real-time simulations.

Reduced order models (ROMs) have been applied to computational fluid dynamics (CFD) models with geometry/shape variations of parametrized carotid artery bifurcations (Manzoni et al., 2012), of parametrized ascending thoracic aortic aneurysm (Biancolini et al., 2020) and of pathological pulmonary arteries implanted with a stent of different diameters (Caiazzo et al., 2016). The potential of ROMs has been addressed to replace high fidelity FE models of soft tissues and organs as the cornea (Niroomandi et al., 2012), the liver (Niroomandi et al., 2012; Lauzeral et al., 2019), buttock's soft tissues for ulcer prevention (Luboz et al., 2018), and tongue to study the functional outcome of surgeries (Calka et al., 2021) (Table 2.1). To evaluate the accuracy of the ROM, both qualitative and quantitative approaches were used. Qualitatively, the distribution over the mesh nodes of one metric predicted by the ROM (e.g., displacement, stress or strain fields) was compared with the one given by the reference FE model; similarly, the distribution of absolute difference was analysed. Quantitatively, global measures of errors as mean, or root mean square errors over the mesh nodes were often used as well as local absolute differences.

Reference	Organ	Error between FE and ROM
Niroomandi et al., (2012)	Cornea	Qualitative good agreement (load vs displacement curve)
Niroomandi et al., (2012)	Liver	Accuracy less than 5% (load vs displacement curve) - the method for calculating the error is not clearly stated
Luboz et al., (2018)	Buttock	Mean relative error of 0.79% and max relative error of 1.64% (strain)
Lauzeral et al., (2019)	Liver	Mean absolute error of about 1 mm (displacement)
Calka et al., (2021)	Tongue	RMS error between 0.038 mm and 0.146 mm (nodal positions)

Table 2.1 – Overview of the numerical studies showing the application of Reduced order modelling techniques to FE models of soft tissues and organs, and respective error between reference FE models and predictions by ROMs.

It is also possible to apply model order reduction approaches to musculoskeletal structural analyses. Perrier et al., (2015) proposed a patient-specific FE model of the foot to compute the internal strains and stresses in response to pressure distributions (measured with a smart sock, for instance), which could be useful in the prevention of dangerous foot ulcers. In a subsequent study, ROMs have been showed to predict the displacement of the foot in function of the force exerted by the tibialis anterior with a maximum relative error norm of 3.8% (Niroomandi et al., 2020) (Figure 2.4). Once the ROM was built, the computation time was dramatically decreased from 12 hours to calculate the FE solution on a PC with only four cores to 0.1 seconds to evaluate the displacement field by ROM.

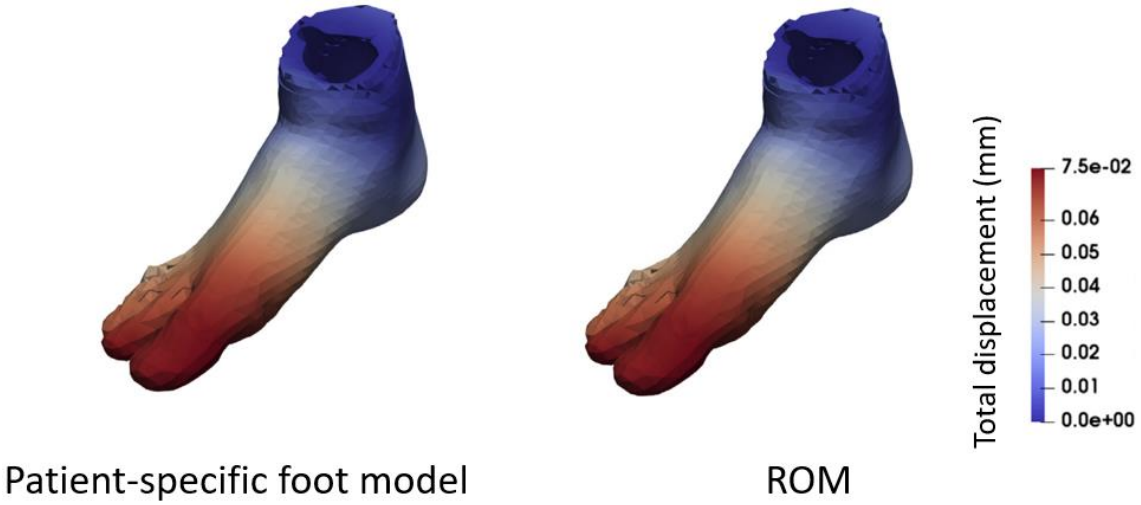

Figure 2.4 – Displacement fields predicted by a patient-specific model of the foot and interpolated by the ROM showed very good accuracy. Adapted with permission from Niroomandi et al. (2020).

ROMs were showed to be effective tools to accelerate the solution of a material parameter identification problem based on *in vitro* experiments (Hoang et al., 2013; Zou et al., 2018). Zou (2018) developed a Reduced Order Modelling approach based on Proper Generalised Decomposition (PGD) and assessed its usability for biomechanical applications on a FE model of a human femur. Hoang et al., (2013) used ROMs coupled with neural networks to identify the Young's modulus of the interfacial tissue between a dental implant and the surrounding bone.

The potential of ROMs in orthopaedics to evaluate the influence of geometric features of implants appears to be under-explored. FE models of spinal segments or single vertebrae implanted with rods and screws have been extensively used to assess the mechanical stability of the construct and to provide quantitative evidence to support the clinical decision process (Section 1.6.1). Non-linear material properties of bony structures as well as complex mechanical interactions between pedicle screws and vertebrae introduce complexity in FE models, and, as a consequence, high computational time to solve the equations is required. For instance, Molinari et al., (2021) reported a computational time of 3.5 hours for an analysis of fracture of the vertebra on a workstation. The computational time becomes inadequate to clinical workflows if parametric analyses are needed to determine the best configuration of implants. The application of ROMs to FE models of spine fixation may overcome this limitation.

Mesh morphing enables the implementation of a parametric model, which is used to build up the ROM framework and data (Biancolini et al., 2020). In fact, mesh morphing allows to control the geometrical parametrization of the model by acting directly on the positions of mesh nodes. In this

way, the fundamental prerequisite for ROM construction is satisfied: snapshots (vectors of results) must have the same dimension, i.e., meshes must have the same connectivity and hence same number of nodes. Mesh morphing has been used in the field of spine biomechanics for different types of applications. A non-exhaustive list of applications is image segmentation (Weese et al., 2001), statistical shape modelling (Heimann and Meinzer, 2009; Clogenson et al., 2015; Campbell and Petrella, 2016; Sun et al., 2021), the automatic construction of patient-specific mesh from segmentations (Castro-Mateos et al., 2016), the implementation of multi-scale patient specific models (Rijsbergen et al., 2018). In this study, Radial basis functions (RBF) based mesh morphing was used to create a parametrized model of the implanted vertebra. In bone biomechanics, RBF mesh morphing has been successfully applied to the femur (Grassi et al., 2011), the mandible (Pascoletti et al., 2021), the rib and the cervical vertebra (Wu et al., 2019) in order to switch from a reference mesh to a target patient-specific mesh. The application of mesh morphing techniques and ROMs to FE models of spine fixation has not been investigated yet. This approach could lead to a tremendous reduction of computational time for parametric models that require high resources to solve.

2.3 Reconstruction of the premorbid shape of a bone by using Statistical Shape Models

Virtual bone reconstruction may support clinicians in establishing the best treatment for a given patient or in the preoperative planning of a surgery. In order to assess the native shape of a bone, one possible approach is to use a template bone neglecting the shape variability among different subjects and between the contralateral sides of the same subject (Gelaude et al., 2007; Hingsammer et al., 2015). In a study exploring the asymmetry between right and left human clavicle bones based on 3D models of 51 patients reconstructed by CT-scans, the contralateral side was found a more reliable reconstruction template compared to a mean-sized bone (85% difference in mean 3D angular error - p-value < 0.001 - and 162% difference in mean translational error - p-value < 0.001) (Hingsammer et al., 2015). An automatic approach to reconstruct acetabular bone based on the contralateral side showed discrepancies of 3.2 ± 2.2 mm in Euclidean distance between the hip joint centres and $3.8° \pm 2.9°$ in enclosed angle between the normal vectors. This procedure requires the contralateral bone to be intact, which is not always the case. In addition, these approaches are limited by the inter- variability among subjects. Instead of adopting a template, another possible method to estimate parameters of native bone is to use correlations between measurements taken on

clinical images or cadaveric specimens, which allow to retrieve one missing parameter by estimating some others (Ganapathi et al., 2011). The disadvantage of this method, however, is that their use is limited to a certain number of predefined measurements.

To date, several studies have explored the performance of Statistical Shape Models (SSMs) to reconstruct the premorbid shape of a bone. SSMs are a powerful tool to represent the possible variations in shape and appearance of an object that belongs to a specific population. Shapes are defined by vectors that contain the coordinates of a set of points on the boundary of the object to model. These points must be in correspondence among different shapes within the population. Principal component analysis (PCA) is applied to the shape vectors to determine the modes of shape variation assuming the probability distribution of shapes is a multivariate Gaussian. Then, each shape can be approximated by a linear combination of these modes of variation.

Recently, different studies assessed the potential of SSMs to aid in reconstruction of the mandible (Wang et al., 2021), scapular bone (Plessers et al., 2018; Salhi et al., 2020) (Figure 2.5), acetabular bone (Vanden Berghe et al., 2017), or pelvis (Krol et al., 2013).

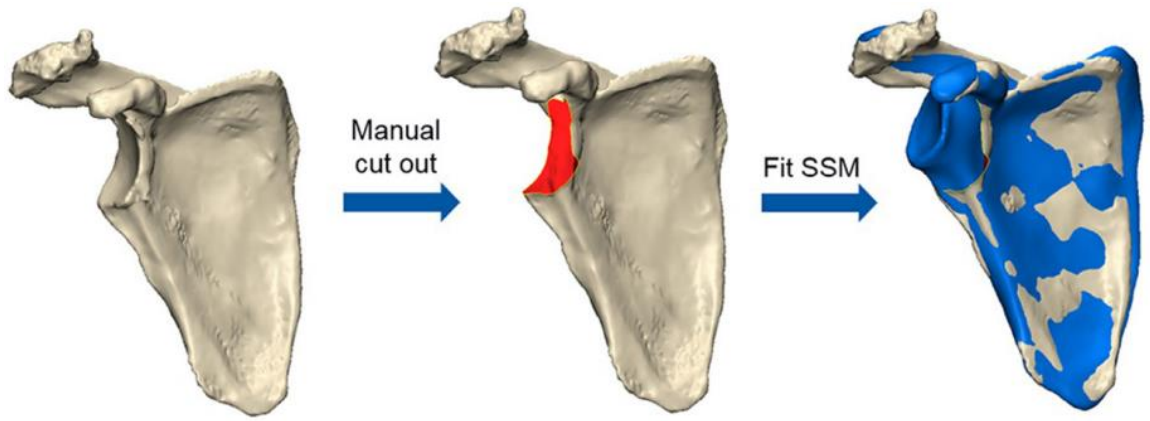

Figure 2.5 – Workflow used for the reconstruction of the scapula based on Statistical shape models (SSM). A region of the scapula is manually removed from the bone. Then, the SSM is fitted to the healthy part of the scapula allowing to retrieve the missing part. Reprinted with permission from Plessers et al., (2018).

With this approach, a SSM is built based on a population of bones without any disease. Then, some defects are artificially created to simulate a pathology with different degrees of severity by removing some portions of bone. The SSM is used to fit the healthy part of the bone (without

defect) under the assumption that this will provide also the shape of the missing part. The predicted shape is compared with the original one to evaluate the performance of the method. This approach has showed 12% -26% lower reconstruction errors with respect to methods assuming the contralateral bone as a template for reconstruction (Krol et al., 2013; Vanden Berghe et al., 2017). Mesh morphing techniques can be used to put in correspondence surface meshes of three-dimensional models of bones. Scalismo software has been showed to perform accurate mesh morphing of scapular bone (Salhi et al., 2020) and cervical vertebrae (Clogenson et al., 2015). Salhi et al., (2020) showed a mean error of 0.97 ± 0.14 mm when comparing the results of missing part prediction with original surface meshes of scapulae but did not report the morphing error for intact parts, which are expected to be lower. Clogenson et al., (2015) used mesh morphing for semi-automatic segmentation of the second cervical vertebra and obtained a mean segmentation error of 0.9 ± 0.12 mm. Scalismo has not been applied to lumbar vertebrae for the prediction of the pre-fracture shape and will be used in this project to morph lumbar vertebral bodies segmented from CT-scan images. de Bruijne et al., (2007) used SSMs to develop conditional shape models, which allowed for the prediction of one vertebra's 2D shape dependent on the shapes of all other vertebrae in clinical X-ray images for the purpose of fracture quantification (Figure 2.6). The outlines of the vertebrae were drawn manually, landmarks were placed equidistantly on those boundaries and were used to build the SSM.

The shape of each vertebra could be found as a weighted combinations of predictions based on knowledge of the shape of other vertebrae, whether healthy or fractured. For each vertebra in the image, fractured or unfractured, its shape could be predicted as a weighted combination of predictions based on the knowledge of the shape of other vertebrae. By building both the SSM and the conditional models on a dataset of healthy spines, and after verifying that the prediction of healthy vertebrae is accurate, this method allowed to estimate the normal shape of vertebrae with an accuracy of 0.8 mm. While this approach appears to be promising for predicting the 3D form of a vertebral body, it has only been used to estimate the 2D shape of vertebrae using X-ray images. An approach to evaluate the 3D geometry of a vertebra at time before the fracture is missing. This information could be used in the pre-operative planning of surgeries to take anatomical measurements and to optimise the treatment.

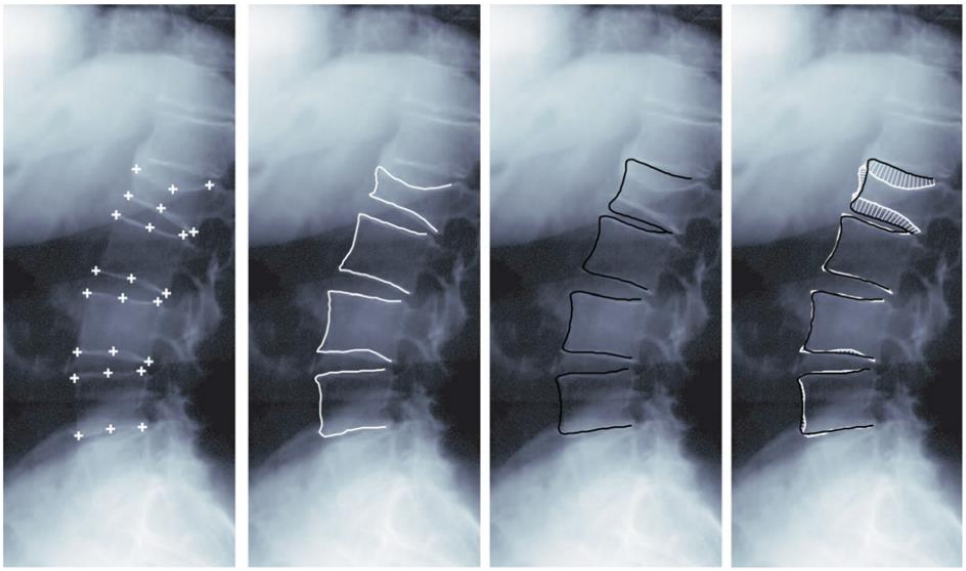

(A) (B) (C) (D)

Figure 2.6 – Approach used by de Bruijne et al., (2007) to quantify the entity of a vertebral fracture from X-ray images. (A) Original X-ray image with a severe fracture and indications of the vertebral heights; (B) Annotation of the shapes of vertebral bodies; (C) Pre-fracture shapes reconstructed for each vertebra, both fractured and unfractured – the pre-fractures shape of unfractured vertebra is very similar to the post-fracture shape; (D) Quantification of the vertebral fracture as difference between the reconstructed pre-fracture and post-fracture shape. Reprinted with permission from de Bruijne et al., (2007).

2.4 Aim and Objectives

The aim of this project was to develop computational tools in order to improve the pre-operative planning of surgeries to treat vertebral fractures, by providing quantitative information about the mechanical competence of the vertebra implanted with two pedicle screws and the geometry of the fractured vertebra before the injury.

This aim has been reached by addressing the four objectives listed below:

1) To generate and verify CT-based FE models of a lumbar vertebra instrumented with two pedicle screws. FE models of lumbar vertebrae were built for three patients from CT-scan images. The verification was performed for one screw size separately for both realistic and simplified design of pedicle screws (Chapter 3).
2) To assess the sensitivity of subject-specific FE models of the vertebra with two pedicle screws to various implant sizes and in cases where the screw design was realistic and simplified. Local and structural properties of the construct were analysed with respect to the screw size suggested by the surgeon (Chapter 3).
3) To explore the application of ROMs to the results of FE models with four shape parameters: diameter, length, sagittal orientation and transversal orientation of pedicle screws. This required the usage of mesh morphing to implement multiple combinations of parameters while keeping the same connectivity of the mesh. The effect of the number of learning points on the accuracy of the prediction of the ROM was studied. The screws' properties were optimised by using the ROM (Chapter 4).
4) To develop a method to reconstruct the 3D shape of the L1 vertebral body from the shapes of adjacent T12 and L2 vertebral bodies obtained by segmentation of 3D CT-scan images, and to validate it on a large dataset of patients. The feasibility of this approach was first assessed on a simpler case where the shape of the vertebral body is described by 7 characteristic heights. Then, the method was applied to predict the 3D shape of the L1 vertebral body. The distribution of heights between the two endplates was estimated and compared to the real 3D shape of L1 (Chapter 5).

Chapter 3: Patient-specific finite element models of posterior pedicle screw fixation: effect of screw's size and geometry

Based on the published manuscript:

Sensale, M., Vendeuvre, T., Schilling, C., Grupp, T., Rochette, M., and Dall'Ara, E. (2021). Patient-Specific Finite Element Models of Posterior Pedicle Screw Fixation: Effect of Screw's Size and Geometry. Front. Bioeng. Biotechnol. 9. doi:10.3389/fbioe.2021.643154.

3.1 Summary

Pedicle screw fixation is extensively performed to treat different kinds of spine injuries or diseases. Post-operative complications may arise from this surgery leading to back pain or revisions. Finite element (FE) models could be used to predict the biomechanical outcomes of surgeries but should be verified when both simplified and realistic designs of screws are used. The aim of this study was to generate patient-specific Computed Tomography (CT)-based FE models of human vertebrae with two pedicle screws, verify the models, and use them to evaluate the effect of the screws' size and geometry on the mechanical properties of the screws-vertebra structure.

FE models of the lumbar vertebra implanted with two pedicle screws were created from anonymized CT-scans of three patients. Compressive loads were applied to the head of the screws. The mesh size was optimized for realistic and simplified geometry of the screws with a mesh refinement study. Finally, the optimal mesh size was used to evaluate the sensitivity of the model to changes in screws size (diameter and length) and geometry (realistic or simplified).

For both simplified and realistic models, element sizes of 0.6 mm in the screw and 1.0 mm in the bone allowed to obtain relative differences of approximately 5% or lower with respect to the finest mesh. Changes in screw's length produced lower differences (1-22%) than changes in screw's diameter (6-47%) in mechanical properties of both the screws (maximum deflection, peak stress) and the bone (mean strain). The maximum deflection of screws and the mean strain in the bone predicted with realistic or simplified screws correlated very well (R^2 = 0.99). The peak stress in screws with realistic or simplified design correlated well (R^2 = 0.82) but simplified models underestimated the peak stress.

In conclusion, the results showed that the diameter of the screw has a major role on the mechanics of the screw-vertebral structure for each patient. Simplified screws can be used to estimate the mechanical properties of the implanted vertebrae, but the systematic underestimation of the peak stress should be considered when interpreting the results from the FE analyses.

3.2 Introduction

Posterior pedicle screw fixation remains the standard surgical treatment for different diseases of the spine as degeneration, trauma, deformity, infection and neoplasia as it can be performed as a minimally invasive surgery enabling the preservation of the paraspinal muscles and resulting in faster recovery, reduced blood loss and rate of infections (Wang et al., 2008). Following posterior spinal instrumentation fusion, screw loosening, screw breakage or postoperative vertebral fracture may lead to back pain, loss of reduction and kyphosis, particularly in case of osteoporotic vertebrae, and revision surgeries may be necessary to improve the outcomes of the treatment (Ponnusamy et al., 2011; Prud'homme et al., 2015). For this reason, surgery-related parameters should be optimized to improve the outcomes of this surgery. While surgeons decide the optimal size, insertion point and orientation of screws based on anatomical measurements on CT-images, finite element (FE) models are efficient tools to mechanically assess the stability of different configurations of the instrumented spine under different loading conditions. FE models of the vertebra should take into account different parameters related to the bone geometry, bone tissue heterogeneity, different boundary conditions, and before clinical applications they should be verified and validated (see for example: Assessing Credibility of Computational Modeling through Verification & Validation: Application to Medical Devices - ASME). The screw size and other insertion-related parameters have been tested with FE models of different complexity in terms of the number of vertebral levels included in the model, how the bone tissue is modelled and screws-bone interactions (Newcomb et al., 2017; Bianco et al., 2019; Wang et al., 2019; Molinari et al., 2021). In most cases a realistic screw geometry was used and only in a few studies a simplified geometry of the screw was modelled (Li et al., 2014; Su et al., 2018). The usage of simplified screws would enable the optimization and automation of the modelling procedure to evaluate vertebral and screws properties, if used in combination with mesh morphing and reduced model order techniques (Campbell and Petrella, 2016). Although FE models of the instrumented spine are often proposed as tools for planning pedicle screw fixations to predict the optimal screw size and orientation for a given patient, little is known about the capability of predicting the biomechanical properties of the screw and of the vertebra if simplified or realistic screws are used (Inzana et al., 2016; Matsukawa et al., 2016, 2020; Bianco et al., 2019). A comprehensive assessment of the effect of the mesh size and the sensitivity of the models to the screw size and geometry, in terms of stress in the screw, strain in the heterogeneous bone, and deflection of the screw within the bone, has not been reported in the literature yet. This gap in the literature makes it difficult to compare the

outcomes from different studies and understanding the potential of the FE models in evaluating the biomechanics of the implanted vertebrae.

The aim of this study was to verify and evaluate the sensitivity of subject specific FE models of the vertebra with two pedicle screws for different sizes of the implant and in case of realistic and simplified geometry of the screw.

3.3 Materials and Methods

Anonymized CT-scans of the thoracolumbar spine of three patients were collected. One vertebra per patient was segmented, converted to a FE model, virtually implanted with pedicle screws, and vertical loads were applied to the head of the screws, perpendicular to their axis. A mesh refinement study for realistic or simplified geometry of the screws was performed to optimize the mesh size. Finally, the optimal mesh size was used to evaluate the sensitivity of the model to changes in screws size (diameter and length) and geometry (realistic or simplified). An overview of the study is presented in Figure 3.1.

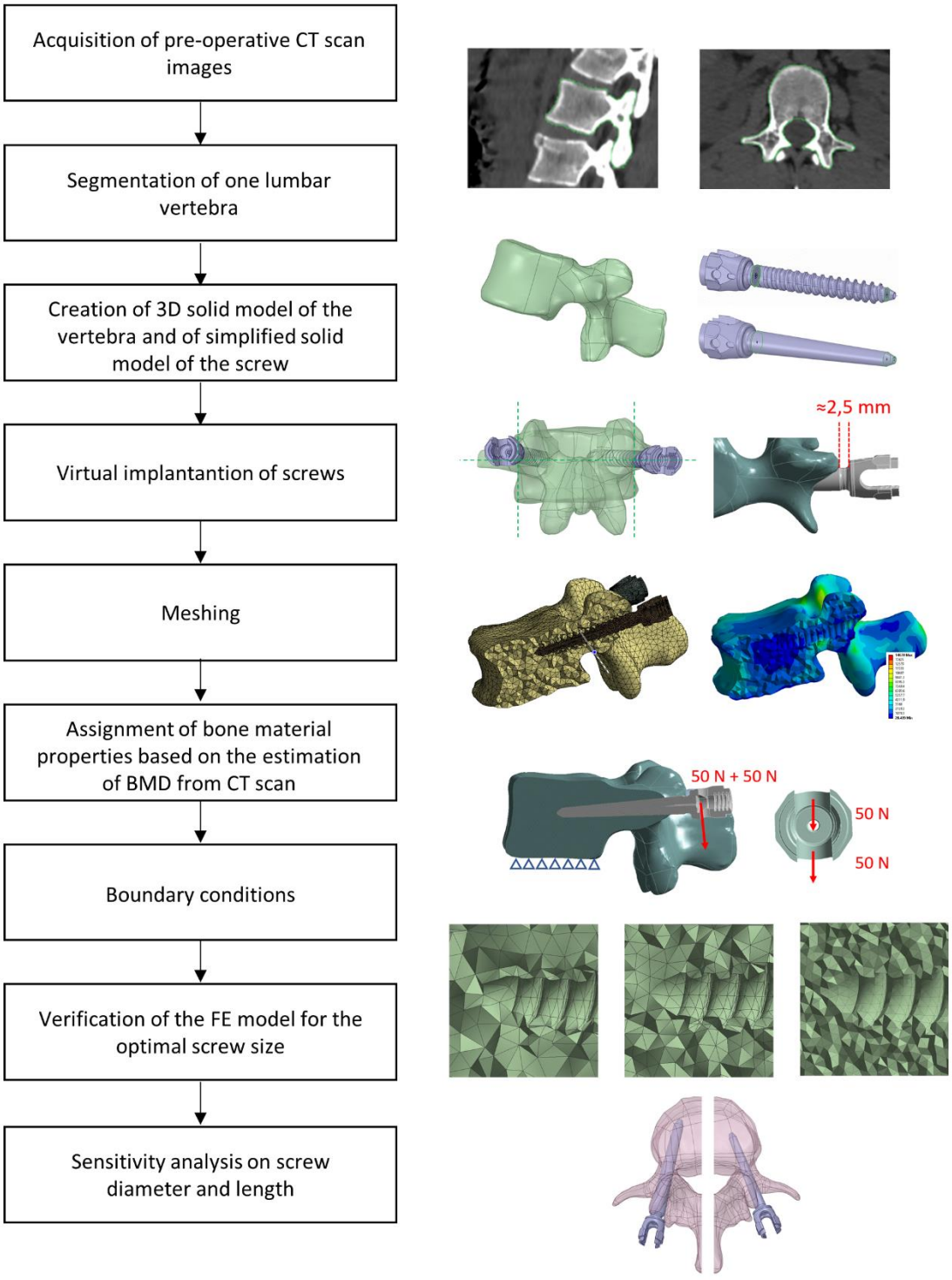

Figure 3.1 - Workflow used to generate, verify, and test the sensitivity of heterogeneous FE models of one vertebra implanted with two pedicle screws.

3.3.1 Imaging and Image processing

Three anonymized clinical pre-operative CT-scans of the thoracolumbar spine of three patients were analysed. The scans were previously acquired at the University Hospital Centre (CHU) of Poitiers (France) and transferred only after anonymization (CHU86-RECH-R2020-02-01). These patients were treated with a posterior pedicle screw fixation for different reasons: two patients reported a vertebral fracture at L1 (Patients #1 and #3), one patient had osteoarthritis (Patients #2). The scanning parameters are reported in Table 3.1.

Scanning parameters	**Patient #1**	**Patient #2**	**Patient #3**
Voltage (kV)	120	135	135
Current (mA)	181	200	273
Exposure (s)	1.38	0.5	0.5
In plane pixel size (mm^2)	0.98 x 0.98	0.88 x 0.88	0.68 x 0.68
Slice thickness (mm)	1.25	1.0	1.0
Model, manufacturer	Optima CT540, GE Healthcare, USA	Aquilion, Toshiba, JP	Aquilion, Toshiba, JP

Table 3.1 - Parameters of acquisition of CT-scan images for the three patients.

In order to simplify the sensitivity study one vertebra with similar size was selected from each patient (L2, L3 and L4 for Patient #1, Patient #2 and Patient #3, respectively). The relative difference in the mean CT based BMD in the vertebral bodies was 21 % between Patient #1 and Patient #2 and -24% between Patient #1 and Patient #3.

The pedicle widths and the distances between the approximated insertion points and the anterior wall of the vertebral body were measured in a cross-section corresponding to the approximated insertion points and including the longitudinal axes of the screws as currently done by the surgeon in the pre-operative planning. From these measurements, and based on the advice of an experienced surgeon, it was concluded that the size of the vertebrae was ideal for the insertion of pedicle screws with diameter (D) equal to 6.5 mm and length (L) equal to 45 mm. The shape of vertebra was reconstructed by manual image segmentation of the CT cross-sections (3D Slicer, v4.10.1) (Fedorov et al., 2012).The resulting mask was smoothed with a Laplacian smoothing. The number of iterations was adjusted in order to preserve the geometric features while avoiding shrinkage of

the volume which was verified by visual inspection of the overlapped CT images and mask (Figure 3.2).

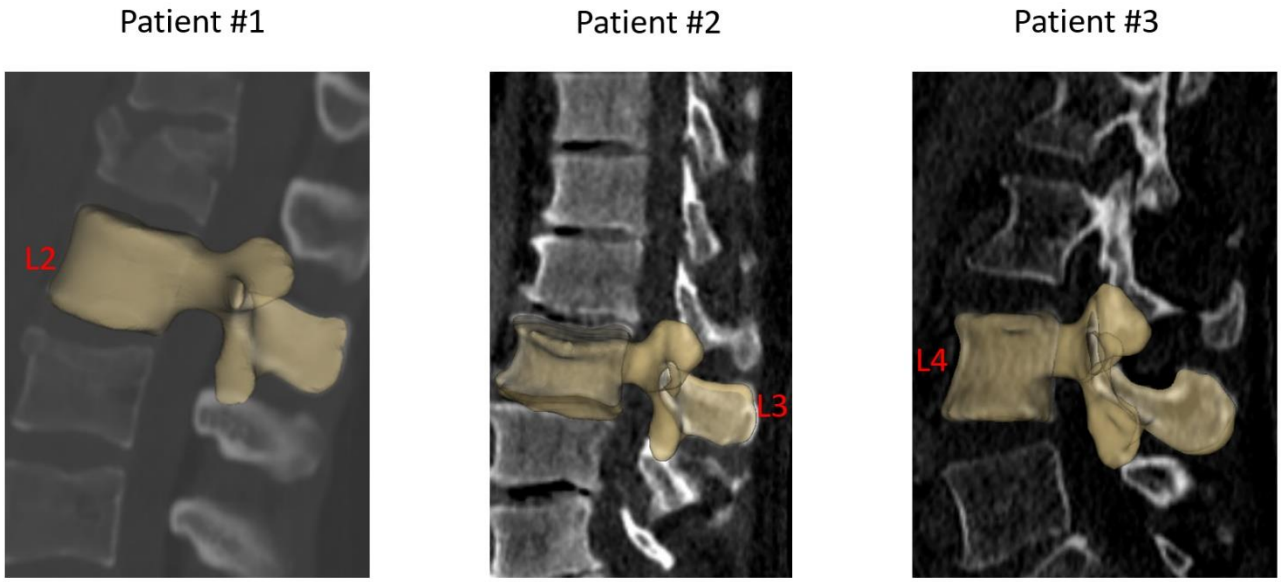

Figure 3.2 - Sagittal mid-section views of the CT images of the three patients and smoothed segmentation masks of lumbar vertebrae used to build the FE models.

3.3.2 Generation of the FE model

The segmented vertebrae were exported as surface meshes (STL) and imported in the 3D modelling software Ansys® SpaceClaim Release 20.2 (Ansys Inc., Canonsburg, PA, USA). Through a reverse engineering process ("SkinSurface" command), a 3D solid model of each vertebra was reconstructed. The surface at the bottom of the model, representative of the inferior endplate, was used to apply the boundary conditions.

Afterwards, two pedicle screws (Aesculap® S4® Element MIS Monoaxial) were virtually inserted within the vertebra. The realistic geometry of the implant was imported as STP file. Nine different sizes of pedicle screws available on the market were tested including D equal to 5.5 mm, 6.5 mm or 7.5 mm and L equal to 45 mm, 50 mm or 55 mm. Nine simplified screws with a smooth conic body without the thread were also generated to evaluate how the thread affected the loading distribution and deformation within the vertebra-screws construct. The solid model of the simplified screws was obtained from each of the nine realistic screws as following. The head of the screw until the end of the junction with the conic feature where the thread begins, and the last portion of the screw after

the end of the thread were kept from the original realistic design. The two circular exposed sections were then connected with a conic surface (Figure 3.3).

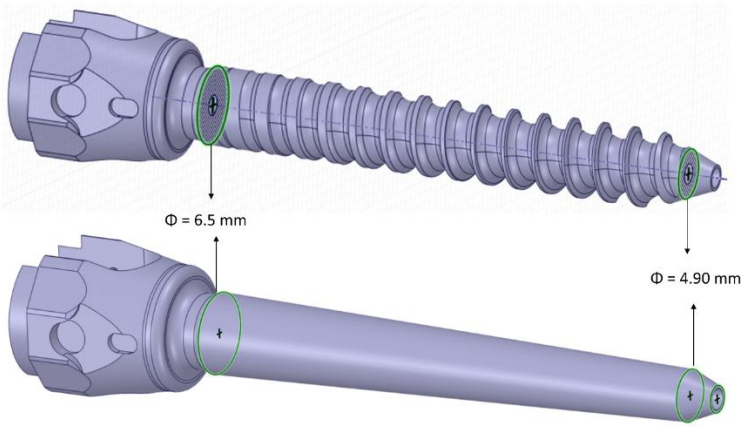

Figure 3.3 - 3D CAD models of simplified (bottom) and realistic (top) screws.

The realistic screws with the largest size (D = 7.5 mm, L = 50 mm) were inserted at pedicles by a Boolean subtraction. The insertion point was determined by following medical guidelines (Gertzbein and Robbins, 1990), which consist of finding the intersection point between a horizontal line passing through the transverse processes and a vertical line adjacent to the lateral border of the superior articular process. Screws were positioned parallel to the superior endplate, converging to the centre of the vertebral body, keeping a distance of approximately 2.5 mm between the head of the screw and the superior articular processes (Figure 3.4).

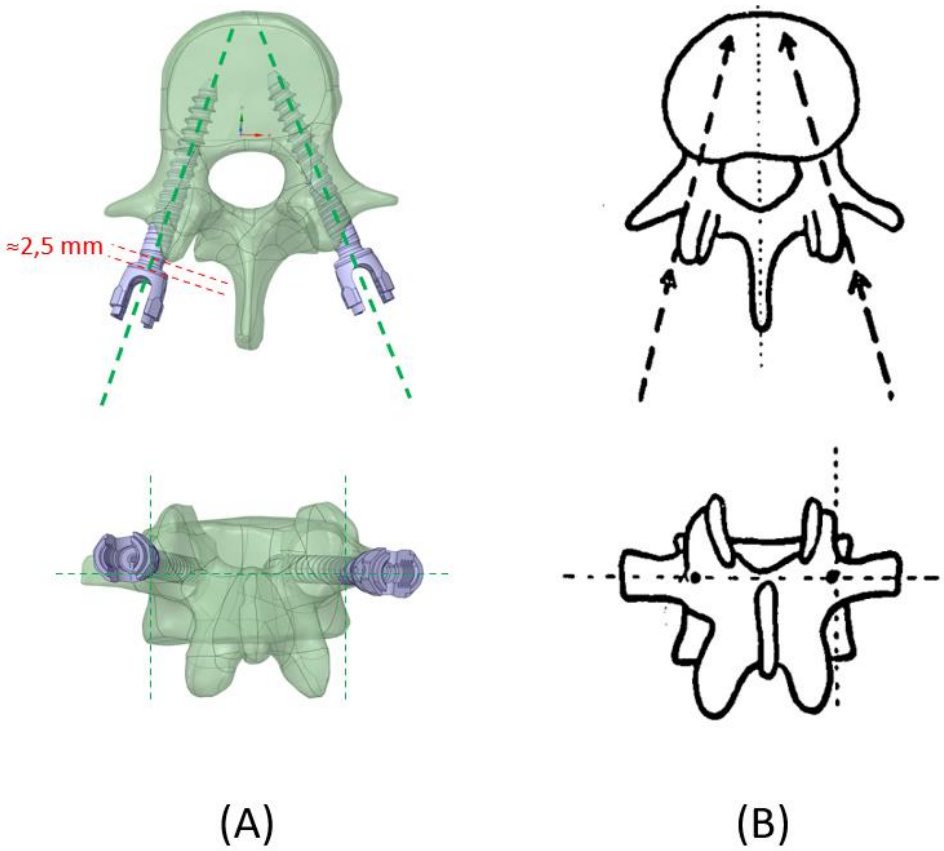

Figure 3.4 – Virtual insertion of pedicle screws showed in cranio-caudal and postero-anterior views for Patient #1 (A) and insertion technique showed by Gertzbein and Robbins, (1990) (B). Image adapted from Gertzbein and Robbins, (1990).

All other realistic and simplified screws were aligned to the position of the largest screws by registering the head of the screws, which were the same for every screw. Boolean subtraction from the original vertebra was applied for each pair of screws. In total eighteen models per vertebra were generated, nine with realistic geometries and nine with simplified geometries.

Each vertebra-screws construct was imported in Ansys® Mechanical Enterprise Release 20.2 (Ansys Inc., Canonsburg, PA, USA) for meshing. The vertebra and the screws were meshed separately with tetrahedral quadratic elements (T10). For the vertebra, a uniform meshing algorithm was used so that the CT-scan grid was sampled uniformly during the definition of material properties of the bone. The element size was defined based on a mesh convergence study (see Section 3.3.3). A bonded contact was imposed at the interface between the screws and the vertebra by kinematic constraints in order to simulate full osseointegration of the devices.

Bone was modelled as isotropic and heterogeneous material with Young's modulus depending on the local BMD estimated from the CT images. In absence of an experimental densitometric

calibration, the Hounsfield units were considered equal to BMD equivalent values (ρ_{QCT}), using a scale factor to convert the physical units to g/cm^3. This assumption was considered acceptable for the goal of this study, which is focused to the verification and sensitivity analysis of the models. In fact, the relationship between Hounsfield units and CT-densities (calibration equation) is typically considered linear for the bone (Schileo et al., 2008). As material models and contact conditions were also linear, considering a linear calibration equation would result in scaling the results of the simulation by a constant value. From the BMD equivalent density, the apparent density (ρ_{App}) was obtained through (Eq. 3.1) (Schileo et al., 2008):

$$\rho_{QCT} = \rho_{Ash} = \rho_{App} \times 0.6 \left(\frac{g}{cm^3}\right) \quad \text{(Eq. 3.1)}$$

The Young's modulus was then calculated using the density-elasticity experimental equation specific for thoraco-lumbar vertebrae (Eq. 3.2) (Morgan et al., 2003):

$$E_{bone} = 4730\, \rho_{APP}^{1.56} \quad \text{(Eq. 3.2)}$$

The Poisson's ratio of the bone was set to v_{bone} = 0.3 (Wirtz et al., 2000). The values of E_{bone} were calculated and assigned for each element by using the Bonemat software (Taddei et al., 2007) (http://www.bonemat.org/index.html). The screw was considered isotropic and homogeneous with Young's modulus and Poisson's ratio of Titanium: E_{screw} = 102 GPa, v_{screw} = 0.36 (Niinomi and Boehlert, 2015).

The model was loaded with a quasi-static uniformly distributed force of 200 N (100 N per screw) applied to the head of the screw in a direction perpendicular to the longitudinal axis of the screw and perpendicular to the superior endplate, towards the caudal direction (Chen et al., 2003; Biswas et al., 2019) (Figure 3.1).The force was equally distributed between the two surfaces of the head of the screw that would interact with the rod (50 N on each surface) (Figure 3.1). This load configuration aimed to represent the load exercised by the upper chest on the most inferior vertebra of a short-segment pedicle screw construct and transmitted by a rod that would be tightened in a direction perpendicular to the screw axis as estimated in an *in-vivo* study (Rohlmann et al., 1997). However, it should be noted that the model is linear and that the results of simulations were interpreted relative to the optimal configuration, therefore the magnitude of the load is not critical. In addition, the nodes of the inferior endplate of the vertebral body were fixed in all three directions (Chen et al., 2003). Ansys ® Mechanical Enterprise Release 20.2 (Ansys Inc., Canonsburg, PA, USA) was used to solve the analysis. A workstation with processor model Intel(R) Xeon(R) CPU E5-2690 v3, 2.60GHz was used. The analysis was run in parallel processing on 4 CPU Cores.

3.3.3 Mesh refinement study

For each patient, the model configuration corresponding to the optimal screw size (D = 6.5 mm, L = 45 mm) as advised by surgeons was tested for verification purposes. A mesh convergence study was conducted to estimate the optimal mesh size. The element size was changed separately in bone and pedicle screws. Six maximum element sizes were tested for the screws between 0.4 and 1.2 mm while keeping the element size in the bone constant and equal to 1 mm. A maximum element size larger than 1.2 mm resulted in an inaccurate discretization of the circular cavity of the screw body; the inferior boundary was considered at 0.4 mm based on the dimension of the smaller thread in the realistic screw (Table 3.2).

E-size screws (mm)	**E-size vertebra (mm)**	**#Elements per Simplified Screw**	**#DOF per Simplified Screw**	**#Elements per Realistic Screw**	**#DOF per Realistic Screw**	**Total CPU time (s) Simplified Screw**	**Total CPU time (s) Realistic Screw**
1.2	1	11489	1.2 E+05	14340	1.5 E+05	384	560
1.0	1	16867	1.7 E+05	20340	2.1 E+05	468	584
0.8	1	28909	2.8 E+05	33893	3.3 E+05	508	608
0.6	1	61918	5.7 E+05	68439	6.5 E+05	548	592
0.5	1	105509	9.5 E+05	112882	1.0 E+06	556	624
0.4	1	199297	1.8 E+06	210545	1.9 E+06	676	760

*Table 3.2 - Number of Elements and Degrees of Freedom per screw, averaged over the three patients, for six element sizes tested for the screws (the maximum element size is reported), in models with simplified or realistic screws; Total CPU time (time * number of CPU Cores) to solve models with simplified or realistic screws.*

Moreover, maximum element sizes in the bone between 0.9 and 3 mm were tested for the finest mesh of the screw (0.4 mm) (Table 3.3). The lowest element size was in line with the voxel size of CT-scan images of the three patients.

The computational time needed to solve the models with different element sizes is reported in Table 3.2 and Table 3.3. As the models were run in parallel computing, the total CPU time is calculated as the CPU time times the number of CPU cores.

E-size vertebra (mm)	E-size screws (mm)	#Elements vertebra (Simplified Screw)	#DOF vertebra (Simplified Screw)	#Elements vertebra Realistic Screw	#DOF vertebra (Realistic Screw)	Total CPU time (s) (Simplified Screw)	Total CPU time (s) (Realistic Screw)
3.0	0.4	8601	1.4 E+05	12154	2.0 E+05	284	260
2.5	0.4	14319	2.3 E+05	17662	2.9 E+05	252	320
2.2	0.4	21114	3.3 E+05	24693	4.0 E+05	256	304
1.9	0.4	32390	5.0 E+05	35424	5.6 E+05	308	352
1.6	0.4	53361	8.1 E+05	55932	8.7 E+05	316	352
1.3	0.4	98509	1.5 E+06	101141	1.5 E+06	424	528
1.0	0.4	215833	3.2 E+06	217860	3.3 E+06	676	760
0.9	0.4	295509	4.4 E+06	296387	4.4 E+06	912	996

*Table 3.3 - Number of Elements and Degrees of Freedom in the vertebra, averaged over the three patients, for eight element sizes tested for the bone (the maximum element size is reported), in models with simplified or realistic screws; Total CPU time (time*number of CPU Cores) to solve models with simplified or realistic screws.*

It should be noted that due to the heterogeneous properties of bone, the value of Young's modulus in each element changes for different element sizes, making it impossible to uncouple the effect of mesh size from changes of material properties on the simulation outcomes. Therefore, the outcomes of the mesh refinement study should be interpreted by considering both changes in element size and material properties in the bone tissue.

The following metrics were calculated for the different mesh sizes:

- The maximum total deflection (d_{max}) of the head of the screw calculated as the magnitude of the displacement vector (nodal value).
- The peak von Mises stress (σ_{VM}) in the screws (nodal value) for the finest mesh. For the coarser meshes the σ_{VM} was evaluated in the same coordinates, using the element shape functions to interpolate nodal values. Since the peak σ_{VM} in the screws always occurred in a node on the external surface, for coarser meshes the coordinates of that node could fall outside the screw. To avoid this issue the outputs of the models were compared in a point within the volume of the screw at a distance equal to 0.05 mm from the peak σ_{VM}.

- The peak Minimum Principal Strain (ε_{p3}) in the bone (nodal value) for the finest mesh. For the coarser meshes the ε_{p3} was evaluated in the same coordinates, using the element shape functions to interpolate nodal values. Some peaks were excluded from the analysis because their location was either close to the boundary conditions of the model, or in geometric sharp corners (for example close to the cuspid at the insertion point or close to the tip of screws), or in an area on the external surface of the vertebra potentially affected by segmentation problems (low values of Elastic modulus for the small elements of the finer mesh). In these cases, the next peak was considered.

3.3.4 Influence of screw size and geometry on mechanical properties of screws-vertebra structure

Once the optimal mesh size was chosen for the bone and the screws, the influence of the diameter and length of screws on the stability of the simulated structure, for both the realistic and simplified models, was evaluated. Left and right screws dimensions were changed simultaneously. The effect of changing the size of the screws was estimated with respect to the structural and local parameters estimated for the optimal screw size (D = 6.5 mm; L = 45 mm). The following parameters were calculated for the three patients:

- The maximum total deflection (d_{max}) of the head of the screw calculated as the magnitude of the displacement vector (nodal value).
- The peak von Mises stress (σ_{VM}) in the screws (nodal value). Some peaks were excluded from the analysis because their location was close to the sharp corner of the bone geometry generated by the Boolean subtraction at the screw insertion point. This happened only for Patient #1, for a screw diameter of 5.5 mm. In this case the next peak, at a distance higher than five element sizes from the sharp corner, was considered in the analysis.
- The mean Minimum Principal Strain (ε_{p3}) in the bone (nodal value). This value was calculated within a Region of Interest (ROI) defined at the screw-bone interface with a shape similar to the smooth conic body of simplified screws (Figure 3.5). The ROI was coaxial with the longitudinal axis of the screw and had a diameter equal to two times the diameter of the screw. Therefore, the dimensions of the ROI were scaled to each screw size. The same ROI was used for both simplified and realistic models.

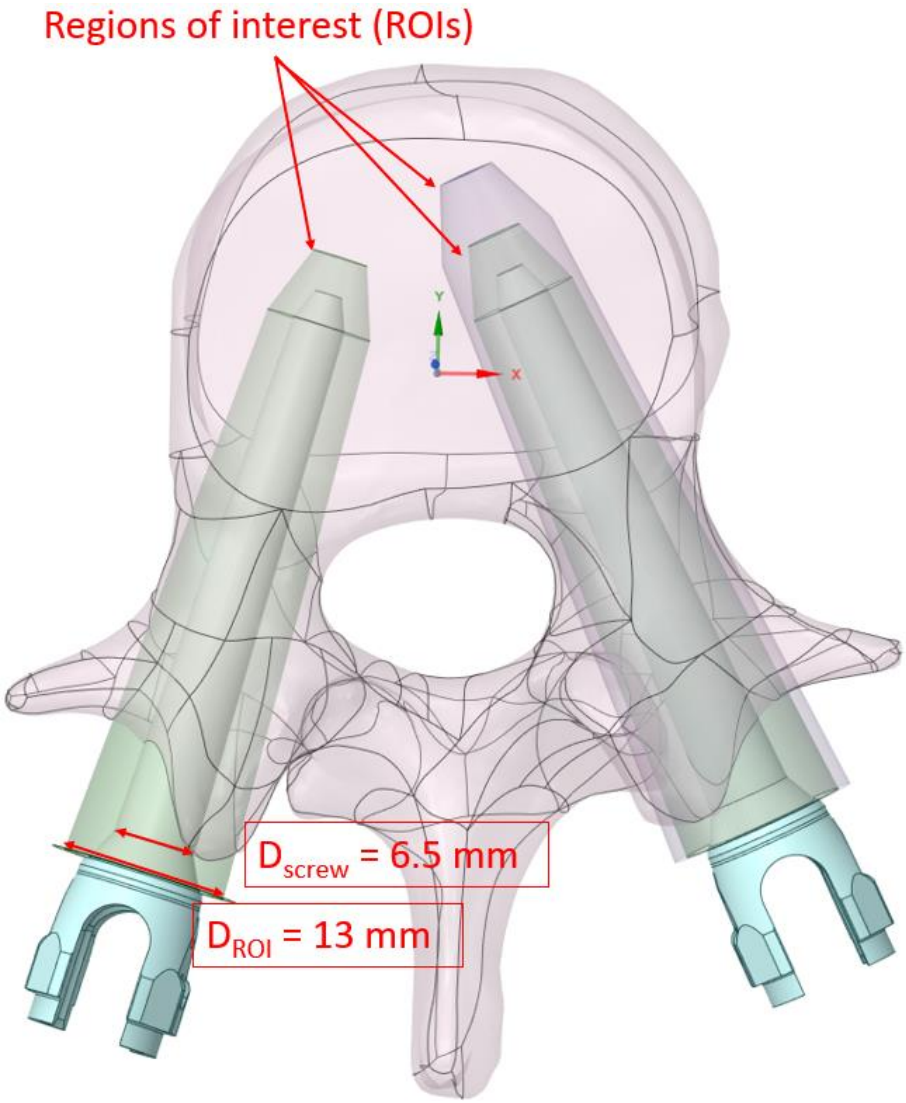

Figure 3.5 – Regions of interest (ROIs) used to calculate the mean Minimum principal strain around the pedicle screws shown in the case with D = 6.5 mm and L = 45 mm on right and left sides (green), and for D = 7.5 mm and L = 50 mm on the right side only (pink). The ROIs were scaled in function of the screw size.

For the patient characterized by the highest relative differences in σ_{VM} in the screws and ε_{p3} in the bone (Patient #2), the frequency plots for ε_{p3} for three screw sizes (D = 7.5 mm and L = 50 mm; D = 6.5 mm and L = 45 mm; D = 5.5 mm and L = 40 mm) were compared for models with simplified and realistic screw geometries.

3.3.5 Comparison between simplified and realistic screw geometry

Linear regression analyses were performed between the predictions of d_{max}, peak σ_{VM} and mean ε_{p3} from the models with simplified and realistic screw geometry. The Slope, Intercept and coefficient of determination (R^2) were calculated for each linear regression.

3.4 Results

3.4.1 Mesh refinement study

The percentage absolute change with respect to the finer mesh in d_{max} for both simplified and realistic screw models was lower than 0.1% (screw) and 0.5% (bone) for each tested element size (Figure 3.6A-B).

The percentage absolute change with respect to the finer mesh in peak σ_{VM} was higher for the realistic screw compared to the simplified one (Figure 3.6C-D). In particular, while for the simplified model a percentage relative difference lower than 5% was observed for each tested element size, for the realistic case an element size of 0.6 mm allowed to achieve relative differences of approximately 5% or below. The σ_{VM} distribution in the screws were similar for the models with different element size for both simplified and realistic screw geometry (Figure 3.7).

The peak ε_{p3} values occurred at the interface between the bone and the left screw for Patient #1 and #2, and at the interface between the bone and the right screw for Patient #3 (Figure 3.8). The absolute percentage relative differences in peak ε_{p3} were much higher than for the peak σ_{VM}. For both simplified and realistic models, element size of 1 mm in the bone led to absolute percentage relative difference of approximately 5% or below for the three patients (Figure 3.6E-F).

For the following analyses, an element size of 0.4 mm was chosen in the screws because the computational time was not significantly affected (Table 3.2, Table 3.3), and an element size of 1.0 mm was chosen in the bone.

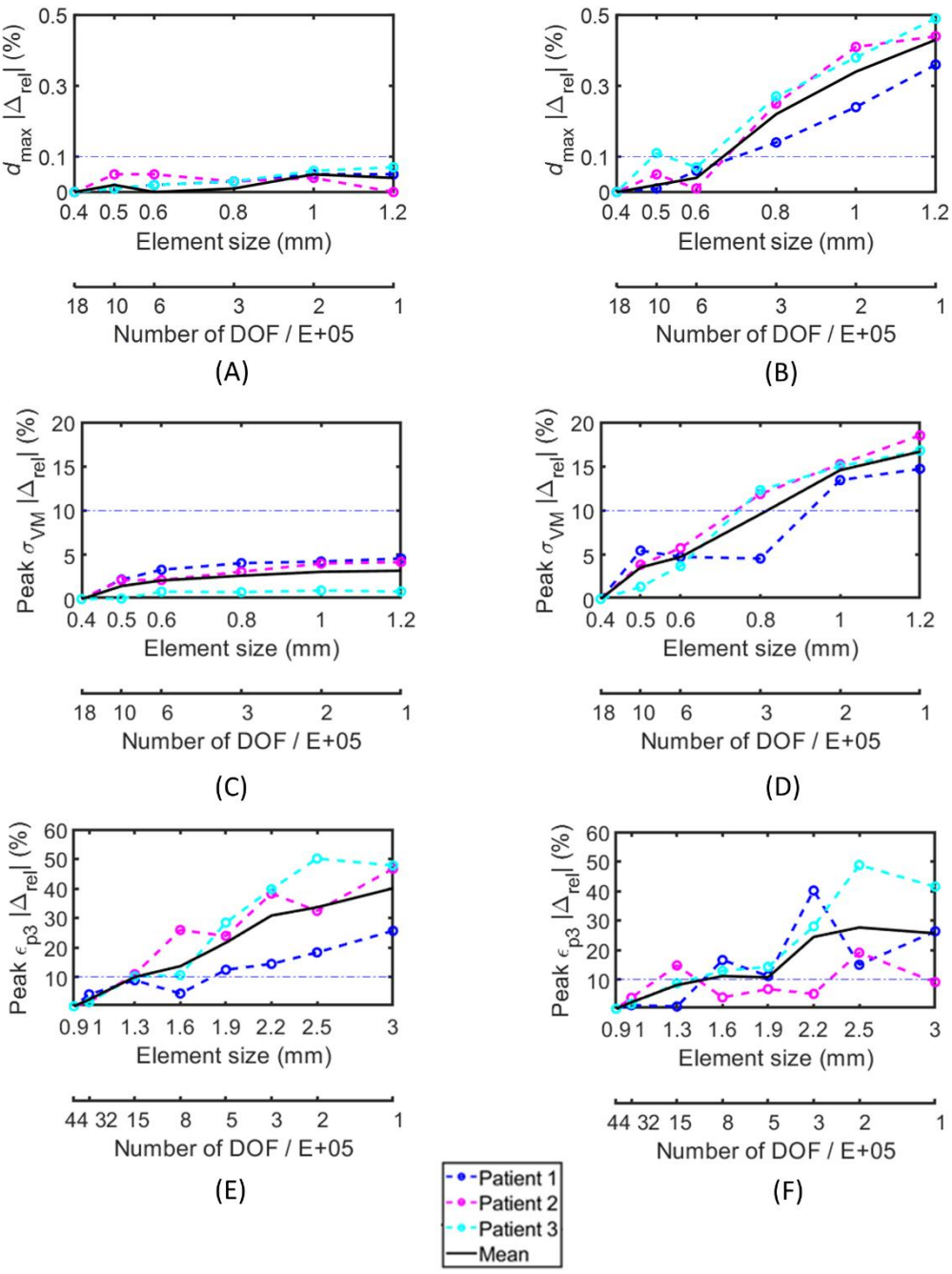

Figure 3.6 - Percentage absolute difference with respect to the finer mesh in the simplified screws (A, C, E) and in the realistic screws (B, D, F) for maximum total deflection (A, B), peak von Mises stress in the screw (C, D), and peak minimum principal strain in the bone (E, F). Dashed lines represent results for each subject, continuous black lines represent averaged values, dash-dotted lines represent the chosen 10% difference chosen as threshold

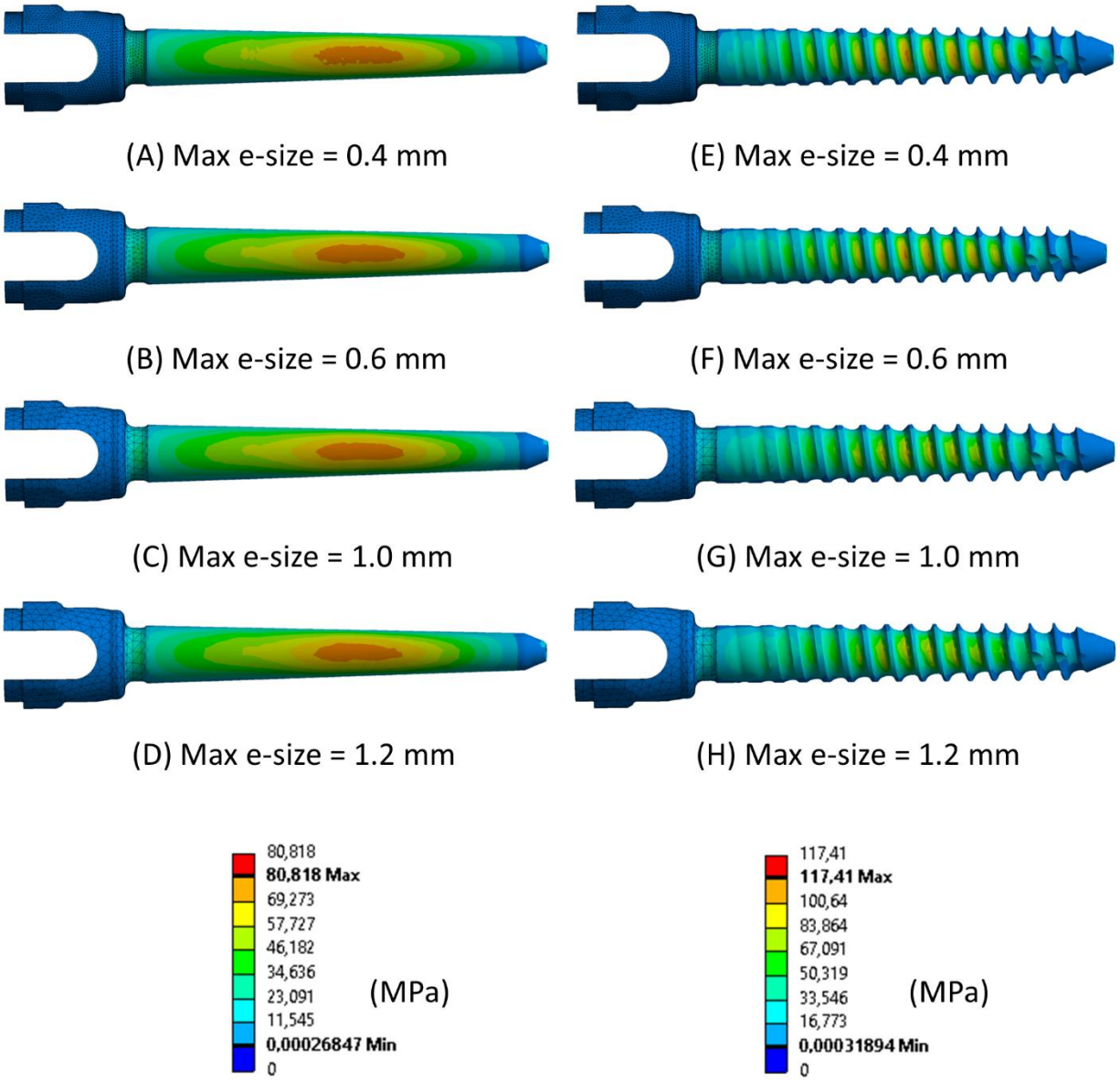

Figure 3.7 - Distribution of von Mises stress in simplified (A-D) and realistic (E-H) left screws (Patient #2) for four different element sizes. Compressed fibers side (caudal view). The mesh was hidden in the main body of the screw to better visualise the stress distribution.

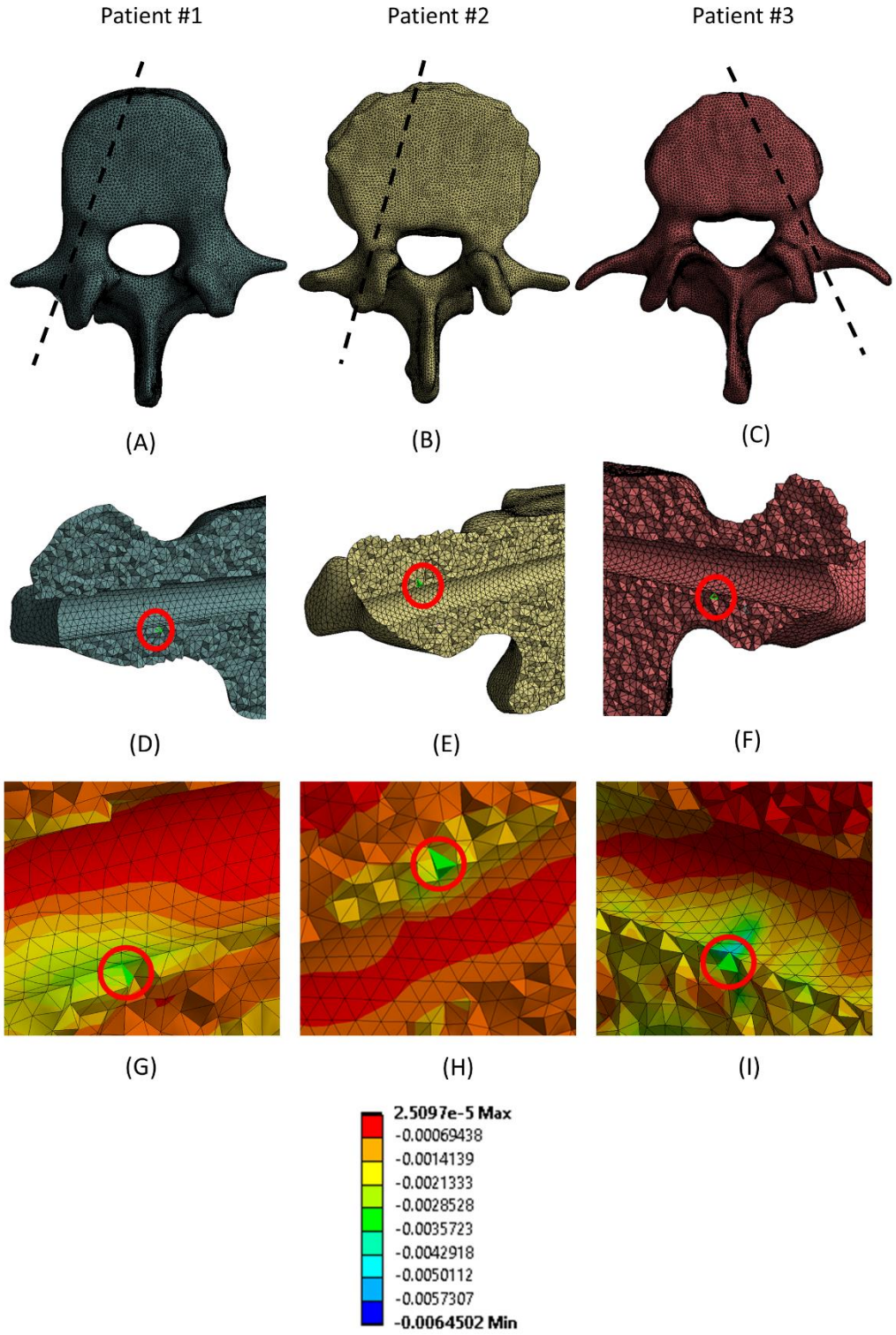

Figure 3.8 - Location of elements where peak ε_{p3} in the bone were. For each patient the following views are reported: the projection of the sagittal section corresponding to the location of the elements in a cranial view (A-C); the location of the peak (red circle) in a sagittal section for each patient (D-F); a magnified view of the mesh in the area corresponding to the selected peaks (G-I).

3.4.2 Effect of size and geometry of the screw

The screw's diameter had a higher influence on d_{max} than the screw's length in both simplified and realistic models, for both left and right screws (Table 3.4). Changes in length resulted in median values of percentage changes in d_{max} between 4% and 10%; whilst, changes in diameter resulted in median values of percentage changes in d_{max} between 28% and 36%. Similar changes were observed between right and left screws, for both simplified and realistic cases, and between simplified and realistic models, for both left and right screws. Very similar trends were found for the three patients. As expected, for a fixed length, the d_{max} increased for lower diameters; for a fixed diameter, the d_{max} decreased for longer screws.

Effect of screw size and shape: Δ_{rel} (%) in d_{max}				
Model - side	**Length**	**Diameter**		
		7.5 mm	6.5 mm	5.5 mm
Simplified Left	40 mm	-10% (-9%, -10%)	4% (4%, - 6%)	21% (18%, 24%)
	45 mm	-15% (-15%, -18%)	REF	18% (15%, 20%)
	50 mm	-19% (-19%, - 23%)	-3% (-3%, -4%)	16% (13%, 17%)
Simplified Right	40 mm	-10% (-10%, -11%)	4% (4%, 5%)	20% (19%, 22%)
	45 mm	-16% (-15%, -17%)	REF	18% (17%, 19%)
	50 mm	-20% (-19%, -22%)	-3% (-2%, -3%)	16% (15%, 17%)
Realistic Left	40 mm	-8% (-8%, -9%)	5% (5%, 6%)	20% (18%, 23%)
	45 mm	-13% (-12%, 15%)	REF	17% (14%, 18%)
	50 mm	-16% (-15%, -18%)	-4% (-4%, -5%)	14% (11%, 14%)
Realistic Right	40 mm	-9% (-9%, -10%)	5% (4%, 6%)	21% (19%, 21%)
	45 mm	-13% (-13%, -14%)	REF	16% (15%, 17%)
	50 mm	-15% (-15%, -17%)	-4% (-3%, -4%)	13% (12%, 15%)

Table 3.4 - Percentage difference in maximum total deflection of the head of the screw, for simplified and realistic models, reported as median value and minimum and maximum values with respect to the nominal condition (D = 6.5 mm and L = 45 mm) over the three patients.

The diameter had higher impact on peak σ_{VM} than the length for both simplified and realistic models (Table 3.5). In fact, changes in length resulted in median values of percentage changes in peak σ_{VM} between 1% and 6%; instead, changes in diameter resulted in median values of percentage changes in peak σ_{VM} between 6% and 27%. For both simplified and realistic models, similar percentage

differences and trends were found between right and left screws. However, an asymmetry was found for Patient #1 in the models with realistic screws with D = 5.5 mm: for the three values of L, percentage differences in peak σ_{VM} between 2% and 11% (left screws) and between 25% and 29% (right screws) were found. Since this patient had the largest pedicle among patients, models with screws with D = 5.5 mm were more sensitive to local changes in material properties. Generally, lower percentage differences in peak stress were found for the realistic screws compared to those obtained from simplified models. The percentage differences presented overall similar trends for the three patients. Also, the peak σ_{VM} in the screw was higher in realistic models compared to those with simplified screws. For a fixed length, the σ_{VM} increased for lower diameters; for a fixed diameter, the σ_{VM} decreased for longer screws. However, in some cases with realistic screws, this behaviour was not observed probably due to differences in local mechanical properties of bone adjacent to screws among models with different screw sizes.

Effect of screw size and shape: Δ_{rel} (%) of peak σ_{VM}				
Model - side	**Length**	**Diameter**		
		7.5 mm	6.5 mm	5.5 mm
Simplified Left	40 mm	-10% (-8%, -13%)	1% (-4%, 4%)	15% (13%, 26%)
	45 mm	-13% (-10%, -13%)	REF	14% (2%, 19%)
	50 mm	-14% (-11%, -14%)	-1% (-1%, 0%)	9% (1%, 23%)
Simplified Right	40 mm	-12% (-9%, -14%)	0% (0%, 2%)	9% (6%, 37%)
	45 mm	-12% (-10%, -13%)	REF	10% (7%, 34%)
	50 mm	-14% (-14%, -16%)	-2% (-1%, -3%)	9% (5%, 35%)
Realistic Left	40 mm	-7% (-11%, 1%)	1% (-3%, 5%)	5% (-3%, 11%)
	45 mm	-7% (-10%, 1%)	REF	5% (0%, 7%)
	50 mm	-3% (-2%, -5%)	-4% (-2%, -4%)	3% (1%, 6%)
Realistic Right	40 mm	-4% (-9%, 0%)	3% (2%, 6%)	9% (5%, 27%)
	45 mm	-3% (-1%, -4%)	REF	5% (2%, 29%)
	50 mm	-3% (-3%, -6%)	-2% (-2%, -3%)	6% (4%, 25%)

Table 3.5 - Percentage difference in peak von Mises stress in the screws, for simplified and realistic models, reported with respect to the nominal condition (D = 6.5 mm and L = 45 mm) as median value and minimum and maximum values over the three patients.

For both simplified and realistic models, the diameter affected the mean ε_{p3} more than the length (Table 3.6). In fact, changes in diameter resulted in median values of percentage changes in mean ε_{p3} between 30% and 47%, while changes in length resulted in median values of percentage changes in mean ε_{p3} between 10% and 22%. For both simplified and realistic models, similar percentage differences and trends were found between right and left screws. Generally, similar percentage differences in mean ε_{p3} were found for the models with realistic or simplified screws. Also, the mean ε_{p3} in simplified models were similar to those with realistic screws. The percentage differences presented overall similar trends for the three patients. For a fixed length, the mean ε_{p3} increased for lower diameters; for a fixed diameter, the mean ε_{p3} decreased for longer screws.

Effect of screw size and shape: Δ_{rel} (%) of mean ε_{p3}				
Model - side	**Length**	**Diameter**		
		7.5 mm	6.5 mm	5.5 mm
Simplified Left	40 mm	-11% (-10%, -14%)	8% (7%, 11%)	33% (22%, 37%)
	45 mm	-22% (-17%, -22%)	REF	25% (17%, 25%)
	50 mm	-26% (-25%, -31%)	-7% (-5%, -10%)	15% (10%, 18%)
Simplified Right	40 mm	-10% (-7%, -13%)	8% (7%, 12%)	31% (26%, 31%)
	45 mm	-19% (-18%, -19%)	REF	20% (18%, 23%)
	50 mm	-25% (-23%, -27%)	-6% (-4%, -8%)	12% (11%, 17%)
Realistic Left	40 mm	-11% (-7%, -11%)	9% (8%, 10%)	34% (26%, 34%)
	45 mm	-17% (-17%, -17%)	REF	24% (20%, 24%)
	50 mm	-24% (-22%, -25%)	-6% (-6%, -10%)	12% (10%, 18%)
Realistic Right	40 mm	-12% (-6%, -13%)	9% (4%, 11%)	30% (30%, 31%)
	45 mm	-17% (-17%, -18%)	REF	19% (18%, 21%)
	50 mm	-22% (-21%, -23%)	-7% (-7%, -10%)	8% (8%, 14%)

Table 3.6 - Percentage difference in mean Minimum principal strain in a ROI at the screw-vertebra interface, for simplified and realistic models, reported with respect to the nominal condition (D = 6.5 mm and L = 45 mm) as median value and minimum and maximum values over the three patients.

3.4.3 Comparison between simplified and realistic screw geometry

If data were pooled for the different patients, sizes and sides, the d_{max} calculated for models with realistic or simplified screws correlated very well (R^2 = 0.99; Slope = 0.918, Intercept = 0.026 mm) (Figure 3.9A). A good correlation was also found between the peak σ_{VM} calculated from the realistic and simplified models (R^2 = 0.82) (Figure 3.9B). Nevertheless, the simplified models systematically underestimated the peak stress compared to the realistic ones (Mean rel diff = 29.2% ± 5.2%, Slope = 1.2, Intercept ~ 17 MPa). For Patient #1, the stress components calculated from the realistic and simplified models at the location of the peak σ_{VM} showed lower correlation than the peak σ_{VM} (Appendix, Section Appendix A1). Models with realistic and simplified screws showed excellent correlation for the prediction of the mean ε_{p3} (R^2 = 0.99; Slope = 0.925, Intercept = 40.185 mm) (Figure 3.9C).

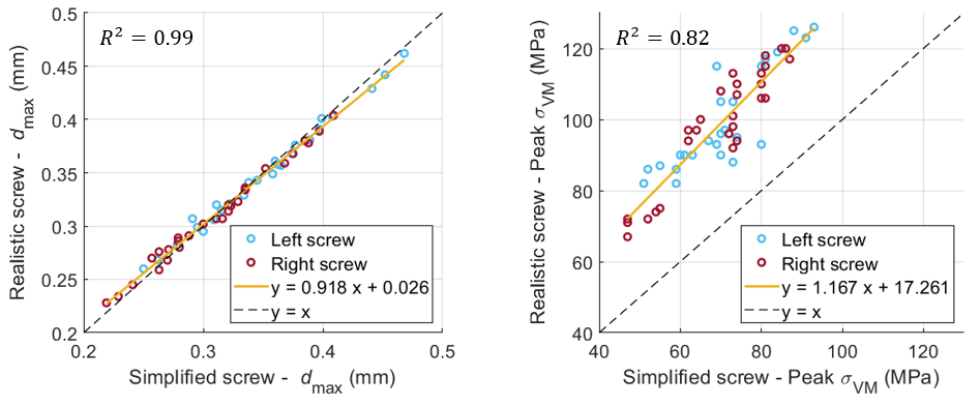

(A)

(B)

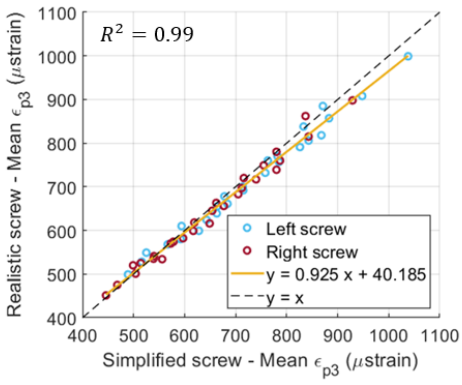

(C)

Figure 3.9 - Linear correlation between d_{max} (A), peak σ_{VM} (B) and mean ε_{p3} (C) for the realistic and simplified models (data pooled for the three patients, two sides, nine sizes).

The peak ε_{p3} was highly influenced by the combination of screw geometry (simplified vs realistic) and the distribution of Young's modulus in the bone, whereas the distribution of values of ε_{p3} within a ROI around the screw was similar for simplified and realistic design of screws, with only a localised increased of strain for a few elements in the realistic screw models (Figure 3.10).

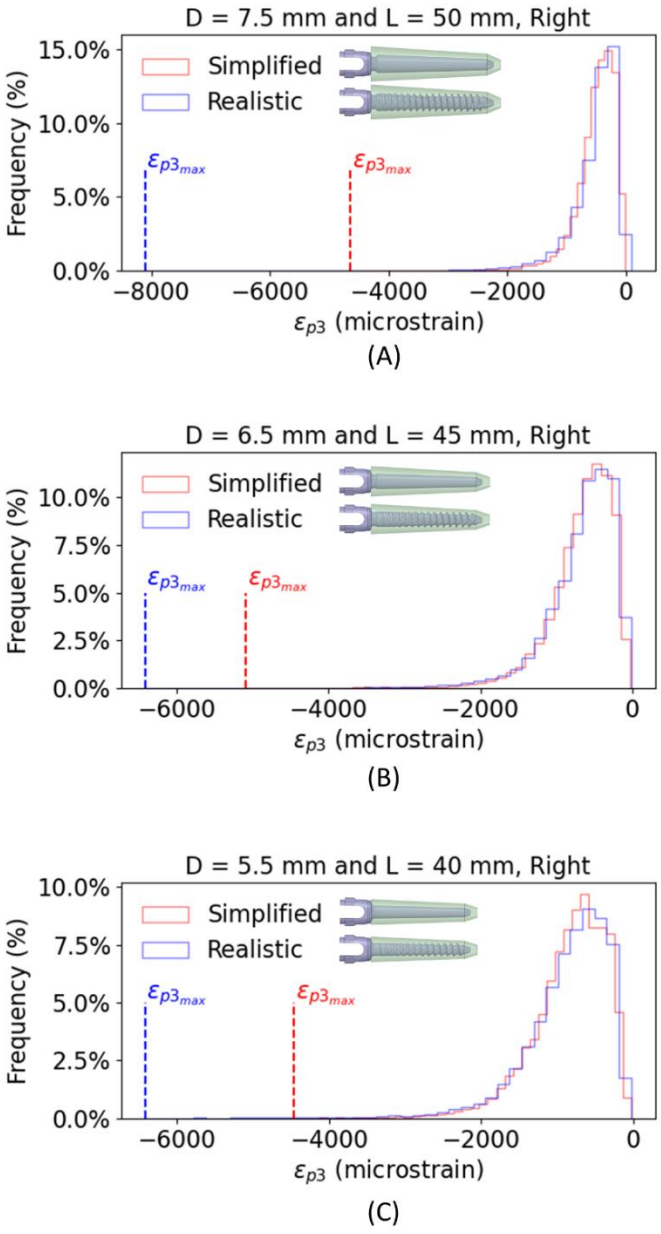

Figure 3.10 - Frequency plots for the values of ε_{p3} within a bone ROI around the right screw, for realistic and simplified models. The data are reported for the largest screw size (A), the optimal screw size (B) and the smallest screw size (C), evaluated for Patient #2. Similar trends were observed for the other patients and the left screws.

3.5 Discussion

This study aimed to generate and verify a subject-specific CT-based FE model of the human vertebra implanted with two pedicle screws. The model was then used to evaluate the effect of the size and geometry of the pedicle screws on the mechanical properties of the screws-vertebra structure.

Element sizes of 0.6 mm in the screw and 1.0 mm in the bone were associated to a relative difference of approximately 5 % for both simplified and realistic models. Similarly, Costa et al., (2019) reported that element size of 1 mm was required for CT-based subject specific heterogeneous FE models of healthy non-instrumented vertebrae loaded in compression. Widmer et al., (2020) reported the results from a validation study for CT-based subject specific heterogeneous animal (bovine and porcine) vertebrae with realistic pedicle screws. They opted for smaller element sizes at the level of the screw cavity compared to the bone farer from the implant resulting in about 230000 tetrahedral elements in the bone and 10000 shell elements in the screw; however, no mesh refinement study was reported. Bianco et al., (2019) compared the fixation strength of realistic pedicle screws with different dimensions, bone engagement and entry point preparation under axial and non-axial forces and chose an element size in the bone of approximately 0.3 mm around the screw thread and 1 mm in regions farer from the implant obtaining differences in results under 8 % with respect to the finest mesh. It should be noted that little details are usually reported in the literature about the choice of the mesh size in models to simulate the biomechanics of vertebrae implanted with pedicle screws. This is critical as “verification” is one of the important steps to give credibility to the models for the assessment of the efficacy of medical devices (Assessing Credibility of Computational Modeling through Verification & Validation: Application to Medical Devices - ASME).

As expected, in this study percentage relative differences in peak σ_{VM} were higher in the realistic screws compared to the simplified ones. In fact, for the realistic screws different element sizes result in a more or a less accurate discretization of the thread features, which is not modelled in the simplified screw. It should be noted that the presence of the thread resulted in a 22-29% higher peak σ_{VM} in realistic models compared to simplified ones for the baseline configuration (D = 6.5 mm, L = 45 mm). This was due to the fact that areas of concentration of stress occurred close to the thread, which may play a larger role compared to the diameter of the screw. However, the σ_{VM} distribution

over the screws was similar among the different mesh sizes for both realistic and simplified models, showing that the stress pattern is not much influenced by the element size.

The diameter of the screw had higher impact on the maximum displacement, on the peak σ_{VM} in the screws and on the mean ε_{p3} in the bone than the length of the screw. This shows that for mono-cortical screws the anchorage in the pedicle, which mainly consists of cortical bone, is more important compared to the anchorage within the vertebral body, which is mainly composed of trabecular bone. Therefore, finding the compromise between the largest diameter of the screws by avoiding iatrogenic fractures is crucial to provide a good anchorage on the cortical bone, which results in lower micromotions at the screw-vertebra interface and better distribution of stress, thus preventing post-operative complications. Even though the results of the sensitivity analysis suggest that increasing the size of the pedicle screws with respect to the optimal size would reduce the stress in the implants and the strain in the bone, the actual clinical need and practical limitations of the surgery have to be taken into account when choosing the size of pedicle screws. In fact, it may be that a screw with a large diameter may not be easy to insert. Our results are in line with most experimental and numerical studies in the literature that showed the predominant effect of the diameter of the screws compared to their length (Zindrick et al., 1986; Chen et al., 2003; Cho et al., 2010; Matsukawa et al., 2016, 2020; Bianco et al., 2019; Biswas et al., 2019), and provide an extensive analysis on mechanical properties of the construct that overcomes the difficulties in comparing results from previous studies. Matsukawa et al., (2016) evaluated the effect of different screw sizes on fixation with a cortical bone trajectory, where screws are inserted pointing laterally in the transverse plane during superior screw angulation in the sagittal plane, and anchor only on cortical bone in the pedicle without the contribution of trabecular bone in the vertebral body (Santoni et al., 2009), by using an FE model including bone heterogeneities and realistic screw design. They found that some mechanical properties of the vertebra-screws construct were not significantly affected by increasing the diameter of screws. Even if our results for the impact of the diameter of the realistic screw seem to disagree with those by Matsukawa et al., (2016), this should be taken with caution as these differences may be due to different modelling techniques and different mechanical metrics used to evaluate the effect of the size of the screw. Matsukawa et al., (2020) investigated the effect of screw size on fixation in osteoporotic vertebrae by FE analysis. Their results showed that by increasing the diameter and the length of screws, the pullout strength and vertebral fixation strength increased; they also showed that the screw diameter had a more important effect than screw length on the vertebral fixation strength, similarly to the results of the present study. However, the modelling approach and boundary conditions of the two studies are

substantially different so both outcomes are complementary. Moreover, even though the results of the sensitivity analysis

Overall, the predictions of the simplified models correlated well with the predictions from the realistic ones, especially for the global structural properties (d_{max}) and averaged local properties in the bone around the screw (mean ε_{p3}). This finding suggests that geometrical differences between the two designs of screws and local differences of material properties around the screw between the two models do not influence the overall stiffness of the model. Inzana et al., (2016) modelled a homogeneous cylindrical block of trabecular or cortical bone and compared a simplified cylindrical screw with a bonded interface and a realistic threaded screw with frictional contact with a pseudo-threaded screw with calibrated contact conditions. They found that the simplified model underestimated the displacement of the screw head (35% and 27% difference for cancellous and cortical bone, respectively; averaged values extracted from Figure 4 in that study) with respect to the realistic case. In this study, it was found that the maximum deflection of the screw head was slightly higher in the simplified case, but a bonded interface was considered for both simplified and realistic models. The different results could be due to differences in material models, interfaces, geometries and applications between the two studies. Moreover, in this study the simplified models underestimated the peak σ_{VM}, due to the lack of stress raisers considered in the realistic design. These differences could also be amplified by local heterogeneity in the Elastic modulus of bone elements. In fact, the distribution of Young's modulus in the bone had a strong influence on the peak ε_{p3}, whereas the distribution of strain as well as the mean strain around the screw-bone interface was similar for simplified and realistic models. This result is consistent with that of Inzana et al., (2016) who showed similar maximum principal strains in large regions of interest around the screw between simplified and realistic screws. This finding highlights the importance of the choice of modelling the screw's geometry realistically or to use a simplified model depending on the application.

There are some limitations in this study. First, it is important to note that before this computational model can be used in the clinical setting, additional to the verification and sensitivity analysis of the model, a direct validation of this approach should be made with respect to measurements from *ex vivo* experiments. This study is the first step in the identification of the best approach to optimise the virtual assessment of pedicle fixation by accounting for realistic vertebral geometry and density distributions and by modelling the screw with a realistic or simplified geometry. Validation of the model against advanced time-lapsed mechanical testing, micro-CT imaging and digital volume correlation approaches (Dall'Ara et al., 2017) to measure the strain distribution in the bone tissue

will follow in future studies. The bone was modelled as isotropic material. However, the bone is an anisotropic material as its trabecular architecture adapts to the mechanical environment along the principal directions of loading (Wolff's law) (Fields et al., 2009). The effect of modelling anisotropic properties of the bone should be explored in future works. However, considering that heterogeneous properties of the bone have been considered and a reasonable small element size has been used, the anisotropy of the bone has been partially taken into account. The screw-bone interface was modelled as perfect bonding to simulate osseointegrated implants. While this choice may lead to less realistic stress and strain patterns in the screw and in the bone, it simplifies the comparison between the models with realistic and simplified screws. Moreover, only the most inferior vertebra of a short-segment pedicle screw construct was modelled, excluding from the analysis the other features of the implanted spine unit. This choice was considered acceptable for this study that focused on vertical loads perpendicular to the axis of the screws. Nevertheless, in order to evaluate the effect of the screw size in physiological conditions, more complex geometry and loading conditions should be modelled. The insertion points of pedicle screws, as well as the orientation of the screw axes in the sagittal and transverse planes are important factors that influence the stress distribution on the screws and the bone. These two parameters should be considered in future parametric studies.

Finally, the effect of the size of the screw has been evaluated with nine discrete configurations instead of analysing the possible range of parameters continuously with statistical methods. While this choice was driven by the configurations of screw size available in the market, a more general approach could have highlighted optimal combinations of diameter and length for the specific patients. In fact, the simplified design of the screw would allow to implement more easily a parametric model, and mesh morphing techniques could be applied to update the nodal positions to accommodate shape variations (Biancolini, 2017). This approach combined with reduced order modelling techniques could be used to accelerate the workflow and test several combinations of geometrical properties of the screw for a population of patients and to expand to nonlinear analyses. Such approach will be explored in Chapter 4.

In conclusion, this study highlights the influence of size and geometry of screws on the biomechanics of a vertebra with two pedicle screws. In particular, the diameter of the screw should be optimised for each patient as it has a large impact on the stress in the screw. Moreover, modelling the screw with simplified geometry systematically underestimate the peak stress and should therefore be accounted for when interpreting the results from the FE analyses.

Chapter 4: Application of Reduced Order Models to Finite Element models of spine fixation

4.1 Summary

Finite Element (FE) models of spine fixation have been proposed as effective pre-operative planning tools to improve the biomechanical outcomes of the surgery and reduce the risk of post-operative complications. Parametric analyses by means of FE models require long computational time and, for this reason, are inadequate to meet the needs of most clinical settings. The aim of this study was to develop a pipeline based on mesh morphing and Reduced Order Models (ROMs) to increase the efficiency of FE models to optimise the size and the orientation of pedicle screws.

Heterogeneous FE models of a lumbar vertebra virtually implanted with simplified screws were built from CT-scan images of one patient. Parametric FE models were created based on mesh morphing techniques applied to change the diameter, the length, the sagittal and transverse orientation of pedicle screws. Reduced Order Models (ROMs) of the deflection and the stress in the screws, as well as the strain in the bone, were built and analysed in function of the number of learning snapshots, the bone material properties, and the screws-bone interface conditions.

The findings indicated that ROMs could predict the deflection and the stress in screws in the parametric design space with a relative error lower than 3% and 6%, respectively, with respect to FE models. Conversely, ROMs of the strain were characterized by an accuracy lower than 5% only in case of homogeneous properties and bonded interface. The optimal screw size and orientation corresponded to the following configuration: Diameter = 7.5 mm, Length = 50 mm, Sagittal angle = 3° and Transverse angle = -3°.

4.2 Introduction

Experimental and numerical studies have investigated the effect of the screw size and/or their orientation within the pedicles to determine which parameters play the most important role on the stability of the spine after surgery. The effect of insertion-related parameters can be studied numerically by means of CT-based FE models (Chapter 3). In order to increase the reliability of these models, non-linearities might be introduced to define the screws-bone interaction or material properties. To solve non-linear FE models with high number of DOFs, the computational time may reach some hours and has to be multiplied by the number of simulations to be run in case of parametric models for optimisation purposes. Because this approach necessitates a large amount of computer resources, it is challenging to meet the needs of workflows delivering clinical treatments. ROMs are powerful tools that enable real-time online computations without simplifying the underlying physics of the model. The potential of ROMs has been addressed in different fields of biomechanics and have showed great potential to create fast and accurate digital twins of human structures. However, the contribution of ROMs has received little attention within the study of spine biomechanics, and in particular for the biomechanics of vertebrae implanted with pedicle screws to optimise the size and the orientation of screws.

The aim of this study was to develop a pipeline to study more efficiently the mechanical properties of the vertebral body with two pedicle screws. In order to decrease the computational burden, the application of a reduced basis approach proposed in Ansys Static ROM Builder software to the mechanical results of FE models was explored. This required the application of mesh morphing to update the shape parameters. A second aim of this study was to show an application of this pipeline to determine the optimal size and orientation of screws to minimise the risks of screw failure for a given patient.

In the Section 4.3, some changes to reference FE models are described and analysed with respect to the FE models used in Chapter 3. In Section 4.4, the application of ROMs to the results of FE models with four shape parameters (diameter, length, sagittal orientation and transversal orientation of screws) are explored and presented, while in Section 4.5 the performance of ROMs in a simplified case with only two parameters (diameter and length of screws) was investigated. In Section 4.6, the application of ROMs to the optimization of the screws' size and orientation is shown for one patient.

4.3 Reference FE model of one vertebra with pedicle screws

A simplified pedicle screw without the thread was designed based on the geometry of Aesculap screws (Chapter 3). In turn, the simplified geometry was furtherly idealised at the junction between the head and the body of the screw to simplify the usage of mesh morphing. Instead of a curved junction, a flat junction was designed (Figure 4.1), and a parametric model of the screw characterised by a linear relationship between the diameter of the screw at different sections and the screw size was created. This geometry was particularly suited to be meshed with hexahedral elements and to be modified by mesh morphing.

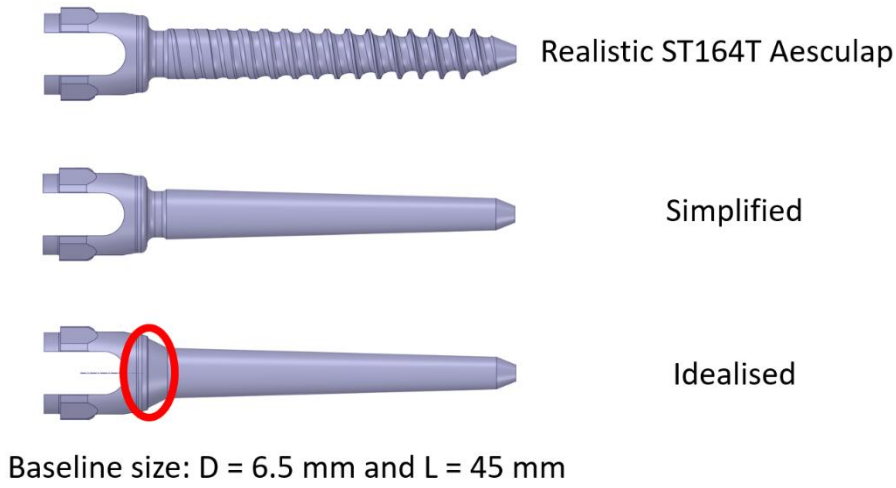

Figure 4.1 – Different designs of screws derived by a commercial Aesculap screw. The idealised screw is used in this chapter.

The idealised screw was meshed with a mixed tetrahedral and hexahedral mesh. The head of the screw was meshed with tetrahedral quadratic elements (T10) while the remaining parts (junction, body, and tip of the screw) were meshed with a structured mesh with hexahedral quadratic elements (H20) (Figure 4.2).

Figure 4.2 – Mid-section view of the mesh of the screw. The head of the screw is meshed with tetrahedral elements, while the remaining part is meshed with a structured hexahedral mesh.

The element size of T10 elements in the screws was 0.6 mm as determined in Chapter 3 through a mesh refinement study. The number of H20 elements was fixed so that the total number of nodes was the same of the unstructured tetrahedral mesh with optimal element size equal to 0.6 mm determined in the mesh refinement study in Chapter 3. An element size of 1.0 mm was used for T10 elements in the bone as in Chapter 3.

The bone was modelled as isotropic, heterogeneous material or isotropic, homogeneous material according to the type of analysis. Heterogeneous properties were determined based on local BMD estimated by CT-scan images as in Chapter 3. In the case of homogeneous properties, the Young's modulus was E_{homo} = 2672 MPa and Poisson's ratio was ν = 0.3 (Wirtz et al., 2000). The Young's modulus was calculated averaging the heterogeneous distribution of Young's moduli assigned to elements. A frictional surface-to-surface contact was considered at the interface between the screws and the vertebra to investigate the primary stability of the screw-bone construct (Ovesy et al., 2018). The friction coefficient was fixed to 0.99 to model the effect of the undercut between the thread and the body of the real screw that increases the contact interface between the bone and the screw and therefore the frictional stress. The sensitivity of the model to the friction coefficient (0.5 - 0.99) was assessed. In order to treat any initial small gaps and penetrations, the standard option implemented by the software was used ("Adjust to touch"). This option applied a global correction to contact elements by imposing an offset dependent on the smallest gap between the bodies in contact to close this gap. As the offset was applied only to contact elements, the stiffness of the model was not affected. In this model, an Augmented Lagrange contact formulation was used. A surface-to-surface contact was preferred to a node-to-surface contact as it includes more nodes into the analysis and results in more accurate stresses at the interface. Contact surfaces of the screws were defined as the master (Contact bodies with Ansys nomenclature), while contact surfaces of the bone were defined

as the slave (Target bodies with Ansys nomenclature) as the bone presented higher element density and the less stiff material properties. The amount of penetration at the end of the solution was assessed. In fact, any contact penetration is impossible as the bodies cannot penetrate each other. The maximum penetration was always lower than 0.01 mm.

The boundary conditions applied to the model are showed in Figure 4.3. The load was applied symmetrically on the two pedicle screws. Ansys ® Mechanical Enterprise Release 21.1 (Ansys Inc., Canonsburg, PA, USA) was used to solve the analysis with the Newton-Raphson method to solve the non-linear problem. The load was applied in 5 steps; within each step, the number of sub-steps varied between 2 and 10. The computational time to solve the equations was about 1 hour using a workstation with processor model Intel(R) Xeon(R) CPU E5-2690 v3, 2.60GHz and running the analyses in parallel processing on 10 CPU Cores.

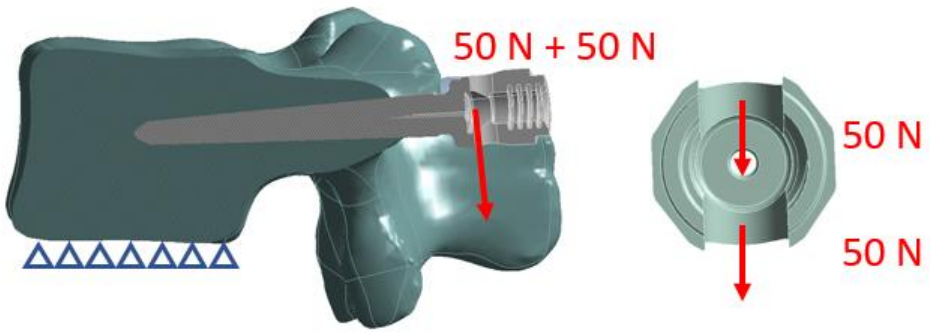

Figure 4.3 – Boundary conditions applied to reference FE models. A quasi-static uniformly distributed caudal force of 100 N was applied to the head of each screw. The nodes of the inferior endplate of the vertebral body were fixed in all three directions.

Under these loading conditions the model was not significantly sensitive to the friction coefficient as differences of about 0.01 mm (3%) and 2-3 MPa (2-3%) were found for the maximum total deflection and the peak σ_{VM} for models with friction coefficients between 0.5 and 0.99. Therefore, a coefficient of 0.99 was chosen to model the effect of the undercut between the thread and the body of the real screw.

For the optimal screw size as estimated by the surgeon (D = 6.5 mm, L = 45 mm), the outcomes of models with simplified and idealised screws were compared in case of frictional screw-bone interface with friction coefficient equal to 0.99. Differences of about 0.01 mm (3%) and 2 MPa

(2%) were found for the maximum total deflection and the peak σ_{VM} between the two models. The location of the maximum total deflection and the peak σ_{VM} was the same. The fact that the outcomes of models were not sensitive to geometric changes was mainly due to the chosen boundary conditions and because the junction is not in contact with the bone. These differences were not considered significant with respect to the envisaged application and therefore we concluded that the FE model was not sensitive to above-mentioned changes in geometry and mesh of the screws.

4.4 Exploration of ROMs for studying the effect of the size and orientation of the pedicle screws

The aim of this subchapter was to assess the performance of Reduced Order Modelling techniques applied to parametric FE models of one vertebra implanted with pedicle screws having different sizes and orientations.

4.4.1 Materials and Methods

4.4.1.1 Summary

FE models of one vertebra implanted with two pedicle screws characterised by realistic screws-bone frictional interface and geometry and mesh optimised to implement mesh morphing were presented in Section 4.3. Four shape parameters of biomechanical interest and their range of variation were defined to create parametric FE models. The mesh of the screws was updated by mesh morphing for multiple combinations of parameters, while the mesh of the vertebra was recomputed at each time. A validation set and different learning sets with increasing number of snapshots were identified. Based on FE solutions of models loaded with vertical load applied to the head of the screws, ROMs of the displacement and the stress in the screws as well as the strain in the bone were built. The influence of the number of learning points on the performance of ROMs was investigated. An overview of the study is presented in Figure 4.4.

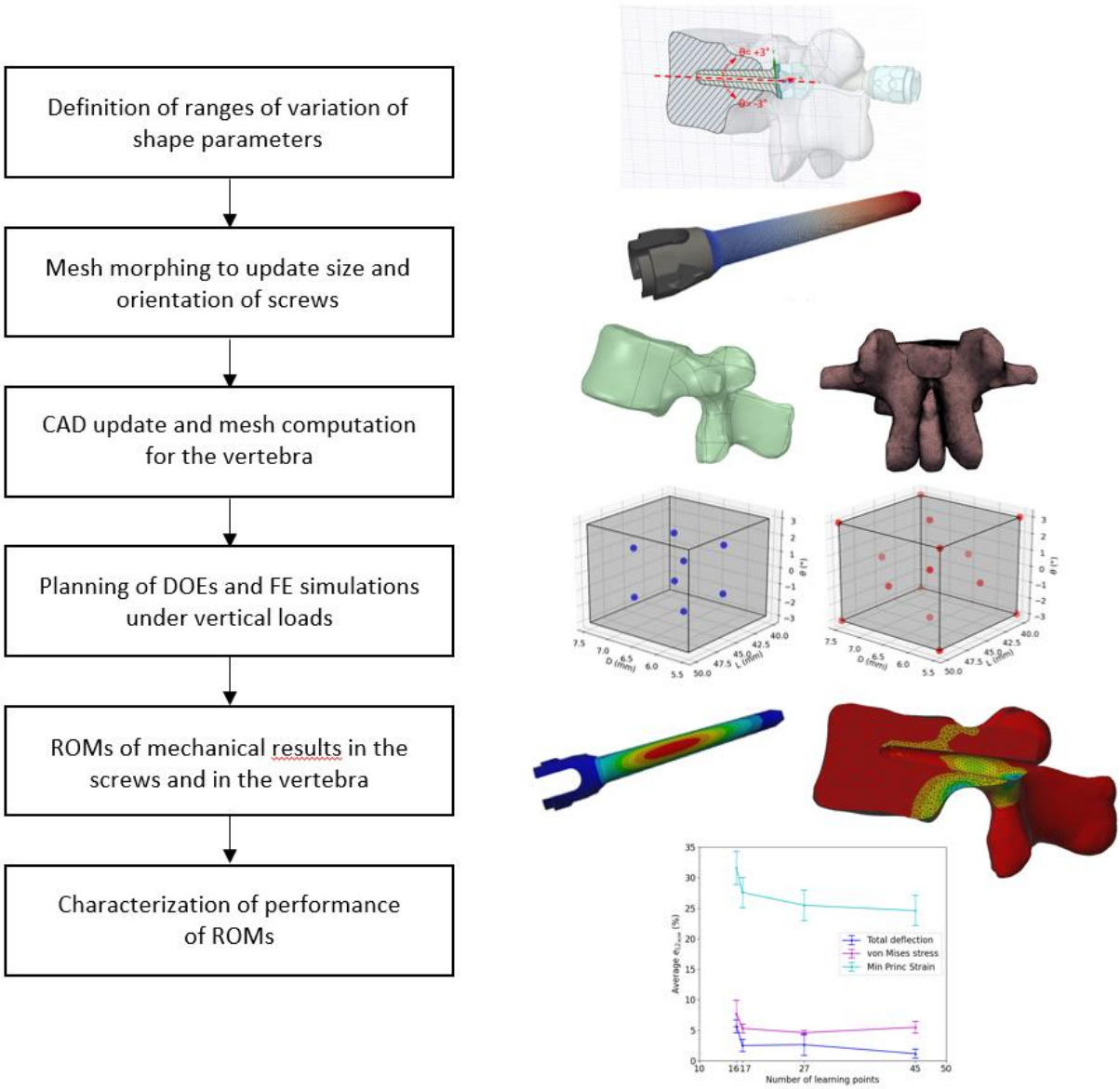

Figure 4.4 – Workflow to create parametric FE models based on mesh morphing whose results are used to build ROMs.

4.4.1.2 Definition of the parameters representing the size and orientation of screws

The FE model included four shape parameters: two parameters for the size of screws - the diameter (D) and the length (L); two parameters for the orientation of screws within the pedicle – the sagittal orientation (θ) and the transverse orientation (φ) (Figure 4.5).

For the considered patient an expert surgeon has identified the optimal screw size with D = 6.5 mm and L = 45 mm. In this study, we considered a range of variation of the diameter between 5.5 mm and 7.5 mm and a range of variation of the length between 40 mm and 50 mm. These parameters

were chosen for this patient based on the dimensions of the two pedicles and the vertebral body measured on CT-scan images.

The parameters defining the orientation of screws within the pedicles were defined as follows. A sagittal plane for each screw was defined as the one including the longitudinal axis of the screw and the direction perpendicular to the longitudinal axis of the screw and perpendicular to the superior endplate (same direction of the external applied load) (Figure 4.5C). The orientation of the screw within this plane was expressed by the angle "θ" between the longitudinal axis of the screw in the optimal configuration and the longitudinal axis of the screw after rotating the screw around the insertion point at the pedicle. This point was fixed and identified according to a medical protocol (Gertzbein and Robbins, 1990) which consist of finding the intersection point between a horizontal line passing through the transverse processes and a vertical line adjacent to the lateral border of the superior articular process. In the sagittal plane, positive angles corresponded to the cranial direction and negative angles to the caudal one (Figure 4.5C). A transverse plane was defined as the plane perpendicular to the sagittal plane that contains the axis of the screw. The orientation of the screw in this plane was identified with the angle φ between the axis of the screw at the optimal configuration and the same axis after rotating the screw around the insertion point (Figure 4.5D). In the transverse plane, we assumed positive angles as lateral and negative angles as medial (Figure 4.5D).

The range of variations of both angles was (-3°, 3°) to avoid perforating the cortical bone layer. As suggested by the surgeon based on the current clinical practice, the parameters were the same for the right and left pedicle screws.

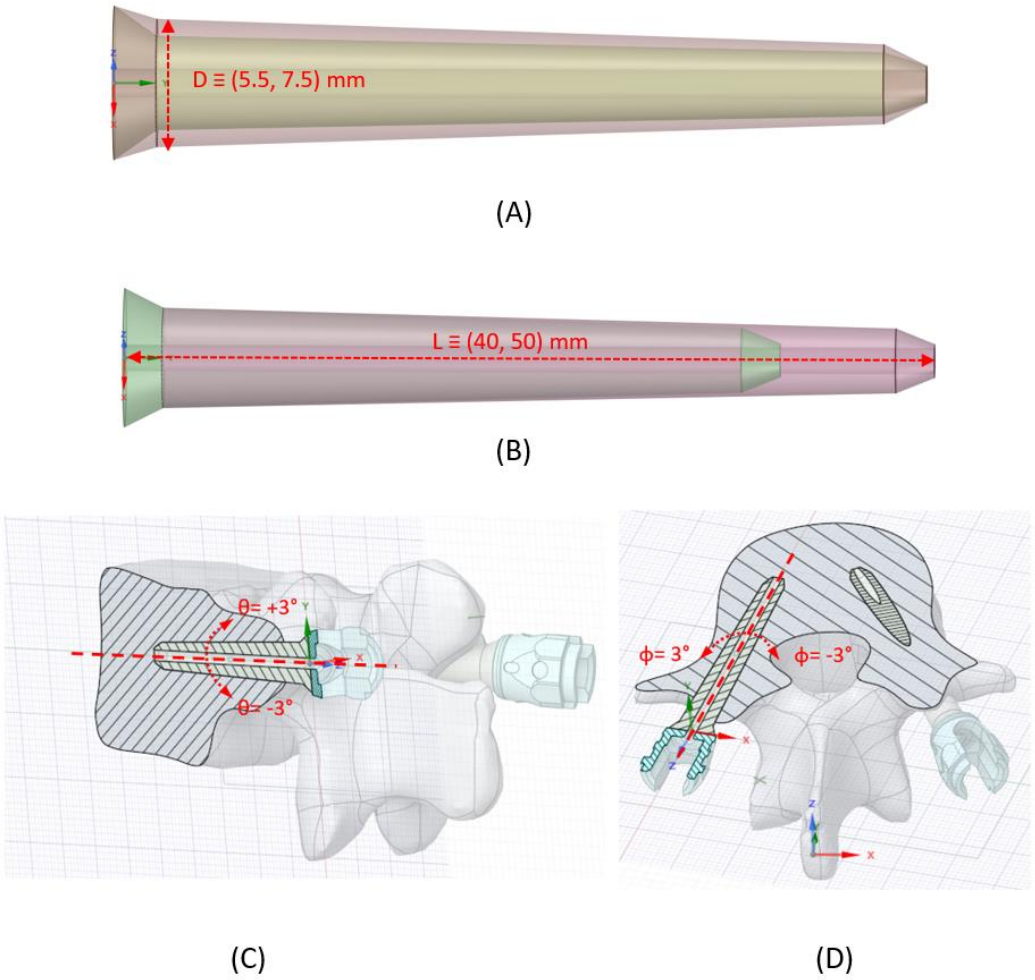

Figure 4.5 – Shape parameters related to the size and orientation of screws. (A) Diameter - D; (B) length - L; (C) sagittal orientation - ϑ; (D) transverse orientation – φ. (C) and (D) show mid-sections of the solid model at the level of the left screw and indicate the convention used.

4.4.1.3 Mesh morphing

The availability of a set of vectors (results of the FE models) of the same size is a major requisite for the application of Reduced Order Modelling techniques. When ROMs are applied to models with physical parameters (e.g., the module of a force, the Young's modulus of a material) without any modification of the initial mesh, this requisite is easily satisfied by evaluating the results at mesh nodes. As in this study the parameters of reduced models are shape parameters, the mesh has to be modified in order to accommodate the variation of the geometry without changing the topology of the mesh. Additionally, the modifications of node positions must guarantee the correspondence of node locations among different models. For example, if one node (and, therefore, one component of the results vector) corresponds to a location on the tip of the screw, the node of

all other models, after modification of the mesh, must correspond to the same location. For this reason, in this work, mesh morphing was used to modify the nodal positions of one baseline mesh to obtain different configurations of shape parameters. RBF Morph software was used to compute the morphing.

4.4.1.3.1 Workflow

The generation of the FE model with different combinations of four shape parameters was done with a mixed workflow based on CAD operations for the solid model of the vertebra and on mesh morphing to update the mesh of the screw (Figure 4.6). In fact, the mesh morphing of the vertebra to update all four shape parameters was challenging because of the large number of transformations needed to apply local corrections to the geometry and the resulting degradation of the quality of elements. Thus, in this study the mesh of the vertebral body was not morphed, and, for each configuration of parameters, the mesh of the bone was created starting from the solid CAD model. For each combination of parameters, the screw size was changed in the CAD software (Ansys® SpaceClaim). Afterwards, the screws were rotated of the angles θ and φ, and a Boolean subtraction was performed to create the holes in the solid model of the bone for the pedicle screws. Each solid model of the vertebra was meshed with tetrahedral quadratic elements (T10) with element size of 1 mm (Chapter 3). On the other hand, the size and orientation of the screws were changed by mesh morphing starting from the hexahedral mesh generated on the model with the optimal screw size (template mesh). First, a transformation was imposed to adapt the mesh to changes in diameter and length of the screws. For each target combination of diameter and length, the RBF control points had the same position with respect to the mesh of the screws, but the displacements assigned to them changed based on two amplification parameters in order to obtain screws with multiple sizes. The procedure to implement this transformation is presented in Section 4.4.1.3.2. The transformation to change the diameter and the length of the screws by mesh morphing was followed by a rigid transformation of the screws to change their orientation both in the sagittal and transversal planes. This rigid transformation was also applied through mesh morphing by using the in-built transformations of RBF Morph. Each time, the Hausdorff distance (Commandeur et al., 2011) between the morphed template mesh and the solid CAD model of the target screw was calculated to evaluate the accuracy of the morphing procedure. The workflow to change the shape parameters of the model is summarised in Figure 4.6. The generation of each model took less than 3 minutes without optimization of the number of control points used in RBF Morph.

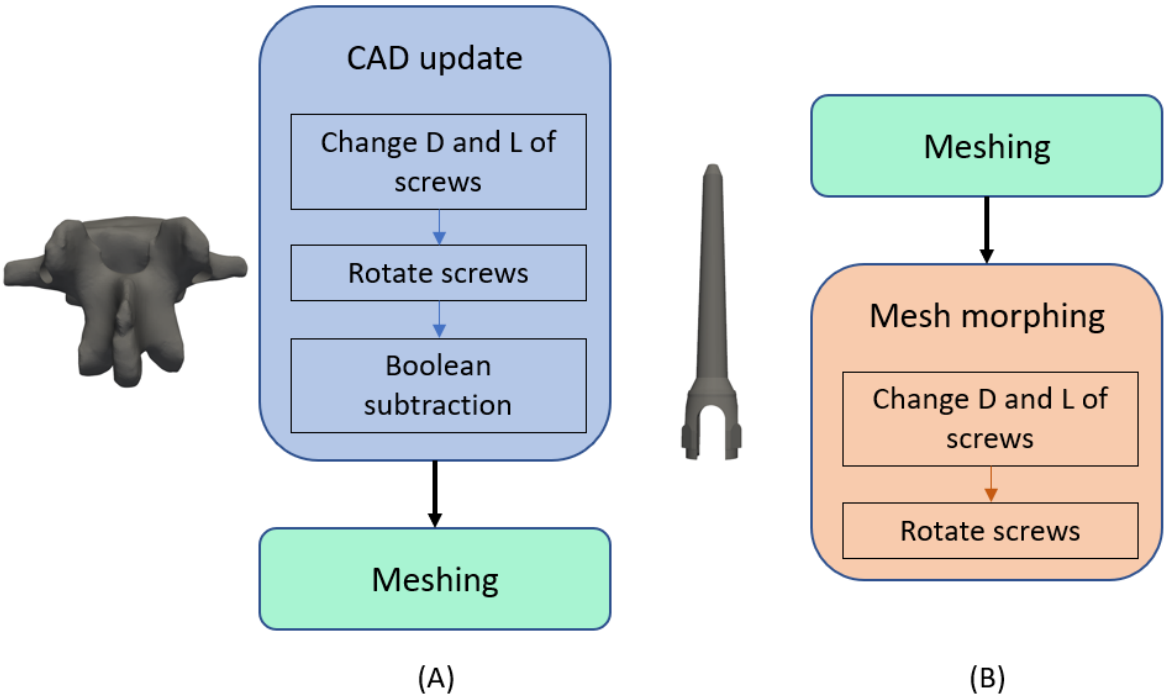

Figure 4.6 – Schematic representation of the workflow based on CAD operations for the vertebra (A) and on mesh morphing for the screws (B) to create the parametric FE model.

4.4.1.3.2 Generation of RBF control points and their displacement field

The idealised screw with D = 6.5 mm and L = 45 mm was positioned at the origin of the coordinates system, so that the z-axis was parallel to the longitudinal axis of the screw and x and y axes were parallel to the transversal section of the screw. As the head of the screw was the same for every screw size, it was not considered in the mesh morphing procedure and the origin of the coordinates system was placed at the initial section of the junction between the head and the body of the screw (Figure 4.7).

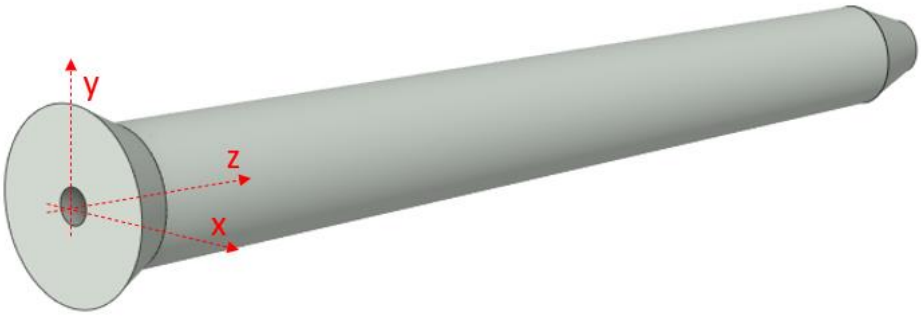

Figure 4.7 – Local coordinates system positioned at the initial section of the junction of the screw to generate the RBF control points for mesh morphing.

A structured mesh (Figure 4.2) with the same number of nodes and elements was built for a screw with D = 6.5 mm and L = 45 mm and a smaller screw with D = 5.5 mm and L = 40 mm. These two meshes had also the same connectivity: same node IDs on the two meshes corresponded to the same topological positions, even if the coordinates of the nodes were different. In this way, for each node on the mesh of the bigger screw it was possible to calculate the displacement to be applied to that node to move it in the corresponding position onto the smaller screw. The nodes belonging to the external surface of the meshes and the nodes belonging to the screw cavity were considered as control points for morphing, while the displacement of nodes within the bodies was interpolated by RBF mesh morphing. As this approach was implemented directly on the mesh used for the simulations, the displacement of nodes on the external surfaces of the body was extremely accurate as it was not interpolated. The construction of the RBF control points, and the imposed displacement was done separately for the junction, the body and the tip of the screw. As an example, the displacements to be applied to the RBF control points on the mesh of the body of the screw to reduce its diameter and its length are reported in Table 4.1 and showed in Figure 4.8.

		Diameter	**Length**
External surface	**Δx**	$A * (x_{D5.5} - x_{D6.5})$	0
	Δy	$A * (y_{D5.5} - y_{D6.5})$	0
	Δz	0	$B * (z_{L40} - z_{L45})$
Internal cavity	**Δx**	0	0
	Δy	0	0
	Δz	0	$B * (z_{L40} - z_{L45})$

Table 4.1 – Example of displacements assigned to control points in order to obtain a reduction of the screw size by mesh morphing. A and B are constants that could be used to amplify the displacements and obtain different screw sizes.

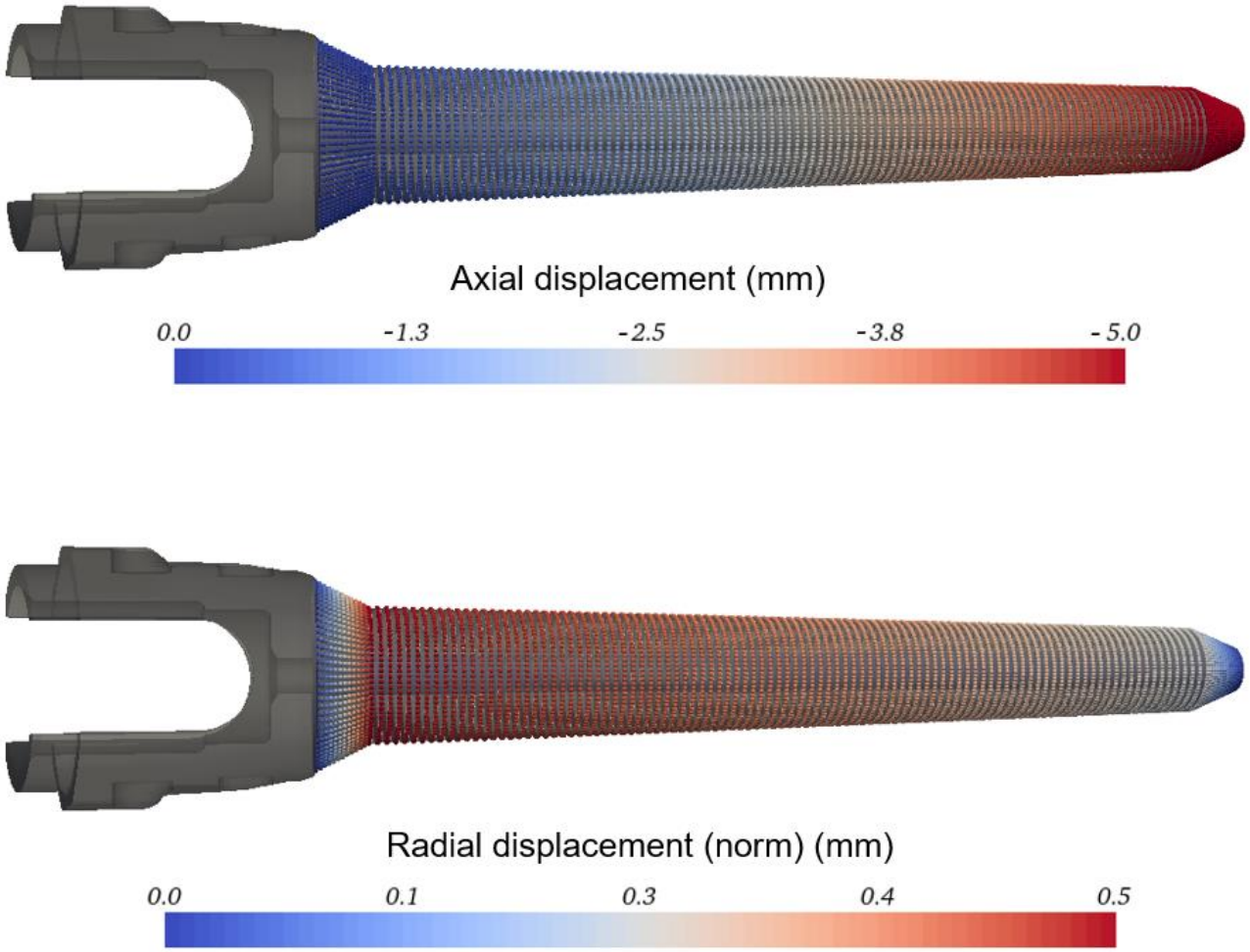

Figure 4.8 – Example of displacements assigned to RBF control points to obtain a reduction of the screw size (from D = 6.5 mm and L = 45 mm, to D = 5.5 mm and L = 40 mm) by mesh morphing. For axial displacement, RBF control points on the tip of the screw are linked to large displacement to reduce the length of the screw, while RBF control points at the beginning of the body of the screws have low displacements. Regarding radial displacement, it is zero at the tip of the screw, whilst it is maximum in correspondence to the maximum diameter of the central part of the screw.

As the parametric model of the idealised screw was characterised by a linear relationship between the diameter of the screw at different sections and the diameter itself, it was possible to obtain different screw sizes by tuning the coefficients A and B. For example, for $A > 0$, $B > 0$ a reduction of the diameter and the length was obtained; for $A < 0$, $B < 0$ an expansion of the diameter and the length was obtained. The displacements along each direction x, y and z must be considered simultaneously to obtain a modification of the diameter and the length of the screw.

It must be noted that, even if the RBF control points were defined in a convenient coordinates system, the same could be used for screws in whichever position in the space by calculating roto-translation matrices between the reference coordinate system and appropriate local coordinate systems defined on the screws.

The Hausdorff distance between the morphed template mesh and the target mesh was lower than 0.01 mm confirming that the morphing procedure was extremely accurate.

4.4.1.4 ROMs of the mechanical results

In this study, a ROM of the total deflection of the screw as well as a ROM of the von Mises stress (σ_{VM}) in the screws, and a ROM of the minimum principal strain (ε_{p3}) in the vertebra were created in function of the 4 parameters defined in the FE model (D, L, θ, φ). The mechanical results in the screws were sampled at mesh nodes to build the set of vectors for the ROMs. However, for the ROM of the mechanical properties in the bone, a grid of sampling points around the screw was morphed for each configuration and the strain in that location was interpolated by using element shape functions. This procedure was needed to build the set of vectors to create the ROM as mesh morphing was not applied to the mesh of the vertebra.

A grid of points was defined around the screw based on the coordinates system showed in Figure 4.7. The design of the grid was constrained by the fact that all sampling points must be inside the vertebra for all the models. For this reason, the grid of points started at a distance of 15 mm from the origin of the coordinates system towards the vertebral body. Along the longitudinal axis of the screw, 27 planes perpendicular to the axis of the screw were considered at a distance of 1 mm from each other for the screw with D = 6.5 mm and L = 45 mm. Within each plane, a circle with the same centre of the section of the screw and a diameter larger by 0.5 mm was considered and sampled with 26 points. In this way, all the grid points were at a distance which was equal to the mesh size in the vertebra for the screw with D = 6.5 mm and L = 45 mm. As the grid was used to sample the strain in the bone, a grid with consistent characteristics, but adapted to each screw size, was computed for each screw size. Then, the sampling points were subjected to a rigid transformation determined by calculating roto-translation matrices between the reference coordinate system and appropriate local coordinate systems defined on the screws in the undeformed configuration (Figure 4.9).

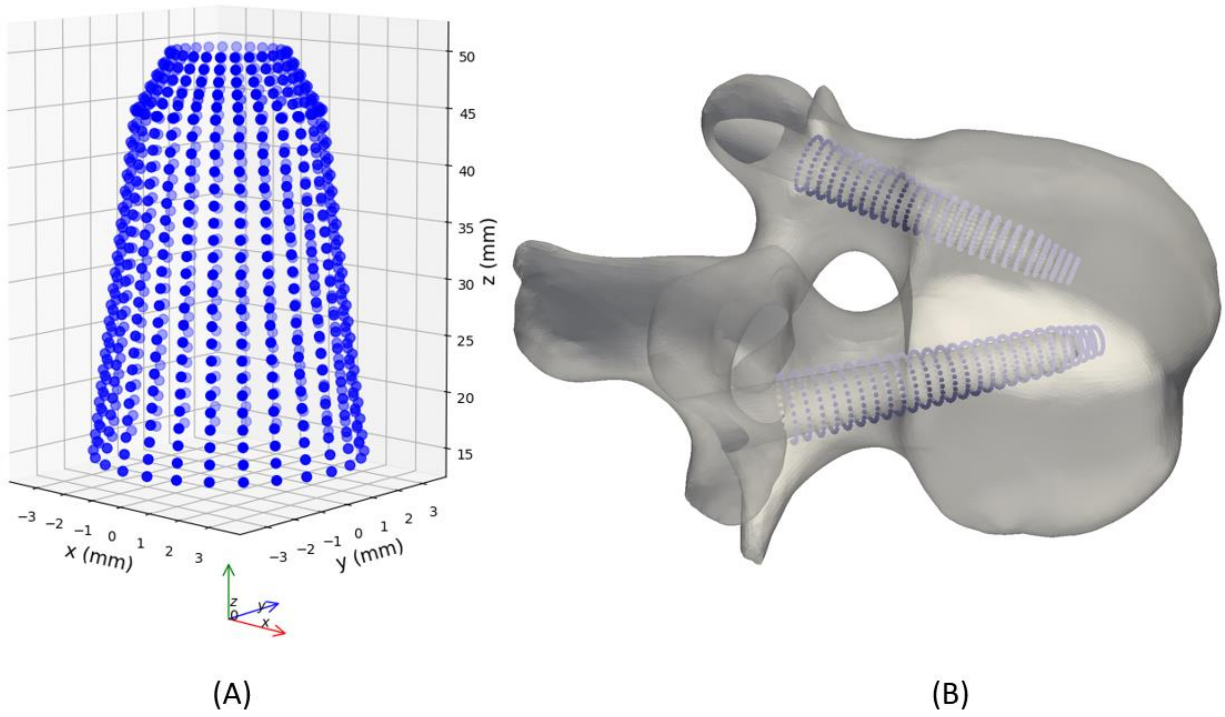

Figure 4.9 – Grid of points to sample the strain in the bone in the region around the screws for an example with D = 6.5 mm, L = 45 mm, ϑ = 0° and φ = 0°, showed in the reference system (A) and within the vertebra after roto-translation (B).

Before the reduced models can be exploited to predict the simulation results, the accuracy of the prediction must be quantified with respect to the reference FE models. Therefore, the first step in the construction of the reduced model is the definition of the learning and the validation sets. These sets are associated with combinations of parameters in the parametric space. It is important to define the location of these combinations in the parametric space as well as the dimensions of the learning and validations sets.

Sixteen validation snapshots were chosen at the centres of the 16 hyper-parallelepipeds that compose the 4D design space (2D case: a square can be divided by 2^2 squares; 3D case: a cube can be divided in 2^3 cubes and so on) (Figure 4.10). By doing so, the design space was uniformly covered by the validation snapshots. As the error was higher for the chosen 16 validation snapshots, this set was retained to assess the performance of the reduced models.

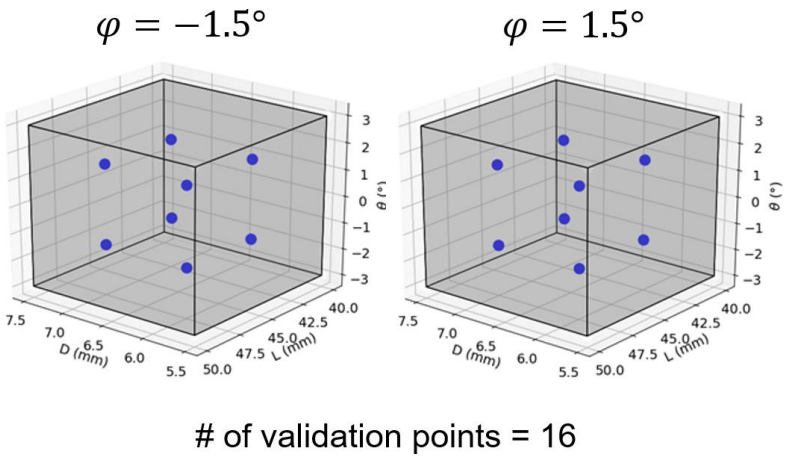

Figure 4.10 - Location of the combinations of the shape parameters D, L, ϑ, ϕ corresponding to the 16 validation snapshots represented (blue dots) in the $\mathbb{R}^4$ subspace.

Considering that the number of learning points will affect the predictive ability of ROMs and that it is not clear what is the best compromise between the accuracy of ROMs and the efficiency of the approach, a sensitivity analyses on the number of learning points was performed. The initial set of learning points was chosen by considering a simple full factorial design with two levels per parameters (DOE1). The two levels corresponded to the minimum and maximum values selected per each parameter (Section 4.4.1.2). By using this type of design, the corners of the design domain (a hypercube) were sampled as showed in Figure 4.11. Then, the number of learning snapshots was increased to 17 (DOE2), 27 (DOE3) and 45 (DOE4) to study the effect of the number of learning snapshots (Figure 4.11). The DOEs were built by progressively adding one or more snapshots to the previous learning set. The maximum number of modes to build the ROMs was chosen for each DOE in order to make the analyses uniform among different DOEs.

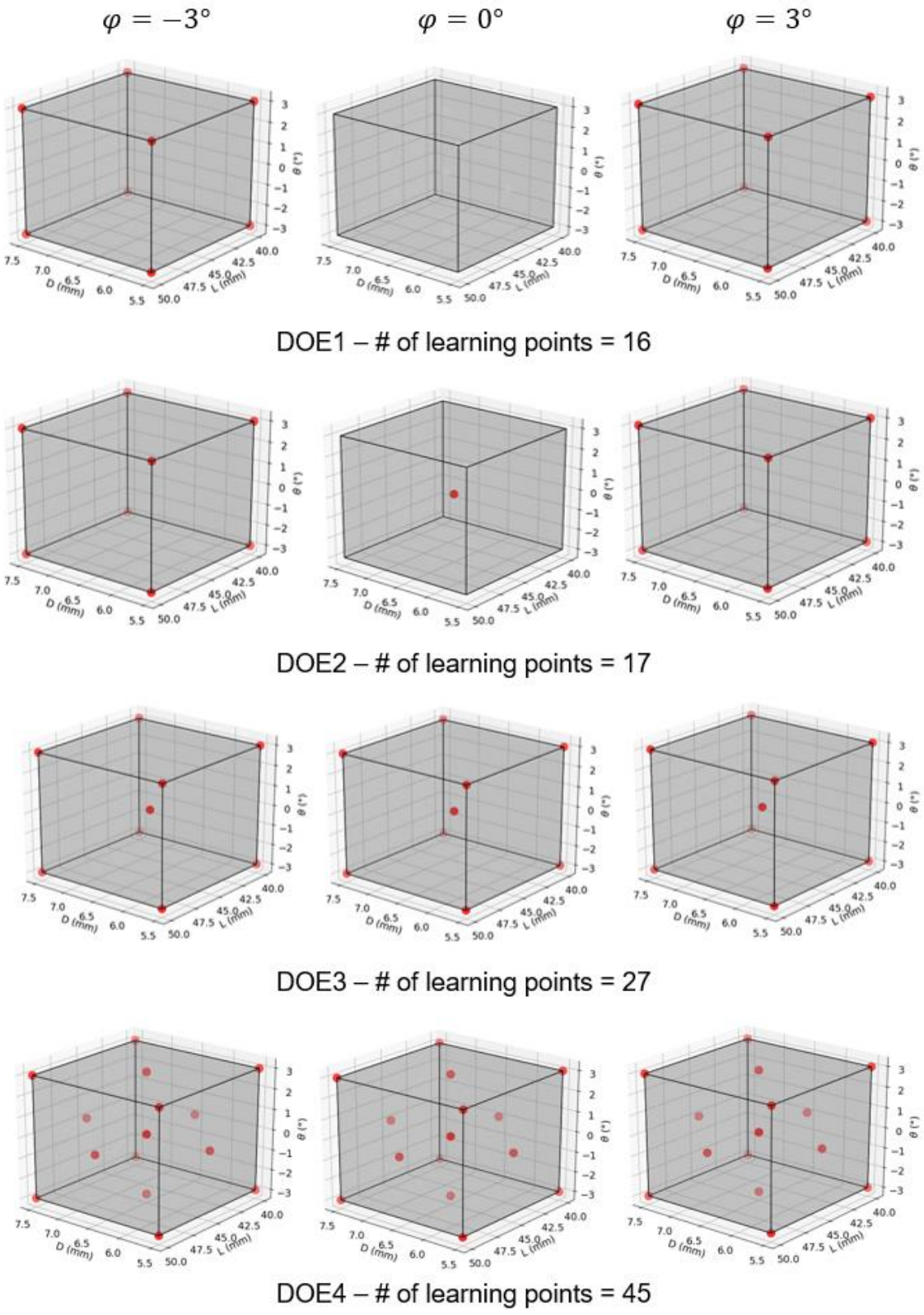

Figure 4.11 – The combinations of parameters D, L, ϑ, ϕ for the learning set (red points) shown in the $\mathbb{R}^4$ subspace for the considered Designs of Experiment (DOE).

To build the reduced models, Ansys Static ROM Builder (accessible in Ansys Twin Builder® software) was used. This software implements a reduced-basis approach (Section 1.8) which is based on a reduction and construction phases. In the reduction phase the learning snapshots are compressed by SVD. An optimal number of modes to represent the learning dataset must be chosen. The ROM is the result of the construction of the response surfaces of the modes coefficients as a function of the input parameters. The creation of response surfaces for each mode is based on the Genetic Aggregation Response Surface (GARS) algorithm (Ben Salem and Tomaso, 2018). This technique selects the interpolator or gives the best combination of several interpolation methods usually used to create response surfaces. It is important to consider two types of metrics to evaluate the performance of ROMs. In fact, both the projection phase, i.e., the creation of a reduced basis, as well as the construction phase, i.e., the creation of response surfaces, must be assessed.

To evaluate the accuracy of the projection phase, the relative norm projection error (Eq. 4.1) ($e_{NORM_{Proj}}$) between the field predicted projected in the basis of modes and the solution of the FE model was calculated. To evaluate the accuracy of the prediction of ROMs, the relative norm ROM error (Eq. 4.2) ($e_{NORM_{ROM}}$) between the field predicted by the ROM and the solution of the FE model was calculated. Additionally, the distributions of absolute ROM error (Eq. 4.3) ($e_{ABS_{ROM}}$) over the domain were evaluated. The ROM error represented the sum of the projection error and the interpolation error introduced by the creation of response surfaces for each mode of the basis.

$$e_{NORM_{Proj}} = \frac{\sqrt{\sum_i \left(x_{SVD_i} - x_{FE_i}\right)^2}}{\sqrt{\sum_i \left(x_{FE_i}\right)^2}} \qquad \text{(Eq. 4.1)}$$

$$e_{NORM_{ROM}} = \frac{\sqrt{\sum_i \left(x_{ROM_i} - x_{FE_i}\right)^2}}{\sqrt{\sum_i \left(x_{FE_i}\right)^2}} \qquad \text{(Eq. 4.2)}$$

$$e_{ABS_{ROM}} = |X_{ROM} - X_{FE}| \qquad \text{(Eq. 4.3)}$$

4.4.2 Results and Discussion

Overall, the average $e_{NORM_{ROM}}$ decreased from DOE1 to DOE4, i.e., by increasing the number of learning points (Figure 4.12).

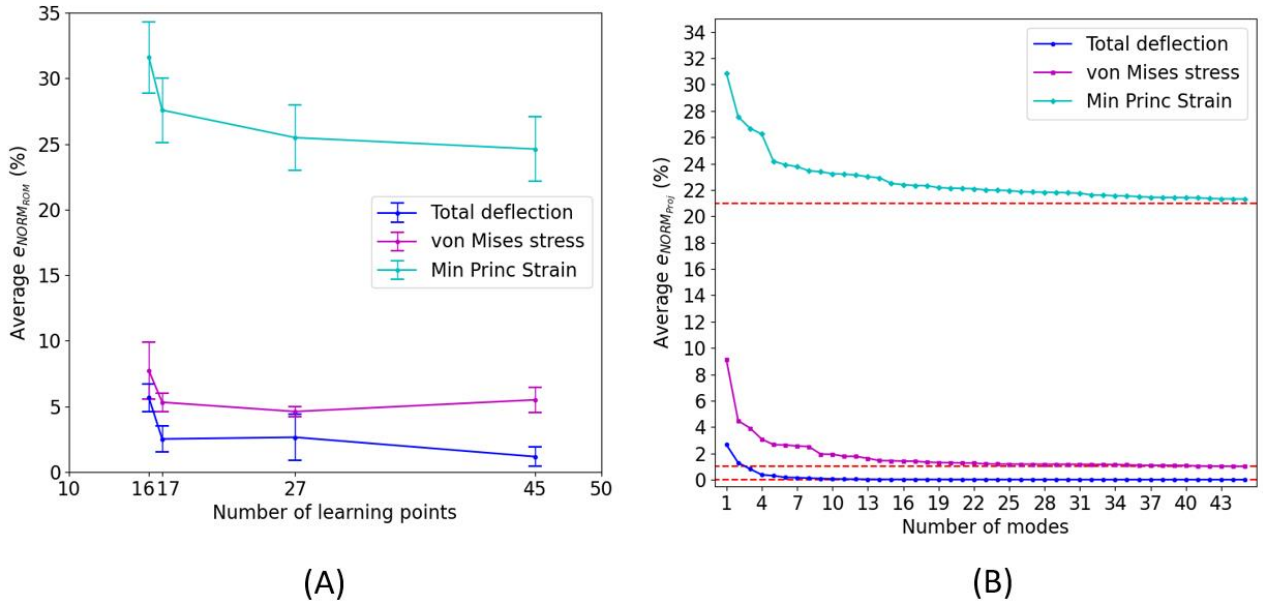

Figure 4.12 – ROM errors on the validation set in function of the number of learning points (A) and projection errors in function of the number of modes retained to build the ROMs in DOE4 (B), reported for the ROM of the total deflection, the ROM of the von Mises stress, and the ROM of the minimum principal strain.

As it concerns the ROMs of results in the screws, the average $e_{NORM_{ROM}}$ over the validation snapshots was lower than 3% for the total deflection, and under 6% for the von Mises, when the ROMs were built with 17 learning points (Figure 4.12A). As expected, ROMs presented better performance for the deflection than for the stress. In fact, the FE solution is more accurate on displacements than on derived quantities. Therefore, inaccuracies in the FE solution could lead to deteriorated performance of ROMs.

In the case with 45 learning points (DOE4), the average $e_{NORM_{ROM}}$ for the deflection significantly decreased by 53% with respect to the case with 17 learning points (DOE2) (Figure 4.12A). However, the average $e_{NORM_{ROM}}$ was lower than 3% for DOE2 (Figure 4.12A). This error was

considered acceptable for the envisaged application in reason of the variability of the deflection in the range of variation of parameters, and the superior computational cost related to DOE4.

The average $e_{NORM_{ROM}}$ error for the σ_{VM} slightly decreased in DOE3 and slightly increased in DOE4 with respect to DOE2. However, the average $e_{NORM_{Proj}}$ over the validation snapshots was higher for DOE2 (2.08%) than for DOE4 (1.00%), considering the maximum number of modes. These results showed that, in the process of construction of the ROM of the σ_{VM}, while the compression phase benefited from the increase of the number of learning snapshots, the interpolation phase presented worsened performance. The construction of the response surface based on the interpolation of modes coefficients is sensitive to possible sources of noise within the FE result fields, as, for instance, the differences among meshes of the vertebra for different models, heterogeneity of the bone etc. (more details are provided below). In addition, the geometry of the tip of the screws presented a sharp angle that act as a stress concentrator where the FE solution is less accurate than in other regions. Due to this characteristic of the stress fields, it would be difficult to find common patterns for the distributions among models with different screw sizes and orientations that could be effectively captured by the compression of snapshots. The possible sources of noise are inter-connected among them and it would be hard to isolate the effect of each cause. Further analyses are presented in Section 4.5 on a simplified model with only two shape parameters (diameter and length) to investigate the source of the error. For the construction of the ROM, DOE2 was chosen as the best compromise between the $e_{NORM_{ROM}}$ and the computational cost related to the generation of the learning snapshots.

The average $e_{NORM_{ROM}}$ over the validation snapshots for the ε_{p3} in the bone decreased in function of the number of learning points, but was higher than 24% when the ROM was built with 45 learning points (Figure 4.12A). Regarding the ROM of the ε_{p3} in the bone, it must be noted that the average $e_{NORM_{Proj}}$ over the validation snapshots reached a plateau at 21% for DOE4 in function of the number of modes (Figure 4.12B). This result showed that the modes created by compression of the learning snapshots were not able to represent the validation snapshots. Therefore, the high $e_{NORM_{ROM}}$ for the ε_{p3} was not due to the construction of response surfaces. This result represents a limitation of this study and will be discussed below.

The distribution of results estimated by FE models, the one predicted by the ROMs as well as the distribution of the $e_{ABS_{ROM}}$ for the validation snapshot with the highest error are showed in Figure 4.13, Figure 4.14, and Figure 4.15, for the ROM of the total deflection (DOE2), the ROM of the

von Mises stress (DOE2), and for the ROM of the minimum principal strain (DOE4), respectively. The distributions of $e_{ABS_{ROM}}$ were similar among the validation snapshots, therefore the worst-case scenario is reported.

The peak $e_{ABS_{ROM}}$ for the deflection was often located at the head of the screws (Figure 4.13). The highest peak $e_{ABS_{ROM}}$ over the snapshots had order of magnitude of 10^{-2} mm, which corresponds to 5.5% in relative error. In addition, the head of the screws was a region characterized by many nodes with high values of deflection and values of $e_{ABS_{ROM}}$ close to the peak value.

The peak $e_{ABS_{ROM}}$ for the σ_{VM} in the screw was localised at the tip of the screws (Figure 4.14). This part of the FE model is characterized by a geometrical singularity that results in an inaccurate σ_{VM} distribution with many local peaks close to the singularity. These values are probably randomly distributed over the different screw sizes and orientations and could not be taken into account by the ROM, which presented high absolute errors in those nodes. The $e_{ABS_{ROM}}$ distribution presented low values in the area where the peak σ_{VM} occurred.

The $e_{ABS_{ROM}}$ distribution of the ε_{p3} in the bone presented high values at both right and left sides. In fact, the peak $e_{ABS_{ROM}}$ shifted between right and left sides among the validation snapshots and was located at the level of the top side of the screws (pulled fibers), close to the tips (Figure 4.15), in the same region where the peak ε_{p3} occurred. This area was subjected to high compressive loads due to the bending of screws. While the strain distributions among models with different combinations of parameters were similar due to the same loading condition, local peaks of strain depended on the distribution of Young's moduli in the bone that, in turn, changed in function of the shape parameters. Therefore, the heterogeneity of material properties may play an important role on the $e_{ABS_{ROM}}$ distribution. In addition, the geometry of the screws presented a sharp corner due to the change of diameter between the body and the tip of the screws close to that region. This geometric feature may affect the accuracy of the strain distribution predicted by FE models, and, as a consequence, the $e_{ABS_{ROM}}$ distribution.

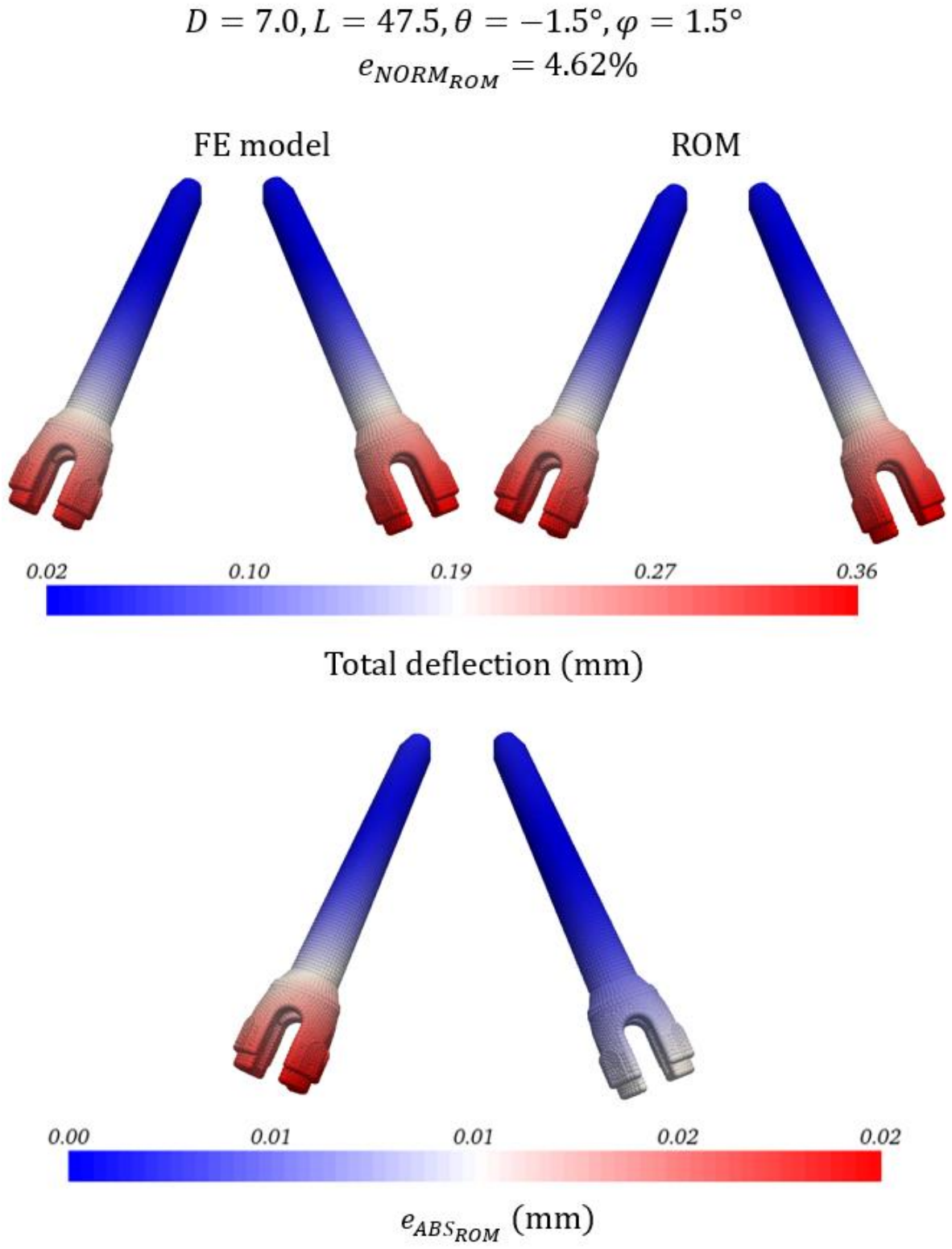

Figure 4.13 - Distribution of total deflection of the screws evaluated by the FE model and by the ROM, as well as the absolute difference between the two fields, for the configurations with the highest ROM error. A view from the top (cranial side) is shown. The distributions were similar among validation snapshots.

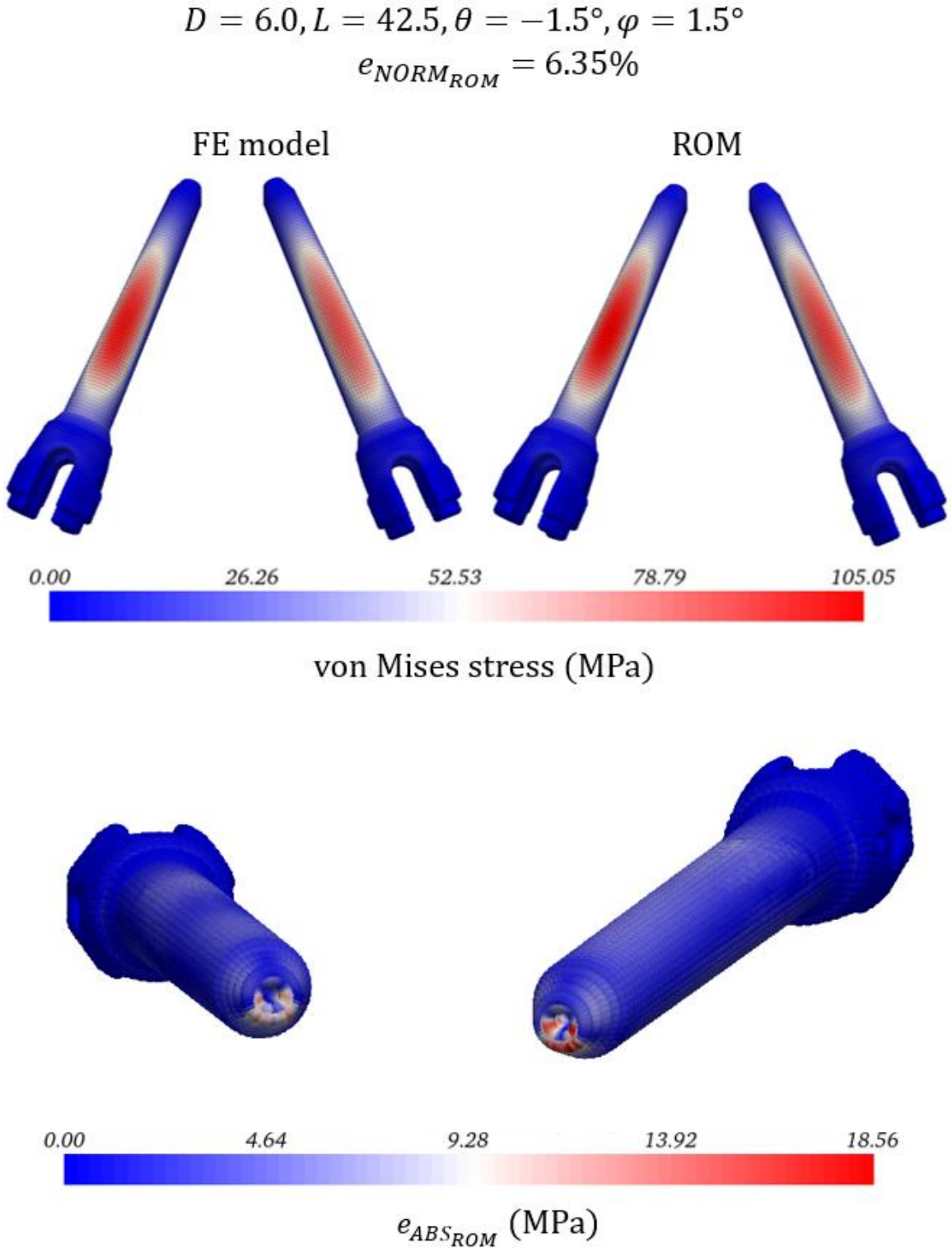

Figure 4.14 - Distribution of von Mises stress on the screws evaluated by the FE model and by the ROM (top view), as well as the absolute difference between the two fields (view from the anterior part of the vertebral body), for the configurations with the highest ROM error. The distributions were similar among validation snapshots.

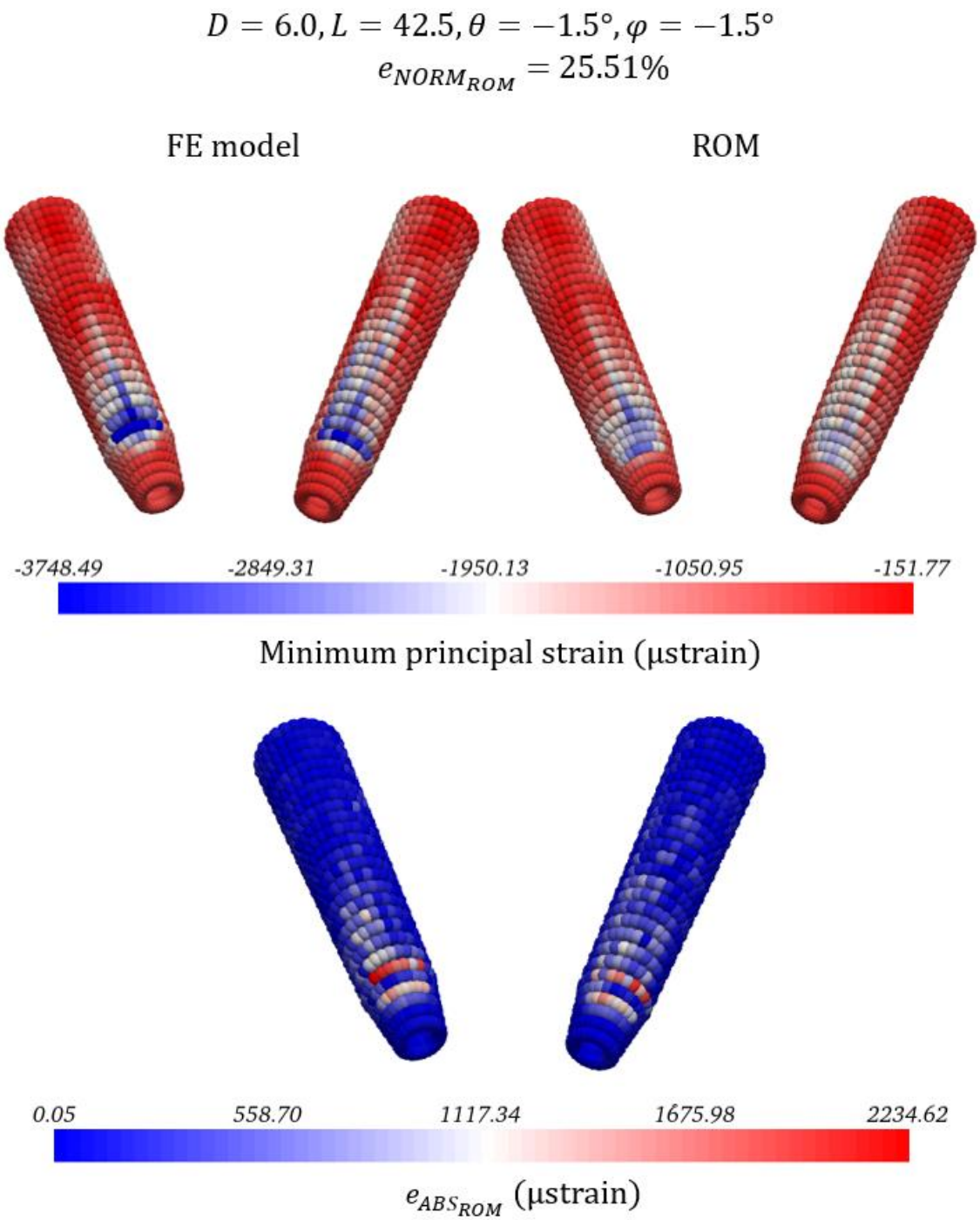

Figure 4.15 - Distribution of minimum principal strain in the vertebra in a region around the screws evaluated by the FE model and by the ROM, as well as the absolute difference between the two fields, for the configurations with the highest ROM error. A view from the anterior part of the superior endplate is proposed. Similar distributions were found for other validation snapshots.

The presented approach is effective to investigate and optimise the shape parameters in order to decrease the risks of failure of screws, even though it could not be reliably used to study the effect of different sizes and orientations of screws on the strain in the bone. It must be noted that the FE model presented some features that could influence the performance of the ROM by introducing some variability into the data that are difficult to capture by compression. First, in this study, different screws' sizes and orientations were represented in the FE model by mesh morphing of the screws, while the mesh of the vertebra was calculated each time based on the solid CAD model. For this reason, the number of nodes and elements of the vertebra changed as well as the interaction between screws and holes in the vertebra for each combination of shape parameters, which could result in introducing some inconsistencies and noise into the model. Additionally, the bone was modelled as heterogeneous material with material properties derived by CT-scan grey levels. Each component of a snapshot, while associated with positions in correspondence among different models, it was also associated with different positions within the vertebra, and, as a consequence, with different Young's moduli. For instance, if the component X within one snapshot corresponded to a certain location close to the tip of the screw, the component X of all other snapshots must correspond to the same location relative to the tip of the screw. However, those locations were in different positions with respect to the geometry of the vertebra, and therefore were associated with different Young's moduli and with a different mechanical response to the external loads. The modelling of the screws-bone interface could also have an important role. With a frictional interface, normal and shear stresses carried by the two contacting geometries are taken into account across their interface. The software allows to manage any initial gaps or penetrations locally or uniformly along the contacting surfaces in order to enforce contact compatibility, i.e., to prevent interpenetration. In this study the default option "Adjust to Touch" was used. With this option the software searches the smallest gap and apply an offset to all contact elements over the interface of one of the bodies to close this gap. Even if the accuracy of the morphing transformations was verified, small gaps or penetrations due to mesh morphing or to mesh discretization would be considered in a different way for each model, therefore introducing some differences among models. The management of initial gaps and penetrations must be furtherly explored. It was hypothesized that the most important issue was the re-computation of the mesh of the vertebra among different models.

The goal of this study was to explore the performance of a ROM-based pipeline to optimize the screw size and positioning for a single patient. Because of this limitation, the findings about the influence of the number of learning points on the ROM error must be evaluated carefully. The

analysis should be extended to more patients in future works to determine an optimal DOE. The optimal DOE could be used to compute the ROM construction phase for patients that does not need an urgent treatment. By using the ROM, it would be possible to explore continuously the range of variation of parameters and to optimize the insertion-related parameters of the screws. Additionally, the number of computations in the *offline* phase could be optimised by evaluating the sensitivity of the model to all the parameters and the interactions among the different parameters. In this way, it would be possible to adjust the sampling of the parametric space and the choice of validation points to explore regions of high sensitivity of the model. Further analyses to explore the effect of different modelling choices on the ROM errors are presented in Section 4.5 for a model where both the screws and the vertebra were morphed to update the screws' size (only two shape parameters). An example of application of ROMs to the minimisation of the total deflection and the σ_{VM} in the screws for one patient is presented in Section 4.6.

4.4.3 Conclusion

In this study, an approach to dramatically reduce the computational time of a parametric FE model to study the effect of the size and orientation of pedicle screws implanted in a vertebra has been presented. Such approach could be used to minimise the risk of rupture of the screws (von Mises stress), but it is not accurate enough to investigate the bone failure due to excessive deformation of trabecular bone at the screws-bone interface. An application of this approach to one patient is presented in Section 4.6. Further analyses are needed to examine the impact of some features of FE models on the performance of ROMs and to test the influence of the identified sources of noise on the ROM of the strain in the bone.

4.5 Exploration of ROMs for studying the effect of the screw size

The goal of this subchapter was to evaluate the efficacy of Reduced Order Modelling approaches using parametric FE models of a single vertebra implanted with pedicle screws of various sizes and lengths, considering different modelling choices in terms of bone material properties and screws-bone interface.

4.5.1 . Materials and Methods

4.5.1.1 Summary

A subject-specific FE model of one vertebra bilaterally instrumented with pedicle screws was adapted to different diameters and length of screws by using mesh morphing. In order to address the challenges presented in Section 4.4.2, three types of models with a decreasing degree of complexity were built in terms of bone material properties and screws-bone interface. For each type of model, FE simulations were run with nine different combinations of shape parameters. The mechanical outputs of models (deflection and stress in the screws, strain in the bone) were exploited to build ROMs that were assessed based on a validation set of simulations. The ROM error was evaluated in function of the number of learning points.

4.5.1.2 Mesh morphing

A mixed tetrahedral/hexahedral mesh as described in Section 4.3 was generated on the model with the optimal screw size (template mesh). This mesh was morphed with a series of multiple transformations that allowed to change the diameter and the length of the screws and of the holes within the vertebra (Figure 4.16). In this study, we considered a range of variation of the diameter between 5.5 mm and 7.5 mm and a range of variation of the length between 40 mm and 50 mm as suggested by an expert surgeon. Each time, the accuracy of morphing operations was verified by calculating the maximum distance between the morphed mesh and the mesh computed on the solid CAD model (target mesh) obtained by Boolean subtraction (cf. Chapter 3), and verifying that this distance was lower than 0.01 mm.

The template mesh of the screws was morphed with a single transformation that allowed to change the diameter (D) and length (L) of the screws simultaneously. The detailed procedure to derive the control points and the displacement field characterising this transformation is reported in Section

4.4.1.3.2. A series of four transformations was needed to accurately morph the template mesh of the vertebra to change the D and L of the two holes. The first transformation was directly derived by the transformation applied to the screws by excluding the control points falling outside of the vertebra (Figure 4.16A). The subsequent transformations were defined based on the in-built transformations of RBF Morph and the set of surfaces and edges of the solid CAD models of the vertebras corresponding to different diameters and length of screws. In fact, in the second transformation, the edges of the holes were morphed onto the edges of the target mesh with a Curve Targeting transformation, the surfaces containing those edges were left free to accommodate the modification and other surfaces were assigned a null displacement (Figure 4.16B). After that transformation, the surfaces on the external surface of the vertebra were projected onto the corresponding surfaces on the target model (Figure 4.16C). Finally, the internal surfaces of the two holes were also projected onto the corresponding surfaces (Figure 4.16D). This series of transformations allowed to obtain differences lower than 0.01 mm for all the meshes of the vertebra with respect to the target meshes.

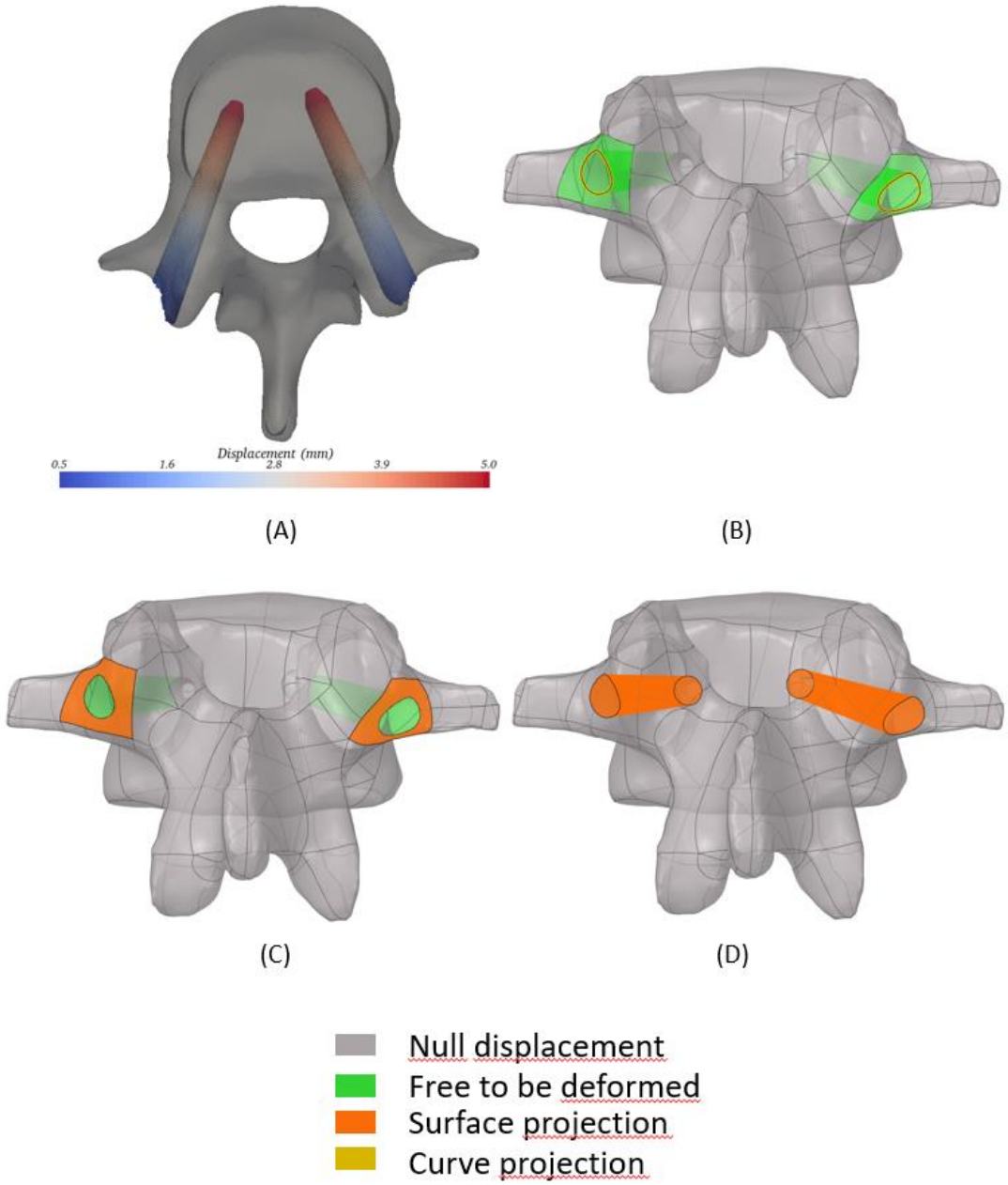

Figure 4.16 – Outline of the transformations to change the diameter and length of the holes by mesh morphing: (A) Update of diameter and length; (B) projection of edges; (C) projection of external surfaces of the holes; (D) projection of internal surfaces of the holes.

4.5.1.3 Material properties and screws-bone interface

In Section 4.4.2, three main features of the FE model that influence the performance of ROMs were identified: the mesh, the material properties of the bone, the screws-bone interface. In this sub-

study, the shape parameters of both the vertebra and the screws were updated by mesh morphing (cf. Section 4.5.1.2). In this way, the finite element computational grid had the same number of nodes and elements for each configuration of parameters. Three types of models with different definitions of material properties and interface conditions were tested in this sub-study:

1. a model with heterogeneous material properties of the bone and frictional screws-bone interface was built as done in Section 4.4;
2. model #1 was simplified in order to assess the effect of material properties: the bone was considered isotropic and homogeneous (E_{homo} = 2672 MPa, ν = 0.3), while the interface was kept frictional;
3. a further simplification was introduced in model #2 in order to investigate the effect of interface conditions between the bone and the screws: the interface was considered bonded as previously assumed in Chapter 3.

For these three types of models with decreasing complexity, different combinations of diameter and length were tested, and ROMs of mechanical results were built and compared.

4.5.1.4 ROMs of the mechanical results

Three different ROMs were built based on the mechanical results of the FE models: a ROM of the total deflection of the screw, a ROM of the σ_{VM} in the screws, and a ROM of the ε_{p3} in the vertebra were created in function of the diameter and the length of the screws. The mechanical results in the screws and in the vertebra were sampled at nodes to build the set of vectors for ROMs. While for the screws all the nodes were used to create the snapshots, for the vertebra only nodes belonging to a region of interest were considered. The ROI had a conic shape and was coaxial with the longitudinal axis of the screw as defined in Section 4.4.1.4. It was defined at the screw-bone interface as this region was identified as the most critical area to assess the mechanical resistance of the bone. The nodes belonging to the ROI were determined for the model with optimal screw size (D = 6.5 mm, L = 45 mm). The results corresponding to the same set of nodes were considered for model with different sizes of screws. The errors obtained by using ROMs was compared with errors obtained by standard linear interpolation of mechanical results in function of the shape parameters D and L.

In this study, 4 different sets of learning snapshots with number of learning snapshots varying from 4 to 9 were tested. The locations of the combinations of parameters within the design space are showed in Figure 4.17. The DOEs were built by progressively adding one or more snapshots to the

previous learning set. The maximum number of modes to build the ROMs was chosen for each DOE in order to make the analyses uniform among different DOEs. As it concerns the validation set, 4 validation snapshots were chosen at the centres of the 4 rectangles that constitute the 2D design space (Figure 4.17).

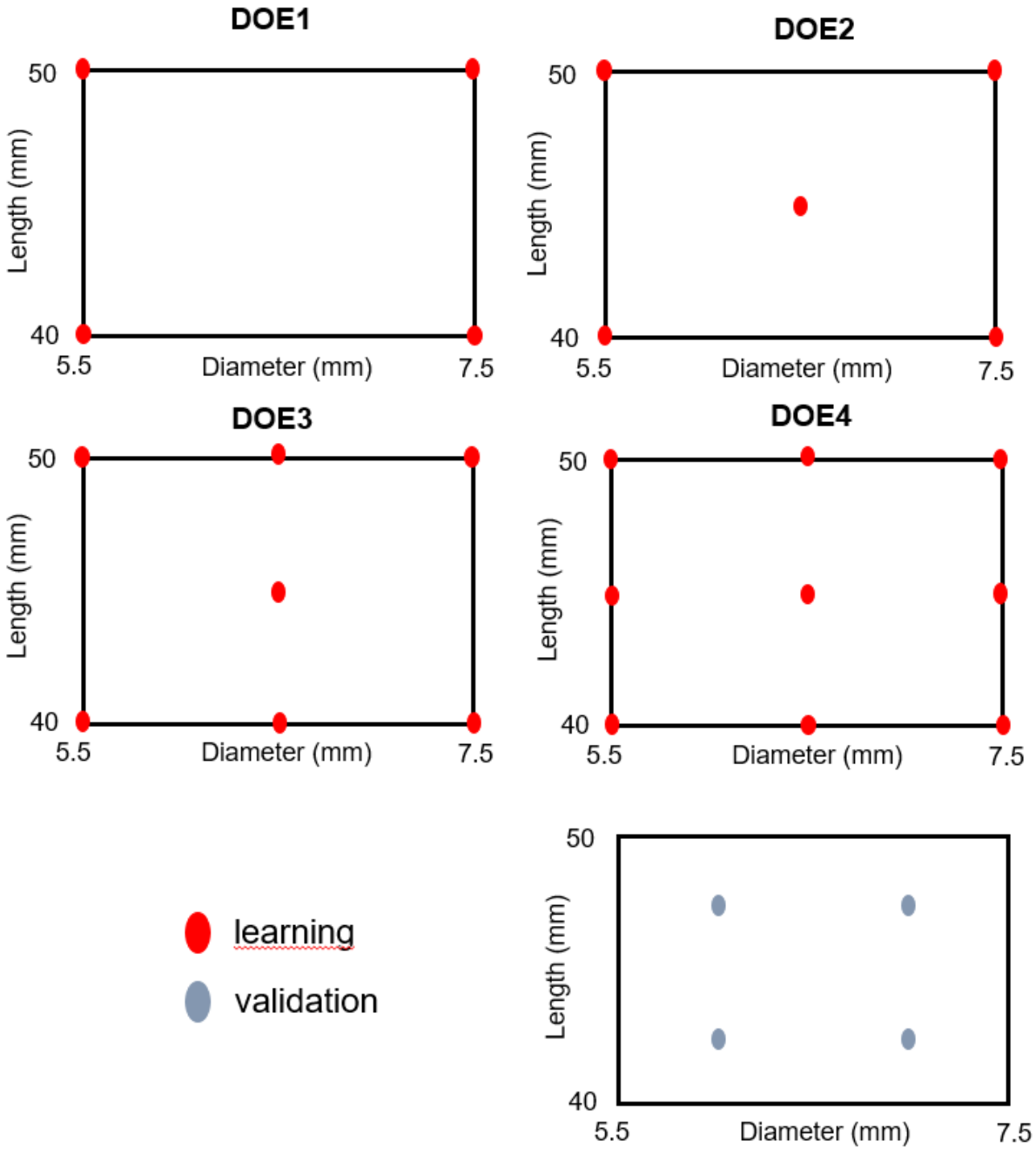

Figure 4.17 - Combinations of diameter and length for the learning sets (red) and the validation set (blue). The learning snapshots varied for each Design of experiment (DOE1-4), while the validation snapshots were fixed.

4.5.2 Results and Discussion

Overall, the best performance was found for linear models with homogeneous material properties and bonded interface for both ROMs of mechanical properties in the screws and in the bone (Figure 4.18). The average $e_{NORM_{ROM}}$ over the validation snapshots was lower than 4% in DOE2 for the ROM of the ε_{p3} in the bone in the case with homogeneous properties and bonded interface (Figure 4.18C). For the ROM of the ε_{p3}, in all the tested DOEs, the model with homogeneous properties and bonded interface provided the lowest average and standard deviation $e_{NORM_{ROM}}$, while the model with heterogeneous properties and frictional interface provided the highest $e_{NORM_{ROM}}$. For other components of the strain it was observed a similar behaviour (Appendix, Section Appendix A2).

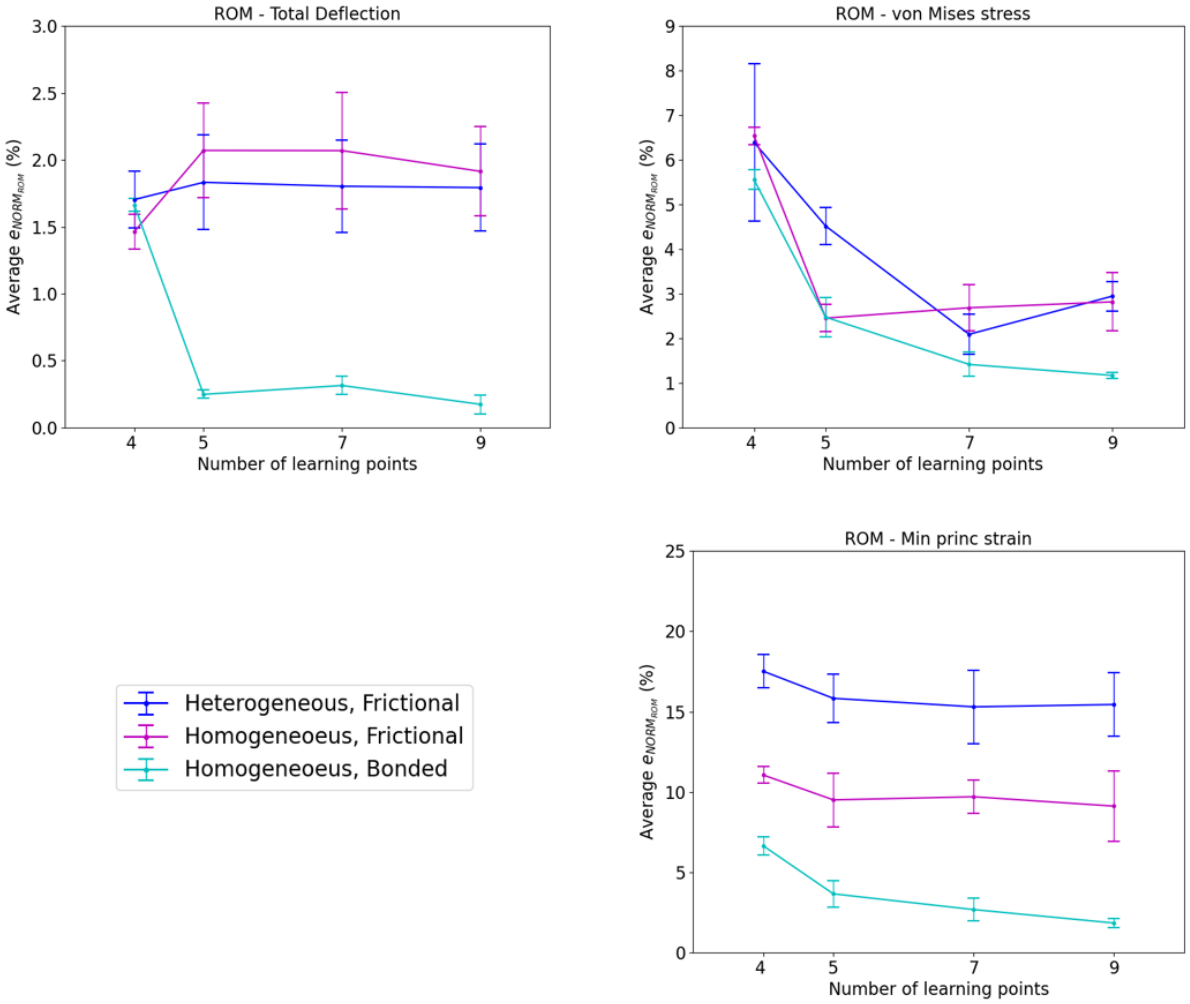

Figure 4.18 – Average ROM errors over the validation snapshots, in function of the number of learning points, for FE models with different combinations of bone material models and screws-bone interface, for the ROM of the total deflection (A), the ROM of the von Mises stress (B) and the ROM of the minimum principal strain (C).

The case with homogeneous properties and bonded interface presented the lowest average $e_{NORM_{ROM}}$ (and standard deviation) also for the ROM of the deflection and the ROM of the σ_{VM} in the screws (Figure 4.18A-B). For the ROM of the deflection, the $e_{NORM_{ROM}}$ for models with homogeneous properties and frictional interface were higher than the case with heterogeneous properties and friction. This was unexpected as the heterogeneous distribution of material properties in the bone increases the level of complexity of the FE models and, therefore, could deteriorate the performance of ROMs. However, it must be noted that the $e_{NORM_{Proj}}$ was higher in the case with heterogeneous properties and frictional interface (Figure 4.19). This showed that, when building the ROM, the interpolation phase played a major role in deteriorating the performance of ROMs for model with homogeneous properties and frictional interface. However, attention should be paid to the fact that the $e_{NORM_{ROM}}$ is about or lower than 2% for both the types of models, therefore very low. Additionally, when comparing models with heterogeneous or homogeneous properties, it is difficult to exclude the effect of a frictional interface from the analysis of the deflection in the screws, especially considering the small differences between the $e_{NORM_{Proj}}$ and the $e_{NORM_{ROM}}$ for the two types of models.

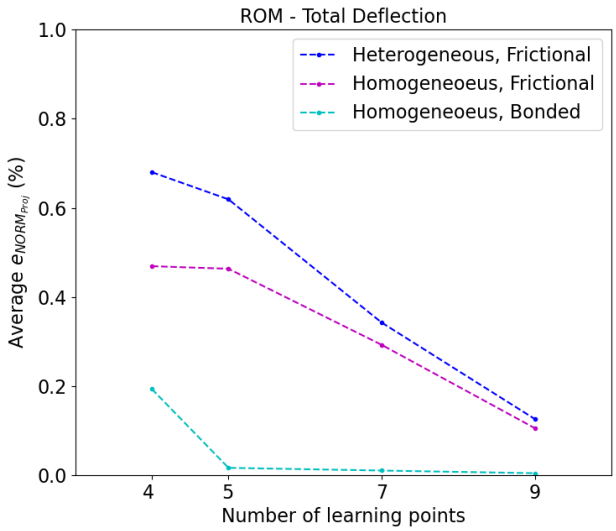

Figure 4.19 - Average projection errors over the validation snapshot, in function of the number of learning points, for FE models with different combinations of bone material models and screws-bone interface, for the ROM of the total deflection.

These results showed that the contact interface between the screws and the bone had the most significant effect on the ROM error. This finding was unexpected as it was previously hypothesized that the absence of mesh morphing in the vertebra had a large influence on ROMs.

For frictional and bonded interface conditions, the management of any initial gaps and penetrations between bodies in contact was different. In fact, for a frictional interface the option "Adjust to touch" (cf. Section 4.3) was used, and, as a result, an offset was applied to all the elements of one of the bodies to close the smallest gap. In case of a bonded contact, the software constrains the nodes of bodies at the interface to have the same displacement. This results in a sort of correction of any initial gaps and penetrations locally along the contacting surfaces. Therefore, a bonded interface provided a more uniform treatment of the initial contact conditions among the different models. In addition, it must be noted that with a bonded interface, connected components always touch each other during the analysis, while with a frictional interface the two contacting geometries can slide relative to each other and separate. Therefore, local phenomena and exchange of forces at the contacting surfaces with a frictional interface are hypothesized to introduce local variability among different models, especially in case of meshes with different type and size of elements, which play a role in the strain distribution in the bone influencing the performance of ROMs. Additionally, the optimal element size identified through a mesh refinement study (Chapter 3) has been used for both the screw and the vertebra. However, smaller elements could be necessary to reduce the error associated with the discretization and excluding local inaccuracies in the FE solution fields. In fact, the strain distribution at the interface could be smoother if the screw and the vertebra were meshed with a similar element size. In addition, it should be noted that the accuracy of the strain distribution predicted with FE models should be assessed with respect to experimental measurements. The strain in the bone could be measured by using a combination of *in situ* mechanical testing, micro-CT scanning and a global Digital Volume Correlation approach. However, it is challenging to implement this approach due to the artifacts induced by implants.

As models with homogeneous properties and bonded interface are characterized by a lower computational time to solve the FE models with respect to non-linear models, attention must be paid when determining the trade-off between the accuracy of ROMs and the computational time needed to obtain the exact FE solution. However, ROMs could be useful to reduce the number of combinations needed to optimise the fixation-related parameters in cases with several parameters (related to the size and orientation of screws, the insertion point, or to the mechanical properties of the bone, the loading conditions etc.), large ranges of variation, more complicated geometries (multiple vertebral levels, intervertebral discs, rods etc.) and material non-linearities. Further

investigations are needed to apply ROMs to FE models including friction and heterogeneous properties in order to analyse the strain in the bone, while the ROM errors related to the metrics in the screws are satisfying.

For the case with homogeneous properties and bonded interface, overall, the error obtained by using ROMs or linear interpolation of results was comparable, but ROMs provided lower errors for cases with 7 or 9 learning points for all the metrics (Figure 4.20). However, as the differences between the two approaches were low, it is hard to justify the usage of more complex mathematical techniques as ROMs. Furthermore, in more complicated cases the errors given by linear interpolation were better than the ROM errors due to the effect of frictional interface or heterogeneous properties (see Appendix A3). It has to be noted that previous studies showing the application of ROMs to models of soft tissues or musculoskeletal structures have not reported about the benefits of ROMs with respect to a standard linear interpolator (Niroomandi et al., 2012, 2020; Luboz et al., 2018; Lauzeral et al., 2019; Calka et al., 2021). The potential of ROMs should be explored in case of high non-linear relationship between the FE models results and the parameters of the model that makes inadequate the usage of standard linear interpolation.

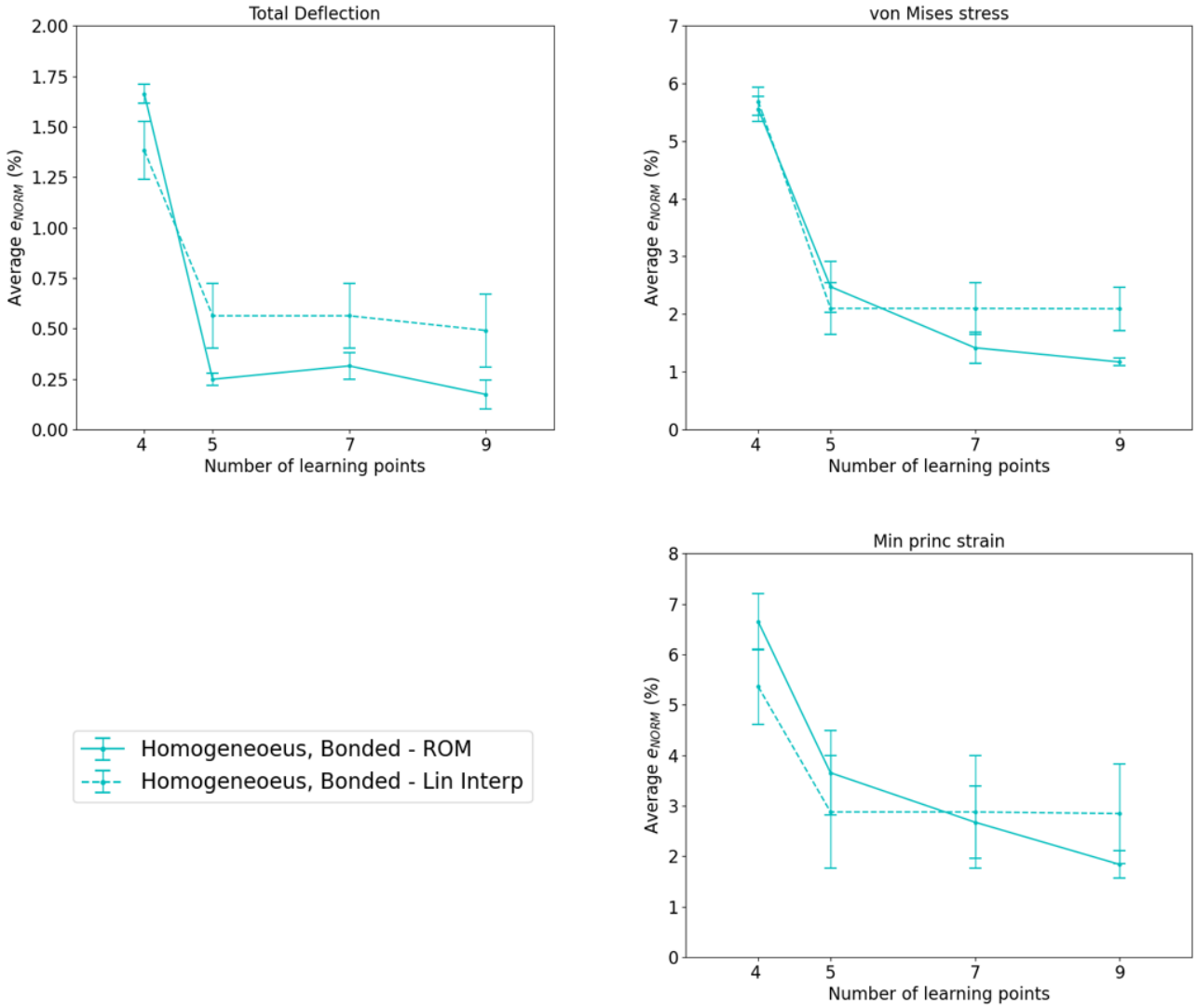

Figure 4.20 - Average errors over the validation snapshot, in function of the number of learning points, obtained by using Reduced Order Modelling techniques (continuous lines) or standard linear interpolation (dashed lines), for FE models with homogeneous bony properties and bonded contact conditions, for the ROM of the total deflection (A), the ROM of the von Mises stress (B) and the ROM of the minimum principal strain (C).

4.5.3 Conclusion

This sub-study aimed at applying a pipeline based on mesh morphing and Reduced Order Modelling techniques to a FE model of one vertebra implanted with pedicle screws of different sizes. The performance of ROMs built from reference FE models of different complexity in terms of bone material models and bone-screws interface.

The performance of ROMs is highly sensitive to the screws-bone contact conditions. For FE models with homogeneous properties and bonded interface, the ROMs of both metrics in the screws and in the bone presented acceptable errors, and, overall, the accuracy of ROMs improved when the number of learning points increased. While ROMs of models with frictional interface presented good accuracy for the deflection and the stress in the screws, those models cannot be used to investigate the strain in the bone. Additional analyses are needed to optimise the screws-bone contact condition with friction.

4.6 Example of application of ROMs to optimise size and orientation of pedicle screws

The aim of this sub-study was to exploit the ROM of the total deflection and the ROM of the von Mises stress built in Section 4.4 to optimise the size and the orientation of pedicle screws for one patient. These metrics could be used in the clinical setting to estimate the global stiffness of the implanted structure and the risk of rupture of the implants.

4.6.1 Material and methods

The size and the orientation of the screws were optimised to minimise the peak total deflection as well as the peak σ_{VM} in the screws. ROMs built in Section 4.4 and based on parametric FE models of one vertebra implanted with pedicle screws with 4 shape parameters (D, L. θ and φ) were used for the optimization. For both the total deflection and the σ_{VM}, DOE2 (17 learning points, cf. Figure 4.11) was chosen to build ROMs that provided an average $e_{NORM_{ROM}}$ lower than 3% for the total deflection and lower than 6% for the σ_{VM}. This was considered the best compromise between the accuracy of ROMs and the computational time needed to run the models corresponding to the learning set. To build the ROMs, the maximum number of modes was retained in order to include in the basis of modes all the variability of data included in the learning set.

Once the independent ROMs for the total deflection and the σ_{VM}, were built, they were exploited to compute a real-time evaluation of combinations of parameters within the 4D parametric space. In fact, a full factorial DOE with 10 levels per parameter was assessed. The 10 levels for each parameter were determined as equally spaced values between the minimum and maximum values. In total 10000 combinations of parameters were explored. For each combination, the ROM solution snapshot was evaluated. Then, the minimum d_{max} and the minimum peak σ_{VM} nodal values were determined separetely.

4.6.2 Results and Discussion

The combination of parameters providing the minimum d_{max} and the minimum peak σ_{VM} nodal values was the same for both the total deflection and the σ_{VM} and corresponded to D = 7.5 mm, L = 50 mm, θ = 3° and φ = -2.3°. Corresponding to this combination, the d_{max} was 0.3119 mm (Figure 4.21A), and the peak σ_{VM} was 58.04 MPa (Figure 4.21B).

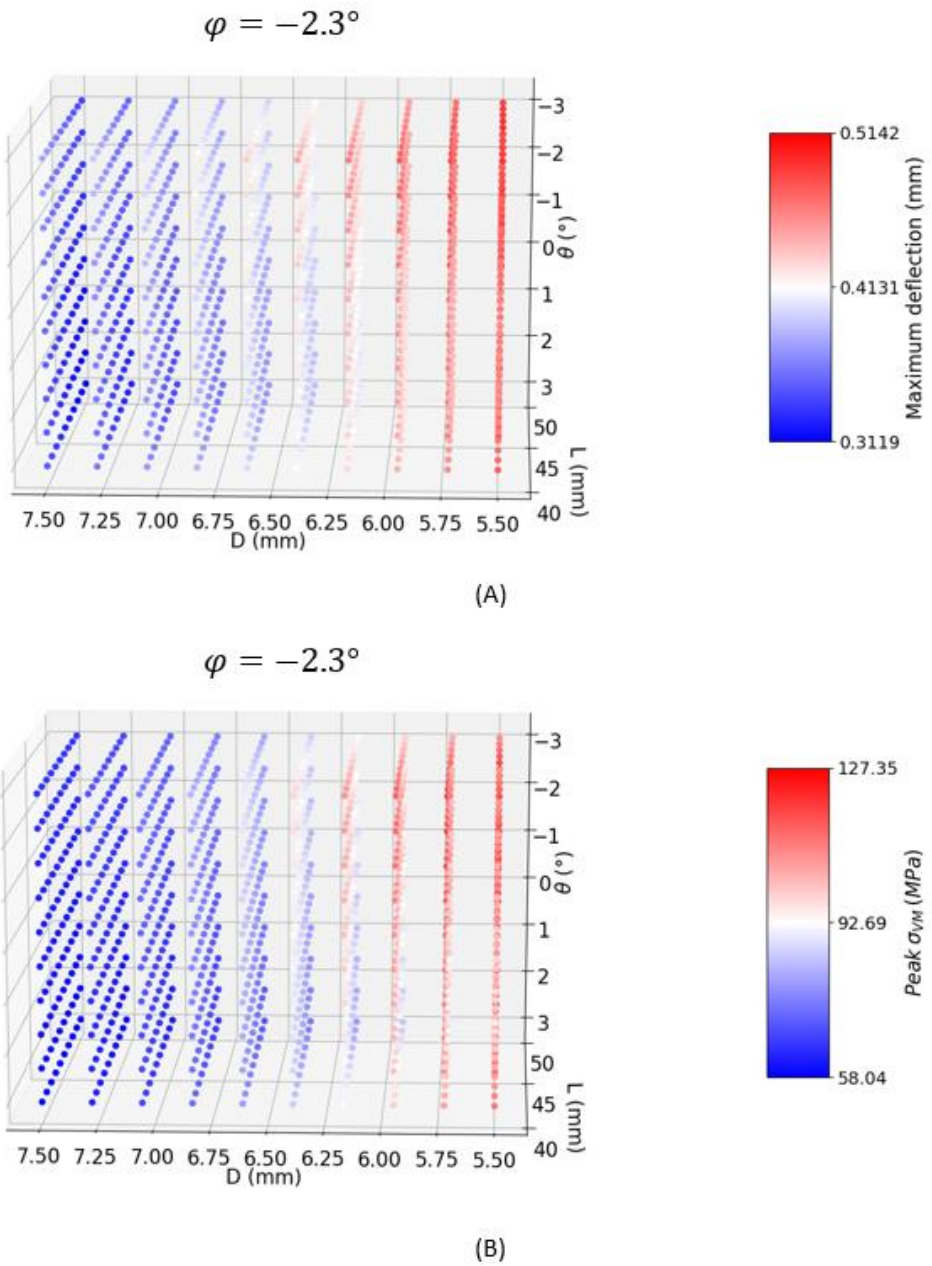

Figure 4.21 – Distribution of maximum deflection (A) and peak von Mises stress (B) in function of the diameter, the length and the sagittal orientation of screws for a given transverse orientation (φ = -2.3°). Lowest values are towards large diameters and lengths and cranial (positive) orientations.

This study aimed to apply the developed pipeline based on ROMs to optimise the screw size and orientation to one single patient. This limitation means that study findings need to be interpreted cautiously and the results may not be generalisable. However, these results are in line with those of Santoni et al., (2009) and Matsukawa et al., (2015) who also indicated cranial trajectories as the

most stable. Those studies compared a “cortical bone trajectory” with the “traditional” one (in this study: $\theta = 0°$ and $\varphi = 0°$). Santoni et al., (2009) proposed a cortical trajectory that “follows a caudocephalad path sagittally and a laterally directed path in the transverse plane, engaging only cortical bone in the pedicle without the involvement of the vertebral body trabecular space”. To perform this technique, the insertion point must be shifted in the caudo-lateral direction with respect to the currently accepted screw trajectory (Gertzbein and Robbins, 1990) and short pedicle screws with a small diameter are needed to avoid perforating the superior endplate and breaching the cortical pedicle wall. Further research should be undertaken to investigate the influence of the insertion point on the mechanical stability of the implanted vertebra in combination with parameters related to the size and orientation of screws. The parametric FE model presented in this study could be integrated with additional parameters representing the distance between the insertion point determined as done by Gertzbein and Robbins, (1990) and closest possible insertion points. The optimal configuration determined in this study is contradictory to a recent study which has suggested the caudomedial trajectory as the least critical case, thus safer from a clinical perspective (Molinari et al., 2021). A note of caution is due here since both studies focus on patient-specific FE models of one single patient. Possible explanations for this discrepancy could be found in the substantial differences in geometric modelling of the screws (simplified versus realistic), loading scenarios (multidirectional motion obtained by the application of simultaneous moment and compressive loads in Molinari et al., 2021) and number of parameters included in the analyses (size and orientation of screws versus only orientation). If the results of the model were validated with respect to experimental measurements, indications about the optimal orientation of screws within the pedicles would be difficult to implement without the usage of navigation systems or robotic arms. Therefore, the applicability of this methodology should be verified in the clinical setting with respect to the accuracy of a free-hand implantation of pedicle screws.

It must be noted that, given the configuration with D = 7.5 mm, L = 50 mm, $\theta = 3°$, the peak total deflection changed by 3.9%, and the peak σ_{VM} changed by 5.6% in the range of variation of φ (-3°, 3°). Therefore, given a sagittal cranial orientation $\theta = 3°$, the transverse orientation φ of screws had not a considerable impact on the mechanical response of the model. These results are in agreement with Newcomb's et al., (2017) findings which showed a 3.4% variation of mean cumulative maximum stress in the screws for different loading conditions (value extracted from Figure 6A in that study). As the ROM of the deflection and the ROM of the σ_{VM} presented an average $e_{NORM_{ROM}}$ of about 2.6% and 4.6%, respectively, indications about the optimal insertion angle φ must be interpreted cautiously.

The optimal combination of parameters was very close to the border of the parametric space and to one of the learning points (D = 7.5 mm, L = 50 mm, θ = 3° and φ = -3°). However, the ranges of variation of shape parameters were determined based on geometrical dimensions of the pedicles, and the maximum screw dimensions and orientation were considered for the given patient in order to avoid perforating the cortical shell. According to the anatomy of each patient, these ranges could be extended or reduced to explore multiple configurations of implants. In case of complex FE models with more vertebral levels, intervertebral discs and rods, exploring the whole range of variation of parameters would allow to gain more insight into the mechanical response of the fixation system.

A limitation of this study is the method used for the optimization. In fact, two objective functions were defined to minimise the total deflection and the peak σVM in the screws. A trade-off between the competing objectives functions should be found by constructing a Pareto front. However, in this study the minimisation was simplified due to the similar behaviour of the considered metrics in the parametric space (Figure 4.21). In fact, the minimum values corresponded to the same set of parameters for both metrics. In case of multiple objective functions with different behaviours, due, for instance, to more complex geometries or boundary conditions considered in the FE model, a more general approach would be needed.

The computational time to evaluate 10000 snapshots fields by using ROMs and to run the optimization was about 20 minutes for each metric. Considering that the computational time to solve the equations for each FE model was about 1 hour using a workstation and running the analyses in parallel processing on 10 CPU Cores, the reduction of the computational burden by using ROMs was massive. This showed the efficiency of ROMs for testing many combinations of parameters. However, it is important to note that the computational time to consume the ROM could be further reduced by doing sensitivity analyses to estimate the most important parameters or by using different types of DOEs.

In this study, the deflection and the stress in the screws were minimised in function of four shape parameters related to the size and the orientation of screws within pedicles. This approach would provide valuable information to the clinicians about the mechanical stability of implants and the risks of failure of screws. However, important information related to the risk of failure of the bone at screws-bone interface and of screws' migration is missing. Additional studies are needed to integrate this approach with metrics regarding the bone mechanical competence.

4.6.3 Conclusion

In this study, the deflection and the stress in the screws were minimised in function of four shape parameters related to the size and the orientation of screws within pedicles. The best size and orientation of screws was D = 7.5 mm, L = 50 mm, $\theta = 3°$ and $\varphi = -2.3°$ for the considered patient. Although these results have not been verified against clinical criteria, this project is the first comprehensive investigation of the application of ROMs to optimise the insertion of the screws by using FE models of spine fixation.

Chapter 5: Prediction of the pre-fracture shape of the L1 vertebral body from adjacent vertebrae

5.1 Summary

The main goals of treatments of vertebral fractures are the reduction and the stabilization of the fracture to allow bone healing and restore the physiological biomechanics of the spine. However, the pre-fracture height and three-dimensional shape of the vertebral body are unknown in the clinical setting. Therefore, it is unclear how much height to restore in order to reestablish the pre-fracture shape. The goal of this study was to develop and evaluate a method based on Singular Value Decomposition (SVD) to predict the shape of the vertebral body of L1 from the shapes of T12 and L2.

The segmentation masks of T12, L1 and L2 of 40 patients were extracted from the VerSe'20 open-access database and processed to isolate the vertebral bodies. Surface triangular meshes of each vertebra were morphed onto a template mesh. The set of vectors with the nodes coordinates of the morphed T12, L1 and L2 was compressed with SVD and used to build a system of linear equations. This system was used to solve a minimization problem and to reconstruct the shape of L1 in a leave-one-out cross validation process. These methods were explored in a simplified 1D case where only 7 heights of the vertebral body were predicted.

The mean and maximum distance between the morphed meshes and the original meshes were 0.14 ± 0.02 mm and 0.96 ± 0.30 mm. The mean and maximum distance between the meshes of L1 projected into the basis of modes and the original meshes were 0.45 ± 0.02 mm and 0.96 ± 0.30 mm. The mean reconstruction error of the 3D shape of L1 was on average 0.51 ± 0.11 mm, while the Hausdorff distance was on average 2.11 ± 0.56 mm.

The results suggest that this method can predict the shape of the vertebral body of L1 from the shapes of the two adjacent vertebrae with a good accuracy. The distances obtained by optimization were similar to the distances obtained by projection into the basis of modes indicating that the optimization was successful. This method could be used to predict the pre-fracture shape of a fractured L1 vertebra and to provide valuable information to the surgeon in the pre-operative setting.

5.2 Introduction

The restoration of the vertebral body height and shape is essential to reduce a vertebral fracture and re-establish the natural curvature of the spine. Kyphoplasty can effectively restore the vertebral body height and local kyphotic angulation (Van Meirhaeghe et al., 2013). Performing both a height and angular restoration reduces the kyphosis and the local stresses responsible of fractures at adjacent levels, and aids at restoring the natural curvature and mechanics of the spine (Pesce et al., 2013). However, the pre-fracture height or, more generally, the 3D shape of the fractured vertebra are often not available to the surgeon in the pre-operative setting. Statistical Shape Models (SSMs) were employed by de Bruijne et al. (2007) to create conditional shape models that allow to predict the shape of one lumbar vertebra based on the shapes of other lumbar vertebrae (between L1 and L4 levels) in the images. The application of this method has been shown only to the 2D shape of vertebrae estimated from sagittal X-ray images. However, it is difficult to measure reliably the shape of the vertebral body from 2D sagittal radiographs, because of the superimposition of soft and hard tissues in the direction of the projection which reduces the contrast between the vertebrae and the background, and the impossibility to distinguish any tilting of the vertebrae (e.g., lateral curving of the spine in patients with scoliosis) with respect to others from a true variation in the shape (de Bruijne et al., 2007). In fact, important variability has been found in inter-observer measures of three vertebral heights based on six anatomical landmarks placed in 2D X-ray images (Genant et al., 1993). As the mean distance between the original and reconstructed 2D shapes was 0.8 mm, this method seems promising to predict the 3D shape of a lumbar vertebral body. The segmentation of 3D bony structures from CT-scan images is well assessed and the usage of a 3D geometry would allow to avoid the bias due to a 2D measurement. Nowadays, low dose CT-scan imaging is more and more integrated in clinical protocols. For example, at the University Hospital of Poitiers, our clinical partner, a CT-scan exam is always performed in case of high-energy injuries; in case of low-energy accidents, first a 2D X-ray is done, then, in case of fracture detection, a CT-scan is always done to plan the treatment. In addition, the pre-fracture 3D shape of the vertebral body would allow to take anatomical measurements that could be used to choose the optimal treatment or to optimize some parameters during a surgical procedure (e.g. direction of injection or volume of cement during a kyphoplasty). Moreover, CT-scan based FE models could be derived by those reconstructions and used to study the mechanical properties of the fractured vertebral body or of the thoracolumbar segment before and after the injury.

The aim of this study was to develop a method to predict the 3D shape of the L1 vertebral body from the shapes of adjacent T12 and L2 vertebral bodies estimated by segmentation of CT-scan images and to validate it for different patients.

First, the feasibility of the presented methods is assessed on a simpler 1D case where the shape of the vertebral body is described by 7 characteristic heights. Then, the application has been expanded to the 3D case where the full shape of the L1 vertebral body is reconstructed. We used a leave-one-out validation with a dataset of 40 healthy patients without signs of fractures. To the author's knowledge this the first time that the premorbid 3D vertebral shape of L1 is reconstructed from the shapes of adjacent vertebral bodies.

5.3 Prediction of the pre-fracture height of the L1 vertebral body from adjacent vertebrae (1D case)

The aim of this subchapter was to develop a method to predict the 3D shape of the L1 vertebral body from the shapes of adjacent vertebral bodies estimated from CT scans. This part of the chapter presents the mathematical approach on a simplified 1D case. The shape of the vertebral body was described by a small number of characteristic heights based on the definition of anatomical landmarks on the two endplates. These characteristic heights of the L1 vertebral body were predicted from heights of adjacent vertebral bodies.

5.3.1 Materials and Methods

5.3.1.1 Summary

The initial database consisted in the 3D shapes of T12, L1 and L2 vertebrae segmented from the CT scans of 20 patients without any sign of fractures, from a public dataset. For each vertebra 14 anatomical landmarks were manually chosen on the superior and inferior endplates defining 7 heights for each vertebral body. For each patient, a vector of 21 heights corresponding to T12, L1 and L2 vertebrae was built. From the dataset of 20 vectors, a subset of principal modes was extracted by Singular Value Decomposition (SVD). Those modes were used to predict the heights of the L1 vertebra by considering only the information corresponding to T12 and L2 with two different optimization methods. A leave-one-out experiment was performed and the performances of the two methods were compared. The workflow is summarised in Figure 5.1.

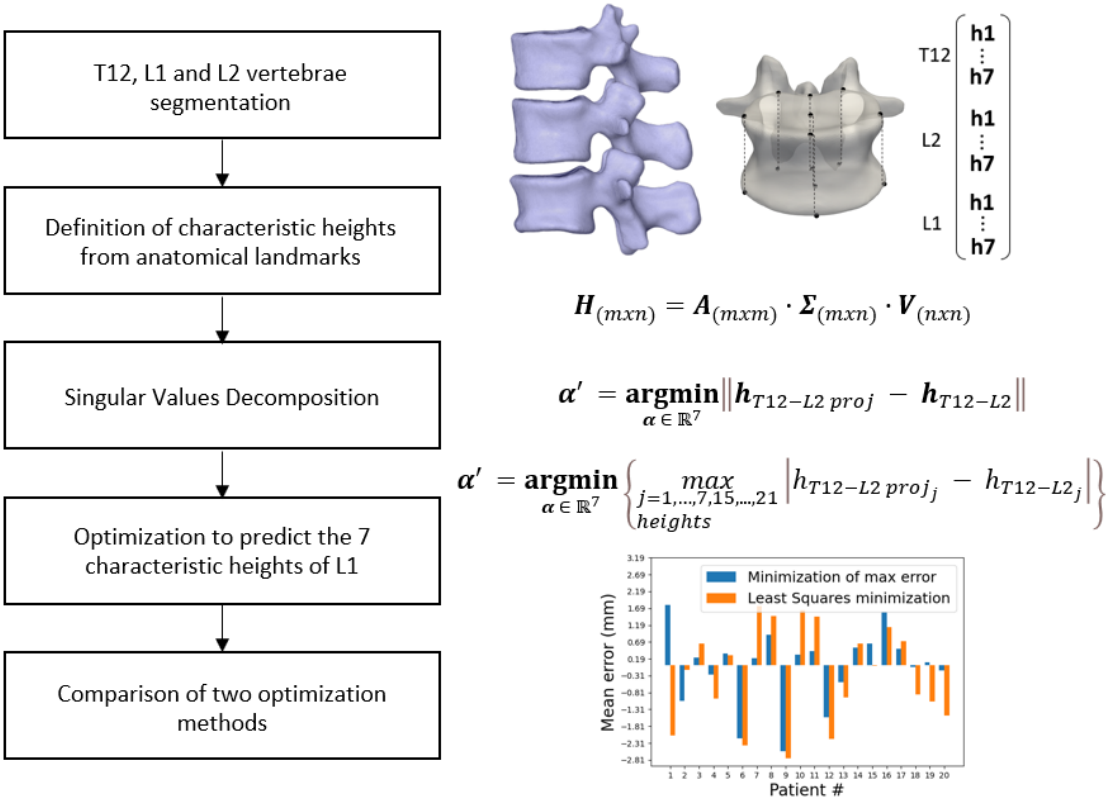

Figure 5.1 - Outline of the steps to predict 7 characteristic heights of L1 vertebral body by using the 7 characteristic heights of the two adjacent vertebral bodies.

5.3.1.2 Height measurement

The Verse 2020 database of CT-scan images and segmentation masks was used to build the dataset (Löffler et al., 2020a; Sekuboyina et al., 2020; Liebl et al., 2021). This anonymised dataset is publicly available (Kirschke et al., 2020). 20 patients without large osteophytes and signs of fractures at T12, L1 and L2 levels from the database were included in this preliminary study (twelve males, eight females, 45.7 ± 13.5 years old).

The segmentation mask of each vertebra available from the dataset was transformed in a STL surface mesh and used to place 14 anatomical landmarks on the vertebral body, 7 on the superior endplate, and 7 on the inferior endplate (Figure 5.2). The instructions to retrieve the anatomical position of the landmarks are reported in Table 5.1.

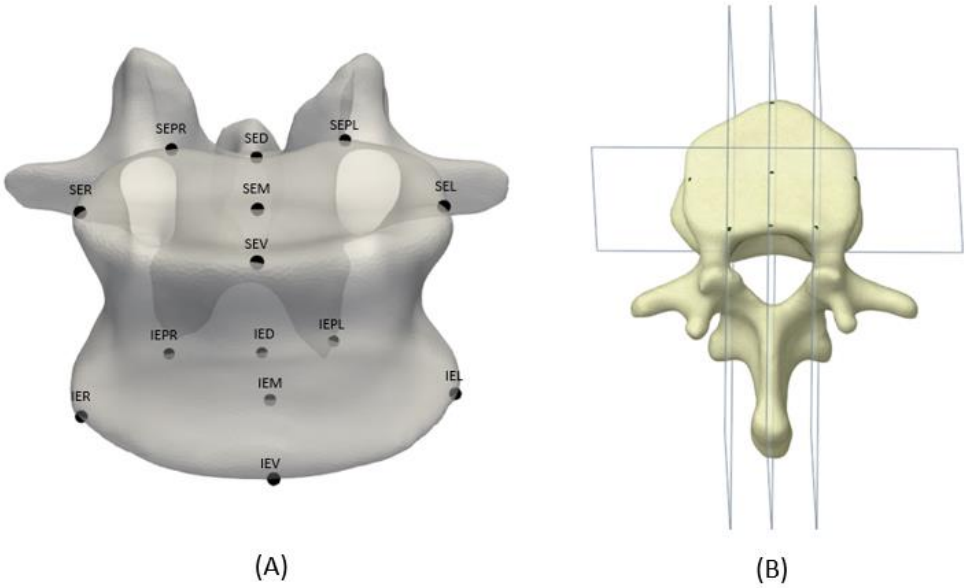

Figure 5.2 - Anatomical landmarks placed on the superior and inferior endplates (A) and anatomical planes to define the landmarks on the superior endplate (B). The anatomical planes to define the landmarks on the inferior endplate were similar.

Name	Abb.	Definition
Superior Endplate Ventral	SEV	Cranial to caudal view, consider the sagittal plane that cut the superior endplate in two halves, consider the most ventral point on the superior endplate
Superior Endplate Dorsal	SED	As SEV but consider the most dorsal point
Superior Endplate Right	SER	Cranial to caudal view, back to front view, consider the coronal plane that cut the superior endplate in two halves, consider the rightest point on the superior endplate
Superior Endplate Left	SEL	As SER but consider the most left point
Superior Endplate Pedicle Right	SEPR	Cranial to caudal view, back to front view, consider the tangent plane to the most inner border of the right pedicle, consider the first point on the superior endplate belonging to the plane
Superior Endplate Pedicle Left	SEPL	As SEPR, but consider the left pedicle
Superior Endplate Middle	SEM	Cranial to caudal view, consider the line on the sagittal plane that cut the superior endplate in two halves, consider the line on the coronal plane that cut the superior endplate in two halves, take the intersection point
Inferior Endplate Ventral	IEV	Caudal to cranial view, consider the sagittal plane that cut the inferior endplate in two halves, consider the most ventral point on the inferior endplate
Inferior Endplate Dorsal	IED	As IEV but consider the most dorsal point
Inferior Endplate Right	IER	Caudal to cranial view, back to front view, consider the coronal plane that cut the inferior endplate in two halves, consider the rightest point on the inferior endplate
Inferior Endplate Left	IEL	As IER but consider the most left point
Inferior Endplate Pedicle Right	IEPR	Caudal to cranial view, back to front view, consider the tangent plane to the most inner border of the right pedicle, consider the first point on the inferior endplate belonging to the plane
Inferior Endplate Pedicle Left	IEPL	As IEPR, but consider the left pedicle
Inferior Endplate Middle	IEM	Caudal to cranial view, consider the line on the sagittal plane that cut the inferior endplate in two halves, consider the line on the coronal plane that cut the inferior endplate in two halves, take the intersection point

Table 5.1- Name, abbreviation and anatomical definition of the 14 landmarks placed on the superior and inferior endplates of each vertebral body.

Two least squares planes that interpolate the landmarks on the superior endplate and the landmarks on the inferior endplate were calculated. The normal lines to those two planes were considered, and directional cosines were calculated. The mean values of directional cosines of the two lines gave a direction that was considered as the reference axis of the vertebral body along the cranio-caudal direction. Each landmark was projected onto this line. 7 heights were calculated by calculating the Euclidean distance between each couple of corresponding points on the two endplates (Figure 5.3). Thanks to this definition of vertebral heights, the methodology was not sensitive to the misalignment of vertebral bodies of different levels and among patients.

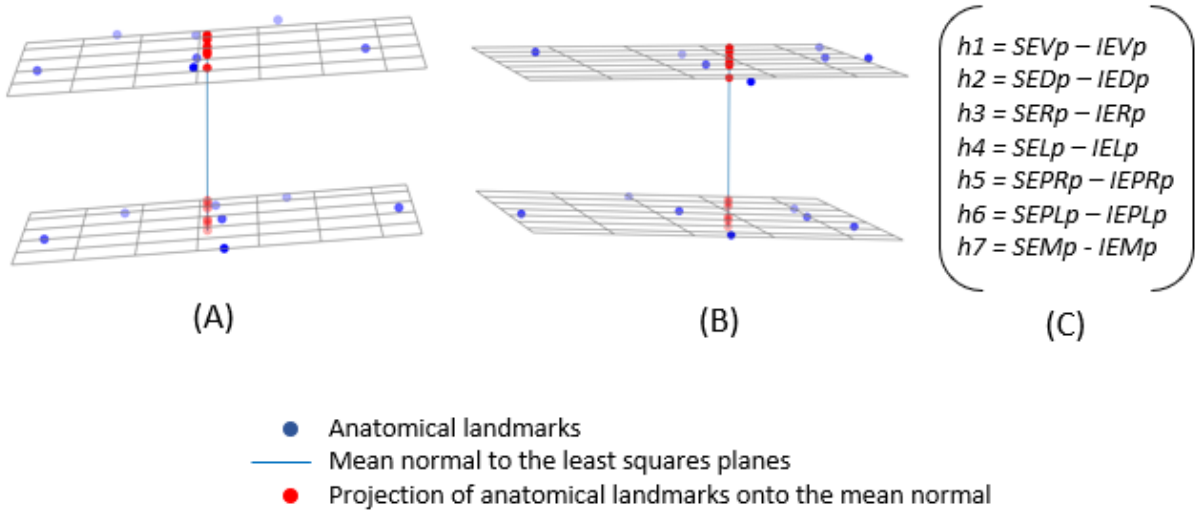

Figure 5.3- Projection of anatomical landmarks onto the vertical axis of the vertebral body in a frontal (A) and a lateral (B) view and evaluation of 7 characteristic heights (C).

5.3.1.3 Singular Value Decomposition

For each of the 20 patients in the dataset, a vector **h** (21 x 1) with the vertebral body heights of T12, L1 and L2 was built. The set of vectors for patients in the dataset was compressed by SVD:

$$\boldsymbol{H}_{(mxn)} = \boldsymbol{A}_{(mxm)} \cdot \boldsymbol{\Sigma}_{(mxn)} \cdot \boldsymbol{V}_{(nxn)} \qquad \text{(Eq. 5.1)}$$

where **H** is the matrix whose columns are the vectors **h** of heights of each patient, **A** is composed of the left singular vectors (modes) of **H**, **Σ** is a diagonal matrix composed of the *k* singular values σ_k

of **H**, **V** is composed of the right singular vectors of **H**, *m* is equal to 21, *n* is equal to 19. The SVD was performed by using a tool developed by Ansys Digital Twin research team.

The number of modes for the optimization to predict the 7 heights of L1 from heights of adjacent vertebral bodies was fixed with the following simplified procedure. The 20 vectors of heights $\mathbf{h}_{i=1\ldots20}$ were compressed by SVD and the number of modes giving an average maximum absolute reduction error lower than 1 mm was retained (Figure 5.4).

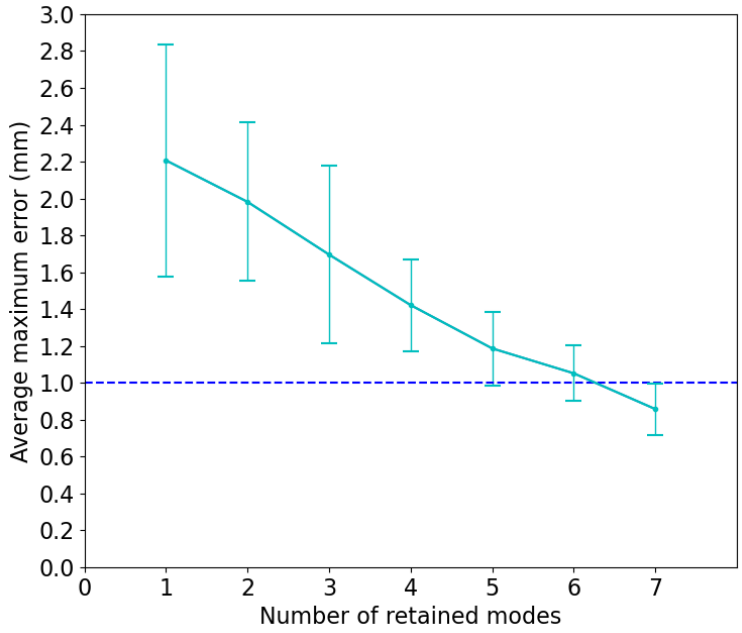

Figure 5.4 – Average (± st dev) maximum reduction error (mm) over the full dataset of vectors of heights in function of the number of retained modes. The dash-dotted line represents the threshold error of 1 mm. 7 modes were retained for further analyses.

The average maximum absolute reduction error was defined as:

$$\underset{20\ patients}{mean}\left(\underset{j=1,\ldots,21\ heights}{max}\left|h_j - h_{proj_j}\right|\right), \qquad \text{(Eq. 5.2)}$$

This simplified procedure was considered acceptable for this preliminary study to investigate the feasibility of the methods and has been improved for the prediction of the 3D shape of the L1 vertebral body (cf. Section 5.4.1.5.1).

5.3.1.4 Optimization to predict the 7 heights of L1

A leave-one-out experiment was performed to predict the heights of the L1 level of each patient by considering the remaining *19* patients. Each time, an SVD was done by using the dataset of *19* patients and two optimization methods were used to predict the heights of the L1 level: a linear least-squares minimization and a minimization of the maximum error. The results were averaged over the *20* leave-one-out repetitions.

5.3.1.4.1 Least square optimization

Once the basis of modes has been built, each vector including the heights of the vertebral bodies could be approximated as a linear combination of the modes as:

$$\boldsymbol{h}_{proj} = \boldsymbol{A} \cdot \boldsymbol{\alpha} \qquad \text{(Eq. 5.3)}$$

where $\boldsymbol{\alpha}$ is a vector of *7* parameters.

Given a patient not belonging to the dataset and for which the *7* heights corresponding to the L1 level are not available, we hypothesize that its vector of heights of T12 and L2 levels $\mathbf{h}_{\text{T12-L2}}$ could be approximated as a linear combination of modes related to the T12 and L2 parts of the matrix as:

$$\boldsymbol{h}_{T12-L2\,proj} = \boldsymbol{A}_{T12-L2} \cdot \boldsymbol{\alpha} \qquad \text{(Eq. 5.4)}$$

where $\mathbf{A}_{\text{T12-L2}}$ is the part of the matrix $\mathbf{A}$ that includes only the heights of T12 and L2 of the *7* modes, and $\boldsymbol{\alpha}$ is a vector of *7* parameters. As the columns of $\mathbf{A}_{\text{T12-L2}}$ are linearly independent, the linear-least-square (LLS) solution $\boldsymbol{\alpha}$**'** of this system is unique. This is equal to solving the following minimization problem:

$$\boldsymbol{\alpha}' = \underset{\boldsymbol{\alpha} \in \mathbb{R}^7}{\mathbf{argmin}} \left\| \boldsymbol{h}_{T12-L2\,proj} - \boldsymbol{h}_{T12-L2} \right\| \qquad \text{(Eq. 5.5)}$$

where $\|\cdot\|$ is the Euclidean norm. Then, we hypothesize that the coefficients $\boldsymbol{\alpha}$**'** can be used also to reconstruct the vector of heights of L1 ($\mathbf{h}_{\text{L1}}$) as:

$$\boldsymbol{h}_{L1} = \boldsymbol{A}_{L1} \cdot \boldsymbol{\alpha}' \qquad \text{(Eq. 5.6)}$$

where $\mathbf{A}_{\text{L1}}$ is the part of the matrix $\mathbf{A}$ that includes only the heights of L1 of the *7* modes. The Euclidean norm error over $\mathbf{h}_{\text{T12-L2}}$, the maximum absolute error over $\mathbf{h}_{\text{L1}}$, the absolute and signed mean error over $\mathbf{h}_{\text{L1}}$ are used to assess the results of the optimization.

5.3.1.4.2 Minimization of the maximum error

Another numerical method was used to minimize directly the maximum absolute error:

$$\boldsymbol{\alpha}' = \underset{\boldsymbol{\alpha} \in \mathbb{R}^7}{\mathbf{argmin}} \left\{ \max_{\substack{j=1,\dots,7,15,\dots,21 \\ heights}} \left| h_{T12-L2\,proj_j} - h_{T12-L2_j} \right| \right\} \qquad \text{(Eq. 5.7)}$$

This consisted in creating a grid within the $\mathbb{R}^7$ space based on the coefficients $\boldsymbol{\alpha}_{i=1\dots19}$ that are needed to approximate the learning vectors within the space of modes (Eq. 5.3). In fact, the mean value between each couple of coefficients ($\boldsymbol{\alpha}_i$ $\boldsymbol{\alpha}_j$) was evaluated a first time starting from the coefficients $\boldsymbol{\alpha}_{i=1\dots19}$, and a second time starting from the coefficients generated in the first iteration. Given one couple of coefficients, this process represented the creation of a virtual patient whose coefficients $\boldsymbol{\alpha}_i$ are the centre of mass in the $\mathbb{R}^7$ subspace of the coefficients of two real patients. A large number Z of virtual patients represented in the $\mathbb{R}^7$ subspace of modes by coefficients $\boldsymbol{\alpha}_{Z=1\dots Z}$ were created. Each new virtual patient was characterized by a vector of heights that could be reconstructed by using (Eq. 5.6. This vector was directly compared with the vector $\mathbf{h}_{T12\text{-}L2}$ of the patient not belonging to the basis, therefore, the minimization problem could be written as:

$$\boldsymbol{\alpha}' = \underset{\boldsymbol{\alpha}_{Z=1\dots Z}}{\mathbf{argmin}} \left\{ \max_{\substack{j=1,\dots,7,15,\dots,21 \\ heights}} \left| (\boldsymbol{A}_{T12-L2} \cdot \boldsymbol{\alpha}_z)_{\boldsymbol{j}} - h_{T12-L2_j} \right| \right\} \qquad \text{(Eq. 5.8)}$$

Then, we hypothesize that the coefficients $\boldsymbol{\alpha}$' can be used also to reconstruct the vector of heights of L1 ($\mathbf{h}_{L1}$) by using (Eq. 5.6. The maximum absolute error over $\mathbf{h}_{T12\text{-}L2}$, the maximum absolute error over $\mathbf{h}_{L1}$, the absolute and signed mean errors over $\mathbf{h}_{L1}$ are used to assess the results of the optimization.

5.3.2 Results

The mean absolute error for least squares optimization and minimization of the maximum error are showed for each patient in Figure 5.5.

5.3.2.1 Least squares optimization

For the 20 leave-one-out repetitions:

- the average Euclidean norm error (± standard deviation) over $\mathbf{h}_{T12\text{-}L2}$ was 1.95 ± 0.76 mm;
- the average maximum absolute error (± standard deviation) over $\mathbf{h}_{L1}$ was 2.78 ± 1.08 mm;
- the average absolute mean error (± standard deviation) over $\mathbf{h}_{L1}$ was 1.23 ± 1.06 mm;

5.3.2.2 Minimization of the maximum error

For the 20 leave-one-out repetitions:

- the average maximum absolute error (± standard deviation) over $\mathbf{h}_{T12\text{-}L2}$ was 1.58 ± 0.82 mm;
- the average maximum absolute error (± standard deviation) over $\mathbf{h}_{L1}$ was 2.01 ± 0.96 mm;
- the average absolute mean error (± standard deviation) over $\mathbf{h}_{L1}$ was 0.79 ± 0.84 mm
- the average absolute mean error was higher after Least Squares minimization than after minimization of the maximum error for 80% of patients; the average signed mean error had always a consistent sign for the two optimization methods except for Patients #1, #15 and #19.

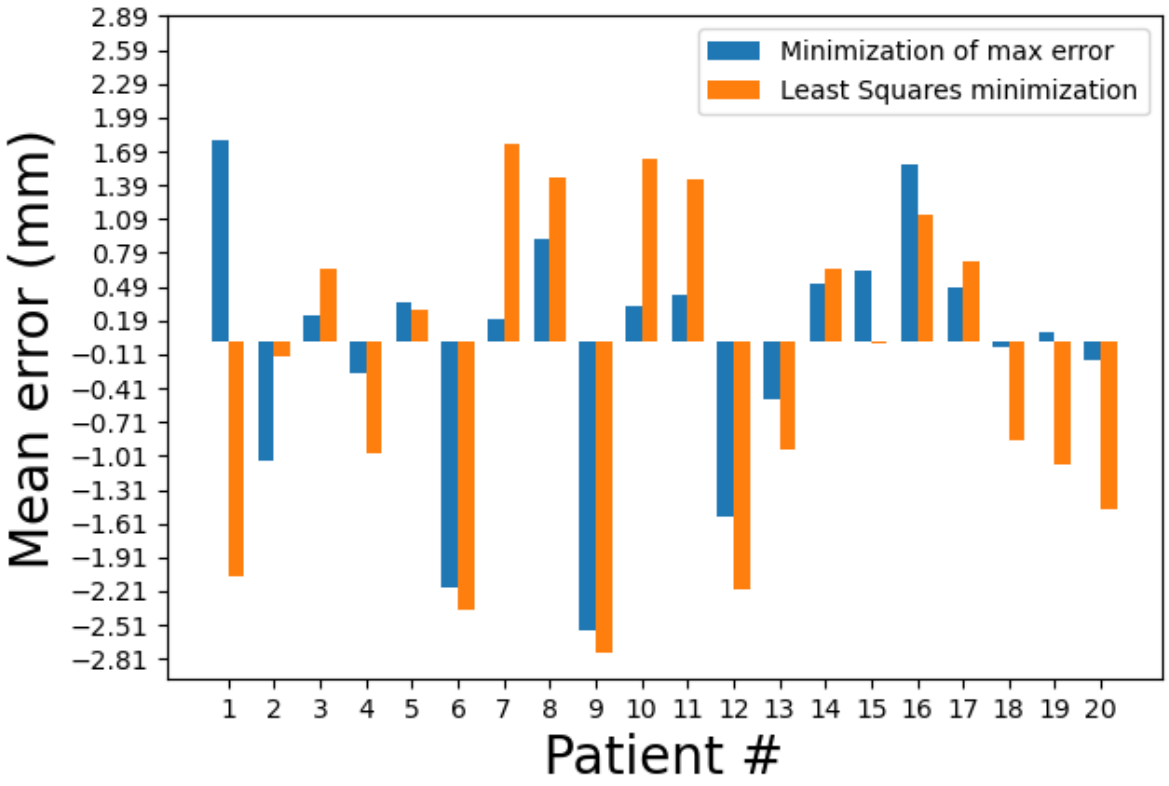

Figure 5.5 - Mean of the absolute error (mm) between the L1 heights predicted by least squares optimization (orange) and the real L1 heights (blue) of each left-out patient.

5.3.2.3 Processing time

The time needed to define anatomical landmarks on the vertebral body was approximately 2 minutes per vertebra. The optimization was an automatic process that required short computational time (seconds).

5.3.3 Conclusion

This preliminary study showed that the developed method could predict the mean height of L1 vertebral body by knowing the height of adjacent T12 and L2 vertebral bodies with an average accuracy lower than 1 mm, if the maximum error is minimised. The maximum absolute error of the estimation of L1 heights was about 2 mm. This study served to assess the potentials of the presented methods to predict the geometric characteristics of the L1 vertebral body from adjacent ones. The average accuracy was promising. However, this methodology allowed to predict only a predefined set of characteristic height of the vertebral body without exploiting the volumetric information of bony structures that can be extracted from CT-scan images. This approach will be extended to the prediction of the 3D shape of the vertebral body. A more extended dataset of patients is needed to account for the inter-patient variability of the 3D shapes of vertebrae Also, the optimal number of modes for the prediction has to be estimated with more sophisticated methods that evaluate the ability of principal modes to represent patients that were excluded from the construction dataset.

5.4 Prediction of the pre-fracture shape of the L1 vertebral body from adjacent vertebrae (3D case)

The goal of the analysis presented in this section was to apply and extend the methods presented in Section 5.3 to a more general 3D case where the whole geometry of the vertebral body is predicted.

5.4.1 Materials and Methods

5.4.1.1 Summary

The segmentation masks of 40 patients were manually processed to isolate the T12, L1 and L2 vertebral bodies and to mesh each of them with a triangular surface mesh. An average reference template mesh was generated and all the meshes in the dataset were aligned and morphed to that reference mesh. The vectors of node coordinates of the morphed meshes were compressed by SVD after choosing the optimal number of modes. The modes were used to build a linear system of equations to predict the 3D shape of the L1 vertebra by considering only the information corresponding to T12 and L2. A leave one out validation was performed. Different metrics were used to compare the predicted shape with the original one. The workflow is showed in Figure 5.6.

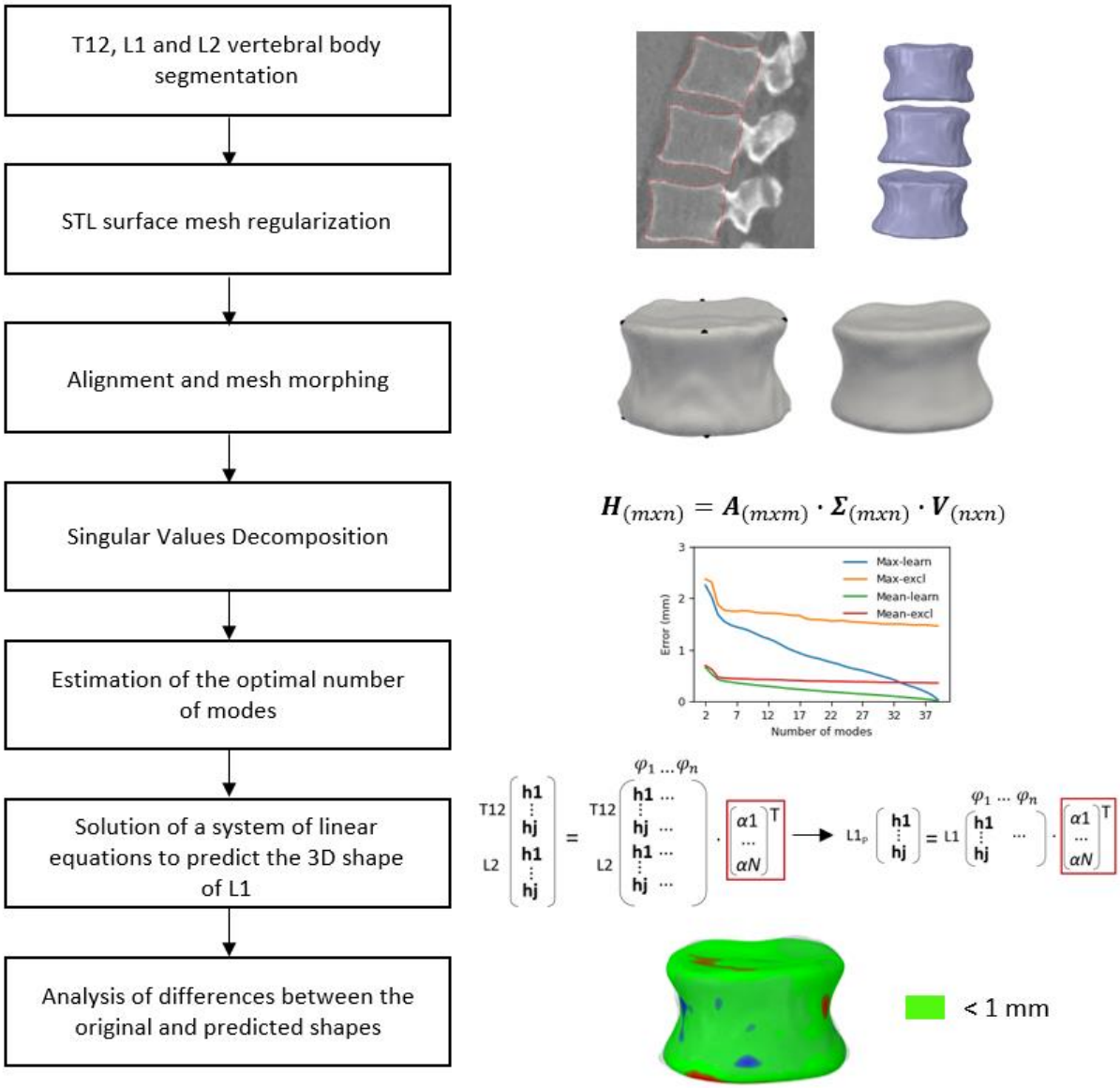

Figure 5.6- An overview of the different steps to predict the 3D shape of the L1 vertebral body by using the 3D shapes of the two adjacent vertebral bodies.

5.4.1.2 Dataset construction

The Verse 2020 database of CT-scan images and segmentation masks was used to build the dataset (Löffler et al., 2020a; Sekuboyina et al., 2020; Liebl et al., 2021). This database is publicly available (Kirschke et al., 2020). A total number of 40 patients from the database were included in this study (22 men, 18 women). A table with the Patient ID used in the Verse 2020 database and associated patients data (Löffler et al., 2020a) is reported in the Appendix (Section Appendix A4). Exclusion criteria were severe bone degeneration (e.g., marked asymmetries along the antero-posterior or right-left directions), presence of large osteophytes (e.g., osteophytes that bridge

between different vertebral levels or osteophytes at the level of the endplates), fractures or signs of previous fractures at T12, L1 or L2 levels. As a result, the mean age of patients within the dataset was 40.9 ± 15.9 years. The voxel size was variable: for CT-images included in this study, the best voxel size was 0.68 x 0.68 x 0.45 mm^3, the worst one was 1.31 x 1.31 x 3 mm^3 (Appendix, Section Appendix A4).

5.4.1.3 Extraction of geometries of vertebral bodies

From the segmentation masks, the geometries of vertebral bodies were obtained with a manual procedure (3DSlicer, v4.11.0) (Fedorov et al., 2012). In a caudal to cranial cross view, the posterior part of the vertebra was cut by considering the contours of the endplates as boundaries of the vertebral body. This procedure was adopted to improve the morphing error at the posterior side of the vertebrae at the level of pedicles (see in Appendix, Section Appendix A5 a comparison with a different method) and to avoid including in the model geometric characteristics of the pedicle that are not relevant for this application. Once the vertebral bodies were cropped, the segmentation masks were smoothed with a gaussian smoothing filter (standard deviation of 0.8 mm) to obtain smoother geometries suited to the mesh morphing. Each vertebral body was overlapped with the CT-scan images to qualitatively assess the extraction of vertebral bodies. In case of errors, the manual procedure to extract vertebral bodies and smoothing were repeated. An example of the segmented geometry is showed in Figure 5.7. A surface mesh was generated from these masks and stored as an STL file. The surface mesh was then regularized with an element size of 0.4 mm without any further smoothing.

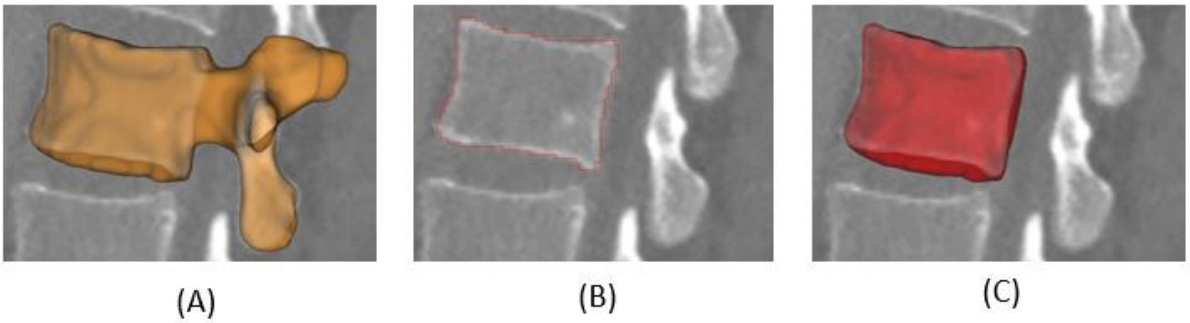

Figure 5.7- Example of segmentation for Patient #5 (L1) in a sagittal view: 3D representation of the whole vertebra (A); segmentation mask of the vertebral body (B); 3D representation of the segmented vertebral body (C).

5.4.1.4 Mesh morphing

The methods used for the morphing of the vertebral bodies and the construction of iso-topological surface meshes (same number of nodes, same number of elements, same connectivity, preserved topology-anatomy correspondence) are based on the combination of the methods published in the study by Clogenson et al. (2015) and on the Scalismo.org webpage (Luthi et al., 2018; unibas-gravis/scalismo, 2021; Scalismo - Scalable Image and Shape Modelling | Scalismo) and are detailed in the next sections. An overview of the different steps to obtain morphed meshes is presented in Figure 5.8.

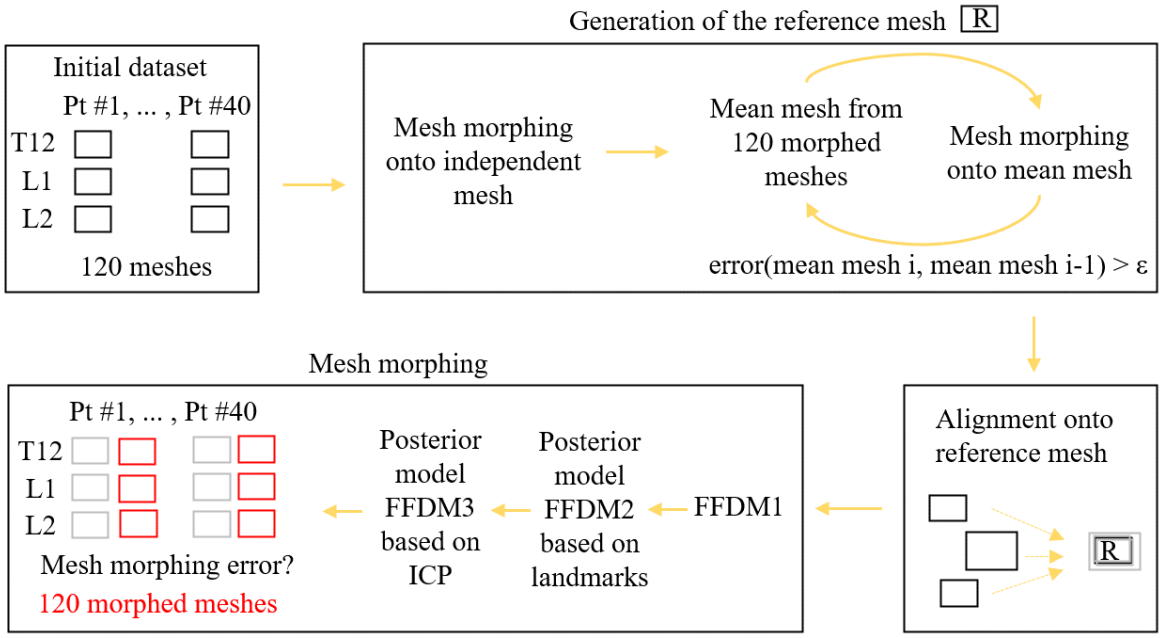

Figure 5.8 – Mesh morphing workflow: the starting point is the set of meshes of the vertebral bodies of 40 patients which are aligned and morphed onto the same reference mesh in order to obtain a new set of aligned geometries with the same number of nodes and elements, connectivity.

5.4.1.4.1 Generation of the reference mesh

A reference mesh was generated through an iterative procedure to avoid biasing the results of the mesh morphing to a particular vertebra chosen in the dataset. To initialize the process, an independent reference mesh with an element size of 0.7 mm and about 12000 nodes was morphed onto the 120 geometries (T12, L1 and L2 vertebral bodies for each patient). Then, a mean mesh was

calculated from the 120 morphed geometries and used as reference mesh in the first step of an iterative mesh morphing process. At each iteration, the mesh morphing of the 120 geometries onto the mean mesh was done by using a mesh morphing algorithm described below, then a new mean mesh was computed and compared with the mean mesh of the previous iteration. As metrics to compare two meshes, the mean error (Eq. 5.9) and Hausdorff distance (Eq. 5.10) with respect to the target mesh were considered:

$$mean\ error\ = \frac{1}{N}\sum_{j=1}^{J} dist\left(\boldsymbol{h}_j, \boldsymbol{S}_{target}\right) \qquad \text{(Eq. 5.9)}$$

$$Haussdorf\ error\ = \max\left\{max\{dist(\boldsymbol{h}_A, \boldsymbol{S}_B)\};\ max\{dist(\boldsymbol{h}_B, \boldsymbol{S}_A)\}\right\} \qquad \text{(Eq. 5.10)}$$

where: N is the number of nodes of the considered mesh, $\mathbf{h}_j$ is the j-node of the considered mesh, $\mathbf{S}_{target}$ is the target mesh; $\mathbf{h}_A$ and $\mathbf{h}_B$ are the nodes of the considered and target meshes $\mathbf{S}_A$ and $\mathbf{S}_B$, *dist* is the Euclidean distance. An algorithm already implemented in VTK was used that allows an accurate calculation of a point-to-cell distance by performing a geometric interpolation of the cells of the surface mesh (Commandeur et al., 2011). In fact, the algorithm computes the minimum distance between each point of the considered geometry and each point belonging to the surface that interpolates the closest element of the target geometry. The iterative process was stopped when the Hausdorff distance between the mean mesh at iteration i and the mean mesh at iteration i-1 was lower than 0.12 mm. This threshold error was fixed as the best compromise between the computation time and the accuracy of the mesh morphing, also considering that the CT-scan with the best resolution in the dataset had the lowest voxel dimension equal to 0.45 mm. In fact, at each iteration the mesh morphing of all the 120 vertebral bodies was computed. The mesh morphing is an automatic but time-consuming process that took approximately 4 minutes per patient (without optimization of the iterative closest points iterations).

The mean and Hausdorff distances between the mean mesh at the i-iteration and the mean mesh at the (i-1)-iteration, in function of the number of iterations, are reported in Figure 5.9. The mean mesh at iteration 1 was compared to the independent reference mesh. The mean mesh at iteration 3 was considered as reference mesh for the mesh morphing as the Hausdorff distance with the mean mesh at iteration 4 was 0.108 mm, therefore below the threshold error. The mean error instead, was already under 0.1 mm at iteration 2. The reference mesh is showed in Figure 5.10.

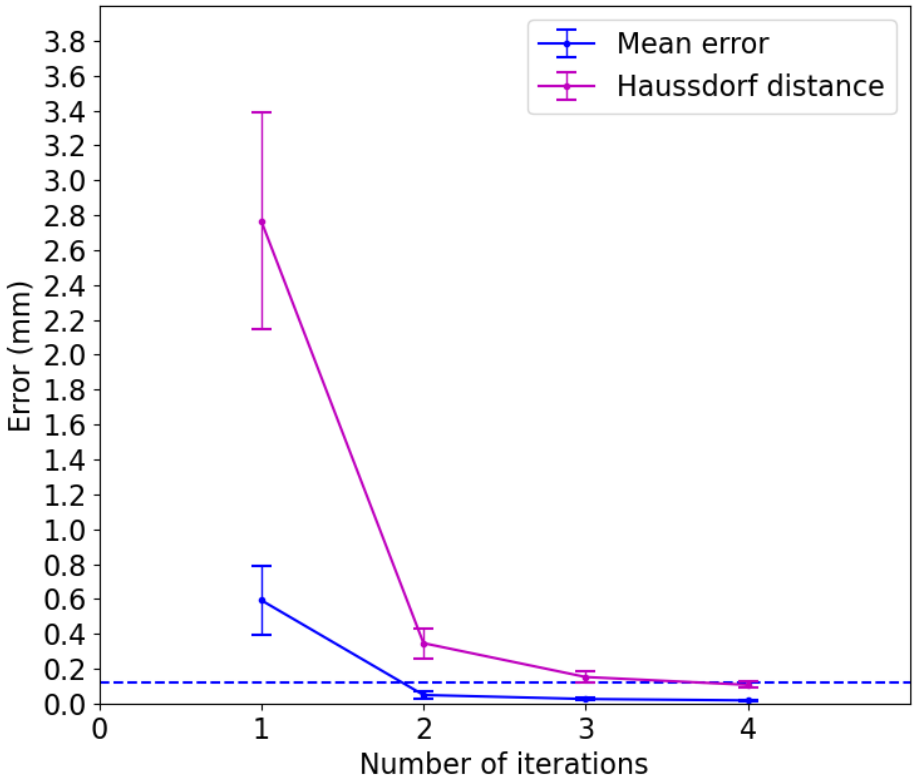

Figure 5.9- Mean and Hausdorff distances (mm) between the mean mesh calculated at iteration i and the mean mesh calculated at iteration i-1. The dash-dotted line represents the threshold error of 0.12 mm. The mean mesh at iteration 3 was considered as reference mesh for further analyses as the Hausdorff distance with the mean mesh at iteration 4 was below the threshold error.

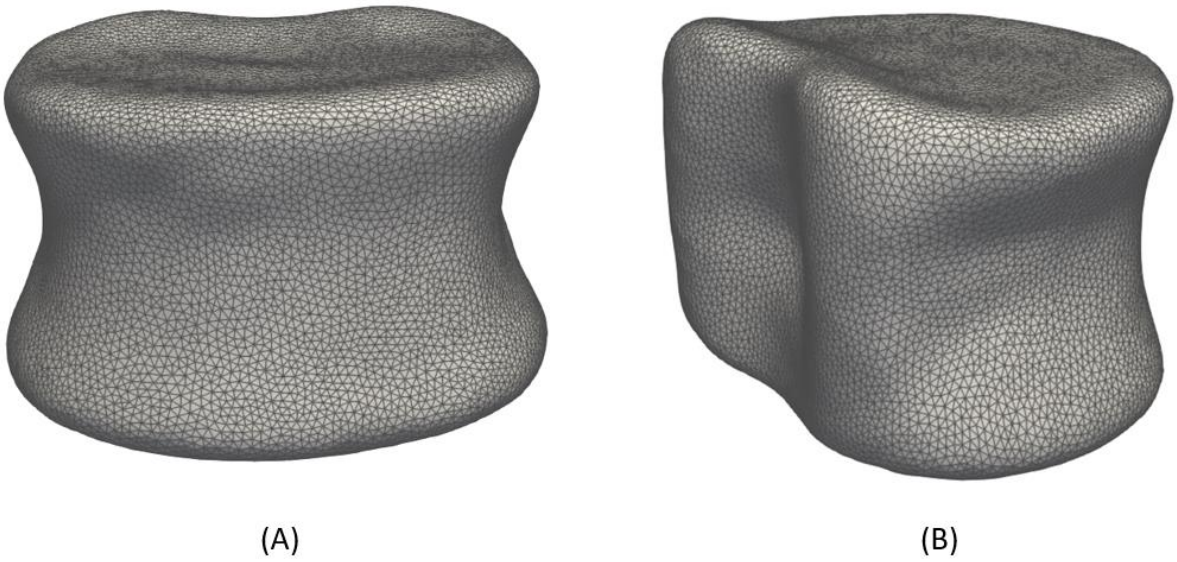

Figure 5.10- Reference mesh obtained from the iterative process to obtain an optimal reference mesh for the current dataset of vertebrae, in frontal (A) and posterolateral (B) view.

5.4.1.4.2 Alignment

Once the reference mesh was calculated, all the meshes of the dataset were aligned to the reference mesh by using the following procedure For each mesh of the dataset, 8 anatomical landmarks were placed on the superior and inferior endplates (Yeung et al., 2020). For example, the landmarks are showed in Figure 5.11 for the three vertebral levels of Patient #33. Then, the best rigid transformation (combination of rotations and translations) that minimizes the distance between the position of landmarks on the reference mesh and the position of landmarks on the considered mesh after the transformation was identified. The minimization problem was solved with a linear least square method.

Figure 5.11- Anatomical landmarks placed on the superior and inferior endplates of the vertebral bodies, for Patient #33, on T12 (A), L1 (B) and L2 (C) in up-frontal, down-frontal, postero-lateral views, respectively.

5.4.1.4.3 Deformable morphing algorithm

Based on the reference mesh, a deformable model was built with a Gaussian Process (GP) and morphed to the dataset of aligned meshes. A low-rank approximation of the GP characterized by a set of mode deformations of the reference mesh was used. The coefficients of these deformation modes needed to be optimised to deform the reference mesh so that this matched the target shapes in the dataset.

A GP is defined by a mean and a kernel. In this case, the reference mesh was chosen as the mean, and a combination of two multi-scale Gaussian kernels was used: a first one to take into account

global shape variations of the geometry (sigma = 50, l = 100); and a second one to consider more local changes (sigma = 5, l = 100). A finite-rank approximation of the GP was computed with a rank (i.e. the number of basis functions of the GP) equal to 200 in order not to exclude important modes of deformation of the geometry. This was done by using the Nystrom method (Luthi et al., 2018), by taking 1500 points uniformly sampled on the reference mesh as samples for the Nystrom approximation. This number was chosen after preliminary analyses on different geometries to optimise the mesh morphing outcome. This GP is often called as a "free-form deformation" model as it allows to model ideally an infinite range of non-meaningful deformations of the reference vertebra, and it will be called FFDM1 for the rest of the chapter.

Then, for each mesh in the dataset, the displacements between the anatomical landmarks placed on the reference mesh and the landmarks on the target mesh were incorporated within the FFDM1 through a GP regression, giving a so-called posterior model (FFDM2). Thanks to this process, the variance of the FFDM1 was constrained and the FFDM2 was able to represent more meaningful shapes than the ones obtained from the FFDM1. In fact, the shapes obtained from the FFDM2 were closer to the ones included in the dataset, while the shapes obtained from FFDM1 were not forced to represent realistic lumbar vertebrae. The same landmarks used for the alignment were used also for the creation of the FFDM2 (Figure 5.11).

The FFDM2 was morphed to the target mesh with an iterative process based on the same idea which is behind the generation of the FFDM2 posterior model: the main difference is that, instead of displacements from anatomical landmarks, displacements between regularly sampled points on the reference mesh and the respective closest points evaluated on the target mesh are incorporated into the model (Salhi et al., 2020). This GP regression, based on a huge number of points, results in a highly constrained GP that represents a full normal distribution of shapes fitting the target shape (FFDM3), and the mean of this process represents the best fit, therefore the final morphing mesh. The closest points on the target mesh were evaluated in an iterative process to improve the fitting (Iterative Closest Point, ICP). Therefore, the mesh morphing process was characterized by the following steps:

1. 10000 sample nodes were sampled on the reference mesh covering regularly the whole geometry;
2. For each of those nodes, the closest point on the target mesh was selected as candidate correspondence;

3. The displacements between the sample nodes on reference mesh and the candidate correspondences on the target geometry were incorporated within the FFDM2 through a GP regression. This allowed to obtain the FFDM3 and, therefore, a morphed mesh;
4. The spatial position of the 10000 nodes previously sampled was computed on the morphed mesh from the previous step, and the closest points on the target mesh were selected as candidate correspondences;
5. The displacements between the sample nodes on reference mesh and the new candidate correspondences identified in the previous step were incorporated within the FFDM2 through a GP regression. This approach allowed us to obtain a new FFDM3 based on a better estimation of the closest points, and therefore a new morphed mesh;
6. Loop to step 4 to update the displacements used in the GP regression based on the new morphed mesh and repeat for 100 iterations.

At the end of this iterative procedure, to evaluate the mesh morphing error, the mean error and Hausdorff distance were considered between the morphed meshes and the original geometries.

This mesh morphing algorithm was compared with another algorithm characterised by a single multi-scale Gaussian kernel (sigma = 100, l = 50), and a number of points equal to 2500 used in the ICP plus two additional landmarks at the centre of the superior and inferior endplates. The first set-up allowed to decrease the average mean error by about 46% and the Hausdorff distance by about 38%, on average over the three levels. Specifically, for T12, the Hausdorff distance decreased by about 42%.

5.4.1.5 Leave-one-out cross validation

5.4.1.5.1 Singular value decomposition and estimation of the optimal number of modes

For each patient in the dataset, a vector **h** with the nodes coordinates of the morphed T12, L1 and L2 surface meshes was built. The set of vectors for patients in the dataset was compressed by SVD. A leave-one-out experiment was performed for different numbers of modes (from 2 to 38 modes) to estimate the optimal number of modes to describe the variability of the geometries within the dataset (Xu and Goodacre, 2018). For a fixed number of modes (**k**), one vector was left-out and the remaining 39 vectors were compressed with a SVD keeping the first **k** modes:

$$\boldsymbol{H}_{(mxn)} = \boldsymbol{A}_{(mxm)} \cdot \boldsymbol{\Sigma}_{(mxn)} \cdot \boldsymbol{V}_{(nxn)} \qquad \text{(Eq. 5.11)}$$

where **H** is the matrix where the columns are the vectors **h** of nodes coordinates of each patient, **A** is composed of the left singular vectors (modes) of **H**, **Σ** is a diagonal matrix composed of the singular values σ_k of **H**, **V** is composed of the right singular vectors of **H**, m is equal to three times the number of node coordinates of a morphed vertebra, *n* is equal to 39.

The basis of **k** modes was assessed to evaluate the accuracy of the representation of the left-out vector and the learning vectors. Each vector was projected in the basis of **k** modes, and the surface mesh of T12, L1 and L2 was reconstructed from the projected vector. These meshes were compared with the morphed and original meshes based on the mean error and Hausdorff distance as before. The error on L1 alone and the average error over T12, L1 and L2 were evaluated. The error was assessed on the left-out patient and on the 39 learning patients by averaging the errors for each patient. This was repeated for each patient, therefore 40 different bases were built for any fixed **k**. As output of the leave-one-out experiment, the average errors among the 40 bases, evaluated on the left-out patients or the learning patients (only on L1 or averaged over the three vertebrae), were considered to define the optimal number of modes.

The same experiment was repeated by randomly removing 5 vectors from the dataset to further test the ability of the modes to represent the geometries of vectors that were not in the construction dataset. This process was repeated 10 times, and the errors considered as averaged over the 10 repetitions, to avoid biasing the results to the 5 selected vectors. By progressively increasing the number of vectors removed from the dataset this experiment can help in determining the minimum number of patients required to obtain the first deformation modes. As in the present study only 5 vectors were removed, this aimed at confirming the results of the leave-one-out approach.

5.4.1.5.2 Prediction of the shape of L1

Once fixed the optimal **k** and extracted the modes, the leave-one-out experiment was repeated as validation of the method to predict the shape of L1 from the shapes of T12 and L2 (Vanden Berghe et al., 2017; Plessers et al., 2018; Salhi et al., 2020; Wang et al., 2021). This method was based on a linear least squares minimization as presented in Section 5.3.1.4.1. The main difference with respect to the simplified case presented in 5.3.1.4 was that the matrix **A** used to build the system of linear equations includes now the nodes coordinates of T12 and L2 of the **k** modes instead of the heights of T12 and L2 of the **k** modes.

By using the solution coefficients **α'**, it was possible to reconstruct the vector of nodes coordinates of L1 ($\mathbf{h}_{L1}$) as:

$$\boldsymbol{h}_{L1} = \boldsymbol{A}_{L1} \cdot \boldsymbol{\alpha}' \qquad \text{(Eq. 5.12)}$$

where $\mathbf{A}_{L1}$ is the part of the matrix **A** that includes only the nodes coordinates of L1 of the **k** modes. For each left-out patient, the mean error and Hausdorff distance were calculated. For patients presenting the best, the worst and average mean error and Hausdorff distance, the distribution of heights of the predicted surface mesh of L1 vertebral body and the respective original mesh were compared. The distribution of heights of the vertebral body was calculated as follows. First, the superior and inferior endplates were manually isolated from the rest of the vertebral body in Ansys® SpaceClaim Release 21.1 (Ansys Inc., Canonsburg, PA, United States) ("Skin surface" command). Then, the directions perpendicular to all the triangles belonging to the superior endplate were used to define an average cranio-caudal direction. For each of those triangles, a height was defined as the Euclidean distance between the centre of the triangle and the intersection point between a line parallel to the average cranio-caudal direction passing through the centre of the triangle and the inferior endplate. A heatmap of the distribution of heights was computed by using a linear interpolator and a step size of 0.7 mm equal to the average size of triangles. Also, frequency plots of the distribution of heights were evaluated. In addition, as not all the groups of data were normally distributed, to compare the distribution of heights the median values were calculated. For the same patients, sagittal and frontal angles between the endplates were calculated based on the original and predicted geometries (Figure 6). The angles were defined in the mid-sagittal and mid-frontal planes based on least-squares planes fitting the endplates. Anterior and right angles were considered positive (Figure 6B). The difference between angles measured on original or predicted geometries was defined as absolute difference if angles were both anterior (posterior) or right (left), or as the sum of the absolute values of the angles if they were of different sign.

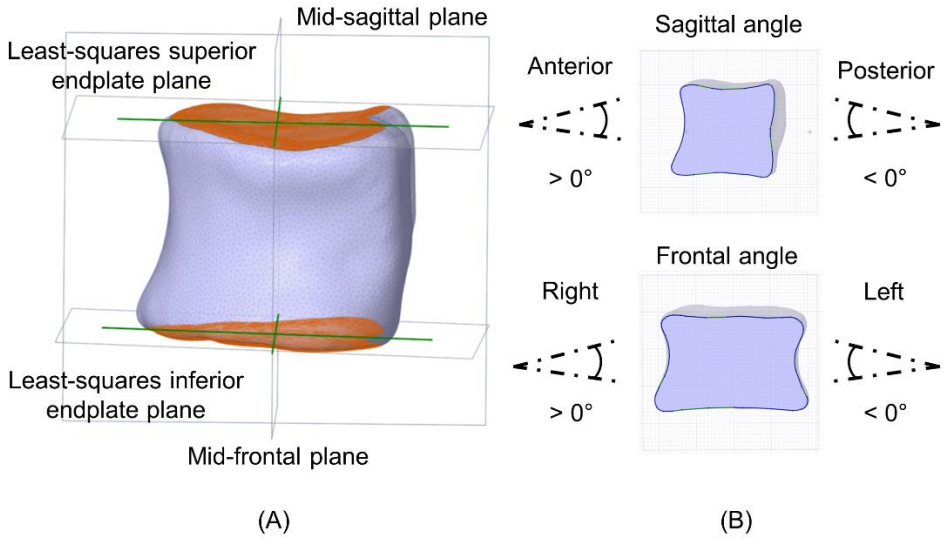

Figure 5.12- Anatomical planes (A) used to define sagittal and frontal angles (B).

For patients showing the best, the worst and average Hausdorff distance a report was prepared to provide a comprehensive assessment of the prediction of the shape of the L1 vertebral body. The report includes: a frontal and a posterolateral view of the original geometry, a frontal and a posterolateral view of the error map, a colormap and a frequency plot of the distribution of heights of the vertebral body for predicted and real geometries, a table reporting the reconstruction mean error and Hausdorff distance, and the median height error. The reports are included in Appendix, Section Appendix A6.

The minimization was repeated to simulate the cases when only T12 or only L2 were available. Therefore, the following systems of linear equations were considered and solved with a LLS method:

$$\boldsymbol{h}_{L2} = \boldsymbol{A}_{L2} \cdot \boldsymbol{\alpha} \qquad \text{(Eq. 5.13)}$$

$$\boldsymbol{h}_{T12} = \boldsymbol{A}_{T12} \cdot \boldsymbol{\alpha} \qquad \text{(Eq. 5.14)}$$

where $\mathbf{A}_{L2}$ is the part of the matrix **A** that includes only the nodes coordinates of L2 of the **k** modes, $\mathbf{A}_{T12}$ is the part of the matrix **A** that includes only the nodes coordinates of T12 of the **k** modes. For each left-out patient, the mean error and Hausdorff distance between the predicted surface mesh of L1 and the respective original meshes were evaluated.

5.4.1.6 Statistical analyses

We used descriptive statistics to investigate: the influence of the vertebral level (variable assuming values T12, L1 or L2) on the mesh morphing error; the influence of the number of levels used to compute the prediction of L1 (T12+L2, T12 only or L2 only) on the reconstruction error; any difference between the reconstruction error evaluated with respect to the original or morphed mesh; any difference between the reconstruction error of L1 and the projection error obtained for the number of modes (6) used to predict the shape of L1 vertebral body

To compare three groups of data, statistical paired analyses were conducted with Friedman test (non-parametric) based on the characteristics of data (normality, sphericity). In fact, data did not satisfy at least one of the two requisites. The normality of data was tested through a Kolmogorov-Smirnoff test. The sphericity of data was tested through a Mauchly's test. When the Friedman test produced a significant result, Nemenyi Post-hoc test was performed to find the groups of data that differ by making pair-wise tests. To compare two groups of data, statistical paired analyses were conducted with paired t-test (parametric) and Wilcoxon signed-rank test (non-parametric). A *p*-value of less than 0.05 was considered to be significant.

5.4.2 Results

5.4.2.1 Mesh morphing

The mean error and mean Hausdorff distance between the morphed mesh and the original geometries are reported in Table 5.2. The average, minimum and maximum errors are reported for each vertebral level and for all the geometries in the dataset.

Mean errors for T12 were higher than those for L1 (3.7%, $p = 0.008$), but lower than those for L2 (-1.4%, $p = 0.006$). Even though in some cases the differences between the mesh morphing errors at different levels were statistically significant, those difference were very low (< 4%). Overall, on the three levels, the average mean error was lower than 0.15 mm, showing an excellent reconstruction of the geometry of each patient through the mesh morphing process. Non-significant differences were found among the average Hausdorff distances for the three vertebral levels ($p = 0.09$). The error maps, in frontal and posterolateral views, were reported for the patients with the highest (Patient #16, T12 level, Figure 5.13A-B), lowest (Patient #14, L2 level, Figure 5.13E-F) and average (Patient #5, L1 level, Figure 5.13C-D) Hausdorff distance. The largest Hausdorff distance occurred at the posterolateral part of the vertebral body for the T12 vertebrae. This area represents

the region where the pedicles unify with the vertebral body and Hausdorff distance has lower interest for the chosen application. Overall, the morphing mesh captured well the shape of the original geometries as it is demonstrated by large parts on the geometry with error inferior to 0.5 mm. For the case with a Hausdorff distance close to the average, this error occurred at the level of the inferior endplate where Patient #5 presented a small osteophyte (see red arrow in Figure 5.13D). It is possible to note as the mesh morphing performed well despite an Hausdorff distance of about 1 mm.

Vertebral level	**Mean error (mm)**		**Hausdorff distance (mm)**	
	Average ± st dev	**(Min, Max)**	**Average ± st dev**	**(Min, Max)**
T12	0.140 ± 0.023	(0.093, 0.180)	1.030 ± 0.360	(0.556, 2.165)
L1	0.135 ± 0.018	(0.099, 0.177)	0.886 ± 0.205	(0.599, 1.628)
L2	0.142 ± 0.022	(0.103, 0.188)	0.961 ± 0.311	(0.478, 1.901)
T12, L1 and L2	0.139 ± 0.021	(0.093, 0.188)	0.959 ± 0.301	(0.478, 2.165)

Table 5.2- Mean error and Hausdorff distance (mm) between the morphed mesh and the original geometry, averaged over all the patients, for T12, L1 and L2 levels, and averaged over the three levels.

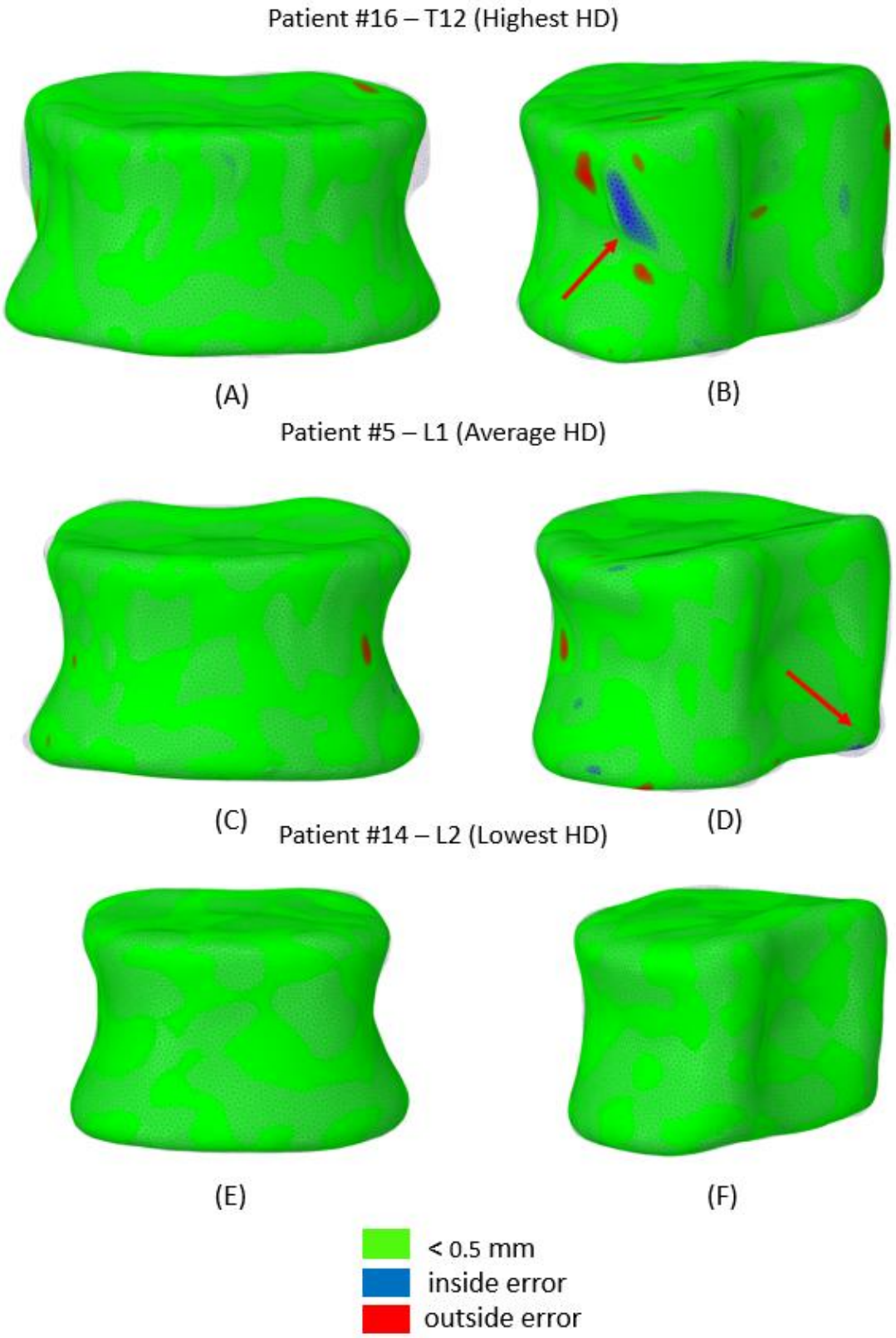

Figure 5.13- Error maps between morphed and original meshes for the worst case (A-B), an average one (C-D) and the best one (E-F), in frontal and posterolateral views, with respect to the Hausdorff distance (HD). Red arrows indicate the area where the HD occurred. The error is considered "inside" when the morphed mesh is inside the original one, and "outside" when the morphed mesh ins outside the original one.

5.4.2.2 Estimation of the optimal number of modes

The results of the experiment to define the optimal number of modes to describe the vectors within the dataset are summarized in Figure 5.14. On the x-axis the number of modes is reported. On the y-axis the average errors (with standard deviations) over the bases generated during the leave-one-out or leave-five-out are reported. In particular, the Hausdorff and mean errors evaluated on the left-out vectors and on all the learning vectors (averaged value) are presented. In Figure 5.14A and Figure 5.14C the error is evaluated with respect to the morphed meshes, which were used to build the matrix **H**; in Figure 5.14B and Figure 5.14D the error is evaluated with respect to the original geometries. The trends of errors were very similar if the errors were averaged over the three vertebrae or only for the L1 vertebrae. For simplicity, in Figure 5.14 the errors averaged over the three vertebrae are reported.

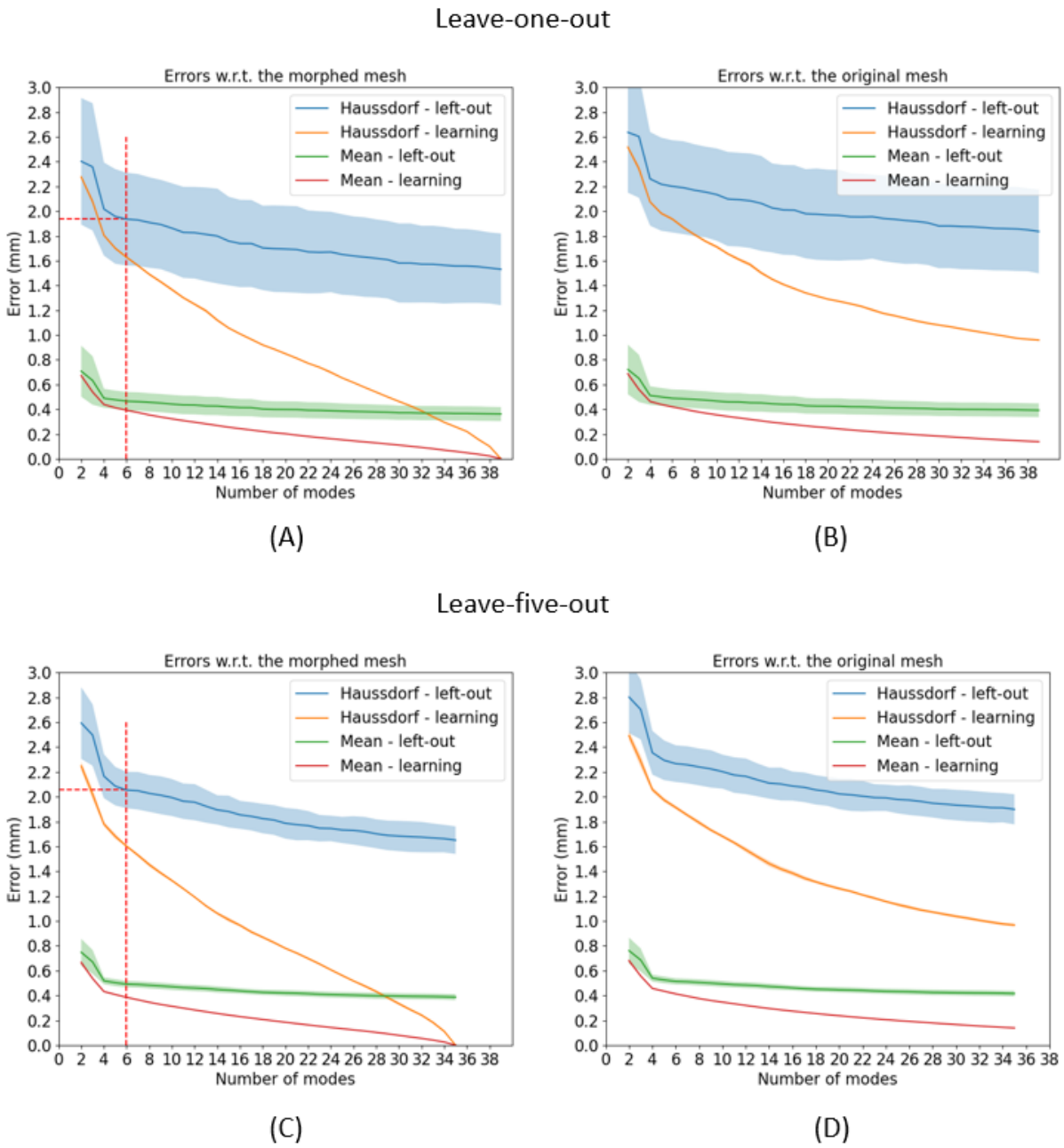

Figure 5.14- Mean and Hausdorff projection errors (mm) in function of the number of modes. The errors are evaluated with respect to the morphed mesh (A-C) and the original mesh (B-D) for the leave-one-out (A-B) and the leave-five-out (C-D). The dotted lines show the optimal number of modes. The shaded region represents the standard deviation. The standard deviation was about zero for the errors evaluated on the learning patients.

As expected, the errors on left-out patients or on learning patients decreased when the number of modes increased. The optimal number of modes was chosen as the best compromise between the number of modes and the projection errors within the basis of modes to avoid increasing the complexity of minimization problem to predict the shape of L1 unnecessarily.

Considering the mean error on the left-out patient (morphed mesh, Figure 5.14A), the error corresponding to 4 modes was lower than the error corresponding to 2 modes by 45%. Instead, increasing the number of modes, the mean error decreased by 18% from 4 to 39 modes. Therefore, the optimal number of modes regarding the mean error was 4 that corresponded to a mean error of 0.49 mm, that was also close to 0.45 mm which corresponded to the lowest voxel dimension (slice thickness) of the CT-scan with the best resolution in the dataset. A similar behaviour was observed for the Hausdorff distance: the error corresponding to 6 modes was lower than the error corresponding to 2 modes by 24%. When increasing the number of modes from 6 to 39 modes the Hausdorff distance decreased by 13%. The optimal number of modes regarding the Hausdorff distance was 6 that corresponded to a Hausdorff distance of 1.93 mm. In conclusion, 6 modes were retained for the minimization problem as optimal number of modes with respect to both the mean error (0.46 mm) and the Hausdorff distance (1.93 mm). Similar trends were found for the leave-five-out curves (Figure 5.14C).

Considering the mean and Hausdorff distances on the learning patients (Figure 5.14B-D), as expected, the errors approached to zero when increasing the number of modes. The curves showing the errors evaluated on the left-out patients with respect to the original meshes (Figure 5.14B-D) presented similar trends than the errors with respect to the morphed meshes (Figure 5.14A-C), but were shifted towards higher errors. In fact, the errors shown in Figure 5.14B-D could be interpreted as the combination of the mesh morphing error and the reduction error. For this reason, the mean and Hausdorff distances on the learning patients did not approach to zero when increasing the number of modes, but converged to a residual error which was about the mesh morphing error.

The standard deviation was overall constant in function of the number of modes for errors on the left-out and on learning patients (Figure 5.14).

5.4.2.3 Prediction of the shape of L1

The mean reconstruction error of the 3D shape of L1 was on average 0.51 mm, while the Hausdorff distance was on average 2.11 mm (Table 5.3). Examples of error maps, in frontal and posterolateral views, are showed in Figure 5.15: Patient #4 (Figure 5.15A-B) and Patient #11 (Figure 5.15E-F)

presented the best (0.29 mm) and worst (0.96 mm) mean error, respectively; Patient #5 (Figure 5.15C-D) presented a mean error of 0.51 mm which was close to the average.

Reconstruction error with respect to the original geometry				
Level(s) used	**Mean error (mm)**		**Hausdorff distance (mm)**	
	Average ± st dev	**(Min, Max)**	**Average ± st dev**	**(Min, Max)**
T12 and L2	0.51 ± 0.11	(0.29, 0.96)	2.11 ± 0.56	(1.38, 4.52)
T12	*0.56 ± 0.13	(0.34, 1.09)	*2.31 ± 0.52	(1.45, 4.42)
L2	*0.55 ± 0.13	(0.32, 0.94)	2.22 ± 0.57	(1.36, 4.60)
Reconstruction error with respect to the morphed geometry				
	Mean error (mm)		**Hausdorff distance (mm)**	
Level(s) used	**Average ± st dev**	**(Min, Max)**	**Average ± st dev**	**(Min, Max)**
T12 and L2	0.49 ± 0.12	(0.26, 0.94)	1.88 ± 0.54	(1.23, 4.06)
T12	*0.54 ± 0.13	(0.32, 1.08)	*2.13 ± 0.49	(1.33, 3.96)
L2	*0.53 ± 0.13	(0.30, 0.92)	1.99 ± 0.55	(1.21, 4.15)

*Table 5.3- Mean error and Hausdorff distance (mm) between the predicted 3D shape of L1 and the original or morphed geometry, in function of the information used for the prediction. * represents a significant difference for the mean error and the Hausdorff distance for the cases where data for T12 alone or L2 alone were used compared to the case where data from both T12 and L2 were used.*

Patient #35 and Patient #11 presented the best (1.38 mm) and worst (4.52 mm) Hausdorff distance, respectively. When the information about T12 alone was used to solve the minimization problem, the mean error and Hausdorff distance worsened by 10% (p = 0.001) and 9% (p = 0.001), respectively (Table 5.3); when the information about L2 alone was used, the mean error worsened by 8% (p = 0.012) but the Hausdorff distance was not significantly different (p = 0.074) (Table 5.3). The mean error and the Hausdorff distance when using T12 alone or L2 alone had not statistical differences (p = 0.75 and p = 0.28, respectively). Patient #4 and Patient #11 presented the best and worst mean error as in the case when the information about both the shapes of T12 and L2 was used. Patient #35 presented the best Hausdorff distance when T12 and L2, and only T12 were used; Patient #4 presented the best Hausdorff distance when only L2 was used. Patient #11 presented the worst Hausdorff distance in all three cases. The Hausdorff distance was often at the posterior part of the vertebra, in correspondence to the pedicles.

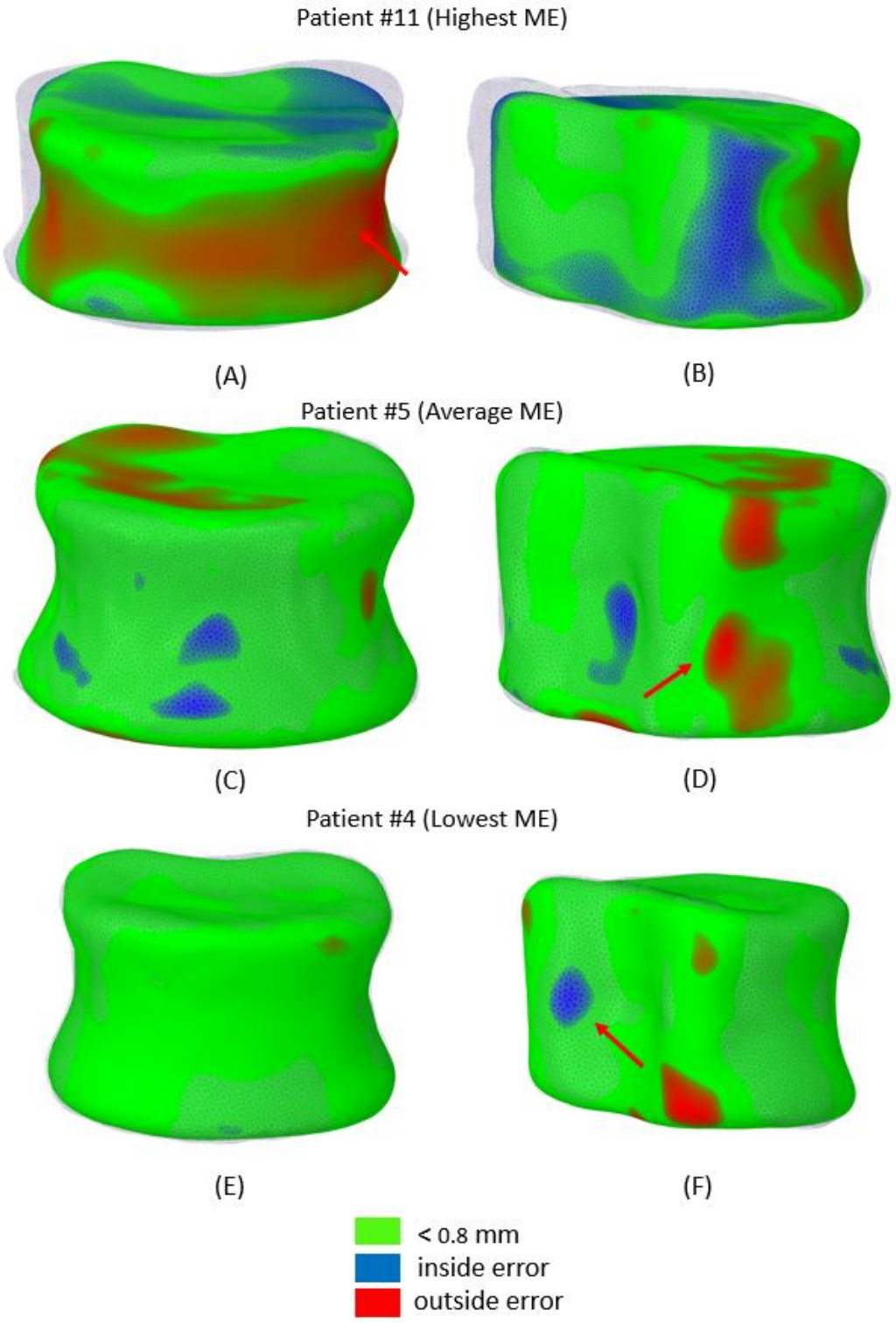

Figure 5.15 - Error maps between predicted and original meshes for the best case (A-B), an average one (C-D) and the worst one (E-F), in frontal and posterolateral views, with respect to the mean error (ME). Red arrows indicate the area where the Hausdorff distance occurred. The error is considered "inside" when the morphed mesh is inside the original one, and "outside" when the morphed mesh ins outside the original one.

Overall, as expected the mean error (3.8%, $p < 0.001$) and Hausdorff distance (10.5%, $p < 0.001$) evaluated on the original meshes (Table 5.3) were significantly higher than the case where the errors were evaluated on the morphed meshes (Table 5.3). The mean error ($p = 0.301$) and Hausdorff distances ($p = 0.248$) evaluated on the morphed meshes (Table 5.3) were similar to the projection errors for the number of modes (6) used to predict the shape of L1 vertebral body (Figure 5.14A).

For Patient #4 (lowest mean error), the distribution of heights of the predicted surface mesh of L1 vertebral body was very similar to the distribution of the original geometry (Figure 5.16E-F, Figure 5.17C). For Patient #5 (average mean error), the predicted surface mesh overestimated the height of the vertebral body (Figure 5.16C-D, Figure 5.17B), while for Patient #11 (highest mean error) the prediction resulted in an underestimation of the height (Figure 5.16A-B, Figure 5.17A). The difference between the median height values of distributions was higher for Patient #11 (-1.41 mm), than for Patient #5 (1.05 mm). For this sub-group of patients, the difference between sagittal and frontal angles measured on original or predicted geometry was always lower than 1.8° and 1.4°, respectively.

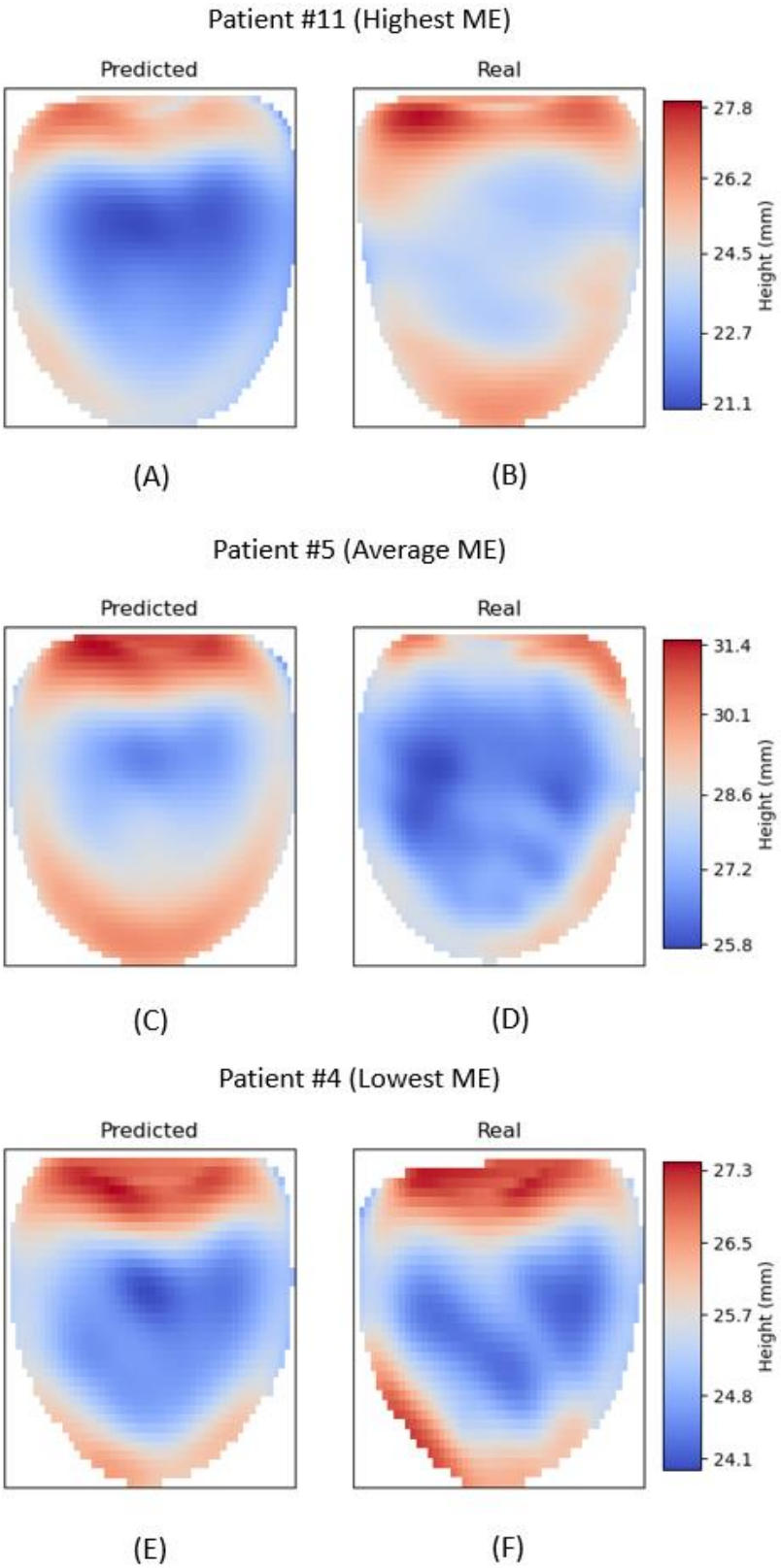

Figure 5.16 - Comparison of the maps of the distribution of heights of the vertebral bodies between predicted (A-C-E) and original meshes (B-D-F). The comparison is done for the best prediction case (A-B), an average one (C-D) and the worst one (E-F) with respect to the mean error (ME).

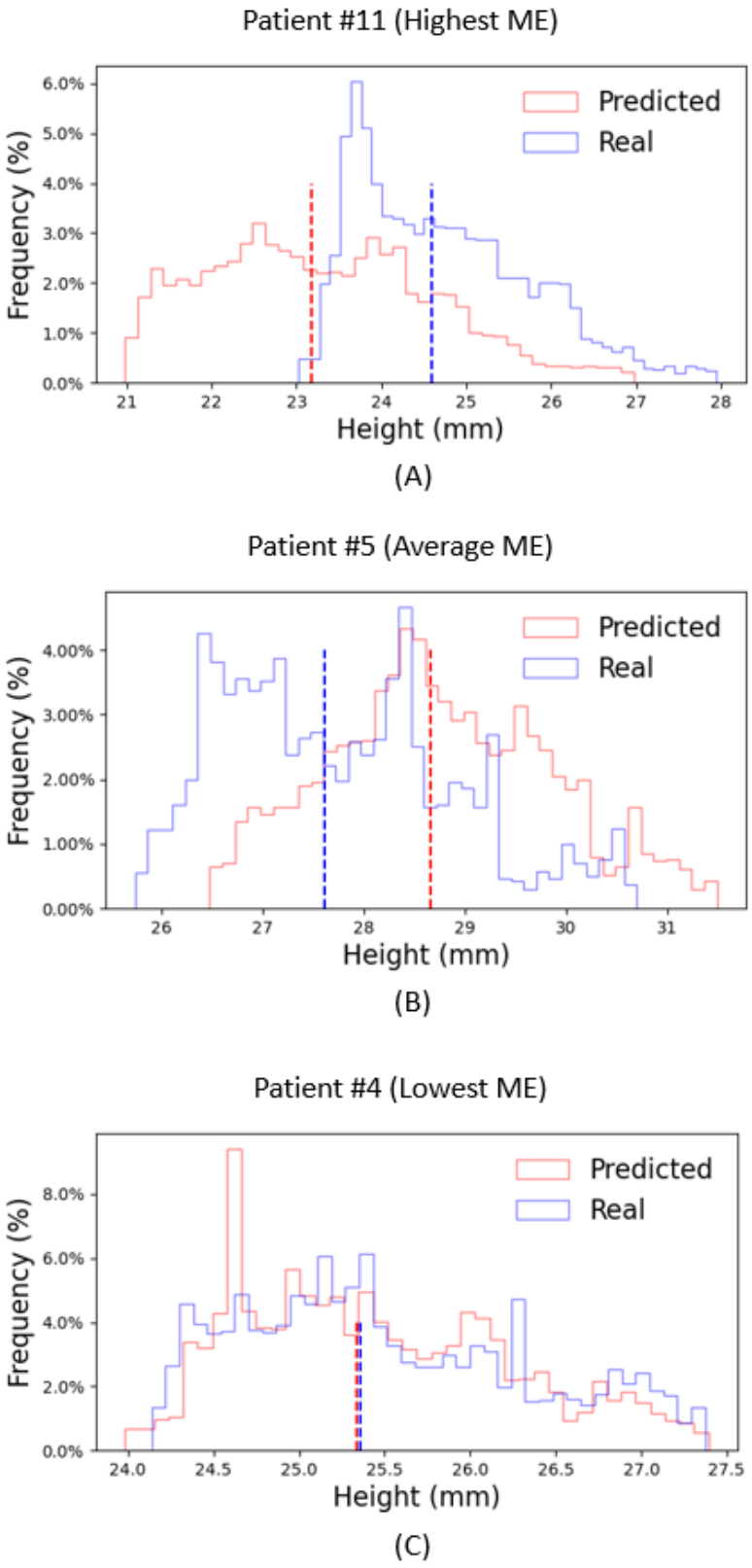

Figure 5.17 - Frequency plots of the heights of the predicted and real vertebral bodies for the best prediction case (A), an average one (C) and the worst one (E) with respect to the mean error (ME). Dotted lines represent the median values of distributions.

5.4.2.4 Processing time

The extraction of the geometry of the vertebral bodies from the segmentation mask took approximately 4 minutes per vertebra. Placing anatomical landmarks on the vertebral bodies took less than 2 minutes. Once the reference mesh was calculated, alignment and mesh morphing were two automatic steps that took approximately 4 minutes per vertebra without any optimization of the fitting procedure. Building and solving the minimization problem to find the reconstructed shape of L1 was a very fast process (seconds). The time needed to process one patient external to the dataset in order to retrieve the pre-fracture shape of L1 would be 20 minutes. This time does not include the time needed to segment the T12 and L2 vertebrae, with a manual or an automatic process.

5.5 Discussion

The goal of this study was to develop a method to reconstruct the 3D shape of a L1 vertebral body by using the shapes of adjacent vertebral bodies.

The mathematical approach used to predict the shape of a L1 vertebral body was tested on a simplified 1D case. The shape of the vertebral body was described by a small number of characteristic heights. These characteristic heights of the L1 vertebral body were predicted from heights of adjacent vertebral bodies with a good accuracy (lower than 1 mm). This approach could be used for some applications where information about characteristic heights would be valuable to the surgeon, considering also the short operator and computational time needed to process the data. In fact, identifying anatomical landmarks on the vertebral mesh took approximately 2 minutes per vertebra and represents the only significant processing time before obtaining information about the heights of L1. Implementing automatic extraction of bone landmarks of lumbar vertebrae would allow to furtherly simplify the workflow (Campbell and Petrella, 2015). The reconstruction of the 3D shape of L1 was more time-consuming and required about 20 minutes per patient starting from already segmented images. An additional time of about 30 minutes per vertebra should be taken into account to perform a manual segmentation from CT images. However, the pre-fracture 3D shape could be used by surgeons to target a thorough reduction of the vertebral fracture in multiple anatomical planes which is essential in case of articular fractures (Aebi, 2007). Moreover, semi-automatic or fully automatic image segmentation techniques could be used to reduce the time needed to process CT-scan images and fasten clinical protocols.

The morphing algorithm applied to lumbar vertebral bodies segmented from CT-scan images allowed to accurately describe patient-specific geometries with a single template mesh. The mean error and the Hausdorff error between the morphed meshes and their corresponding original geometries were lower than 0.15 mm and 1 mm on average over the 40 patients included in the dataset. The mesh morphing error of geometries used to build a SSM of mandible (Wang et al., 2021), scapular bone (Plessers et al., 2018; Salhi et al., 2020) and acetabular bone (Vanden Berghe et al., 2017) to reconstruct the premorbid shape of the bone, or to build a SSM of C2 cervical vertebra (Clogenson et al., 2015) was not reported. Campbell and Petrella (2016) built an SSM of the lumbar spine using a subject-specific mesh morphing technique characterized by a Euclidian node to surface distance lower than 1e-5 mm, i.e., a perfect matching between the morphed and original geometries. However, the mean mesh morphing error in the present study was lower than the lowest voxel size (0.45 mm) among all the segmentations used to build the dataset and the geometry of each patient was very accurately described by the morphed meshes. The Hausdorff distance was concentrated in small areas of the vertebral bodies (Figure 5.13), in particular it occurred at the posterolateral part of the vertebral body at the T12 level, which is an area of reduced interest for the present application, or at the level of small protuberances or porosities peculiar of the anatomy of certain patients. Additionally, it has to be remarked that the mesh morphing error may be affected by the number of iterations of the algorithm to define the reference mesh and may be improved by increasing the number of iterations. This is a time-consuming process and was not addressed in the present work as the mesh morphing error was considered acceptable for the present application.

The optimal number of modes to build the minimization problem and to predict the shape of L1 vertebral body was determined by repeating a leave-one-out experiment for all possible number of modes, end evaluating the projection error of patients external to the basis. This parameter has to be chosen based on the accuracy of the representation that is aimed, and on the compromise of representing the variability of the training data without overfitting it (Brunton et al., 2016). For a SSM-based reconstruction of the scapular bone, Salhi et al. (2020) retained the first 15 modes that allowed to account for the 95% of the variability in a training set of 82 samples. This approach is frequently used in literature, but it does not consider the ability to represent data outside the training set. By using the leave-one-out approach it is measured the ability of the model to represent data which is not part of the training set, and, therefore, this approach was preferred in this study.

The accuracy of the reconstruction was validated with a leave-one-out cross validation on a large dataset of patients with healthy thoracolumbar spines and can be used to reconstruct the pre-fracture

shape of a L1 vertebral body. The 3D shape of L1 vertebral body was predicted with a mean error of 0.51 mm and Hausdorff distance of 2.11 mm, on average over the 40 patients in the dataset. Nowadays, the O-Arm is an advanced imaging system combining 2D and 3D acquisition modes which is often used in the operating room during spinal surgical procedures. Considering that the spatial resolution of the O-arm image is generally about 0.4 mm, the mean reconstruction error was comparable with the precision associated with the detection of the contour of the vertebra in clinical protocols (Zhang et al., 2009). In works on SSM-based reconstruction of bones with artificial defects, the mean reconstruction error was 1 mm for the acetabular bone (mean Euclidean point to mesh distance) (Vanden Berghe et al., 2017), 1.2 mm (root mean square error) (Plessers et al., 2018) or 0.97 mm (mean closest point distance) (Salhi et al., 2020) for the scapula; Salhi et al. (2020) and Wang et al. (2021) reported also the average Hausdorff reconstruction distance that was 5.86 mm and 4.51 mm, respectively. The prediction errors observed in the present study were lower than those reported in Vanden Berghe et al. (2017), Plessers et al. (2018), Salhi et al. (2020) and Wang et al. (2021). Nevertheless, it should be noted that these studies focused on acetabular bones and scapulae that present different morphologic characteristics than the vertebra, studied in this project. Moreover, the reconstruction approaches used are different: in this work the T12 and L2 vertebral body shapes were used for an SSM-based reconstruction of L1, while the healthy part of the L1 vertebra was not used; instead, in SSM-based reconstruction of bones with artificial defects, the healthy part of one bone is used as a target of the SSM in order to estimate the shape of the part with defects. Finally, different distance metrics to evaluate the difference between the predicted and the original shapes were used. de Bruijne et al. (2007) found a mean distance between the original and reconstructed 2D shapes of 0.8 mm (closest point distance) for unfractured vertebrae, which is higher than the mean prediction distance in the present study focused on the 3D shape of the vertebral body. That error worsened in the case of L1 and L4 levels where only one adjacent vertebra was considered for the prediction. This is in line with the findings of the present study as the errors worsened by about 10% when the information of only one adjacent vertebra was used in the minimization process. It has to be noted that the worst mean error and Hausdorff distance in the present study occurred for Patient #11 which was the oldest patient in the dataset. The osteophytes of the vertebral bodies of Patient #11 were considered as borderline. The segmentation mask of Patient #11 was obtained by a CT-scan with a slice thickness of 3 mm. The Hausdorff distance is expected to be lower for a dataset including only young patients without any osteophytes of spine degeneration. With the number of modes retained to compute the prediction (6 modes), the projection errors for patients excluded from the basis of modes were about 0.45 mm (mean error)

and 1.95 mm (Hausdorff error) (Figure 5.14A). The projection error corresponds to the lower bound error that would be possible to find with the LLS optimization. The projection errors were very close to the reconstruction errors found after minimization with the LLS method, therefore confirming that the optimization allowed to approach the optimal set of coefficients.

The height of L1 vertebral body was accurately predicted for Patient #4, while it was overestimated and underestimated for Patient #5 and Patient #11. For both Patient #5 and Patient #11, the difference between the median height values (Patient #5: 1.05 mm; Patient #11: -1.41 mm,) was higher than the mean reconstruction error (Patient #5: 0.51 mm; Patient #11: 0.96 mm) but lower than the Hausdorff distance (Patient #5: 1.99 mm; Patient #11: 4.52 mm). Therefore, these results are promising for those cases where surgeons are mostly focused on retrieving the height of the fractured vertebra rather than the 3D shape. However further studies are needed to assess the quality of the prediction of the height's distribution on the whole dataset.

There are some limitations in this study.

First, it is important to note that this method was tested on a dataset of healthy spines without severe bone degeneration or large osteophytes. In fact, this method is based on the generation of principal modes by SVD that contain the information about the most prominent shape variations in a dataset of healthy vertebrae. Introducing patients with a severe pathology that affect the shape of vertebrae in the training dataset, would be disadvantageous in detecting the main modes as those geometries would act as noise by increasing the variability in the dataset. Instead, testing this method built on a dataset of healthy patients on a patient with disease, is not expected to provide an accurate reconstruction as the information of the shape of diseased patients is not contained in the training set. A possible solution would be to create a training dataset specific for each disease or pathological characteristics (e.g. a dataset that contains vertebrae with large osteophytes) in order to describe the variability of those shapes, and use it specifically to predict the premorbid shape of vertebrae with patients with the same disease/characteristics. However, this has not been assessed in the present study and will be challenged in future works.

Secondly, this method has been assessed only on the vertebrae at the thoracolumbar junction (T12, L1 and L2). The thoracolumbar junction is the area where traumatic fractures of the spine occur more often (Wood et al., 2014). Traumatic vertebral fractures are a common disease and since these injuries are often due to high-energy events, as motor accidents, falls, sport traumas, they are common in persons of different ages (Schousboe, 2016). The incidence of traumatic fractures at the thoracolumbar junction has been associated to the anatomy and functionality of the spine: the

thoracolumbar junction is characterised by a sudden change in curvature, from dorsal to lumbar spine, and stiffness, from the less mobile thoracic spine, where vertebrae sustain the rib cage, to the dynamic lumbar spine which has higher range of motion, resulting in a concentration of biomechanical stress (Oxland et al., 1992). The approach presented in this study can be extended to lumbar and lower thoracic vertebral bodies that present similar geometries. In this way, different kinds of vertebral fractures could be targeted. In fact, CT-scan imaging is the standard exam to characterise a vertebral fracture, therefore the availability of clinical data to use this approach is not limited to traumatic fractures. Additionally, this method focused only on the prediction of the vertebral body shapes. This was due to the fact that fractures injuring the posterior part of the column are generally due to violent forces and are often associated with other musculoskeletal trauma and neurologic injury (Magerl et al., 1994; Wood et al., 2014). In those cases, the primary objective of any treatment is to avoid neurological deficit, and the reconstruction of posterior elements is not pursued.

Thirdly, we hypothesized that for the prediction of the pre-fracture shape of L1 vertebral body, the healthy shapes of two or at least one adjacent vertebra are available. We expect a degradation of the quality of the prediction in case also the adjacent vertebrae present signs of fractures or microfracture, as showed by de Bruijne et al. (2007). However, this method is agnostic of the shape of the predicted level, and it is not based on the assumption that some healthy parts of the bone must be available as in SSM-based reconstruction studies.

5.6 Conclusion

This project was undertaken to develop, test and validate a methodology to predict the 3D shape of the L1 vertebral body from adjacent ones. The results of the validation on a large dataset of patients indicate that the reconstruction was performed with excellent accuracy. This research has practical application as it may be used to provide surgeons with information about the geometry before a vertebral fracture and to optimise the treatment. In the future this approach can be extended to study multiple thoracolumbar levels.

Chapter 6: Conclusions

6.1 Original contributions

The goal of this project was to create computational models to aid in the pre-operative planning of spinal surgeries. The developed approaches provide a quantitative assessment of the biomechanical properties of the vertebra implanted with two pedicle screws as well as of the geometry of the fractured vertebra prior to injury. These models could be used to optimise the treatment of several spinal diseases and injuries, in particular of vertebral fractures, by optimising parameters related to the surgeries and to improve personalised treatments. This goal was accomplished by the development of a pipeline based on FE models and ROMs of screw fixation (Chapter 3, 4) and of a method to predict the pre-fracture shape of L1 vertebra (Chapter 5).

In Chapter 3, a comprehensive assessment of the effect of the mesh size and the sensitivity of subject-specific FE models of three lumbar vertebrae implanted with pedicle screws to the screw size and geometry, in terms of stress in the screw, strain in the heterogeneous bone, and deflection of the screw within the bone, was reported. For both simplified and realistic models, element sizes of 0.6 mm in the screw and 1.0 mm in the bone allowed to obtain relative differences of approximately 5% or lower in peak deflection of screws, peak von Mises stress in the screws and peak Minimum principal strain in the vertebra with respect to the finest mesh. The diameter of the screw had a major role on the mechanics of the screw-vertebral structure for each patient for all the considered metrics. A very good correlation was found for the maximum deflection and the mean Minimum principal strain around the screws predicted with realistic or simplified screws (R^2 = 0.99). Simplified models underestimated the peak stress with respect to realistic ones (R^2 = 0.82). This study showed that the diameter of the screw should be optimised for each patient as it has a large impact on the mechanical properties of the construct. In addition, the underestimation of peak stress in the screws when using simplified geometry of pedicle screws should be accounted for when using the results of FE models for clinical decision making.

In Chapter 4, the performance of ROMs applied to the results of subject-specific FE models of an instrumented vertebra was assessed. This study showed that ROMs could predict with an accuracy lower than 3% the deflection of the screws and lower than 6% the von Mises stress in the screws, but presented large errors for the prediction of the strain in the bone, for a model with shape

parameters representing the size and orientation of screws. In a simplified case with homogeneous properties of the bone, bonded contact conditions at the screws-bone interface and only two shape parameters (diameter and length of screws) ROMs of the strain were characterized by an accuracy lower than 5%. The screws-bone contact condition was identified as the major feature of FE models impacting the ROMs. While at this stage this approach cannot be used to accurately predict biomechanical properties of the bone that are associated to some of the possible failure modes of the fixation (screw migration, failure of the bone), the ROMs of parametric FE models of posterior fixation have high potential in studying the biomechanics of complex spine fixation. However, they need to be optimised in future studies (see below).

In Chapter 5, a methodology based on Singular Value Decomposition (SVD) was developed to predict the shape of the vertebral body of L1 from the shapes of adjacent vertebral bodies. The development of this method involved the creation of a dataset of vertebral bodies from a public database, the mesh morphing of all the geometries onto a template mesh, and the solution of a minimisation problem formulated starting from the compression of mesh coordinates through SVD. Based on a leave-one-out cross validation process over a dataset with 40 patients, the mean reconstruction error of the 3D shape of L1 was on average 0.51 ± 0.11 mm, while the Hausdorff distance was on average 2.11 ± 0.56 mm. The distribution of heights between the two endplates was also accurately predicted. This method could be used to provide valuable information to the surgeon in the pre-operative setting and to optimise the treatment based on geometric characteristics of the vertebra at time before the fracture.

6.2 Limitations and future works

A number of limitations need to be noted regarding this thesis and shall be addressed in future works.

One issue with the current study was that the FE model of the implanted vertebra, although verified and the results subjected to sensitivity analysis, was not validated with respect to measurements from *ex-vivo* experiments. This step is fundamental for providing the needed credibility to the models before their application in clinics. This study was the initial stage toward the construction and optimisation of a computational approach to assess the mechanical stability of posterior fixation by considering realistic geometries and structural properties of the vertebra and by modelling the screw with a realistic or simplified geometry. In future investigations, the model will be validated

against state-of-the-art time-lapsed mechanical testing, micro-CT imaging, and digital volume correlation techniques to evaluate the strain distribution in bone tissue (Palanca et al., 2022). Moreover, the current research has only examined one vertebra implanted with two pedicle screws. Nevertheless, in posterior pedicle screw fixation surgeries usually more complex geometries are involved (at least two vertebrae, two rods, four pedicle screws). In addition, the biomechanical assessment was performed under vertical loads perpendicular to the screw axis. More sophisticated geometry should be developed in order to determine the influence of screw size in physiological settings.

As it concerns the exploration of the application of ROMs to FE models of the implanted vertebra, in case of complex models with heterogeneous properties and screws-bone frictional interface, the ROM presented good performance for metrics in the screws, but bad performance for the strain in the bone, which limits the effectiveness of the methodology. I have identified the problem of the ROMs in the prediction of the frictional properties of the bone-screw interface, with issues associated with the correction of initial gaps and penetrations and the optimization of the element type and size at the interface. However, future studies are needed to optimise the ROMs for the frictional case. Moreover, the ROMs were found to have similar accuracies as the linear interpolation of the results of FE models. This was probably due to the type of parameters included in the model and to their range of variation that resulted in a linear relationship between the FE results and the shape parameters. Nevertheless, the application of ROMs has great potential for complex highly computational expensive models including complex geometries (multiple vertebral levels) geometric or material non-linearities (e.g., large deformations, hyper-elastic material properties of the intervertebral discs, elasto-plastic properties of the bone), or in case more shape parameters are introduced into the model (e.g., the insertion point of pedicle screws or the amount of screws inserted in the bone).

The methodology to predict the 3D shape of a L1 vertebral body from adjacent vertebrae was tested only on L1 vertebral levels of adult healthy patients. A natural progression of this work is to include more lumbar and thoracic vertebrae to assess whether this method could be effective to predict the 3D shapes at different levels. However, the application of this methodology has been showed onto the thoracolumbar junction which is the region where traumatic fractures of the spine occur more often (Wood et al., 2014). In the future, it will be important to explore the potential application of this method to old patients presenting bone degeneration and osteophytes. Considering a dataset of patients with pathologies could deteriorate the quality of the compression through SVD because of

the large variability of shapes associated with diseases and the reconstruction of pre-fracture shape is challenging.

References

Abbeele, M. V. den, Valiadis, J.-M., Lima, L. V. P. C., Khalifé, P., Rouch, P., and Skalli, W. (2018). Contribution to FE modeling for intraoperative pedicle screw strength prediction. *Comput. Methods Biomech. Biomed. Engin.* 21, 13–21. doi:10.1080/10255842.2017.1414200.

Aebi, M. (2007). *AOSpine Manual*. AOSpine International.

Assessing Credibility of Computational Modeling through Verification & Validation: Application to Medical Devices - ASME Available at: https://www.asme.org/codes-standards/find-codes-standards/v-v-40-assessing-credibility-computational-modeling-verification-validation-application-medical-devices [Accessed October 26, 2020].

BEN SALEM, M., and Tomaso, L. (2018). Automatic selection for general surrogate models. *Struct. Multidiscip. Optim.* Available at: https://hal.archives-ouvertes.fr/hal-01685848 [Accessed July 9, 2021].

Bianco, R.-J., Arnoux, P.-J., Mac-Thiong, J.-M., and Aubin, C.-E. (2019). Thoracic pedicle screw fixation under axial and perpendicular loadings: A comprehensive numerical analysis. *Clin. Biomech.* 68, 190–196. doi:10.1016/j.clinbiomech.2019.06.010.

Bianco, R.-J., Arnoux, P.-J., Wagnac, E., Mac-Thiong, J.-M., and Aubin, C.-É. (2017). Minimizing Pedicle Screw Pullout Risks: A Detailed Biomechanical Analysis of Screw Design and Placement. *Clin. Spine Surg.* 30, E226–E232. doi:10.1097/BSD.0000000000000151.

Biancolini, M. E. (2017). "RBF Mesh Morphing," in *Fast Radial Basis Functions for Engineering Applications*, ed. M. E. Biancolini (Cham: Springer International Publishing), 93–117. doi:10.1007/978-3-319-75011-8_6.

Biancolini, M. E., Capellini, K., Costa, E., Groth, C., and Celi, S. (2020). Fast interactive CFD evaluation of hemodynamics assisted by RBF mesh morphing and reduced order models: the case of aTAA modelling. *Int. J. Interact. Des. Manuf. IJIDeM* 14, 1227–1238. doi:10.1007/s12008-020-00694-5.

Biswas, J. K., Sahu, T. P., Rana, M., Roy, S., Karmakar, S. K., Majumder, S., et al. (2019). Design factors of lumbar pedicle screws under bending load: A finite element analysis. *Biocybern. Biomed. Eng.* 39, 52–62. doi:10.1016/j.bbe.2018.10.003.

Brunton, A., Salazar, A., Bolkart, T., and Wuhrer, S. (2016). "STATISTICAL SHAPE SPACES FOR 3D DATA: A REVIEW," in *Handbook of Pattern Recognition and Computer Vision* (WORLD SCIENTIFIC), 217–238. doi:10.1142/9789814656535_0012.

Caiazzo, A., Guibert, R., and Vignon-Clementel, I. E. (2016). A reduced-order modeling for efficient design study of artificial valve in enlarged ventricular outflow tracts. *Comput. Methods Biomech. Biomed. Engin.* 19, 1314–1318. doi:10.1080/10255842.2015.1133811.

Calka, M., Perrier, P., Ohayon, J., Grivot-Boichon, C., Rochette, M., and Payan, Y. (2021). Machine-Learning based model order reduction of a biomechanical model of the human

tongue. *Comput. Methods Programs Biomed.* 198, 105786. doi:10.1016/j.cmpb.2020.105786.

Campbell, J. Q., and Petrella, A. J. (2015). An Automated Method for Landmark Identification and Finite-Element Modeling of the Lumbar Spine. *IEEE Trans. Biomed. Eng.* 62, 2709–2716. doi:10.1109/TBME.2015.2444811.

Campbell, J. Q., and Petrella, A. J. (2016). Automated finite element modeling of the lumbar spine: Using a statistical shape model to generate a virtual population of models. *J. Biomech.* 49, 2593–2599. doi:10.1016/j.jbiomech.2016.05.013.

Castro-Mateos, I., Pozo, J., Lazáry, A., and Frangi, A. (2016). *Automatic construction of patient-specific finite-element mesh of the spine from IVDs and vertebra segmentations*. doi:10.1117/12.2217343.

Chen, S.-I., Lin, R.-M., and Chang, C.-H. (2003). Biomechanical investigation of pedicle screw–vertebrae complex: a finite element approach using bonded and contact interface conditions. *Med. Eng. Phys.* 25, 275–282. doi:10.1016/S1350-4533(02)00219-9.

Chevalier, Y., Matsuura, M., Krüger, S., Fleege, C., Rickert, M., Rauschmann, M., et al. (2018). Micro-CT and micro-FE analysis of pedicle screw fixation under different loading conditions. *J. Biomech.* 70, 204–211. doi:10.1016/j.jbiomech.2017.12.023.

Cho, W., Cho, S. K., and Wu, C. (2010). The biomechanics of pedicle screw-based instrumentation. *J. Bone Joint Surg. Br.* 92, 1061–1065. doi:10.1302/0301-620X.92B8.24237.

Clogenson, M., Duff, J. M., Luethi, M., Levivier, M., Meuli, R., Baur, C., et al. (2015). A statistical shape model of the human second cervical vertebra. *Int. J. Comput. Assist. Radiol. Surg.* 10, 1097–1107. doi:10.1007/s11548-014-1121-x.

Commandeur, F., Velut, J., and Acosta, O. (2011). A VTK Algorithm for the Computation of the Hausdorff Distance. *VTK J.*, 839.

Cootes, T. F., Taylor, C. J., Cooper, D. H., and Graham, J. (1995). Active Shape Models-Their Training and Application. *Comput. Vis. Image Underst.* 61, 38–59. doi:10.1006/cviu.1995.1004.

Costa, M. C., Eltes, P., Lazary, A., Varga, P. P., Viceconti, M., and Dall'Ara, E. (2019). Biomechanical assessment of vertebrae with lytic metastases with subject-specific finite element models. *J. Mech. Behav. Biomed. Mater.* 98, 268–290. doi:10.1016/j.jmbbm.2019.06.027.

Dall'Ara, E., Pahr, D., Varga, P., Kainberger, F., and Zysset, P. (2012). QCT-based finite element models predict human vertebral strength in vitro significantly better than simulated DEXA. *Osteoporos. Int. J. Establ. Result Coop. Eur. Found. Osteoporos. Natl. Osteoporos. Found. USA* 23, 563–572. doi:10.1007/s00198-011-1568-3.

Dall'Ara, E., Peña-Fernández, M., Palanca, M., Giorgi, M., Cristofolini, L., and Tozzi, G. (2017). Precision of Digital Volume Correlation Approaches for Strain Analysis in Bone Imaged with Micro-Computed Tomography at Different Dimensional Levels. *Front. Mater.* 4. doi:10.3389/fmats.2017.00031.

de Bruijne, M., Lund, M. T., Tankó, L. B., Pettersen, P. C., and Nielsen, M. (2007). Quantitative vertebral morphometry using neighbor-conditional shape models. *Med. Image Anal.* 11, 503–512. doi:10.1016/j.media.2007.07.004.

Elmasry, S., Asfour, S., and Travascio, F. (2017). Effectiveness of pedicle screw inclusion at the fracture level in short-segment fixation constructs for the treatment of thoracolumbar burst fractures: a computational biomechanics analysis. *Comput. Methods Biomech. Biomed. Engin.* 20, 1412–1420. doi:10.1080/10255842.2017.1366995.

Fedorov, A., Beichel, R., Kalpathy-Cramer, J., Finet, J., Fillion-Robin, J.-C., Pujol, S., et al. (2012). 3D Slicer as an image computing platform for the Quantitative Imaging Network. *Magn. Reson. Imaging* 30, 1323–1341. doi:10.1016/j.mri.2012.05.001.

Fields, A. J., Eswaran, S. K., Jekir, M. G., and Keaveny, T. M. (2009). Role of Trabecular Microarchitecture in Whole-Vertebral Body Biomechanical Behavior. *J. Bone Miner. Res.* 24, 1523–1530. doi:10.1359/jbmr.090317.

Ganapathi, A., McCarron, J. A., Chen, X., and Iannotti, J. P. (2011). Predicting normal glenoid version from the pathologic scapula: a comparison of 4 methods in 2- and 3-dimensional models. *J. Shoulder Elbow Surg.* 20, 234–244. doi:10.1016/j.jse.2010.05.024.

Gelaude, F., Clijmans, T., Broos, P. L., Lauwers, B., and Vander Sloten, J. (2007). Computer-aided planning of reconstructive surgery of the innominate bone: Automated correction proposals. *Comput. Aided Surg.* 12, 286–294. doi:10.3109/10929080701684762.

Genant, H. K., Wu, C. Y., van Kuijk, C., and Nevitt, M. C. (1993). Vertebral fracture assessment using a semiquantitative technique. *J. Bone Miner. Res. Off. J. Am. Soc. Bone Miner. Res.* 8, 1137–1148. doi:10.1002/jbmr.5650080915.

Gertzbein, S. D., and Robbins, S. E. (1990). Accuracy of Pedicular Screw Placement In Vivo. *Spine* 15, 11–14.

Global Pedicle Screw System Market by Product, Surgery Type, Indication, Application, Region, Industry Analysis, Size, Share, Growth, Trends, and Forecast 2018 to 2025 - Fior Markets Available at: https://www.fiormarkets.com/report/global-pedicle-screw-system-market-by-product-polyaxial-375967.html [Accessed October 26, 2020].

Grassi, L., Hraiech, N., Schileo, E., Ansaloni, M., Rochette, M., and Viceconti, M. (2011). Evaluation of the generality and accuracy of a new mesh morphing procedure for the human femur. *Med. Eng. Phys.* 33, 112–120. doi:10.1016/j.medengphy.2010.09.014.

Heimann, T., and Meinzer, H.-P. (2009). Statistical shape models for 3D medical image segmentation: a review. *Med. Image Anal.* 13, 543–563. doi:10.1016/j.media.2009.05.004.

Hingsammer, A. M., Vlachopoulos, L., Meyer, D. C., and Fürnstahl, P. (2015). Three-dimensional corrective osteotomies of mal-united clavicles—is the contralateral anatomy a reliable template for reconstruction? *Clin. Anat.* 28, 865–871. doi:10.1002/ca.22572.

Hoang, K. C., Khoo, B. C., Liu, G. R., Nguyen, N. C., and Patera, A. T. (2013). Rapid identification of material properties of the interface tissue in dental implant systems using reduced basis method. *Inverse Probl. Sci. Eng.* 21, 1310–1334. doi:10.1080/17415977.2012.757315.

Ignasiak, D., Dendorfer, S., and Ferguson, S. J. (2016). Thoracolumbar spine model with articulated ribcage for the prediction of dynamic spinal loading. *J. Biomech.* 49, 959–966. doi:10.1016/j.jbiomech.2015.10.010.

Inzana, J. A., Varga, P., and Windolf, M. (2016). Implicit modeling of screw threads for efficient finite element analysis of complex bone-implant systems. *J. Biomech.* 49, 1836–1844. doi:10.1016/j.jbiomech.2016.04.021.

Kirschke, J. S., Löffler, M., and Sekuboyina, A. (2020). Verse 2020. Available at: https://osf.io/t98fz/ [Accessed March 11, 2021].

Kopperdahl, D. L., Morgan, E. F., and Keaveny, T. M. (2002). Quantitative computed tomography estimates of the mechanical properties of human vertebral trabecular bone. *J. Orthop. Res.* 20, 801–805. doi:10.1016/S0736-0266(01)00185-1.

Krol, Z., Skadlubowicz, P., Hefti, F., and Krieg, A. H. (2013). Virtual reconstruction of pelvic tumor defects based on a gender-specific statistical shape model. *Comput. Aided Surg. Off. J. Int. Soc. Comput. Aided Surg.* 18, 142–153. doi:10.3109/10929088.2013.777973.

Kumar, A., Aujla, R., and Lee, C. (2015). The management of thoracolumbar burst fractures: a prospective study between conservative management, traditional open spinal surgery and minimally interventional spinal surgery. *SpringerPlus* 4, 204. doi:10.1186/s40064-015-0960-4.

Lauzeral, N., Borzacchiello, D., Kugler, M., George, D., Rémond, Y., Hostettler, A., et al. (2019). A model order reduction approach to create patient-specific mechanical models of human liver in computational medicine applications. *Comput. Methods Programs Biomed.* 170, 95–106. doi:10.1016/j.cmpb.2019.01.003.

Li, C., Zhou, Y., Wang, H., Liu, J., and Xiang, L. (2014). Treatment of Unstable Thoracolumbar Fractures through Short Segment Pedicle Screw Fixation Techniques Using Pedicle Fixation at the Level of the Fracture: A Finite Element Analysis. *PLoS ONE* 9. doi:10.1371/journal.pone.0099156.

Liebl, H., Schinz, D., Sekuboyina, A., Malagutti, L., Löffler, M. T., Bayat, A., et al. (2021). A Computed Tomography Vertebral Segmentation Dataset with Anatomical Variations and Multi-Vendor Scanner Data. *ArXiv210306360 Cs Eess*. Available at: http://arxiv.org/abs/2103.06360 [Accessed March 21, 2021].

Liu, H., Wang, H., Liu, J., Li, C., Zhou, Y., and Xiang, L. (2019). Biomechanical comparison of posterior intermediate screw fixation techniques with hybrid monoaxial and polyaxial pedicle screws in the treatment of thoracolumbar burst fracture: a finite element study. *J. Orthop. Surg.* 14, 122. doi:10.1186/s13018-019-1149-2.

Löffler, M. T., Sekuboyina, A., Jacob, A., Grau, A.-L., Scharr, A., El Husseini, M., et al. (2020a). A Vertebral Segmentation Dataset with Fracture Grading. *Radiol. Artif. Intell.* 2, e190138. doi:10.1148/ryai.2020190138.

Löffler, M. T., Sekuboyina, A., Jacob, A., Grau, A.-L., Scharr, A., El Husseini, M., et al. (2020b). A Vertebral Segmentation Dataset with Fracture Grading. *Radiol. Artif. Intell.* 2, e190138. doi:10.1148/ryai.2020190138.

Luboz, V., Bailet, M., Boichon Grivot, C., Rochette, M., Diot, B., Bucki, M., et al. (2018). Personalized modeling for real-time pressure ulcer prevention in sitting posture. *J. Tissue Viability* 27, 54–58. doi:10.1016/j.jtv.2017.06.002.

Luthi, M., Gerig, T., Jud, C., and Vetter, T. (2018). Gaussian Process Morphable Models. *IEEE Trans. Pattern Anal. Mach. Intell.* 40, 1860–1873. doi:10.1109/TPAMI.2017.2739743.

Magerl, F., Aebi, M., Gertzbein, S. D., Harms, J., and Nazarian, S. (1994). A comprehensive classification of thoracic and lumbar injuries. *Eur. Spine J.* 3, 184–201. doi:10.1007/BF02221591.

Mahar, A., Kim, C., Wedemeyer, M., Mitsunaga, L., Odell, T., Johnson, B., et al. (2007). Short-Segment Fixation of Lumbar Burst Fractures Using Pedicle Fixation at the Level of the Fracture. *Spine* 32, 1503–1507. doi:10.1097/BRS.0b013e318067dd24.

Manzoni, A., Quarteroni, A., and Rozza, G. (2012). Model reduction techniques for fast blood flow simulation in parametrized geometries. *Int. J. Numer. Methods Biomed. Eng.* 28, 604–625. doi:10.1002/cnm.1465.

Matsukawa, K., Yato, Y., Hynes, R. A., Imabayashi, H., Hosogane, N., Asazuma, T., et al. (2017). Cortical Bone Trajectory for Thoracic Pedicle Screws: A Technical Note. *Clin. Spine Surg.* 30, E497. doi:10.1097/BSD.0000000000000130.

Matsukawa, K., Yato, Y., and Imabayashi, H. (2020). Impact of Screw Diameter and Length on Pedicle Screw Fixation Strength in Osteoporotic Vertebrae: A Finite Element Analysis. *Asian Spine J.* doi:10.31616/asj.2020.0353.

Matsukawa, K., Yato, Y., Imabayashi, H., Hosogane, N., Abe, Y., Asazuma, T., et al. (2016). Biomechanical evaluation of fixation strength among different sizes of pedicle screws using the cortical bone trajectory: what is the ideal screw size for optimal fixation? *Acta Neurochir. (Wien)* 158, 465–471. doi:10.1007/s00701-016-2705-8.

Matsukawa, K., Yato, Y., Imabayashi, H., Hosogane, N., Asazuma, T., and Nemoto, K. (2015). Biomechanical evaluation of the fixation strength of lumbar pedicle screws using cortical bone trajectory: a finite element study. *J. Neurosurg. Spine* 23, 471–478. doi:10.3171/2015.1.SPINE141103.

Mobbs, R. J., Sivabalan, P., and Li, J. (2011). Technique, challenges and indications for percutaneous pedicle screw fixation. *J. Clin. Neurosci.* 18, 741–749. doi:10.1016/j.jocn.2010.09.019.

Molinari, L., and Falcinelli, C. (2021). On the human vertebra computational modeling: a literature review. *Meccanica*. doi:10.1007/s11012-021-01452-x.

Molinari, L., Falcinelli, C., Gizzi, A., and Di Martino, A. (2021). Effect of pedicle screw angles on the fracture risk of the human vertebra: A patient-specific computational model. *J. Mech. Behav. Biomed. Mater.* 116, 104359. doi:10.1016/j.jmbbm.2021.104359.

Monier-Faugere, M.-C., Chris Langub, M., and Malluche, H. H. (1998). “Chapter 8 - Bone Biopsies: A Modern Approach,” in *Metabolic Bone Disease and Clinically Related*

Disorders (Third Edition), eds. L. V. Avioli and S. M. Krane (San Diego: Academic Press), 237–280e. doi:10.1016/B978-012068700-8/50009-8.

Morgan, E. F., Bayraktar, H. H., and Keaveny, T. M. (2003). Trabecular bone modulus–density relationships depend on anatomic site. *J. Biomech.* 36, 897–904. doi:10.1016/S0021-9290(03)00071-X.

Musuamba, F. T., Skottheim Rusten, I., Lesage, R., Russo, G., Bursi, R., Emili, L., et al. (2021). Scientific and regulatory evaluation of mechanistic in silico drug and disease models in drug development: building model credibility. *CPT Pharmacomet. Syst. Pharmacol.* Available at: https://eprints.whiterose.ac.uk/175265/ [Accessed December 14, 2021].

Nakahashi, M., Uei, H., Tokuhashi, Y., Maseda, M., Sawada, H., Soma, H., et al. (2019). Vertebral fracture in elderly female patients after posterior fusion with pedicle screw fixation for degenerative lumbar pathology: a retrospective cohort study. *BMC Musculoskelet. Disord.* 20, 259. doi:10.1186/s12891-019-2534-z.

Newcomb, A. G. U. S., Baek, S., Kelly, B. P., and Crawford, N. R. (2017). Effect of screw position on load transfer in lumbar pedicle screws: A non-idealized finite element analysis. *Comput. Methods Biomech. Biomed. Engin.* 20, 182–192. doi:10.1080/10255842.2016.1209187.

Niinomi, M., and Boehlert, C. J. (2015). "Titanium Alloys for Biomedical Applications," in *Advances in Metallic Biomaterials: Tissues, Materials and Biological Reactions* Springer Series in Biomaterials Science and Engineering., eds. M. Niinomi, T. Narushima, and M. Nakai (Berlin, Heidelberg: Springer), 179–213. doi:10.1007/978-3-662-46836-4_8.

Niroomandi, S., Alfaro, I., Cueto, E., and Chinesta, F. (2012). Accounting for large deformations in real-time simulations of soft tissues based on reduced-order models. *Comput. Methods Programs Biomed.* 105, 1–12. doi:10.1016/j.cmpb.2010.06.012.

Niroomandi, S., Perrier, A., Bucki, M., and Payan, Y. (2020). "Chapter 5 - Real-time computer modeling in prevention of foot pressure ulcer using patient-specific finite element model and model order reduction techniques," in *Innovations and Emerging Technologies in Wound Care*, ed. A. Gefen (Academic Press), 87–102. doi:10.1016/B978-0-12-815028-3.00005-5.

Ovesy, M., Voumard, B., and Zysset, P. (2018). A nonlinear homogenized finite element analysis of the primary stability of the bone-implant interface. *Biomech. Model. Mechanobiol.* 17, 1471–1480. doi:10.1007/s10237-018-1038-3.

Oxland, T. R., Lin, R.-M., and Panjabi, M. M. (1992). Three-Dimensional mechanical properties of the thoracolumbar junction. *J. Orthop. Res.* 10, 573–580. doi:https://doi.org/10.1002/jor.1100100412.

Pahr, D. H., Schwiedrzik, J., Dall'Ara, E., and Zysset, P. K. (2014). Clinical versus pre-clinical FE models for vertebral body strength predictions. *J. Mech. Behav. Biomed. Mater.* 33, 76–83. doi:10.1016/j.jmbbm.2012.11.018.

Palanca, M., Oliviero, S., and Dall'Ara, E. (2022). MicroFE models of porcine vertebrae with induced bone focal lesions: Validation of predicted displacements with digital volume correlation. *J. Mech. Behav. Biomed. Mater.* 125, 104872. doi:10.1016/j.jmbbm.2021.104872.

Pascoletti, G., Aldieri, A., Terzini, M., Bhattacharya, P., Calì, M., and Zanetti, E. M. (2021). Stochastic PCA-Based Bone Models from Inverse Transform Sampling: Proof of Concept for Mandibles and Proximal Femurs. *Appl. Sci.* 11, 5204. doi:10.3390/app11115204.

Perera, A., Qureshi, A., and Brecknell, J. E. (2015). Mono-segment fixation of thoracolumbar burst fractures. *Br. J. Neurosurg.* 29, 358–361. doi:10.3109/02688697.2014.987216.

Perrier, A., Bucki, M., Luboz, V., Vuillerme, N., and Payan, Y. (2015). 3D musculoskeletal finite element analysis of the foot kinematics under muscle activation with and without ankle arthrodesis. *Comput. Methods Biomech. Biomed. Engin.* 18, 2022–2023. doi:10.1080/10255842.2015.1069605.

Pesce, V., Piazzolla, A., Moretti, L., Carlucci, S., Parato, C., Maxy, P., et al. (2013). The vertebral biomechanic previous and after kyphoplasty. *Aging Clin. Exp. Res.* 25, 71–74. doi:10.1007/s40520-013-0073-2.

Plessers, K., Berghe, P. V., Dijck, C. V., Wirix-Speetjens, R., Debeer, P., Jonkers, I., et al. (2018). Virtual reconstruction of glenoid bone defects using a statistical shape model. *J. Shoulder Elbow Surg.* 27, 160–166. doi:10.1016/j.jse.2017.07.026.

Ponnusamy, K. E., Iyer, S., Gupta, G., and Khanna, A. J. (2011). Instrumentation of the osteoporotic spine: biomechanical and clinical considerations. *Spine J.* 11, 54–63. doi:10.1016/j.spinee.2010.09.024.

Prud'homme, M., Barrios, C., Rouch, P., Charles, Y. P., Steib, J.-P., and Skalli, W. (2015). Clinical Outcomes and Complications After Pedicle-anchored Dynamic or Hybrid Lumbar Spine Stabilization: A Systematic Literature Review. *J. Spinal Disord. Tech.* 28, E439–E448. doi:10.1097/BSD.0000000000000092.

Rajaee, S. S., Bae, H. W., Kanim, L. E. A., and Delamarter, R. B. (2012). Spinal fusion in the United States: analysis of trends from 1998 to 2008. *Spine* 37, 67–76. doi:10.1097/BRS.0b013e31820cccfb.

Rijsbergen, M. van, van Rietbergen, B., Barthelemy, V., Eltes, P., Lazáry, Á., Lacroix, D., et al. (2018). Comparison of patient-specific computational models vs. clinical follow-up, for adjacent segment disc degeneration and bone remodelling after spinal fusion. *PloS One* 13, e0200899. doi:10.1371/journal.pone.0200899.

Rohlmann, A., Bergmann, G., and Graichen, F. (1997). Loads on an internal spinal fixation device during walking. *J. Biomech.* 30, 41–47. doi:10.1016/S0021-9290(96)00103-0.

Rohlmann, A., Graichen, F., Kayser, R., Bender, A., and Bergmann, G. (2008). Loads on a telemeterized vertebral body replacement measured in two patients. *Spine* 33, 1170–1179. doi:10.1097/BRS.0b013e3181722d52.

Salhi, A., Burdin, V., Boutillon, A., Brochard, S., Mutsvangwa, T., and Borotikar, B. (2020). Statistical Shape Modeling Approach to Predict Missing Scapular Bone. *Ann. Biomed. Eng.* 48, 367–379. doi:10.1007/s10439-019-02354-6.

Sanderson, P. L., Fraser, R. D., Hall, D. J., Cain, C. M. J., Osti, O. L., and Potter, G. R. (1999). Short segment fixation of thoracolumbar burst fractures without fusion. *Eur. Spine J.* 8, 495–500. doi:10.1007/s005860050212.

Santoni, B. G., Hynes, R. A., McGilvray, K. C., Rodriguez-Canessa, G., Lyons, A. S., Henson, M. a. W., et al. (2009). Cortical bone trajectory for lumbar pedicle screws. *Spine J. Off. J. North Am. Spine Soc.* 9, 366–373. doi:10.1016/j.spinee.2008.07.008.

Scalismo - Scalable Image and Shape Modelling | Scalismo Available at: https://scalismo.org/ [Accessed March 5, 2021].

Schileo, E., Dall'Ara, E., Taddei, F., Malandrino, A., Schotkamp, T., Baleani, M., et al. (2008). An accurate estimation of bone density improves the accuracy of subject-specific finite element models. *J. Biomech.* 41, 2483–2491. doi:10.1016/j.jbiomech.2008.05.017.

Schousboe, J. T. (2016). Epidemiology of Vertebral Fractures. *J. Clin. Densitom.* 19, 8–22. doi:10.1016/j.jocd.2015.08.004.

Sekuboyina, A., Bayat, A., Husseini, M. E., Löffler, M., Li, H., Tetteh, G., et al. (2020). VerSe: A Vertebrae Labelling and Segmentation Benchmark for Multi-detector CT Images. *ArXiv200109193 Cs Eess*. Available at: http://arxiv.org/abs/2001.09193 [Accessed March 5, 2021].

Sieger, D., Menzel, S., and Botsch, M. (2013). High Quality Mesh Morphing Using Triharmonic Radial Basis Functions. in *Proceedings of the 21st International Meshing Roundtable*, eds. X. Jiao and J.-C. Weill (Berlin, Heidelberg: Springer), 1–15. doi:10.1007/978-3-642-33573-0_1.

Su, Y., Wang, X., Ren, D., Liu, Y., Liu, S., and Wang, P. (2018). A finite element study on posterior short segment fixation combined with unilateral fixation using pedicle screws for stable thoracolumbar fracture. *Medicine (Baltimore)* 97. doi:10.1097/MD.0000000000012046.

Sun, X., Wang, H., Wang, W., Li, N., Hämäläinen, T., Ristaniemi, T., et al. (2021). A Statistical Model of Spine Shape and Material for Population-Oriented Biomechanical Simulation. *IEEE Access*, 1–1. doi:10.1109/ACCESS.2021.3129097.

Taddei, F., Schileo, E., Helgason, B., Cristofolini, L., and Viceconti, M. (2007). The material mapping strategy influences the accuracy of CT-based finite element models of bones: an evaluation against experimental measurements. *Med. Eng. Phys.* 29, 973–979. doi:10.1016/j.medengphy.2006.10.014.

Ueno, M., Sakai, R., Tanaka, K., Inoue, G., Uchida, K., Imura, T., et al. (2015). Should we use cortical bone screws for cortical bone trajectory? *J. Neurosurg. Spine* 22, 416–421. doi:10.3171/2014.9.SPINE1484.

unibas-gravis/scalismo (2021). Graphics and Vision Research Group University of Basel Available at: https://github.com/unibas-gravis/scalismo [Accessed March 5, 2021].

Van Meirhaeghe, J., Bastian, L., Boonen, S., Ranstam, J., Tillman, J. B., and Wardlaw, D. (2013). A Randomized Trial of Balloon Kyphoplasty and Nonsurgical Management for Treating

Acute Vertebral Compression Fractures. *Spine* 38, 971–983. doi:10.1097/BRS.0b013e31828e8e22.

Vanden Berghe, P., Demol, J., Gelaude, F., and Vander Sloten, J. (2017). Virtual anatomical reconstruction of large acetabular bone defects using a statistical shape model. *Comput. Methods Biomech. Biomed. Engin.* 20, 577–586. doi:10.1080/10255842.2016.1265110.

Varghese, B., Short, D., Penmetsa, R., Goswami, T., and Hangartner, T. (2011). Computed-tomography-based finite-element models of long bones can accurately capture strain response to bending and torsion. *J. Biomech.* 44, 1374–1379. doi:10.1016/j.jbiomech.2010.12.028.

Verma, K., Boniello, A., and Rihn, J. (2016). Emerging Techniques for Posterior Fixation of the Lumbar Spine. *JAAOS - J. Am. Acad. Orthop. Surg.* 24, 357–364. doi:10.5435/JAAOS-D-14-00378.

Wang, E., Tran, K. L., D'heygere, E., and Prisman, E. (2021). Predicting the Premorbid Shape of a Diseased Mandible. *The Laryngoscope* 131, E781–E786. doi:https://doi.org/10.1002/lary.29009.

Wang, H., Mo, Z., Han, J., Liu, J., Li, C., Zhou, Y., et al. (2018). Extent and location of fixation affects the biomechanical stability of short- or long-segment pedicle screw technique with screwing of fractured vertebra for the treatment of thoracolumbar burst fractures. *Medicine (Baltimore)* 97, e11244. doi:10.1097/MD.0000000000011244.

Wang, J., Zhou, Y., Zhang, Z. F., Li, C. Q., Zheng, W. J., and Liu, J. (2013). Radiological study on disc degeneration of thoracolumbar burst fractures treated by percutaneous pedicle screw fixation. *Eur. Spine J.* 22, 489–494. doi:10.1007/s00586-012-2462-1.

Wang, M. Y., Anderson, D. G., Poelstra, K. A., and Ludwig, S. C. (2008). MINIMALLY INVASIVE POSTERIOR FIXATION. *Neurosurgery* 63, A197–A203. doi:10.1227/01.NEU.0000320434.83458.10.

Wang, W., Pei, B., Pei, Y., Shi, Z., Kong, C., Wu, X., et al. (2019). Biomechanical effects of posterior pedicle fixation techniques on the adjacent segment for the treatment of thoracolumbar burst fractures: a biomechanical analysis. *Comput. Methods Biomech. Biomed. Engin.* 22, 1083–1092. doi:10.1080/10255842.2019.1631286.

Weese, J., Kaus, M., Lorenz, C., Lobregt, S., Truyen, R., and Pekar, V. (2001). Shape Constrained Deformable Models for 3D Medical Image Segmentation. in *Information Processing in Medical Imaging* Lecture Notes in Computer Science., eds. M. F. Insana and R. M. Leahy (Berlin, Heidelberg: Springer), 380–387. doi:10.1007/3-540-45729-1_38.

Widmer, J., Fasser, M.-R., Croci, E., Spirig, J., Snedeker, J. G., and Farshad, M. (2020). Individualized prediction of pedicle screw fixation strength with a finite element model. *Comput. Methods Biomech. Biomed. Engin.* 23, 155–167. doi:10.1080/10255842.2019.1709173.

Wirtz, D. C., Schiffers, N., Pandorf, T., Radermacher, K., Weichert, D., and Forst, R. (2000). Critical evaluation of known bone material properties to realize anisotropic FE-simulation of the proximal femur. *J. Biomech.* 33, 1325–1330. doi:10.1016/S0021-9290(00)00069-5.

Wood, K. B., Li, W., Lebl, D. S., and Ploumis, A. (2014). Management of thoracolumbar spine fractures. *Spine J.* 14, 145–164. doi:10.1016/j.spinee.2012.10.041.

Wu, J., Cai, M., Li, J., Cao, L., Xu, L., Li, N., et al. (2019). Development and validation of a semi-automatic landmark extraction method for mesh morphing. *Med. Eng. Phys.* 70, 62–71. doi:10.1016/j.medengphy.2019.04.007.

Xu, G., Fu, X., Du, C., Ma, J., Li, Z., Tian, P., et al. (2014). Biomechanical comparison of mono-segment transpedicular fixation with short-segment fixation for treatment of thoracolumbar fractures: A finite element analysis. *Proc. Inst. Mech. Eng. [H]* 228, 1005–1013. doi:10.1177/0954411914552308.

Xu, Y., and Goodacre, R. (2018). On Splitting Training and Validation Set: A Comparative Study of Cross-Validation, Bootstrap and Systematic Sampling for Estimating the Generalization Performance of Supervised Learning. *J. Anal. Test.* 2, 249–262. doi:10.1007/s41664-018-0068-2.

Yeung, S., Toor, A., Deib, G., Zhang, J., Besier, T., and Fernandez, J. (2020). Relationship between lower lumbar spine shape and patient bone metabolic activity as characterised by 18F NaF bio-markers. *Comput. Biol. Med.* 116, 103529. doi:10.1016/j.compbiomed.2019.103529.

Zhang, J., Weir, V., Fajardo, L., Lin, J., Hsiung, H., and Ritenour, E. (2009). Dosimetric characterization of a cone-beam O-arm (TM) imaging system. *J. X-Ray Sci. Technol.* 17, 305–17. doi:10.3233/XST-2009-0231.

Zindrick, M. R., Wiltse, L. L., Widell, E. H., Thomas, J. C., Holland, W. R., Field, B. T., et al. (1986). A biomechanical study of intrapeduncular screw fixation in the lumbosacral spine. *Clin. Orthop.*, 99–112.

Zou, X. (2018). Simulation tools for biomechanical applications with PGD-based reduced order models. *TDX Tesis Dr. En Xarxa*. Available at: https://upcommons.upc.edu/handle/2117/116305 [Accessed November 24, 2021].

Zou, X., Conti, M., Díez, P., and Auricchio, F. (2018). A nonintrusive proper generalized decomposition scheme with application in biomechanics. *Int. J. Numer. Methods Eng.* 113, 230–251. doi:10.1002/nme.5610.

Appendix

Appendix A1: Comparison between simplified and realistic screw geometry – additional results

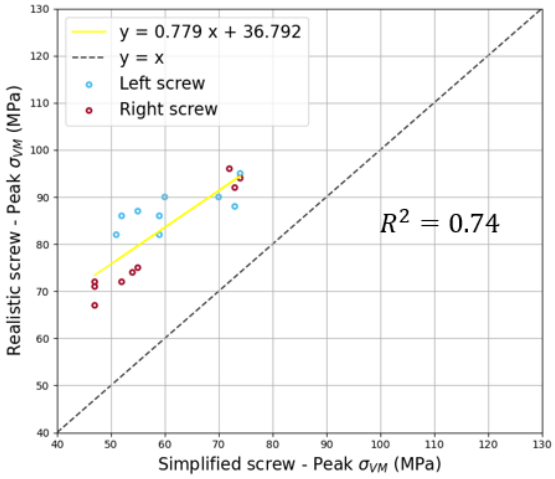

Figure A1.1 – Linear correlation between peak σ_{VM} for the realistic and simplified models (Patient #1, two sides, nine sizes).

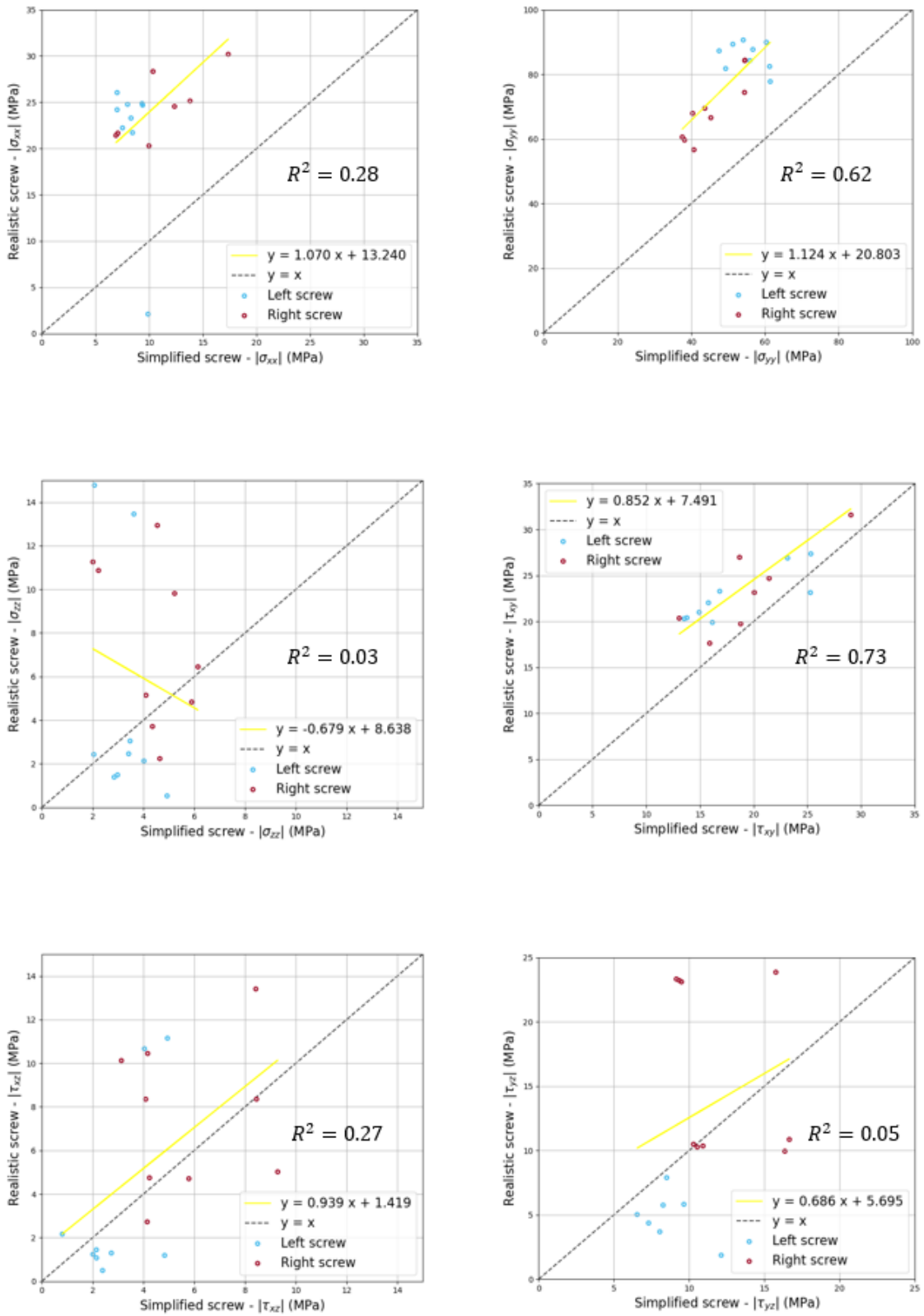

Figure 2 – Linear correlation between stress components evaluated at the location of the peak σ_{VM} for the realistic and simplified models (Patient #1, two sides, nine sizes).

Appendix A2: ROM of the strain – additional results

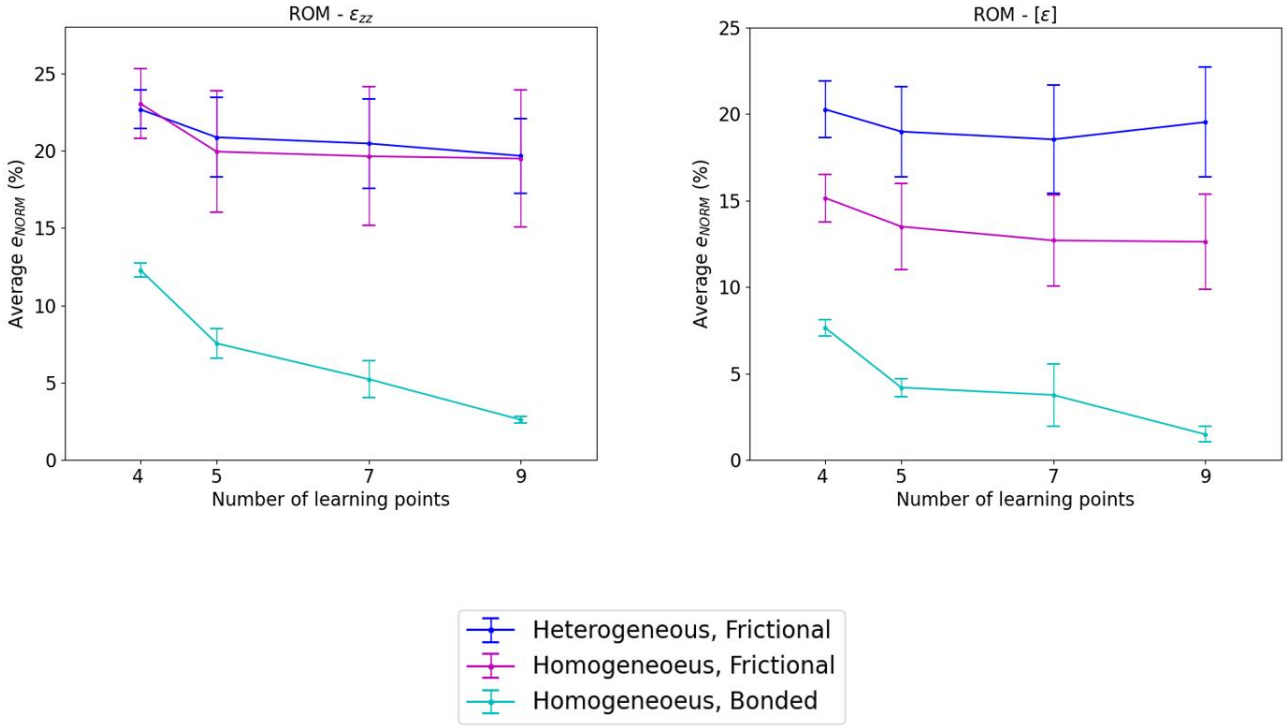

Figure A2.1 – Average ROM errors over the validation snapshots, in function of the number of learning points, for FE models with different combinations of bone material models and screws-bone interface, for the ROM of the zz component (along the direction of loading) of the strain (A) and the ROM of the six components of the strain tensor together (B).

Appendix A3: Comparison between linear interpolation and ROM

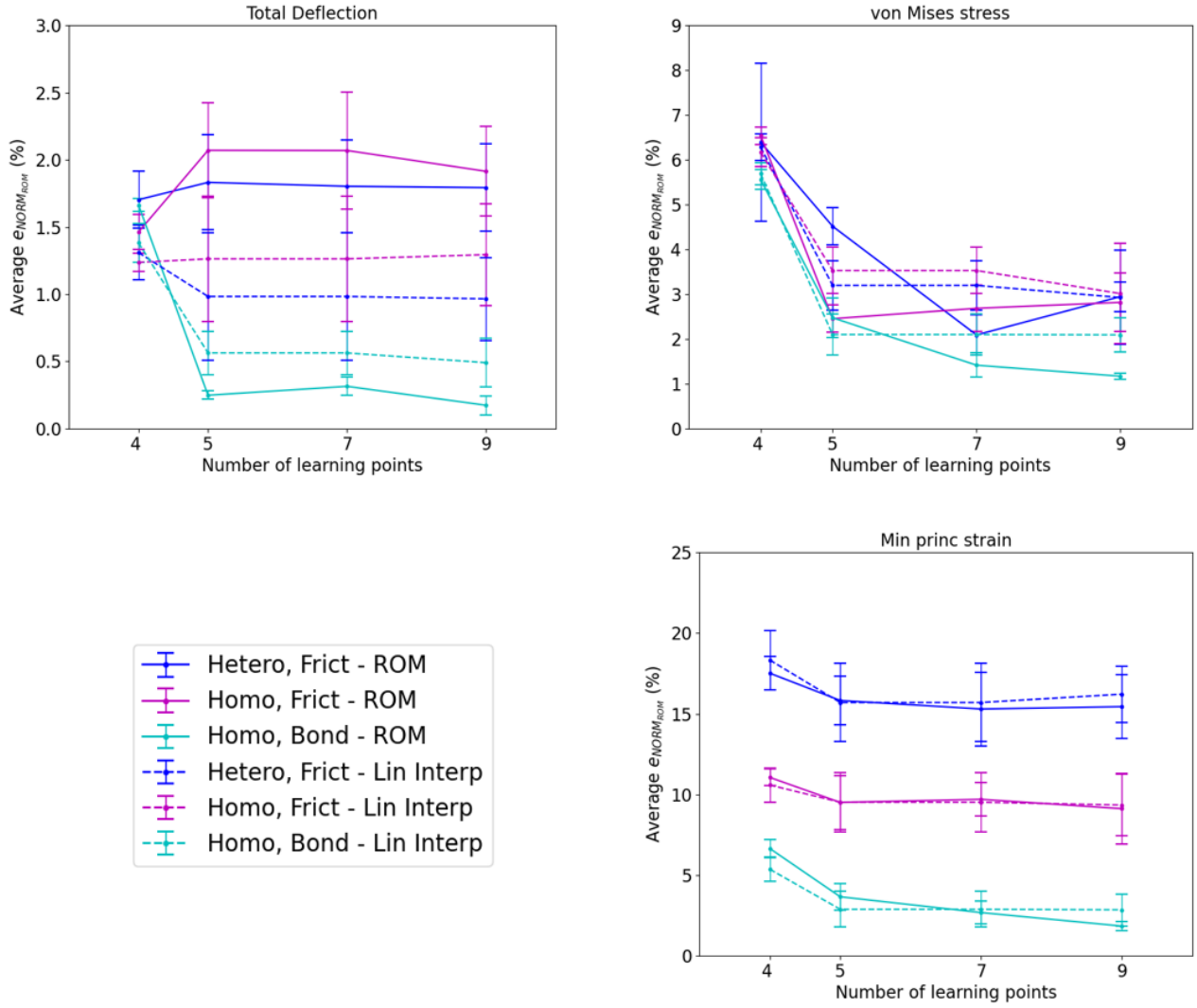

Figure A3.1 – Comparison between the errors obtained by standard linear interpolation (dashed lines) and by using Reduced Order Modelling techniques (continuous lines) in the case with two shape parameters (Diameter and Length of screws). Average errors over the validation snapshots are reported in function of the number of learning points, for FE models with different combinations of bone material models and screws-bone interface, for the total deflection (A), the von Mises stress (B) and the minimum principal strain (C).

Appendix A4: Table of correspondence between patient IDs and Verse 2020 IDs

Patient #	Verse 2020 ID	In-plane resolution (mm x mm)	Slice thickness (mm)	Sex	Age (years)	CT-scanner
1	517	0.68 x 0.68	0.9	M	42	3
2	540	0.98 x 0.98	0.9	W	19	3
3	550	0.78 x 0.78	0.8	M	38	2
4	075	1 x 1	1	W	56.6	2
5	552	0.75 x 0.75	0.9	M	67	3
6	570	0.91 x 0.91	0.9	M	50	3
7	591	0.81 x 0.81	0.9	M	67	3
8	597	0.80 x 0.80	0.9	M	64	2
9	141	1 x 1	2	W	62.6	4
10	254	1 x 1	2	M	27.4	4
11	702	0.80 x 0.80	3	M	77	10
12	402	1 x 1	2	M	35.2	4
13	407	1 x 1	2	M	18.9	4
14	413	1 x 1	1	W	23	2
15	415	1 x 1	2	M	34.8	4
16	500	0.68 x 0.68	0.90	M	35	3
17	708	0.78 x 0.78	0.80	W	50	10
18	521	0.68 x 0.68	1	W	35	7
19	532	0.93 x 0.93	0.6	M	23	4
20	533	0.72 x 0.72	0.6	M	41	4
21	508	0.988 x 0.98	0.70	M	39	4
22	522	0.73 x 0.73	0.9	W	71	3
23	529	0.68 x 0.68	0.9	W	20	3
24	547	0.92 x 0.92	0.9	W	24	3
25	763	1.07 x 1.07	3	M	19	9
26	554	0.92 x 0.92	0.9	M	70	3
27	805	0.73 x 0.73	0.7	W	44	8
28	569	0.73 x 0.73	0.9	W	46	3
29	573	0.98 x 0.98	0.9	W	37	2
30	576	0.78 x 0.78	0.9	W	36	3

31	580	0.76 x 0.76	0.9	M	27	3
32	606	0.68 x 0.68	0.45	W	58	3
33	609	0.68 x 0.68	0.9	M	31	3
34	502	0.98 x 0.98	0.6	W	35	4
35	618	0.98 x 0.98	0.9	M	28	2
36	627	0.78 x 0.78	0.9	W	47	3
37	636	0.75 x 0.75	0.9	W	42	3
38	703	0.66 x 0.66	0.8	M	32	10
39	753	0.83 x 0.83	2.5	W	28	9
40	761	1.31 x 1.31	3	M	36	9

Table A4.1- Patient IDs and Verse 2020 IDs, voxel size, sex (M = man, W = woman), age and CT-scan used for the acquisition of images (CT-Scanner (2: Philips ICT; 3: Philips IQON, 4: Siemens Somatom AS+; 8 Siemens external; 9: GE external; 10 Toshiba external) (Löffler et al., 2020b).

Appendix A5: Creation of geometries of vertebral bodies

The construction of the dataset of vertebral bodies of 40 patients from the segmentation masks of entire vertebrae was adopted after comparison with a different method acting directly on STL surface meshes in Ansys® SpaceClaim Release 20.2 (Ansys Inc., Canonsburg, PA, USA). This method consisted in generating first a surface mesh from the segmentation masks after application of a gaussian smoothing filter with a standard deviation of 0.8 mm (3DSlicer, v4.11.0). Then, each vertebra was manually cut with a coronal plane parallel to the posterior wall of the vertebral body cutting the pedicles at approximately 3 mm from the vertebral bodies (Figure A3).

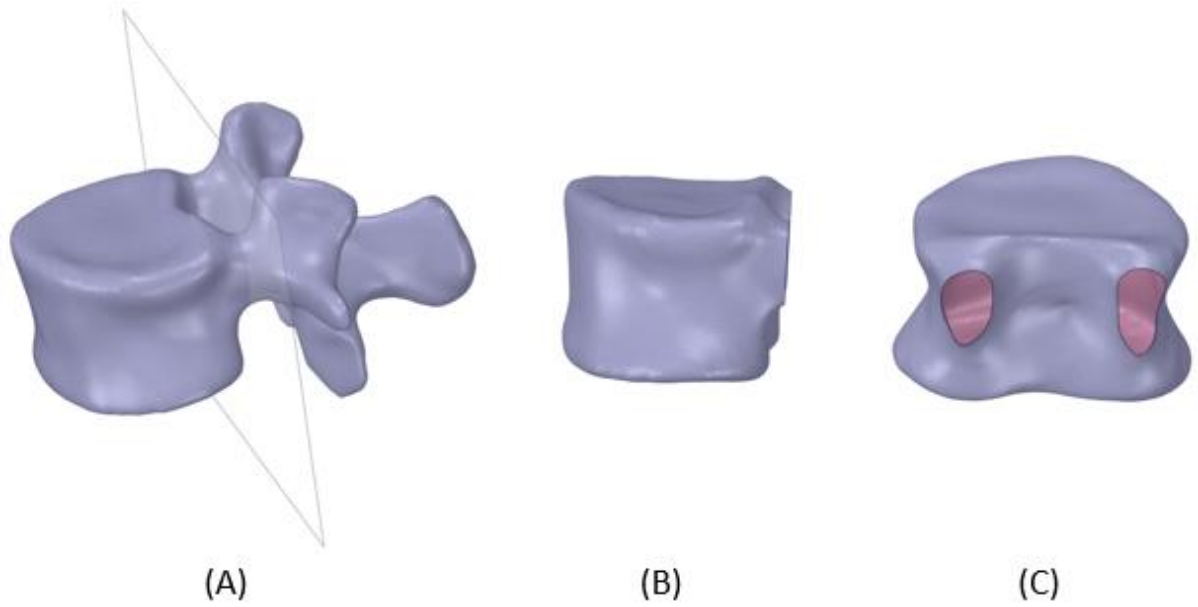

Figure A3.1 - An example of geometry obtained by cutting the STL of a vertebra with a coronal plane (Patient #1 L1). A view of the vertebra and the cutting plane (A). A lateral (B) and posterior (C) view of the vertebral body after the cut.

This procedure resulted in including in the geometric model two holes at the posterior part of the vertebral body corresponding to the pedicles. However, the morphed geometries presented Hausdorff distances higher than 2 mm (Table A4.) with respect to the original geometries, and were difficult to morph because of the sharpness of the mesh at the level of the holes. In fact, it was noted that the Hausdorff distance often occurred at the level of the two holes (Figure A5.2). In addition, including in the geometry the part of the pedicles that join with the vertebral body would result in an additional characteristic that the statistical model would represent. In fact, it is expected that some modes would refer to the shape of the pedicles. As this characteristic is not relevant for this application, it is preferable to include only the vertebral body within the model.

Vertebral level	Mean error (mm)		Hausdorff distance (mm)	
	Average ± st dev	**(Min, Max)**	**Average ± st dev**	**(Min , Max)**
T12	0.32 ± 0.03	(0.27, 0.39)	2.95 ± 0.58	(2.14, 4.37)
L1	0.30 ± 0.03	(0.22, 0.37)	2.29 ± 0.34	(1.78, 3.04)
L2	0.30 ± 0.03	(0.25, 0.36)	2.28 ± 0.40	(1.58, 3.20)
T12, L1 and L2	0.31 ± 0.03	(0.22, 0.39)	2.28 ± 0.34	(1.58, 4.37)

Table A4.1 - Mean error and Hausdorff distance (mm) between the morphed mesh and the original geometry, averaged over all the patients, for T12, L1 and L2 levels, and averaged over the three levels.

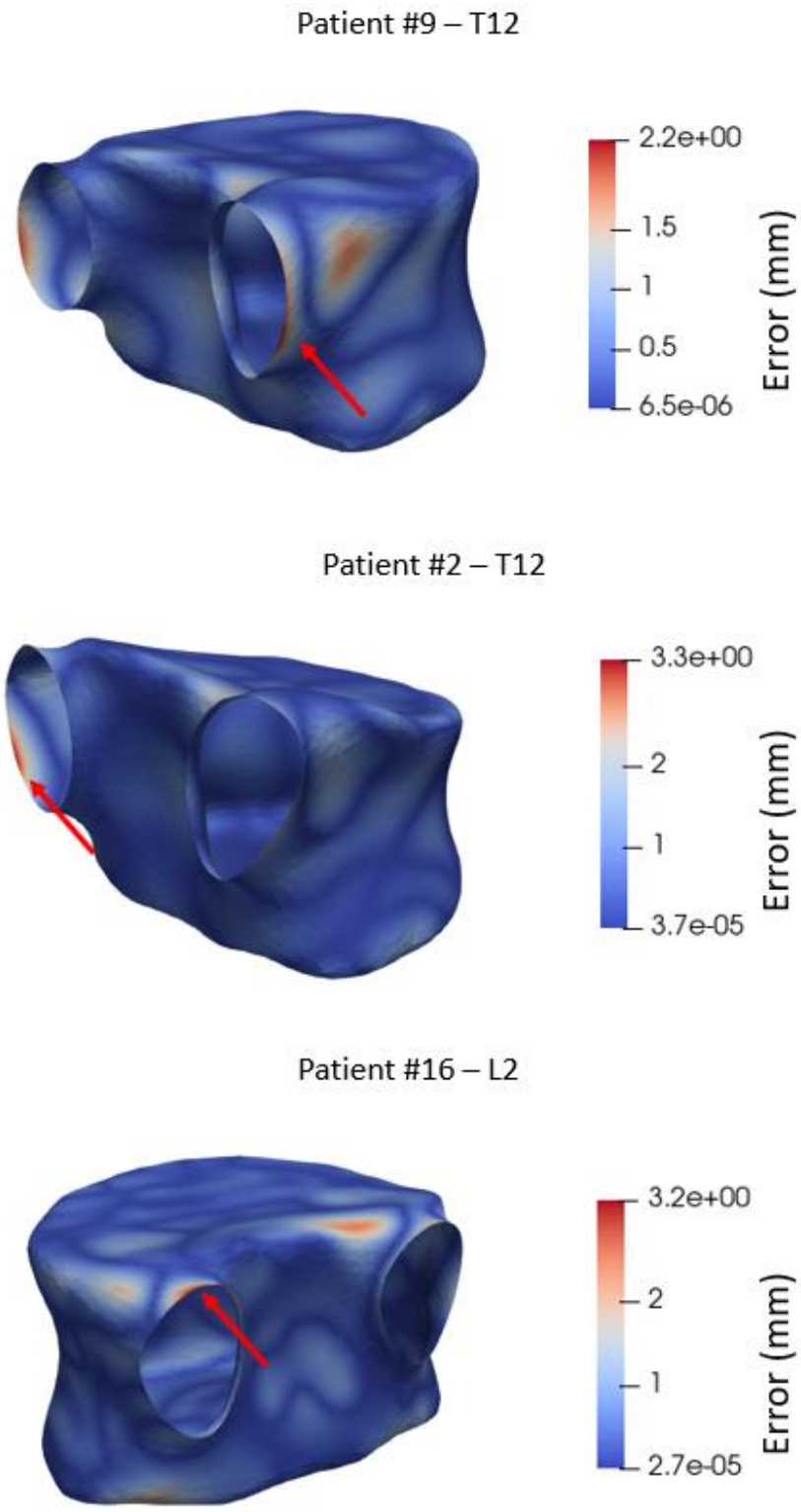

Figure A5.2 - Examples of error maps showing a concentration of the mesh morphing error at the pedicles. Error maps for Patient #9 (T12) (A), Patient #2 (T12) and Patient #16 (L2) are showed. Red arrows indicate the area where the Hausdorff distance occurred.

Appendix A6: Prediction of the shape of L1 – additional results

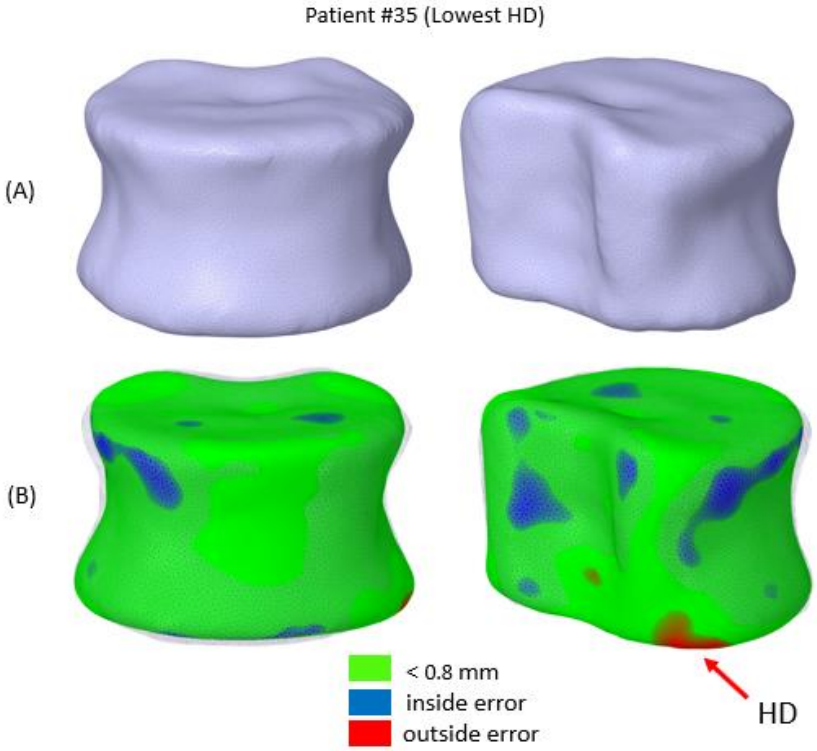

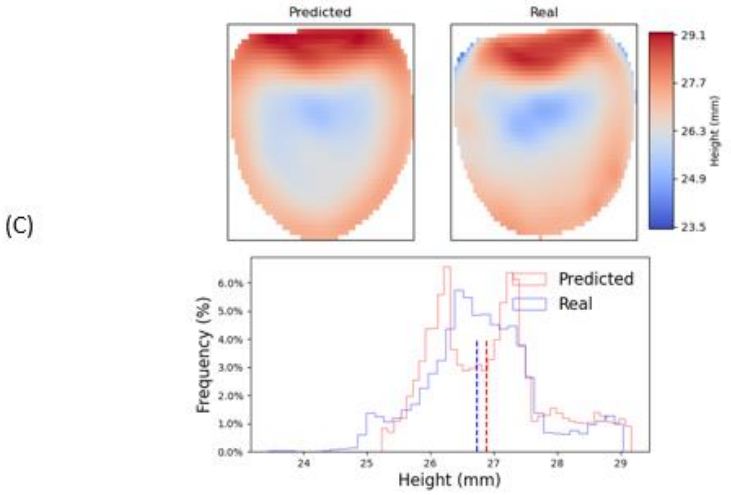

(D)

Mean error (mm)	0.45
Hausdorff distance (mm)	1.38
Median height error (mm)	0.15

Figure A6.1- Report for Patient #35.

Patient #40 (Average HD)

(A)

(B)

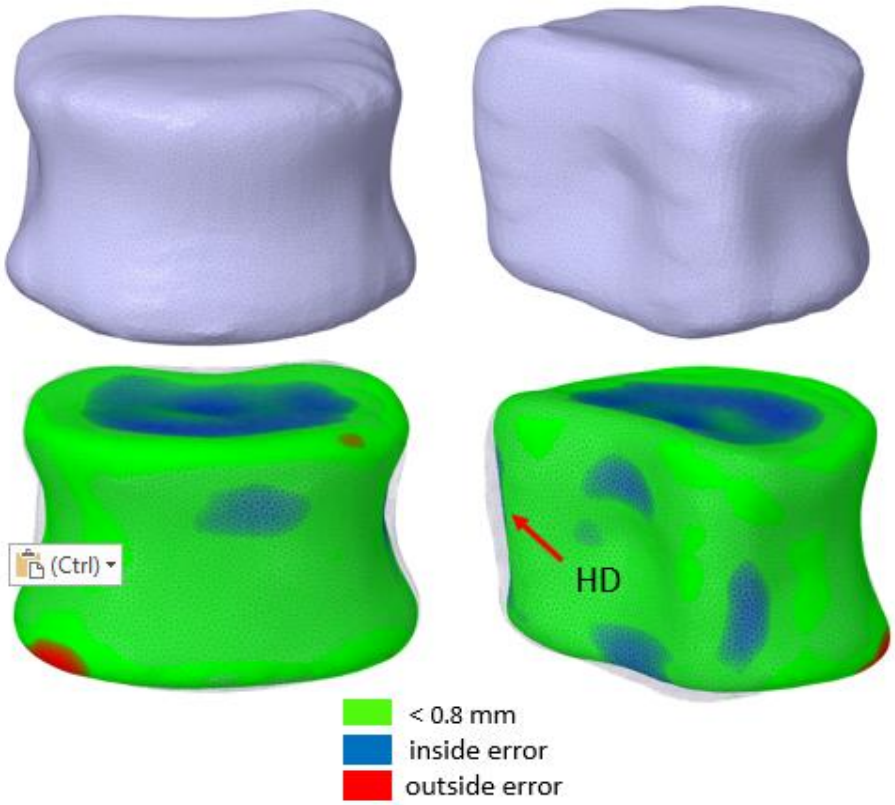

(C)

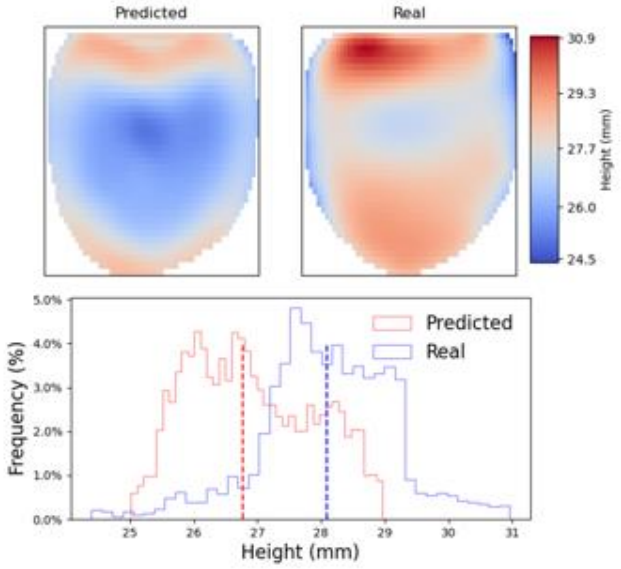

(D)

Mean error (mm)	0.56
Hausdorff distance (mm)	2.05
Median height error (mm)	-1.31

Figure A6.2- Report for Patient #40.

Patient #11 (Highest HD)

(A)

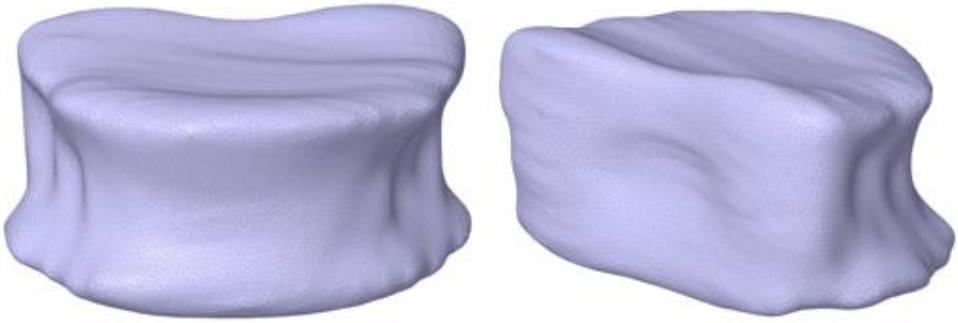

(B)

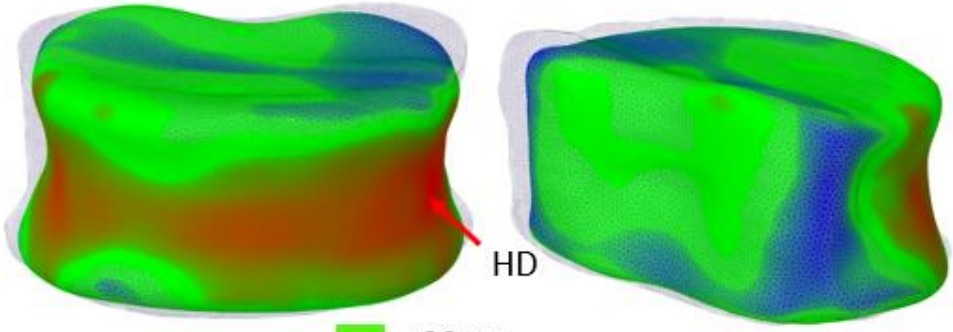

HD

< 0.8 mm
inside error
outside error

(C)

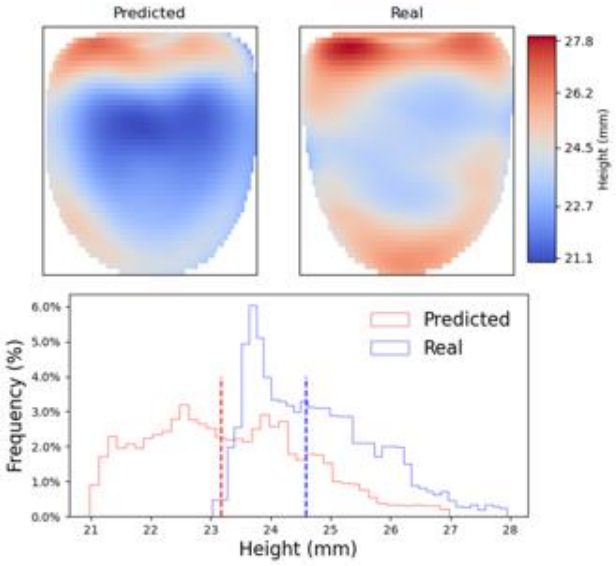

(D)

Mean error (mm)	0.96
Hausdorff distance (mm)	4.52
Median height error (mm)	-1.41

Figure A6.3- Report for Patient #11.